NOVEL ANTI-JAM ANTENNAS FOR AIRBORNE GPS NAVIGATION

A DISSERTATION
SUBMITTED TO THE DEPARTMENT OF ELECTRICAL ENGINEERING
AND THE COMMITTEE ON GRADUATE STUDIES
OF STANFORD UNIVERSITY
IN PARTIAL FULFILLMENT OF THE REQUIREMENTS
FOR THE DEGREE OF
DOCTOR OF PHILOSOPHY

Frank Neil Bauregger
August 2003

UMI Number: 3104193

UMI®

UMI Microform 3104193

Copyright 2003 by ProQuest Information and Learning Company.
All rights reserved. This microform edition is protected against
unauthorized copying under Title 17, United States Code.

ProQuest Information and Learning Company
300 North Zeeb Road
P.O. Box 1346
Ann Arbor, MI 48106-1346

© Copyright by Frank Neil Bauregger 2003
All Rights Reserved

I certify that I have read this dissertation and that, in my opinion, it is fully adequate in scope and quality as a dissertation for the degree of Doctor of Philosophy.

Per K. Enge
(Principal Adviser)

I certify that I have read this dissertation and that, in my opinion, it is fully adequate in scope and quality as a dissertation for the degree of Doctor of Philosophy.

Bruce B. Lusignan

I certify that I have read this dissertation and that, in my opinion, it is fully adequate in scope and quality as a dissertation for the degree of Doctor of Philosophy.

Dennis M. Akos

Approved for the University Committee on Graduate Studies.

Abstract

The Global Positioning System (GPS) is a worldwide passive radio navigation system that has found use in many civilian applications such as personal navigation by hikers, motorists, mariners, and aviators. In addition, GPS has become a standard means of providing demanding time transfer and frequency calibration services. The capabilities and performance of GPS are so impressive the FAA has mandated that GPS be incorporated into the next generation aircraft landing system. The Local- and Wide-Area Augmentation Systems (LAAS/WAAS) are the enabling technologies for this advanced guidance system. Despite the robustness of WAAS and LAAS, users may lose these services if strong radio frequency interference (RFI) is present at the airborne receiver. Spurs from high power television and cellular phone transmitters are examples of possible unintentional RFI sources. Intentional RFI may arise from terrorist groups or simply from disgruntled individuals. Regardless of the source, RFI presents a potential danger to the aircraft and its passengers, especially during GPS guided approaches in poor visibility conditions. Since military users of GPS must plan for and countermand intentional jamming of the GPS signal, military grade GPS equipment is designed to handle these situations. For example, adaptive null-steering antenna arrays for military aircraft can steer 20 - 40 dB nulls toward multiple jammers. However, these antennas are complex and bulky. Because of their expense, they are generally not attractive to general aviation (GA) pilots. In fact, there is no commonly available anti-jam GPS antenna on the market today suitable for civil aviation.

In this thesis, two antenna designs are proposed that serve as simple, small, and inexpensive anti-jam GPS antennas. The dielectric cavity antenna (DCA) makes use

of an artificially soft surface to reduce the signal strength of ground-based jammers. A 2.5-D FDTD code was developed to simulate the performance of this antenna. The code is used to compute far-field radiation patterns of the antenna. In order to validate the concept of the DCA, a prototype antenna was constructed and tested. It was determined that the DCA provides modest (3 - 10 dB) protection against ground based jammers. The antenna attenuates low elevation satellites however, and is not the ideal stand alone solution to the problem at hand.

The dual patch reconfigurable antenna (DPRA) is an improved antenna design that employs two modes of operation. A wide-angle mode is selected for GPS navigation when no RFI is present, and allows reception of all visible GPS satellites. If RFI is present, the antenna may be placed in anti-jam mode, which rejects ground-based RFI and enhances signals from high elevation satellites. Mode switching is accomplished by means of a DC control signal on the feedline, and may be performed manually or automatically. The DPRA is only slightly larger than conventional aviation GPS antennas, and may replace existing antennas with no modification to the fuselage. The DPRA was analyzed with an improved multiport network method (MNM) technique. The standard rectangular patch MNM model was modified to account for the presence of PIN diodes embedded within the patch substrate. These PIN diodes are required to isolate the wide-angle and anti-jam modes. The DPRA has been built and tested in flight. Relative to a standard aviation patch antenna, the anti-jam mode attenuated a ground based simulated jammer by 15 dB. What this means is that a hostile jammer would need to be 6 times closer to the aircraft, or use 30 times the amount of power normally required to jam GPS. The DPRA is considered to be an elegant solution to the RFI problem for GA aircraft using GPS/WAAS as the primary navigation system.

Acknowledgements

The results reported in this thesis would not have been possible without help from many supportive colleagues. First, I would like to thank my principal research adviser, Professor Per Enge, for his advice and mentoring throughout the years. He gave me the freedom to study computational electromagnetics antenna analysis techniques, and apply these methods to anti-jam GPS antennas. Recognizing that research is a non-linear process, Professor Enge provided guidance and wisdom during those times when the path was not clear. He is one of the few people I've met who has a genuine, selfless interest in the well-being of his students and fellow colleagues. Professor Bruce Lusignan and Dr. Dennis Akos graciously agreed to be second and third readers for this thesis, as well as serve on my oral defense committee. I thank them for their technical and editorial comments, and argue that this thesis is a much better work as a result of their efforts.

Flight testing of the dual-patch anti-jam antenna was a very important step in validating its performance, and significant results from the flight test are reported in this thesis. It was also a very special event for me personally. This antenna, which began as a theoretical concept with an unknown chance of success, evolved into an innovative, working product which has received praise from many people whom I admire and respect. The flight test unequivocally demonstrated the worthiness of this invention, and I will never forget the feeling I had on 16 September 2002 when I realized what had been accomplished. I will also not forget the sacrifices made by the students and staff in the Stanford GPS WAAS and LAAS Labs, and by folks from outside the labs. These people set aside their needs to help my flight experiment succeed. Dr. Sharon Houck volunteered to be among the air crew personnel, to assist

in operation of the airborne data recording equipment, and serve as air-captain. Logi Vidarsson operated the ground station, which was key to the success of the experiment. Claude Hammond travelled from the FAA PASS Office in Washington D.C. to provide invaluable assistance during the flight test, especially with ground-to-air communications. Lee Boyce, Mike Koenig, Yolanta Lubos, and Stu Cobb were members of the ground crew who were essential in coordinating the aircraft approaches. Todd Walter and Dennis Akos provided funding and donated lab equipment for this flight experiment. Ben Hovelman of Sky Research Inc. is an exceptional pilot, and helped install the antenna and electronics in the Caravan. Geary Tiffany, the chief airfield manager at Moffett Field, handled the approval process and other management and coordination issues so that I could focus solely on the scientific aspects of my experiment.

The work reported in this thesis was supported by a research grant from the FAA Satellite Program Office. I wish to thank the FAA for their generous funding, which makes the Stanford GPS WAAS and LAAS Labs stimulating research environments from which great technological advances emerge.

The sequence of events leading to this point in my life has been orchestrated with great persistence and without deviation. My interest in radio and electronics began at a very early age when I taught myself how to build shortwave radios. I decided without question to dedicate my life to this fascinating field. I dreamed of going to college and someday becoming a practicing electrical engineer, as I believed this was the highest goal one could achieve in life. Twenty years later, I still feel the same way about electrical engineering. There is no other field that I would rather be in. I feel more inspired than ever to continue my journey which began so long ago, and look forward to applying the new skills I've learned at Stanford to advance the field of electrical engineering. I wish to thank to everyone in my life who has helped me along this journey.

Contents

Abstract iv

Acknowledgements vi

1 Introduction 1

1.1 The Global Positioning System 1

1.2 GPS Fundamentals 2

1.2.1 Space Segment 2

1.2.2 Signal Structure 3

1.2.3 User Segment 5

1.3 GPS Augmentation Systems 6

1.3.1 Differential GPS (DGPS) 6

1.3.2 Local Area Augmentation System (LAAS) 6

1.3.3 Wide Area Augmentation System (WAAS) 7

1.4 GPS Modernization 9

1.4.1 M-Code and L2 C/A-Code (Block IIR-M) 9

1.4.2 L5 Civil Code (Block II-F) 10

1.4.3 GPS III 10

1.4.4 Galileo 10

1.5 GPS Antennas 11

1.5.1 Wish List 11

1.5.2 Popular GPS Antennas 13

1.6 Aviation Navigation 16

1.6.1 The National Airspace System 16
1.6.2 Flight Categories 16
1.6.3 Traditional Navigation Aids 19
1.7 Airborne Navigation Using GPS 23
1.7.1 Benefits of GPS 25
1.7.2 WAAS and LAAS 25
1.8 Interference to GPS 26
1.9 Previous Research 27
1.9.1 Artificially Soft Surfaces 27
1.9.2 Reconfigurable Patch Antennas 28
1.10 Research in this Thesis 29
1.11 Thesis Contributions 29
1.12 Thesis Outline 30

2 Radio Frequency Interference **32**
2.1 Sources of RFI 33
2.1.1 Unintentional RFI 33
2.1.2 Intentional RFI – Jamming 38
2.2 RFI Spectral Categories 40
2.2.1 Broadband RFI 41
2.2.2 CW and Narrowband RFI 41
2.2.3 Pulsed Interference 42
2.3 RFI Suppression Techniques 42
2.3.1 Receiver Techniques 43
2.3.2 Antenna Techniques – Spatial Filtering 44
2.4 Effects of RFI on the GPS Receiver 46
2.4.1 Interference Free Case 46
2.4.2 Interference Case 54
2.4.3 Typical Receiver Performance 56
2.4.4 GPS WAAS Interference Mask 58
2.4.5 MAAST 60

3 2.5-Dimensional FDTD Technique **64**
3.1 Computational Electromagnetics Basics 64
3.1.1 Antenna vs. Scattering Problems 64
3.1.2 Time Domain vs. Frequency Domain 65
3.2 FDTD History 67
3.3 Basic FDTD Derivation 69
3.3.1 Maxwell's Equations 69
3.4 Absorbing Boundary Layer 73
3.4.1 Split-Field PML 73
3.5 Discretization 75
3.5.1 PML Practical Considerations 76
3.6 Source Considerations 77
3.6.1 Square Patch Approximation 77
3.6.2 Circular Polarization 79
3.7 Near-to-Far-Field Transformation 81
3.8 Canonical Problem – Small Magnetic Loop Radiator 83

4 The Dielectric Cavity Antenna **85**
4.1 Hard and Soft Surfaces in Electromagnetics 85
4.1.1 Electromagnetic Soft Surface 86
4.1.2 Electromagnetic Hard Surface 88
4.2 Grounded Dielectric Slab 89
4.3 Grounded Dielectric Disk 93
4.3.1 Optimum Cavity Dimensions 96
4.4 2.5-D FDTD Simulations of the DCA 99
4.5 A Prototype DCA 101
4.5.1 Experimental Results 105
4.6 Size Considerations 107

5 Modelling Microstrip Patch Antennas **109**
5.1 The Microstrip Patch Antenna 110
5.1.1 History 110

5.1.2 The Rectangular Patch Antenna 111
5.2 Basic Cavity Model 114
5.2.1 Radiation Effects 117
5.3 Multiport Network Method (MNM) 118
5.3.1 Wall Admittance 119
5.3.2 Segment Self-Admittance 121
5.3.3 Patch Wall Field Distributions 126
5.3.4 Segment Mutual Admittance 127
5.3.5 Computing Relevant Antenna Parameters 129
5.4 MNM – Multiple Patch Antennas 130
5.4.1 Basic Model 131
5.4.2 Electric Field 133
5.4.3 Input Impedance 133
5.5 Far-Field Radiation Patterns 135
5.5.1 Axial Ratio 139
5.5.2 Gain 139
5.5.3 Efficiency 140
5.6 Inhomogeneous Substrates 141
5.7 Canonical Problems 143
5.7.1 Rectangular Patch Antenna 144
5.7.2 Patch Antenna Array 145
5.8 Summary 147

6 The DPRA **148**
6.1 Single-Element Anti-Jam Antenna 149
6.2 The Need for a Dual-Element Antenna 152
6.3 Concept of the DPRA 152
6.4 PIN Diodes 154
6.5 Analyzing the DPRA 156
6.5.1 Substrate Materials 157
6.5.2 Closely Spaced Patch Antennas 158

6.5.3 Stacked Patches 162
6.5.4 Stacked Patches with PIN Diodes – The DPRA 163
6.6 A Prototype DPRA 170
6.6.1 Design Procedure 170
6.6.2 Structural Considerations 174
6.7 Flight Test Experiment 176
6.7.1 Procedure and Equipment 178
6.8 Flight Test Results 181
6.8.1 Differential Phase Response 186
6.9 Benefits to Airborne WAAS Users 188
6.10 Antenna Performance Summary 191

7 Conclusions **194**
7.1 Summary of Research 194
7.1.1 DCA 194
7.1.2 DPRA 195
7.2 Future Research 196
7.2.1 DCA 196
7.2.2 DPRA 197

A Relevant 2.5-D FDTD Equations **201**
A.1 Split-Field PML Field Equations 201
A.2 Discretized 2.5-D FDTD Equations with Split-Field PML 202

B Microstrip Design Formulas **206**
B.1 Effective Permittivity 206
B.2 Microstrip Patch Wall Extension 208

C MNM Segment Mutual Admittance **209**

Bibliography **214**

List of Tables

1.1 Selected WAAS Airborne Antenna Specifications [64]. 13
1.2 Required Navigation Performance for Various Phases of Flight. 17
1.3 WAAS and LAAS Alert Limits. 24

2.1 GPS Receiver and RFI Parameters. 57

4.1 Properties of Hard and Soft Surfaces. 88
4.2 Example Grounded Dielectric Disk Properties. 97

5.1 Rectangular Patch Antenna Physical Characteristics. 145

6.1 PIN Diode Specifications. 155
6.2 Prototype DPRA Dimensional and Material Data. 157
6.3 PIN Diode Locations. 165
6.4 DPRA Specifications. 193

List of Figures

1.1 GPS Satellite Constellation [Courtesy FAA]. 3
1.2 Local Area Augmentation System (LAAS) [Courtesy:FAA]. 7
1.3 Wide Area Augmentation System (WAAS) [Courtesy: FAA]. 8
1.4 RTCA GPS Airborne Antenna Specification [64]. 14
1.5 Frequency Response of Typical Microstrip Patch Antenna. 15

2.1 Commercially Available GPS Jammer. 39
2.2 Signals Present at the GPS Receiver Antenna. 40
2.3 GPS Receiver DLL Block Diagram [25]. 48
2.4 DLL 1-σ Pseudorange Error vs. S/N_0. 50
2.5 Costas Loop Discriminator Block Diagram [80]. 50
2.6 PLL 1-σ Phase Jitter vs. S/N_0. 52
2.7 Cycle Slip Rates vs. S/N_0. 53
2.8 GPS Receiver S/N_0 for Various SV Received Power Levels. 56
2.9 GPS Receiver S/N_0 for Various RFI Power Levels. 57
2.10 RFI Power Levels Causing Loss of Lock. 58
2.11 RTCA RFI Mask [66]. 59

3.1 Maximum Desktop Computer Processor Speed and Number of Transistors per Processor [62]. 68
3.2 Number of FDTD Related Publications per Year [68]. 69
3.3 Cylindrical Coordinate System. 70
3.4 FDTD Lattice in Cylindrical Coordinates. 75
3.5 ω_ρ Radial Profile. 77

3.6 Rectangular Microstrip Patch Antenna Model. 78
3.7 Circular Microstrip Patch Antenna Model. 79
3.8 Circular vs. Square Patch Antenna Radiation Patterns. 80
3.9 FDTD Electromagnetic Near-Field Structure. 81
3.10 FDTD Equivalent Electromagnetic Problem. 82
3.11 Magnetic Loop Antenna. 83
3.12 Radiation Pattern of Magnetic Loop Antenna. 84

4.1 Geometry Relating to Hard and Soft Surfaces [44]. 86
4.2 Various Implementations of Soft Surfaces [84]. 87
4.3 Geometry of the Grounded Dielectric Slab. 90
4.4 Geometry of Grounded Dielectric Disk. 93
4.5 Grounded Dielectric Disk Radial Field Distribution. 96
4.6 Disk Critical Thickness d_c. 98
4.7 Disk Inner and Outer Radii, a and b. 98
4.8 Theoretical Radiation Pattern of Trimble Patch Antenna Mounted on 30 cm Diameter Plate. 100
4.9 Theoretical Radiation Pattern of NovAtel Choke Ring Antenna. . . . 100
4.10 Theoretical Radiation Pattern of Prototype DCA. 100
4.11 Near-Field H_ϕ Component of the NovAtel Choke Ring. 101
4.12 Near-Field H_ϕ Component of the Optimized DCA. 101
4.13 Near-Field Components of Three Antennas. 102
4.14 Prototype DCA. 103
4.15 DCA Test Setup. 104
4.16 Residual Measurement Error. 105
4.17 Radiation Pattern of Trimble Patch Antenna Mounted on 30 cm Diameter Plate. 106
4.18 Radiation Pattern of NovAtel Choke Ring Antenna. 106
4.19 Radiation Pattern of Prototype DCA. 106

5.1 Rectangular Patch Antenna Geometry. 111
5.2 Rectangular Patch Antenna Equivalent Problem. 113

5.3 Segment Geometry. 119
5.4 Slot Embedded in an Infinite Ground Plane. 122
5.5 Comparison of Slot Conductance Formulations. 124
5.6 Comparison of Slot Susceptance Formulations. 126
5.7 An Array of Four Patch Antennas. 131
5.8 Equivalent Problem for Rectangular Patch Antenna. 135
5.9 Coordinate System for Near-Field Calculations. 136
5.10 Coordinate System for Far-Field Calculations. 138
5.11 Patch Antenna with Lumped Loads Embedded in Substrate. 141
5.12 Input Impedance of Rectangular Patch Antenna. 144
5.13 Radiation Pattern of Rectangular Patch Antenna. 145
5.14 Radiation Pattern of 2×2 Array of Rectangular Patch Antennas. . . 147

6.1 Simplified Model of a Patch Antenna. 149
6.2 Radiation Pattern of a Small Patch Antenna on an Infinite Ground Plane. 150
6.3 Radiation Pattern of a Small Patch Antenna on a 3λ Ground Plane. . 150
6.4 Radiation Pattern of a $\lambda/2$ Square Patch Antenna on a 3λ Ground Plane. 150
6.5 Patch Antenna Substrate Permittivity vs. Length. 151
6.6 Block Diagram of the DPRA. 153
6.7 Circuit Model for the PIN Diode. 155
6.8 Geometry for Mutual Impedance Study. 158
6.9 Mutual Coupling vs. Edge Separation. 160
6.10 Input Impedance vs. Edge Separation. 161
6.11 Radiation Pattern of Isolated Patch Antenna. 161
6.12 Radiation Pattern of Closely-Spaced Patch Antennas. 161
6.13 Radiation Pattern of Lower Patch Antenna – no PIN Diode Isolation. 162
6.14 The DPRA Concept. 164
6.15 PIN Diode Placement Geometry. 166
6.16 Effect of PIN Diodes Along Principal Axes. 167
6.17 Effect of PIN Diodes Along Diagonals. 167

6.18 Pitch Plane Radiation Pattern of the DPRA. 170
6.19 Roll Plane Radiation Pattern of the DPRA. 170
6.20 Perspective View of the Prototype DPRA. 171
6.21 BPF/LNA Response. 172
6.22 Schematic of the DPRA Circuitry. 173
6.23 Side View of the DPRA. 175
6.24 Top View of the DPRA. 176
6.25 Bottom View of the DPRA. 177
6.26 Moffett Federal Air Field, Mountain View, CA, 16 September 2002. . 177
6.27 Flight Test Aircraft – Cessna Caravan. 178
6.28 DPRA Mounted on the Caravan. 178
6.29 2-Watt Power Amplifier. 179
6.30 Pseudolite Transmitter Setup. 180
6.31 Airborne Data Recording Equipment Rack. 181
6.32 Receiver C/N_0 vs. Received Power. 182
6.33 Received Jammer Power in Wide-Angle and Anti-Jam Modes. 183
6.34 Real-Time Switching from Wide-Angle to Anti-Jam Mode. 184
6.35 J/S Ratio in the Wide-Angle and Anti-Jam Modes. 185
6.36 Theoretical vs. Measured Received Pseudolite Power. 186
6.37 Percentage of Time the Receiver Remains Locked. 187
6.38 LPV WAAS Availability with no RFI in Wide-Angle Mode. 189
6.39 LPV WAAS availability with no RFI in Anti-Jam Mode. 189
6.40 LPV WAAS Availability with 500 mW Jammer at 10 km in Wide-Angle Mode. 190
6.41 LPV WAAS Availability with 500 mW Jammer at 10 km in Anti-Jam Mode. 190
6.42 LPV WAAS Availability with 1 Watt Jammer at 10 km in Anti-Jam Mode. 192
6.43 Missed Approach WAAS Availability with 4 Watt Jammer at 10 km in Anti-Jam Mode. 192

B.1 Microstrip Patch Dimensions. 207

C.1 Segment Geometry. 210

Chapter 1

Introduction

1.1 The Global Positioning System

The global positioning system (GPS) is a space-based worldwide passive radio navigation system. With appropriate receiving equipment, GPS users can obtain an accurate three-dimensional position fix anywhere in the world 24 hours a day. Since 1995 when GPS was declared fully operational, commercial GPS receivers have become inexpensive and readily available. This has made GPS ideal for personal navigation by hikers, motorists, mariners, and aviators. Accurate timing information is also available from the GPS satellites to synchronize ground based time-critical systems such as wireless communications and power transfer systems. As GPS technology continues to evolve, more robust and demanding applications of GPS are emerging such as inexpensive GPS locked frequency standards, precision guided munitions, precision aircraft landing systems, and autonomous navigation systems for ground, air, and space vehicles.

GPS has proven to be an invaluable service to many critical and casual users. Both the performance and popularity of GPS have greatly exceeded the expectations of the original designers. Today, millions of people around the world benefit from GPS, both directly and indirectly. The future of GPS is bright, as newly launched satellites are equipped with much more capability and more features than older units. For example, GPS ranging signals will soon be broadcast to civilians on three different frequencies,

reducing the position error by a factor of 10. We are likely to see GPS increasingly integrated into people's lives as new applications continue to be developed and made available to consumers.

1.2 GPS Fundamentals

1.2.1 Space Segment

The full operation capability GPS space segment consists of 24 satellites (minimum) in medium earth orbit (20,183 km altitude) in 6 orbital planes inclined at 55°. The radius of the orbit is approximately 4 Earth radii, and the orbital planes are separated by 60° in longitude. The satellites are in circular orbits having a period of 11 hours 58 minutes. On any given day, a ground-based user would observe the same satellite geometry 4 minutes earlier than the previous day. Four satellites are arranged unevenly in each orbital plane to minimize the impact of a single satellite failure, and to provide space for spares. This orbital configuration can support up to 30 satellites. There are currently 29 operational GPS satellites, as newer satellites are being launched to replace ageing units and to fill in the spare slots. The satellites are three-axis stabilized so that their solar panels are directed toward the sun, and their high-gain antennas are pointed toward Earth. The satellites consume 700 watts of power continuously over their 7.5 year design lifetime (Block IIA). Fig. 1.1 shows a scale drawing of the satellite configuration. Multiple rubidium and cesium atomic clocks aboard the satellites keep time to within 30 nS of UTC. The ranging signals broadcast by the satellites are right-hand circular polarized (RHCP). This polarization is achieved by means of 12 helix antennas arranged in a phased array. These antennas are fed such that the resulting radiation pattern presents an equal power density to users on the surface of the Earth. The GPS satellites generate 50 watts of RF power at the antenna terminals. This power is distributed equally between the C/A and P(Y) ranging codes [28].

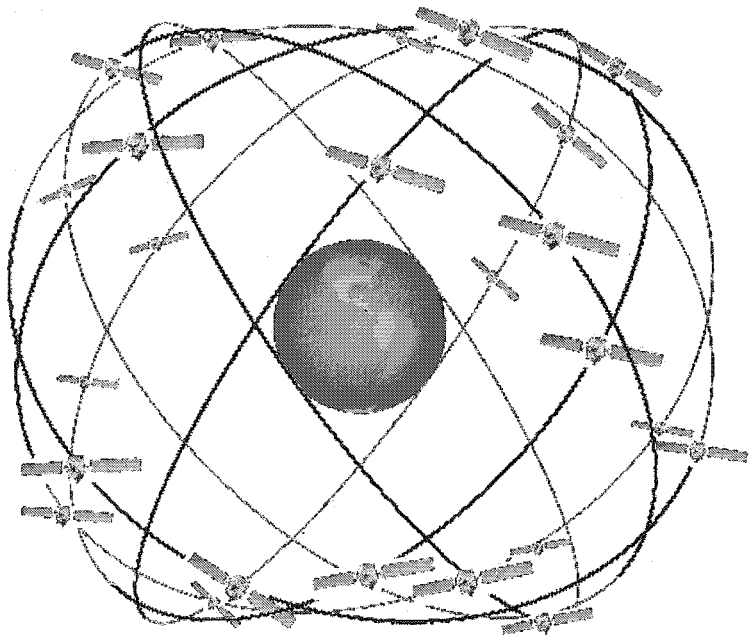

Figure 1.1: GPS Satellite Constellation [Courtesy FAA].

1.2.2 Signal Structure

Standard Positioning Service (SPS)

There are two types of positioning services available to users of GPS. The *standard positioning service* (SPS) is intended for civilian use. The SPS employs a ranging signal called the C/A (coarse acquisition) code. The C/A-code is a direct sequence spread spectrum signal broadcast on 1,575.42 MHz, also known as the L1 frequency. The spreading code is a 1.023 million bits per second (Mbps) pseudo-random noise (PRN) Gold code which repeats each millisecond. The bit rate of a PRN code is commonly referred to as its *chipping rate*. The power spectrum of the C/A-code is a $\text{sinc}^2(x)$ function, with 90% of the power contained in a 2 MHz bandwidth centered on the carrier frequency [25].

Precise Positioning Service (PPS)

The *precise positioning service* (PPS) is the second positioning system offered by GPS. The PPS is an encrypted system, available only to DoD authorized users. This feature is known as *anti-spoofing* (AS). The PPS uses a wide-bandwidth spreading code having a chipping rate of 10.23 MHz and a length of 38 weeks. GPS satellites broadcast only a one week long segment of this code, which is known as the P(Y)-code. The P(Y)-code appears on the the L1 frequency and also on 1,227.6 MHz, the L2 frequency. The P(Y)-code bandwidth is 20 MHz, as measured between the first nulls in the power spectrum. Military grade GPS receivers track the P(Y)-code on both L1 and L2 frequencies. This allows the receiver to remove errors associated with the ionosphere, and thus obtain a very accurate position fix [25].

Navigation Message

A navigation data message containing satellite specific housekeeping information is modulated onto the ranging signals at 50 bps. This message is composed of 1,500 bit frames of satellite almanac data (for all satellites), satellite clock and ephemeris corrections, ionospheric corrections, and satellite health status. This message is decoded by GPS receivers in its entirety every 12.5 minutes. Critical ephemeris and clock parameters are repeated every 30 seconds [25].

Selective Availability (SA)

In the past, the L1 C/A-code signal was purposely degraded to deny the full capabilities of the SPS to hostile users who may try to use the service against the U.S. in some fashion. The satellite clock was dithered, which caused a large error in the measured range to the satellite. This policy was known as *Selective Availability* (SA). Fortunately for civil users, it was determined that SA was not serving national security interests, and was terminated in May 2000. This action resulted in a fivefold increase in position accuracy for users of the SPS [25].

1.2.3 User Segment

The GPS satellite signals propagate to line-of-sight users with relatively little attenuation. The minimum received power for users on Earth with a 0 dBic gain antenna are -160 dBW for the C/A-code, -163 dBW for the P(Y)-code on L1, and -166 dBW for the P(Y) code on L2. Recently launched satellites have yielded power levels 3 – 5 dB higher than this minimum specification. Even so, the signal present at the GPS receiver antenna terminals is extremely weak. In fact, it is below the thermal noise floor, which is at -141 dBW in a 2 MHz bandwidth. We rely on the de-spreading process to provide 43 dB-Hz of processing gain (C/A-code), resulting in a positive signal to noise ratio (SNR). The P(Y) code provides 53 dB-Hz of processing gain due to its higher chipping rate. The C/A-code ranging signals from all visible GPS satellites are broadcast simultaneously on the same frequency. The receiver can differentiate between these overlapping signals because the PRN codes assigned to each satellite are nearly orthogonal.

The receiver computes a position fix by means of trilateration [25]. In the ideal case, the ranges between the user and a minimum of three GPS satellites yield an unambiguous three-dimensional position fix. The distance to each satellite (called the *pseudorange*) is determined by measuring the travel time for each of the ranging signals. Ideally, the clock in the receiver must be synchronized with the GPS satellite clock. However, clocks in most GPS receivers are controlled by inexpensive crystal oscillators which have poor long term stability, and could result in a large pseudorange error. Fortunately, this clock bias is resolved in practical receivers by using a fourth GPS satellite range observation in the position solution. The fourth satellite is used to solve for the user's clock error, which is common to all satellite range measurements. A linearized system of equations is solved to provide the user's position. The accuracy of this solution depends on the satellite geometry and the quality of the range measurements. Position errors with the SPS are on the order of tens of meters, while errors under 10 meters are achievable with the PPS. Residual position errors result from un-modelled ionosphere and troposphere delays, satellite clock and ephemeris errors, and receiver multipath and noise. The dominant pseudorange error contribution is from un-modelled ionospheric delay.

1.3 GPS Augmentation Systems

1.3.1 Differential GPS (DGPS)

While stand alone GPS has proven to be a very robust positioning service, it can be improved upon. One such improvement is an augmentation system known as differential GPS (DGPS). In this arrangement, an accurately surveyed reference station determines its pseudorange to each visible GPS satellite. If the user is close to the reference station, certain pseudorange errors will be common to both the user and the reference station. These common errors can be removed from the user's position solution if the user has access to the reference station pseudorange measurements. This information is broadcast free of charge by 50 U.S. Coast Guard reference stations with transmitters operating in the medium frequency (MF) marine radio beacon band, which covers 285 – 325 kHz. These MF transmitters have ranges on the order of 100 km. While ionosphere, troposphere, and satellite ephemeris and clock errors may be removed, multipath and receiver noise errors cannot since they are particular only to the user. Nonetheless, the improvement in accuracy over stand alone GPS is significant. Code based DGPS provides meter level accuracy, while carrier based DGPS enables surveyors to obtain centimeter level accuracy.

1.3.2 Local Area Augmentation System (LAAS)

A variation of DGPS which is used primarily for aircraft precision approaches is the local area augmentation system (LAAS). LAAS is very similar to DGPS in that a single reference station (or several closely spaced reference stations) provides differential corrections to users. These corrections are typically broadcast on a VHF data link to users in a very localized area, at or near an airport. Fig. 1.2 shows several airborne GPS users in the vicinity of an airport. These aircraft are receiving GPS satellite signals and signals from the VHF data beacon located on airport property. LAAS position errors can be under one meter. Perhaps more important than increased accuracy is the ability of LAAS to detect system failures and notify the user in a timely manner. The metric for quantifying this capability is *integrity*, which is

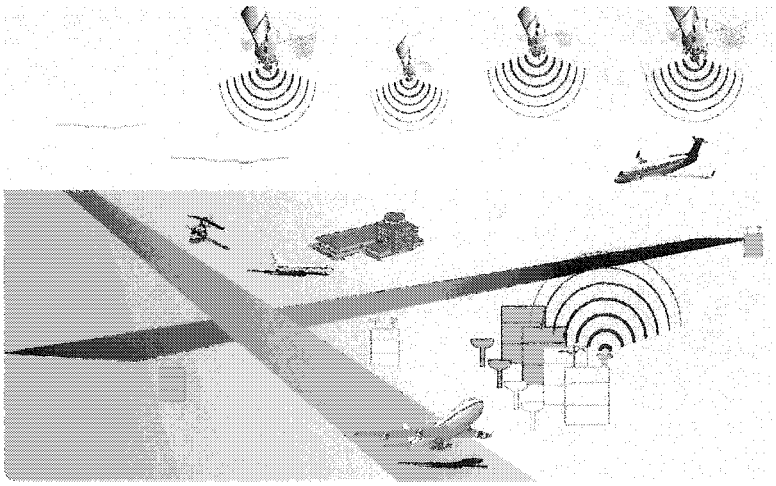

Figure 1.2: Local Area Augmentation System (LAAS) [Courtesy:FAA].

measured as a probability (per operation) of a system failure going unreported for a time greater than the specified time-to-alarm. A separate requirement for the GPS LAAS navigation system is to maintain both accuracy and integrity requirements throughout the duration of an operation, without interruption. This metric is known as *continuity*. The continuity requirement is limiting for the demanding application of aircraft precision approaches. LAAS *time availability* is the fraction of time for which accuracy, integrity, and continuity requirements are simultaneously satisfied. Once it is certified by the FAA, LAAS is expected to meet the accuracy, integrity, and continuity requirements for Category I precision approaches. Further work must be performed to guarantee that Category II/III performance requirements will be met. If LAAS can be certified for Category II/III approaches, it will likely replace the instrument landing system (ILS) at many airports.

1.3.3 Wide Area Augmentation System (WAAS)

The wide area augmentation system (WAAS) is DGPS (or LAAS) applied on a larger scale. WAAS makes use of a network of 25 reference stations located throughout the United States. Differential corrections are collected from these reference stations

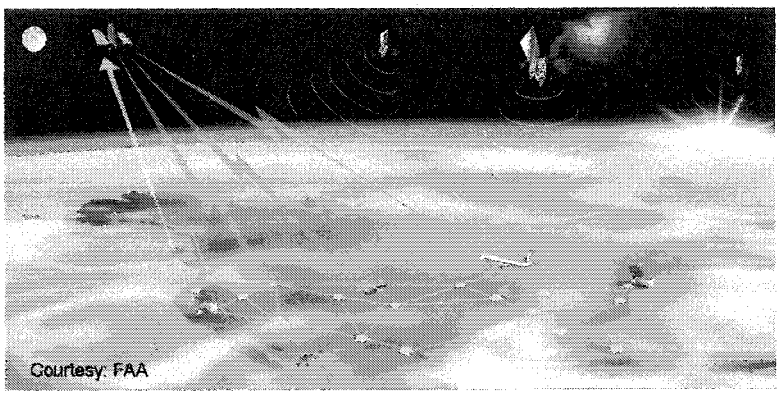

Figure 1.3: Wide Area Augmentation System (WAAS) [Courtesy: FAA].

by a master station, and then disseminated to users in a large area of operation. Currently, two Inmarsat-3 geosynchronous satellites provide GPS-like ranging signals to users in the U.S., while broadcasting the WAAS corrections in a 250 bps navigation data message. Fig. 1.3 shows several airborne GPS users in various locations around the United States. The reference station network is shown, along with the Inmarsat acting as a "bent pipe" for the WAAS correction messages. WAAS users enjoy position accuracies of less than 10 meters. Like LAAS, WAAS users also benefit from requirements on availability, accuracy, integrity, and continuity. The WAAS position solution is less accurate than LAAS. Fully certified Phase I WAAS will meet the accuracy, availability, integrity, and continuity requirements for LPV (lateral precision with vertical guidance) precision approaches. The navigation performance requirements for LPV precision approaches (and others) are listed in Table 1.2. An aircraft landing system meeting LPV requirements must have a 95% horizontal accuracy of 16 m. This is true of the APV-II (approach with vertical guidance) and Category I landing systems as well. However, the vertical accuracy requirement is more stringent for APV-II and Category I approaches, and Phase I WAAS will fall short of this requirement. After gaining operational experience with Phase I WAAS, it is anticipated that the final implementation of WAAS will support APV-II precision approaches. In the future, as the L5 signal becomes available worldwide, WAAS will likely meet the navigation performance requirements for Category I precision approaches [73].

1.4 GPS Modernization

1.4.1 M-Code and L2 C/A-Code (Block IIR-M)

GPS satellites launched to date have been in the Block I, II, IIA, and IIR categories. The fundamental capabilities and signal structures of these satellite categories are essentially the same as those discussed in Section 1.2.2. Starting in 2003, newly launched Block IIR-M satellites will broadcast the C/A-code on L2. Availability of the C/A-code on this second frequency will allow commercial GPS receivers to track the C/A-code on both L1 and L2, and remove errors due to the ionosphere, which is the largest source of position error for stand-alone GPS. This will result in stand alone position errors under 10 meters. Having C/A-codes on both L1 and L2 provides a means of anti-jam capability through frequency diversity. If RFI were present on the L1 frequency for instance, users could simply switch to the L2 signal. Since the L2 frequency is in the middle of a band of frequencies primarily allocated for ground radar service, there is some concern that civil users of the L2 C/A-code signal will experience substantial unintentional RFI. This has made the L2 C/A-code less attractive for incorporation into the WAAS and LAAS aircraft approach systems, which have strict availability requirements [73]. Block IIR-M satellites will also transmit an improved military encrypted code called the M-code. The M-code will appear on L1 and L2, and will be encrypted for military use only. The M-code is a split spectrum code. The modulated spectrum has a null at the center frequency and peaks at $\pm$ 10 MHz. This arrangement places the peaks of the M-code power spectral density in the nulls of the P(Y) code power spectral density, minimizing the potential for interference between the two signals. By placing the bulk of the signal power in two spectral peaks separated by 20 MHz, the M-code will be more robust in the face of intentional interference or jamming. It is likely that the M-code will operate at power levels 10 dB higher than the P(Y) code, further increasing resistance to jamming.

1.4.2 L5 Civil Code (Block II-F)

Starting in 2005, newly launched Block IIF GPS satellites will broadcast a second civil code on a third frequency of 1,176.45 MHz, the L5 frequency. This code will have a wide bandwidth (20 MHz) similar to the P(Y)-code, but will not be encrypted. GPS receivers designed to process both the L1 and L5 civil codes will be able to remove ionospheric delay, the largest source of pseudorange error. As a result, use of the L1 and the new civil L5 codes offers a tenfold improvement in position accuracy over the C/A-code alone. It is likely that WAAS and LAAS will make use of the L5 civil code in the future since it is in the protected aeronautical radio navigation service (ARNS) frequency band. This will probably turn WAAS into a Category I landing system, and will help LAAS meet the more stringent Category II/III requirements [73].

1.4.3 GPS III

The next generation GPS satellite, known as GPS III, will provide the same ranging signals as Block IIF satellites. One improvement over Block IIF satellites will include higher RF output power, perhaps by a factor of 10. GPS III is likely to employ high gain antennas which can direct spot beams toward regions of military interest, as necessary. The spot beam antenna gain will be on the order of 20 dB. This will provide a significant increase in anti-jam capability for military users in the region.

1.4.4 Galileo

The U.S. Department of Defense (DoD) manages all aspects of the global positioning system. Other nations argue that the DoD could decide at any time to deny the civil SPS service on a worldwide basis. SA could once again be activated, increasing user errors to over 100 meters. Because of this, other nations have been reluctant to become dependent on GPS for critical applications. The European Union decided in 1999 to design a satellite-based positioning system based on international agreement and management. This new positioning system, which will be interoperable with GPS, is called *Galileo* [37]. Galileo will provide an *open service* (OS) on a free,

worldwide basis on the E5 (1,189 MHz), and L1 (1,575.42 MHz) frequencies. The Galileo OS will make use of wide-bandwidth binary offset carrier (BOC) split codes which will be inherently more accurate for ranging than the GPS C/A-code. Galileo is very attractive because of this fact, and also since it has the potential to double the number of visible navigation satellites in the sky when used in conjunction with GPS.

1.5 GPS Antennas

1.5.1 Wish List

The ideal GPS receive antenna for airborne applications would have the following properties:

- Uniform gain (+3 dBic, RHCP) for positive elevation angles
- Zero response (gain = $-\infty$ dBic) for negative elevation angles
- Axial ratio = 0 dB
- Uniform group and phase delay response
- Low SWR (< 1.5) over a broad bandwidth

Uniform gain in the upper hemisphere would allow the user to acquire and track all GPS satellites in view. An antenna with no response below the horizon would be immune to multipath reflections arriving from beneath the antenna. It would also reject interference arriving from negative elevation angles. Unfortunately, achieving an infinitely sharp cutoff at the horizon is not possible, as the antenna would need to be infinitely large. We can approximate this condition by designing large phased arrays. But with the current trends toward minimization, large GPS antennas are not very popular among mobile users. We must build small antennas which approximate the ideal radiation pattern as closely as possible.

GPS antennas should possess a low axial ratio over the entire upper hemisphere. The axial ratio is a measure of the purity of the antenna's desired polarization. For

circular polarization, the axial ratio is $|20\log(|E_v|/|E_h|)|$ dB, where E_v and E_h are the orthogonal (vertical and horizontal) components of the electric field as measured in the far-field region of the antenna. An axial ratio of 0 dB is usually taken to indicate pure circular polarization, but this is not necessarily true if the differential phase between the orthogonal components is not 90°. Axial ratio usually suffers at low elevation angles, since the horizontally polarized electric field (E_h) vanishes at the horizon for many popular antennas. While this may seem unacceptable, it amounts to only a 3 dB loss in received signal strength for low elevation satellites. Maintaining polarization purity is good engineering practice though, and also serves to reject the ever present, undesired multipath reflections of the GPS satellite signals. The reason for this immunity to multipath is that the RHCP GPS signals switch polarization to LHCP when reflected near grazing incidence. Ideally, a RHCP antenna will have no response to the LHCP polarized reflected signals.

GPS antennas should also have a constant phase and group delay response over the upper hemisphere. Another way to say this is that the antenna should have a stable phase center. A constant group delay is indistinguishable from a clock bias, and is absorbed in the user clock error term during the GPS position solution procedure. Spatial variations in group delay and phase response yield code and carrier phase pseudorange errors which vary with the satellite position in the sky. These errors are unpredictable and are difficult to remove at the receiver.

Obviously, the GPS antenna must have a bandwidth wide enough to pass the GPS ranging signal free of distortion. This means that the magnitude response of the antenna should be flat and the phase response should be linear over the GPS passband. Theoretically, the bandwidth of the C/A-code is infinite. However, 90% of the signal power resides in a 2 MHz bandwidth centered on the carrier frequency. This could be considered the absolute minimum bandwidth for an L1 GPS antenna. For aviation grade GPS antennas, the Radio Technical Commission for Aeronautics (RTCA) requires no more than 3 dB gain variation in a 20 MHz bandwidth centered at L1 [64]. For the P(Y)-code, a minimum bandwidth of 20 MHz is required to pass 90% of the signal power. Wide-bandwidth antennas are desirable since they pass the high frequency content of the ranging code, resulting in sharper correlation peaks

Parameter	Value
Frequency	1,575.42 MHz
Bandwidth	±10 MHz
Gain Variation (over 20 MHz)	< 3 dB
SWR	< 1.5:1
Axial Ratio (>10° elevation)	< 3 dB
Axial Ratio (5° – 10° elevation)	< 6 dB
Noise Figure	< 4 dB

Table 1.1: Selected WAAS Airborne Antenna Specifications [64].

and more accurate position estimation. However, significant rejection at frequencies outside the GPS passband is advantageous as out-of-band noise and interference will be attenuated relative to the GPS signal.

In order to standardize these parameters, the RTCA has developed a specification for airborne WAAS antennas. In the DO-228 specification, minimum operational performance standards (MOPS) for airborne WAAS antennas are listed. Some selected specifications from the MOPS are listed in Table 1.1. Table 1.1 is meant to illustrate some of the more important specifications only, and is by no means a comprehensive list of requirements for airborne WAAS antennas. The elevation radiation pattern of GPS antennas is important because it indicates how well the antenna will track GPS satellites at various elevation angles. For reference, the allowable gain for airborne GPS antennas is shown in Fig. 1.4 [64]. Low elevation satellites are the most difficult to track because the received satellite signal strength is at a minimum here. Therefore, the antenna gain below 5° elevation is controlled more strictly than at higher angles.

1.5.2 Popular GPS Antennas

Microstrip Patch Antennas

The most popular GPS antenna is the microstrip patch antenna. It is small, lightweight, inexpensive, and has a low vertical profile. It has a nearly uniform radiation pattern for positive elevation angles, with a typical gain of +5 dBic toward the zenith. Gain at the horizon is typically -6 dBic. The response at negative elevation

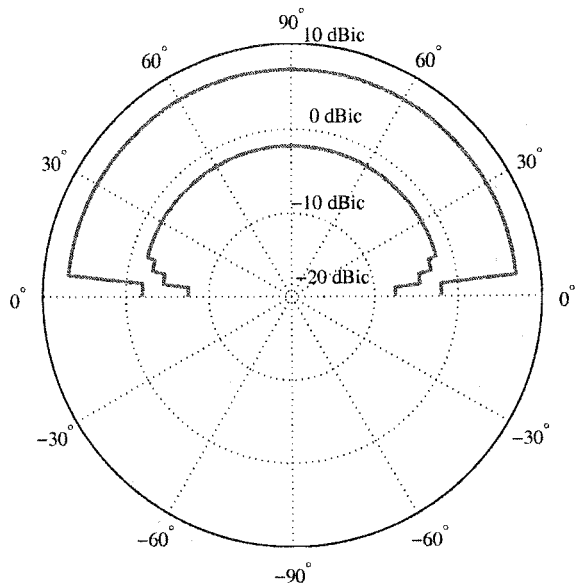

Figure 1.4: RTCA GPS Airborne Antenna Specification [64].

angles is a function of the size of the ground plane upon which the patch is mounted. Large ground planes offer higher zenith gain and reduced response at negative elevation angles. The size of the patch resonant element also affects the radiation pattern. Compact antennas yield lower gain and more response from negative elevation angles. The patch antenna makes an excellent airborne GPS antenna because of its low profile and broad radiation pattern. The broad radiation pattern allows the pilot to maneuver the aircraft and continually track enough satellites to maintain a position fix. Patch antennas mounted on aircraft have a substantial ground plane to work against, as the fuselage is usually many wavelengths in diameter. The phase center of patch antennas can be stable if care is taken in the design. Nearly-square patches fed with a single probe feed have fair phase center stability. Dual-feed patches have more stable phase centers since the designer has more control of the amplitude and phase of the orthogonal modes within the patch. Dual-feed patches are also symmetrical, which further aids phase center stability. The frequency response of patch antennas is not flat, but falls off at the edges of the passband. For RHCP patch antennas,

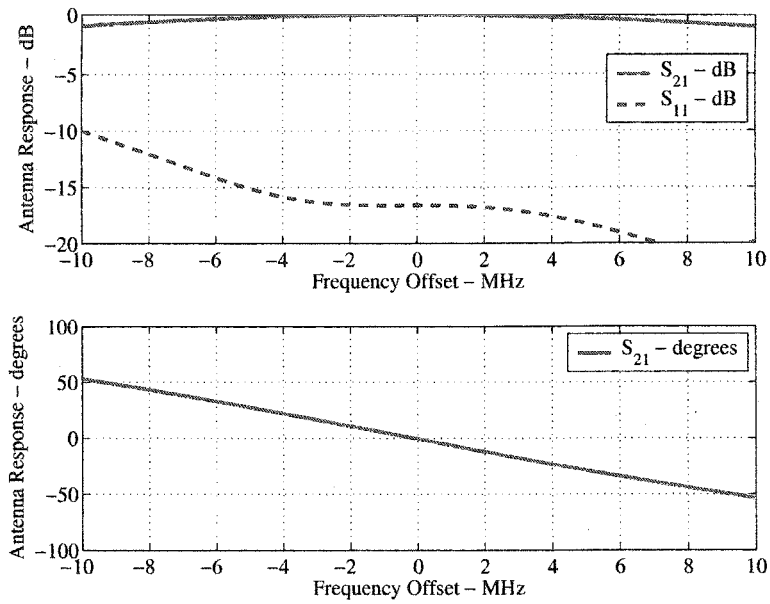

Figure 1.5: Frequency Response of Typical Microstrip Patch Antenna.

the phase response is approximately linear over the passband. Bandwidths of well-designed patch antennas are more than adequate for both the C/A and P(Y)-codes. The frequency response of a typical patch antenna is shown in Fig. 1.5. The return loss s_{11} is a measure of the impedance match of the antenna. A return loss of -15 dB or less presents a good match to the receiver, with minimal signal power loss due to impedance mismatch. The response of the antenna to a RHCP signal is plotted as s_{21}. In Fig. 1.5, we observe that the response is quite flat over a GPS receiver passband of 16 MHz, and the phase response is linear.

Helical Antennas

Helix and quadrifilar helix antennas have desirable properties that make them popular for certain GPS applications. Axial mode helix antennas have high gain (> 10 dBic), stable phase center, and low SWR and axial ratio over a very wide bandwidth. They are used in applications requiring a directional beam. A typical application is a pseudolite transmit antenna. Quadrifilar helices share the same advantages as axial mode helices, except that they have lower gain. Because of this, the quadrifilar helix

is an excellent alternative to the microstrip patch antenna when a conformal antenna is not required. They are found occasionally on hand-held GPS receivers.

Crossed Dipole Antennas

Finally, a third popular GPS antenna makes use of two or more crossed dipoles fed 90° out of phase to achieve RHCP. Crossed dipoles offer a more stable phase center than patch antennas. These antennas are extended in the vertical dimension, so they are not suitable for high speed vehicles. Crossed dipoles typically have a higher radiation efficiency than patch antennas. Their radiation patterns are comparable to those of microstrip patch antennas.

1.6 Aviation Navigation

1.6.1 The National Airspace System

The National Airspace System (NAS) is the environment in which aviation operations take place within in the United States. In brief, it is a complex network of ground-based and airborne systems which work in concert to ensure safe aircraft navigation and maintain safe separation between these air vehicles. The NAS is managed and regulated by the Federal Aviation Administration (FAA) [31].

1.6.2 Flight Categories

Phases of Flight

Flight operations in the U.S. are divided among various categories. Each category has its own safety requirements and applicable navigation aids. The most common phases of flight are listed in Table 1.2. The en route phase covers those operations between a point of departure and the terminal area, at which point the air traffic control (ATC) tower directs the aircraft. En route operations have the least stringent requirements on navigation accuracy. While en route, aircraft engage in area navigation (RNAV) operations. Here, a flight management system (FMS), commonly

Phase	Horizontal Accuracy (95%)	Vertical Accuracy (95%)	Integrity (P_{HMI})	Time-to-Alert	Continuity Risk (1-σ Continuity)	Availability
En Route	3.7 km	N/A	10^{-7}/hr	1 min	10^{-4}/hr–10^{-8}/hr	0.99 – 0.99999
Terminal	0.74 km	N/A	10^{-7}/hr	15 sec	10^{-4}/hr–10^{-8}/hr	0.999 – 0.99999
LNAV (NPA) (Missed Approach)	220 m	N/A	10^{-7}/hr	10 sec	10^{-4}/hr–10^{-8}/hr	0.99 – 0.99999
LNAV/VNAV	220 m	20 m	2×10^{-7} per approach	10 sec	8×10^{-6}/15 sec	0.99 – 0.999
LPV	16 m	20 m	2×10^{-7} per approach	10 sec	8×10^{-6}/15 sec	0.99 – 0.999
APV-II	16 m	8 m	2×10^{-7} per approach	6 sec	8×10^{-6}/15 sec	0.99 – 0.999
GLS/CAT I	16 m	4 – 6 m	2×10^{-7} per approach (150 sec)	6 sec	8×10^{-6}/15 sec	0.99 – 0.99999
CAT II/IIIa	6.9 m	2 m	10^{-9}/15 sec	1 sec	4×10^{-6}/15 sec	0.99 – 0.99999
CAT IIIb	6.2 m	2 m	10^{-9}/30 sec (lateral) 10^{-9}/15 sec (vertical)	1 sec	2×10^{-6}/30 sec (lateral) 2×10^{-6}/15 sec (vertical)	0.99 – 0.99999

Table 1.2: Required Navigation Performance for Various Phases of Flight.

called a navigation computer, blends measurements from the INS (if available) and other nav-aids to optimally compute aircraft position and velocity. The navigation computer guides the aircraft through pre-defined three-dimensional waypoints located along the flight path [39]. Terminal operations occur at or near airports where air traffic control service is provided. The LNAV flight category meets the minimum performance requirements for non-precision approaches, i.e., approaches with lateral but no vertical guidance. LNAV performance requirements are also applicable during missed approaches. The LNAV/VNAV phase is used during operations which require vertical guidance. The LPV phase (lateral precision with vertical guidance) is used during precision approach operations where both horizontal and vertical guidance are required. APV-II (approach phase with vertical guidance) is similar to LPV, but with tighter vertical accuracy requirements to enable operation at lower aircraft altitudes. Category I/II/III precision approaches are currently performed with the ILS or MLS only. Category III approaches and landings belong to the most challenging phase of operations, whereby the landing must occur in extremely poor weather conditions. Category IIIc ILS/MLS approaches are amazing in that the navigation system brings the aircraft down to the runway, even in zero visibility conditions.

Visual vs. Instrument Flight Rules

Visual flight rules (VFR) apply when the visibility exceeds 5 NM and the ceiling is greater than 3,000′ above ground level (AGL). *Instrument flight rules* (IFR) apply when the ceiling is 500′ – 900′ AGL, and/or visibility is 1 – 3 NM. *Low instrument flight rules* apply when visibility is less than 1 NM and the ceiling is below 500′. During an IFR approach, pilots can make the landing if the visibility is better than the runway visual range (RVR) requirement at the *minimum decision altitude* (MDA), or decision height, specified for that particular approach category (Table 1.3). Otherwise, the pilot must execute a missed approach procedure [15].

Approaches

Approaches to airports are divided into two classes of operation. *Non-precision approaches* (NPA) are those for which the pilot has horizontal, but no vertical guidance. *Precision Approaches* (PA) are performed with vertical (glide-slope) guidance as well as horizonal guidance [39]. Requirements on aircraft position accuracy are more stringent for precision approaches than for non-precision approaches.

1.6.3 Traditional Navigation Aids

The civil aviation community has traditionally relied on ground-based navigational aids (nav-aids) to guide the aircraft along complicated flight paths in all meteorological conditions. Examples of these conventional nav-aids are LORAN-C (long range radio navigation), VHF omni-directional range (VOR), distance measuring equipment (DME), and non-directional beacons (NDB). For landing operations, the instrument landing system (ILS) is a very accurate and reliable guidance system which can bring the aircraft down to the runway in zero visibility conditions. The ILS is used for precision approaches, while the other traditional nav-aids are used during RNAV and NPA operations.

Navigation System Categories

A *sole-means* navigation system for a given phase of flight (e.g., Category I precision approach) meets the availability, accuracy, integrity, and continuity requirements for that phase. No other system is required to be on board the aircraft for that phase of operation. The ILS is a sole-means navigation system for Category I approaches. A *primary-means* navigation system need only meet the integrity and accuracy requirements for a particular phase of flight. A primary-means system does not require an accompanying sole-means system on board. Procedural restrictions and backup procedures are in place to prevent flight during those times when the primary-means system could be inoperable. Like primary-means systems, *supplemental* navigation systems meet only the integrity and accuracy requirements for a given phase of flight. However, a sole-means system must accompany the supplemental system [24]. The

following sections describe various traditional navigation systems and instruments which are in common use today.

Magnetic Compass

The magnetic compass was one of the first flight instruments. This simple instrument provides the heading of the aircraft relative to magnetic north. Magnetic north deviates from true north in the northern hemisphere because Earth's magnetic north pole is not co-located with the true north pole. The same is true in the southern hemisphere. This discrepancy, defined as *magnetic deviation*, has been mapped in great detail over the surface of the Earth, and can be obtained from a lookup table or computed from a model by a simple computer program [14]. Although the magnetic compass is not a primary means of determining heading, it is a very simple and reliable instrument requiring no external power. Because of this, all aircraft have a magnetic compass installed in the event of an emergency.

LORAN-C

LORAN-C is a hyperbolic navigation system operated by the U.S. Coast Guard and primarily intended for use in coastal areas or near the Great Lakes. LORAN-C can provide a two-dimensional position solution with 0.25 NM accuracy, sufficient for en route and terminal operations. Being in the low frequency (LF) radio spectrum covering 30 – 300 kHz, LORAN-C is susceptible to RFI from both man-made and natural sources, especially lightning. A phenomenon called precipitation static also degrades the performance of LORAN-C. Here, electrical charge builds up on the receive antenna in flight and is discharged when the aircraft travels through precipitation or moist air. This problem can be alleviated to some extent by using an H-field antenna, such as a shielded loop. LORAN-C also suffers from degradation due to interference from other distant LORAN-C transmitters at night when long range propagation is possible.

Non-Directional Beacons (NDB)

NDBs are ground based VLF transmitters which broadcast an omni-directional signal. Pilots use a directional antenna (loop) to obtain a bearing to the transmitter. Like LORAN-C, NDBs are sensitive to man-made and atmospheric interference. There is less reliance on NDBs than the other nav-aids which provide heading information.

VHF Omni-Directional Range (VOR)

The VOR is a one-way VHF transmitter which provides a bearing line (azimuth) from the VOR to the aircraft. Two VORs, or a VOR and DME, are required to determine the absolute heading and position of the aircraft. The several hundred VORs in the U.S. each have a range of roughly 50 NM. Being in the VHF radio spectrum, VORs are relatively insensitive to atmospheric noise, making them very popular for heading determination. VOR derived bearings are accurate, with angular errors ranging from 1° to 4°. Nominal errors are ±3° [78].

Distance Measuring Equipment (DME)

The DME is a two-way radio ranging system whereby the pilot obtains the range from the aircraft to the known location of the DME transmitter. The airborne equipment measures the round trip time-of-flight of a pulse train transmitted through the ground-based transponder. DMEs operate in the 1,100 MHz range, and are immune to atmospheric noise. Unlike the VOR, a single DME is limited to 100 simultaneous users [28]. For aircraft at altitude, the DME has a range of 200 NM and an accuracy of 0.25 NM or 1.25% of the range, whichever is greater. Approach DMEs have a range of 40 NM [78]. VORs and DMEs are usually co-located, and may be found at or in the vicinity of airports. The VOR/DME combination is very popular among aircraft travelling along extended or complex flight paths, e.g., RNAV operations.

Baro-Altimeter

None of the previously discussed navigation systems provide a measure of aircraft altitude. Aircraft altitude is obviously an important parameter to the prudent pilot. The baro-altimeter is a heavily used instrument that senses atmospheric pressure and computes aircraft altitude assuming an exponentially decaying pressure gradient. Airports broadcast ground-based atmospheric pressure measurements that are used by pilots to periodically calibrate the altimeter. Calibration is performed manually by adjusting a knob on the instrument panel.

Inertial Navigation System (INS)

Commercial aircraft and high-end GA aircraft are equipped with inertial navigation systems (INS). The INS continuously measures the specific force of the aircraft. Gravity is removed from the measurement, which is then integrated to obtain velocity and position. Even the highest quality INS is subject to long term drift, resulting in increasing position errors over time on the order on $1 - 2$ NM per hour. The INS is periodically reset in flight using VOR/DME measurements to remove this substantial drift.

Instrument Landing System (ILS)

While the previously discussed nav-aids are used primarily for en route operations or non-precision approaches, the instrument landing system (ILS) provides landing guidance for aircraft on final approach. The ILS, whose technology was developed in the 1940's, consists of the localizer, glide-slope, and marker signals. The localizer provides an indication of lateral deviation from the runway centerline. The glide-slope signal provides vertical guidance during the approach. The marker beacons alert the pilot to when he or she has reached a critical check point along the final approach flight path. The outer marker is between $4 - 7$ NM out from the touch down point, and notifies the pilot that he or she is on the glide-slope and has begun the final approach. The middle marker is placed near the missed approach decision point ($200' - 250'$ altitude) for a Category I approach. Here, the pilot must decide whether

to make the landing or execute a missed approach procedure. The inner marker is placed where the glide slope intersects a point 30 meters above the runway, and is used during Category II/III approaches only [28]. The ILS is an amazing precision approach navigation system which is highly accurate and dependable. After 30 years it is still operational at 1,000 airports in the U.S., and establishes the integrity goal for GPS.

Microwave Landing System (MLS)

An improved precision approach and landing guidance system called the microwave landing system (MLS) was developed in the 1970's to overcome certain limitations of the ILS. Unlike the ILS, the MLS is not affected by snow on the runway, and can be used for curved approach paths. The MLS is more accurate than the ILS. The MLS uses a scanning phased array antenna operating at 5 GHz to provide vertical and horizontal guidance. Range information is also available. In spite of the improvements over the ILS, the MLS has not replaced the ILS in the United States, as was originally intended. Instead, the FAA decided in 1994 to abandon the MLS in favor of a promising new technology called GPS [57].

1.7 Airborne Navigation Using GPS

The FAA is in the process of modernizing the NAS to enhance the safety, flexibility, and efficiency of flight operations for all aircraft. Because of its demonstrated utility in airborne navigation, and for all of the reasons discussed in Section 1.3, GPS has been recommended as the primary navigation system for all phases of flight in all sectors of aviation [57]. The FAA plan also calls for retaining a skeleton network of supplemental traditional nav-aids, improvements to LORAN-C, and maintaining the ILS at selected airports for Category II/III landing capability [31]. The goal of the FAA transition plan [56] is to certify WAAS and LAAS for as many phases of flight as possible. The phases of flight for which WAAS and LAAS will be certified are listed in Table 1.3.

Phase	Horizontal Alert Limit	Vertical Alert Limit	Minimum Decision Height	Runway Visual Range	Navigation System
En Route	4 NM	N/A	N/A	1 NM	SPS, WAAS, LAAS, Other Nav-Aids†
Terminal	2 NM	N/A	N/A	N/A	SPS, WAAS, LAAS, Other Nav-Aids
LNAV (NPA) (Missed Approach)	0.3 NM [73]	N/A	250′	1 NM	SPS, WAAS, LAAS, Other Nav-Aids
LNAV/VNAV	0.3 NM	50 m	250′	1 NM	WAAS, LAAS Other Nav-Aids
LPV	40 m	50 m	250′	1 NM	WAAS, LAAS, ILS
APV-II	40 m	20 m	250′	1 NM	WAAS‡, LAAS, ILS
GLS/CAT I	40 m	10 – 12 m	200′	2,400′	LAAS, ILS
CAT II	17.3 m	5.3 m	100′	1,200′	LAAS‡, ILS
CAT IIIa	17.3 m	5.3 m	None	700′	LAAS‡, ILS
CAT IIIb	15.5 m	5.3 m	None	150′	LAAS‡, ILS
CAT IIIc	N/A	N/A	None	0′	LAAS‡, ILS

† INS, LORAN-C, NDB, VOR, DME, and Baro-Altimeter
‡ Desired End-State

Table 1.3: WAAS and LAAS Alert Limits.

1.7.1 Benefits of GPS

There are many reasons why GPS should serve as a primary means of aircraft navigation, replacing the conventional navigation aids discussed in Section 1.6.3. GPS is easier to use and more accurate than traditional nav-aids. In contrast to the traditional nav-aids, the GPS solution is available 24 hours a day in any part of the world in any meteorological conditions. GPS allows pilots to follow arbitrary flight paths during RNAV operations, eliminating the geographical dependency inherent to the use of VORs and DMEs. GPS has the potential of reducing aircraft separation during en route operations, and during closely spaced parallel approaches [39], resulting in more efficient use of the airspace. GPS supports precision approaches for *all* runways, as opposed to ILS approaches which require properly equipped runways. Of the 11,000 runways in the U.S., only 1,000 are ILS equipped. The GPS avionics package is less expensive than ILS avionics. In addition, one set of GPS avionics supports all phases of flight. For the traditional nav-aids, multiple sets of equipment (VOR, DME, ILS, etc.) are required to support the various phases of flight. The traditional nav-aids are expensive to operate and maintain. Many of them provide guidance only in localized areas. Some nav-aids are unreliable: LORAN-C and NDBs are unavailable at times due to man-made and natural interference. Pilot training will be greatly simplified with GPS, as only one navigation system will need to be mastered [55]. Finally, pilots really like GPS because it is easy to use and provides very accurate, instantaneous position and velocity information. Stand alone GPS has been very beneficial for pilots thus far. Although WAAS and LAAS are not currently certified for precision approaches, pilots routinely use stand alone GPS as a supplemental navigation system during the en route, terminal, and non-precision approach phases of flight [46].

1.7.2 WAAS and LAAS

During a GPS guided precision approach, the airborne GPS receiver computes vehicle position and velocity. In addition, the airborne receiver dynamically computes a user protection level. The horizontal and vertical protection levels (HPL/VPL)

are conservative over bounds on the user's position error. Factors such as satellite geometry, ionospheric delay, and satellite clock and ephemeris errors contribute to the HPL/VPL calculation. The details of the protection level calculation for WAAS are documented in the Minimum Operational Performance Standards (MOPS) [65]. If the protection level exceeds the alert limit for that landing category (Table 1.3), the pilot must revert to a backup navigation system. If GPS is the primary means of navigation for that approach, a missed approach procedure is executed. GPS must also meet the integrity and continuity requirements for a given landing category, listed in Table 1.2.

1.8 Interference to GPS

Once WAAS and LAAS are certified, it is expected that pilots will depend increasingly on GPS for air navigation – especially for precision approaches. Unlike en route navigation where other radio-navigation services are available to meet the navigation performance requirements, GPS outages will be unacceptable during GPS precision approaches if no backup navigation system is available. The threat of RFI is the main obstacle preventing certification of GPS as a sole-means airborne navigation system. Undesired signals occupying the GPS passband could interfere with the weak GPS satellite signals, taking the receiver off line. In this case, no position information would be available to the pilot from GPS. Such a scenario would violate the continuity requirement for the precision approach, and a backup navigation system would be required to complete the landing. If the runway were not equipped with an ILS approach, the pilot would need to execute a missed approach procedure and fly to a different airport equipped with such equipment. If the aircraft did not possess instrument landing equipment at all, the pilot would need to find an an airport with better meteorological conditions where a VFR landing is possible. In the worst case, an aircraft which is low on fuel may need to attempt an emergency landing in poor visibility with no GPS or ILS guidance. All of these options are undesirable.

It is unlikely, but not impossible, that a pilot could end up in one of these hazardous situations due to GPS jamming. Commercial and GA pilots carefully check the

weather prior to any flight. Also, aircraft flying in IFR conditions must be equipped with an instrument landing system. GA aircraft without instrument landing systems would not be permitted to fly in poor weather. So it is more likely that RFI would be a nuisance rather than an immediate danger to the aircraft and its passengers. Nonetheless, a GPS navigation system hardened against jamming or unintentional interference would prevent the potential unnecessary missed approaches, saving time for GA pilots, and ultimately saving money for the commercial airlines.

1.9 Previous Research

1.9.1 Artificially Soft Surfaces

Artificially hard and soft surfaces are well known in acoustics applications. In the field of electromagnetics, artificially soft surfaces have long been used in the design of corrugated horn antennas with symmetrical radiation patterns and low cross polarization [17]. The popular GPS choke-ring antenna makes use of a corrugated ground plane, which functions as an artificially soft surface to reduce multipath reflections arriving from negative elevation angles. Recently, formal definitions for artificially hard and soft surfaces as they apply to electromagnetic waves have been put forth [44]. Later, researchers at the University of Florence used artificially soft surfaces to reduce the back lobe radiation from a vertical monopole [50]. In this work, a grounded dielectric slab was formed into a flat cylindrical shape, like a disk. The monopole was placed at the center of the disk. Experiments were carried out to characterize the radiation pattern of the disk compared to a standard monopole on a conducting ground plane. These workers analyzed both antennas with a two-dimensional (2-D) finite difference time domain (FDTD) code. Since the antenna structure and the source were rotationally symmetric, this was a suitable approach. The FDTD results agreed favorably with the measurements.

For rotationally symmetric geometries with asymmetric sources, the 2-D FDTD assumption still applies, but a modified source formulation is required [16]. This method is called the 2.5-dimensional (2.5-D) FDTD approach. It is very useful for

modelling circular microstrip patch antennas in rotationally symmetric geometries, as the circular patch can be represented by a magnetic current source varying in azimuth only ($\cos\phi$ variation). The 2.5-D problem is solved nearly as quickly as the 2-D FDTD problem, and all six electromagnetic field components are computed in the near-field region of the antenna.

FDTD problems require an absorbing layer around the outer perimeter of the work space to simulate the propagation of electromagnetic waves into un-bounded free space. In cartesian coordinates, the perfectly matched layer (PML) [8] is commonly used for this purpose. An exact formulation for the PML in cylindrical coordinates has been developed by workers at the University of Illinois at Urbana-Champaign [75]. In this technique, called the split-field PML, spatial quantities (ρ, ϕ, z) are transformed to complex variables, allowing for attenuation of the fields in the PML region. Each field quantity must be split into two independent components in order to express Maxwell's equations in a suitable form for time-stepping. The 2.5-D FDTD formulation in combination with the split-field PML is a powerful analysis tool for antennas with rotationally symmetric geometries and sources which vary sinusoidally in azimuth.

1.9.2 Reconfigurable Patch Antennas

Researchers have developed reconfigurable microstrip patch antennas to meet a variety of needs. Most applications involve the use of PIN diodes which function as RF switches. Workers in Thailand used PIN diodes in a switched-beam patch antenna to select between two different radiation patterns [54]. This patch antenna is vertically polarized, and the PIN diodes are used to direct a 10 dB null along one of the orthogonal axes in the plane of the patch. Professor Rahmat-Samii's antenna research laboratory at UCLA demonstrated a reconfigurable antenna employing switchable slots to achieve a high degree of polarization diversity [82]. Here, PIN diodes placed across slots in a rectangular patch element are biased appropriately to select either left or right-hand circular polarization (L/RHCP).

Lumped Load Modelling

Shorting pins are used underneath patch elements to increase bandwidth or allow dual frequency operation [47]. Workers in Turkey recently recognized the need to accurately model shorting pins within the patch substrate [53]. They were interested in obtaining the complete field distribution underneath the patch with the shorting pin present. They achieved this goal by modifying the microstrip patch antenna cavity model [61]. Here, the shorting pin is replaced by an ideal current source, and its unknown amplitude and phase are determined by enforcing the appropriate boundary condition at the location of the pin. This concept led to the development (in this thesis) of a generalized technique suitable for microstrip patch antennas with any number of lumped loads having arbitrary impedances. Specifically, the multiport network method (MNM) was modified to account for the presence of lumped loads embedded in the patch antenna substrate.

1.10 Research in this Thesis

The purpose of the research reported in this thesis is to develop novel GPS anti-jam antennas which are simple, small, lightweight, inexpensive, and suitable for aircraft. Two novel antenna designs are presented in this work – the dielectric cavity antenna (DCA) and the dual-patch reconfigurable anti-jam antenna (DPRA). The DPRA met all of the goals of this research.

1.11 Thesis Contributions

Specific contributions of this thesis are

1. Having invented the dielectric cavity antenna (DCA),
   (a) Optimized the DCA for suppression of ground-based RFI,
   (b) Developed an efficient 2.5-dimensional FDTD software package to model microstrip patch antennas on artificially soft surfaces,

(c) Planned and executed a ground test to validate a prototype antenna,

2. Having invented the dual patch reconfigurable anti-jam GPS antenna (DPRA),

   (a) Devised the concept of a reconfigurable dual-radiation pattern GPS antenna for RFI mitigation,

   (b) Derived an improved MNM model for simulating the effect of multiple embedded lumped loads,

   (c) Planned and executed a flight test to validate a prototype antenna,

   (d) Analyzed the benefits of this antenna for GPS WAAS airborne navigation in the presence of RFI.

1.12 Thesis Outline

Radio frequency interference (RFI) was briefly introduced in Section 1.8, but a more detailed discussion on this phenomenon is presented in Chapter 2. Existing anti-jam techniques are discussed, with emphasis on antenna technologies. The effect of RFI on GPS receivers is quantified. Modifications to the Matlab Algorithm Availability Simulation Tool (MAAST) are described. These changes allow one to determine WAAS time availability for practical receivers and antennas in the presence of RFI. Chapter 3 provides a detailed discussion on the finite difference time domain (FDTD) technique for solving electromagnetic radiation problems. The 2.5-dimensional FDTD technique is derived in detail. This method is essential for simulating the performance of the dielectric cavity antenna (DCA), which is a new type of interference resistant GPS antenna introduced in Chapter 4. Also in Chapter 4, a method for designing the DCA is derived. Results from roof testing of a prototype DCA are presented. In Chapter 5, the rectangular microstrip patch antenna MNM analysis technique is introduced. Input impedance and radiation patterns of microstrip patch antennas may be computed quickly and efficiently with the MNM. Modifications to the basic MNM model are required so that lumped loads embedded within the antenna substrate may be modelled. Mutual impedance between two or more patch elements is also computed with the MNM. In Chapter 6, the dual-patch reconfigurable anti-jam antenna

(DPRA) is introduced. The improved MNM model is used to analyze the DPRA. Results show that the two modes of operation for the DPRA are essentially independent of each other due to clever biasing of the PIN diodes embedded within the substrates. Chapter 6 also presents results from a flight test which was designed to validate a prototype DPRA. These results, along with analytical results from the cavity model, are used to evaluate the benefits of the DPRA to aviators using GPS WAAS as the primary navigation system. Finally, conclusions are provided in Chapter 7, along with some suggestions for future work.

Chapter 2

Radio Frequency Interference

Radio frequency interference, or RFI, can broadly be defined as any electrical signal or noise which, when present at the input terminals of a GPS receiver, degrades its navigation accuracy and performance. Severe interference to GPS occurs when RF energy is present at the GPS receiver antenna terminals at a sufficient power level to reduce the post-correlation carrier-to-noise level (C/N_0) to below the tracking threshold for one or more GPS satellites. Depending on the severity, RFI can increase user GPS position errors, or cause the receiver to lose lock on tracked satellites or be unable to acquire newly visible satellites. If fewer than four satellites are tracked, three-dimensional position information will not be available from the GPS receiver.

Upon certification of WAAS in mid-2003, GPS will be a primary-means navigation system for aircraft precision approaches in the United States. As we are moving into a new era where pilots will rely increasingly on GPS for air navigation, a reduction in WAAS availability or a violation of the WAAS continuity requirement due to RFI would be very undesirable. The consequences of RFI may be minor, such as a missed approach maneuver followed by an ILS landing. This would delay the landing, causing an annoyance to the passengers. Other aircraft in the vicinity could be delayed as well, ultimately resulting in a monetary penalty for a commercial carrier. In the worst case scenario, malevolent jamming could cause an accident, with resulting equipment damage or loss of life. While aviation grade GPS WAAS receivers are required to monitor for the presence of RFI, aviation GPS receivers are not hardened

against RFI [65]. The current mind-set of consumer GPS equipment manufacturers is that their customers are not likely to be victims of intentional RFI, since reported incidents of unintentional RFI have been rare, and cases of intentional jamming are non-existent [80]. While this may be good enough for the casual hiker who needs to find one's car again after a long hike, it is not adequate reasoning to satisfy the Federal Aviation Administration (FAA) when it comes to designing and implementing precision aircraft landing navigation systems. This chapter explores the threat of RFI to airborne GPS/WAAS users. Some existing anti-jam technologies and their limitations are discussed. Potential sources of RFI are identified and their effect on GPS receivers is quantified.

2.1 Sources of RFI

RFI may arise from unintentional sources such as commercial broadcast stations or from avionics on-board the aircraft. Intentional jamming could also cause RFI to GPS receivers. This section investigates both scenarios and lists examples of documented interference to GPS users in the past.

2.1.1 Unintentional RFI

AM Radio

AM radio broadcast stations operate in the 535 – 1,605 kHz frequency range, and transmit high power levels, up to 50,000 watts effective isotropic radiated power (EIRP). FCC regulations require that spurious emissions be suppressed by 80 dB relative to the carrier (dBc). Although interference to GPS is possible from AM transmitters, it is highly unlikely, and there have been no reported cases of such interference [66].

FM Radio

FM radio broadcast stations operate in the 88 – 108 MHz spectrum, and transmit power levels up to 100,000 watts EIRP. Like AM, FM radio spurious emissions must

be attenuated by 80 dBc. Considering the worst case scenario with a transmitter at maximum output power and a harmonic in the L1 band at -80 dBc, the FM radio station could jam GPS within a 10 mile radius. In spite of this, there have been no documented instances of GPS jamming by FM radio transmitters [66]. For most commercial broadcast stations, it is likely that the harmonics are attenuated much more than 80 dBc by low pass filtering at the transmitter site.

Analog Television

Analog television (TV) broadcasts occupy 6 MHz channels in the VHF (54 – 88 MHz) and UHF (174 – 216 MHz and 512 – 806 MHz) bands. VHF and low UHF band TV transmitters run at 100,000 watts EIRP maximum, while upper UHF band transmitters can operate at 5 MW EIRP. In practice, TV stations rarely operate at these maximum allowable power levels. Spurious emissions are required to be lower than -60 dBc. Worst case calculations of the threat posed by harmonics of TV transmitters indicate interference to GPS could occur up to 100 miles from the transmitter. Fortunately, field measurements at TV transmitter sites revealed that harmonics near the L1 band are suppressed by 100 dBc because anti-ghosting encourages this lower level [66].

In a documented case of unintentional RFI, the Hudson, Massachusetts channel 66 TV transmitter caused interference to a nearby L1 C/A-code GPS receiver. The frequency allocation for channel 66 is 782 – 788 MHz, producing second harmonic energy between 1,564 and 1,576 MHz. Although this television station happened to meet the FCC specifications for spurious emissions, GPS outages were reported up to 2 miles from the transmitter [41].

Digital Television

Digital Television (DTV) makes use of digital compression techniques to allow the transmission of high quality digital video and audio over the 6 MHz bandwidth currently allocated for an analog TV channel. The maximum data rate using this bandwidth is 19 Mbps. DTV transmit power levels are limited to 1 MW EIRP,

compared to 5 MW EIRP for analog TV. In addition, spurious emissions from DTV transmitters must be attenuated by 93.2 dB in the GPS L1 band. While DTV will someday replace analog TV, DTV has only found limited, experimental use to date, and there have been no reported cases of RFI to GPS users. The lower transmit power level and relatively stringent limits on spurious emissions should prevent future instances of RFI, even when DTV has fully replaced analog TV [66].

Amateur Radio

The amateur radio service operates in fixed and mobile service on many HF, VHF, UHF, and microwave frequencies from 1 MHz to above 300 GHz. Power levels up to 1,500 watts are allowed, while spurious emissions are limited to -60 dBc. The 6 meter and 1.25 meter bands have harmonics which fall within the L1 GNSS band. Worst case calculations predict that amateur radio transmitters could disrupt GPS service within a ten mile radius. However, interference to GPS from amateur radio service is unlikely since transmitters and antennas are tuned to the desired operating frequency, reducing harmonic content well below the FCC limit. On the other hand, some amateur equipment is experimental, and is more likely to produce spurious output than commercial gear [66].

Wireless LAN Devices

Unlicensed digital communications (IEEE 802.11) takes place in the 902 – 928 MHz, 2,400 – 2,483.5 MHz, and 5,725 – 5,875 MHz bands. This service is growing rapidly, as consumers increasingly demand more wireless connectivity between laptop computers, personal digital assistants, and other devices. Emissions from 802.11 devices are limited to 500 μV/m at 3 meters in the GNSS L1 band. This amounts to -71 dBW/MHz of RF power to an omni-directional transmit antenna [20]. Although there have been no reported cases of interference to GPS from these devices, a large number of these devices on-board an aircraft could pose a threat by raising the noise floor in the L1 band to an unacceptable level. Commercial airlines have procedures in place to prevent use of these devices during takeoff and landing.

VHF Air-Band Transceivers

Aircraft pilots rely heavily on their air-band VHF transceivers. These radios are used to communicate with air traffic control (ATC) during departures and landings. During RNAV operations, pilots routinely "check-in" with ATC at airports along the flight path. These transceivers are capable of producing tens of watts of RF output power from 118 to 137 MHz. The radios use AM for voice transmission, occupying a 6 kHz wide bandwidth. The transmitted signal contains the carrier as well, which allows asynchronous demodulation. Interference to GPS receivers can result if the 12th or 13th harmonic from these radios is within 1 MHz of the L1 GNSS band center frequency of 1,575.42 MHz. Fortunately, the VHF air band is far enough away from the L1 band that a low pass filter at the output of the VHF transceiver is sufficient to adequately attenuate these higher order harmonics. Modern air band transceivers are equipped with such filters, and have only rarely caused interference to GPS in recent years. In the past however, there have been reports of interference to GPS from on-board VHF air band communications transceivers without filters. The filter should be located within the transceiver, or very close to the RF output connector, to prevent leakage of harmonic energy through the coaxial cable connecting the radio to the antenna. VHF transceivers should be adequately shielded and grounded to prevent radiation of VHF harmonics and local oscillator harmonics directly from the chassis [66].

Passenger Electronic Devices

A number of electronic devices such as laptop computers, electronic games, and mobile phones all emit undesired RF energy. This energy can reach the external GPS antenna through aircraft windows and door seals. Much of the undesired radiation arises from microprocessors, which are clocked at increasingly higher frequencies as technology advances. In fact, the fundamental clock rate of personal computer microprocessors has recently exceeded the L1 frequency. These devices are required to meet Part 15 FCC rules on unlicensed electronic devices, which impose an upper limit equivalent to -71 dBW/MHz transmit power into an omni-directional antenna [20].

Unfortunately, the wideband output powers from many such devices will add, increasing the total noise power level at the GPS receiver input. Even if these devices meet the Part 15 rules, it is still possible to cause interference to GPS if a sufficient number of devices are active close to a GPS receiver.

Mobile Telephony

Mobile telephones operate in frequency bands of 824 – 849 MHz, 869 – 894 MHz, and 1,850 – 2,100 MHz in the United States. These phones can transmit up to 3 watts. Due to the large number of mobile phones in use today, one would naturally be concerned about the threat posed to GPS by these devices. However, the frequencies used by mobile phones are not harmonically related to the L1 GNSS band, and there have been no reported instances of interference to GPS as a result of mobile phone use aboard an aircraft. Nonetheless, their use is prohibited during takeoff and landing operations aboard the commercial carriers.

Ultra-Wideband (UWB)

Ultra-wideband (UWB) signals consist of a sequence of very narrow (sub-nS) pulses radiated by broadband transmitting equipment. The signal power in the pulse train is spread over a very wide bandwidth (several GHz). For data transmission, pulse-position or bi-phase modulation may be used. Of course, the spreading gain of such a wide bandwidth is enormous, so UWB signals can be effective even if they are very weak. Similar to GPS signals, UWB signals can be well below the noise floor and still be demodulated by suitable receiving equipment. While GPS receivers are inherently immune to pulse type interference, UWB transmissions could cause problems if there are a large number of UWB transmitters in operation in close proximity to a GPS receiver. Testing at Stanford revealed that low pulse repetition frequency (PRF) UWB signals are less damaging to GPS than high PRF signals. In fact, for PRF values less than 1/10 of the GPS receiver bandwidth, the UWB signals behave like pulsed noise interference, having minimal effect on the receiver. Certain PRF values (19.94 MHz) were found to cause significant interference to the receiver,

as spectral lines of the UWB pulse train appeared directly on top of the L1 C/A-code spectral lines, causing CW-like interference. Very high PRF UWB signals affected the GPS receiver in the same manner as white noise [48] [49]. The effect of UWB signals on GPS receivers is not completely understood, and more testing and analytical work are required to develop a working RFI model [66].

Unexpected RFI Sources

Interference to GPS could result from unexpected electronic devices. For example, significant GPS outages were reported in the Moss Landing, California harbor in early 2001. These RFI sources jammed the entire harbor, including the Monterey Bay Aquarium Research Institute differential GPS reference station receiver. With the help of direction finding equipment, three sources of RFI were located. These RFI emitters were VHF/UHF TV preamplifiers which were found to be oscillating in the L1 band [18]. Poor RF engineering and manufacturing techniques resulted in an unstable preamplifier design. This RFI incident proved to be quite a nuisance to the many users of the harbor, and the source of the RFI was rather difficult to track down.

2.1.2 Intentional RFI – Jamming

Intentional jammers could be very effective in disabling GPS receivers since the GPS satellites are so far from the user, and the received signal strength is very weak. Suitable equipment is commercially available for those serious about jamming GPS. A portable jammer produced and sold by the Aviaconversiya Company in Moscow, Russia sells for $40,000. This device, shown in Fig. 2.1 produces 8 watts of power in the L1 and L2 GPS bands, and also in the two GLONASS (Russian equivalent to GPS) bands. The company claims effective jamming ranges of several hundred kilometers. An application for this jammer, as stated by the company, is to prevent successful targeting of U.S. Tomahawk cruise missiles. Both omni-directional and high-gain antennas are provided with the device [33]. If this price seems a bit excessive, consider that a 2 watt jammer could be built with a handful of parts for under $100, and a 100

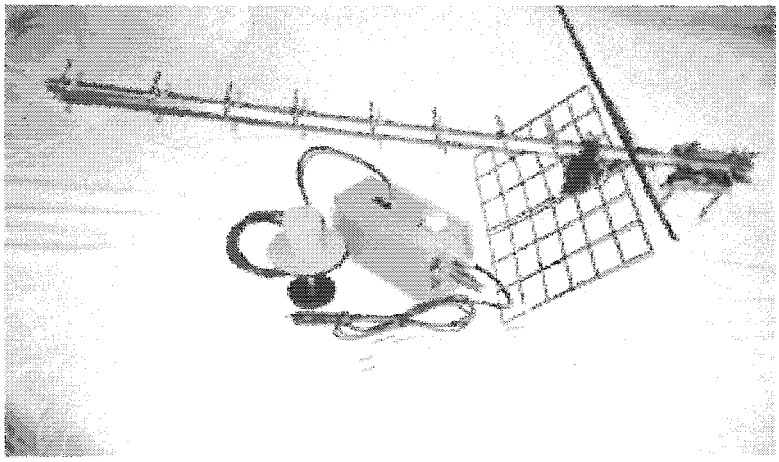

Figure 2.1: Commercially Available GPS Jammer.

mW jammer could be built at virtually no cost. Some knowledge of microwave circuit design is required to design and build these devices, however. In a report issued by the Department of Transportation *prior* to September 11, 2001, it was determined that "... the GPS signal is subject to degradation and loss through attacks by hostile parties ... The consequences of loss of the GPS signal can be severe ... in terms of safety and environmental and economic damage to the nation, unless the threats are mitigated." The report recommended that "Continuing assessments should be made of the applicability of military anti-jam technology, including receiver and antennas, to the civil sector. U.S. Government agencies should be encouraged to identify the more promising anti-jam technologies, and to work with industry to make them affordable and suitable for civilian applications." The FAA is wisely concerned about RFI incidents which may occur during GPS guided aircraft landing operations, and has been conducting an RFI mitigation program since 1993. This program involves efforts to measure and characterize the impact of RFI on GPS receivers, design of RFI localization equipment, and developing on-site RFI monitors [34]. In spite of the ease with which one could jam GPS, there have been no reported cases of intentional jamming of aircraft. Nonetheless, the threat always exists, and efforts continue to develop inexpensive, effective anti-jam technologies for civilian use.

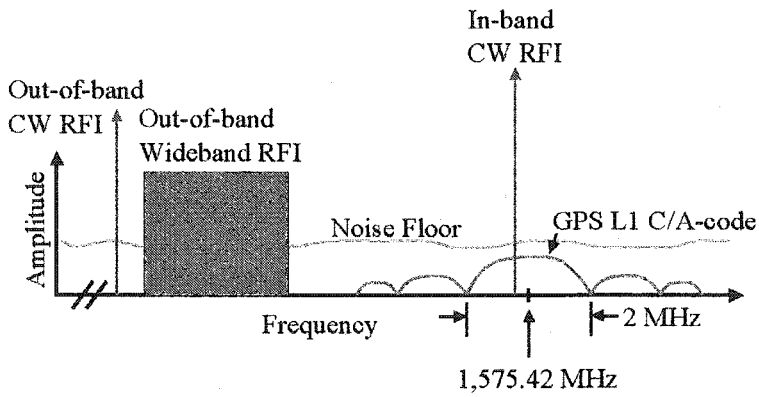

Figure 2.2: Signals Present at the GPS Receiver Antenna.

2.2 RFI Spectral Categories

This section considers the types of RF signals which might appear at the input to a GPS receiver. A spectral representation of this energy is shown in Fig. 2.2. If the antenna is well-designed, GPS satellite signals will be present, of course. Interfering signals are always present in the RF spectrum, but these signals may or may not be located within the L1 passband. If they are located far enough away from the L1 band, and the GPS antenna and/or receiver employ RF bandpass filtering, then these signals are rarely of concern. In addition to discrete bandlimited signals, there is always broadband noise present at the input to the receiver. This "noise floor" is due to thermal noise in the receiver front end as well as sky noise. For a typical GPS receiver with a microstrip patch antenna, the noise power at the receiver input in a 2 MHz bandwidth is on the order of -107 dBm. This spectrum is flat over the bandwidth of interest (and well beyond), and can be represented mathematically as additive white gaussian noise (AWGN). In the following sections, discrete in-band interference sources are considered. Specifically, wide and narrow-band RFI sources, as well as pulsed interference are described.

2.2.1 Broadband RFI

Broadband interference is a term used to describe interfering signals which occupy the entire RF bandwidth of the GPS receiver. If the signal has a flat power spectrum over the passband of the receiver, it is known as bandlimited AWGN, and is considered non-coherent. An example of a practical broadband noise source found in the microwave lab is an avalanche diode noise generator, commonly used with noise figure meters. These sources generate a flat power spectrum from DC to above 24 GHz. This noise source, followed by an L1 bandpass filter and a high gain power amplifier, would make an effective GPS jammer. If bandlimited AWGN is present at the receiver input, it will simply be added to the noise floor in a root-mean-square sense (non-coherently). This "raising" of the noise floor effectively decreases the post-correlation carrier-to-noise density ratio (C/N_0) of the GPS satellite signals. C/N_0 will be formally defined in Section 2.4, but for the purposes of this discussion, consider C/N_0 to represent the strength of the satellite signal compared to the strength of the broadband noise. If a strong broadband noise source is nearby, the noise floor may rise to the level where the post-correlation C/N_0 of the GPS satellite signals is below the threshold value required for tracking. At this point, the GPS receiver is effectively jammed by the broadband noise source, as it loses lock on the GPS satellites.

2.2.2 CW and Narrowband RFI

A continuous wave (CW) source is a sinusoidal signal source operating at only one frequency, ideally having zero bandwidth. This type of power spectrum is also called a line spectrum, as it is represented in the spectral domain as a Dirac delta function (Fig. 2.2). CW RFI may be composed multiple CW line spectra, in which case it is termed "CW-like" RFI. In addition, narrowband spectra (relative to the spacing of the C/A-code spectral lines, or 1 kHz) are often called CW-like RFI. The effect of CW interference on GPS receivers is more complex than the wideband noise case. The C/A-code at L1 is a line spectrum, with the lines separated by 1 kHz. Interfering signals which are highly correlated with this spectrum will leak through the correlator, and potentially lead to a false lock being detected in the code tracking loop. Therefore,

CW signals which fall directly on the C/A-code spectral lines present the greatest danger to the receiver. The problem is further exacerbated by the fact that the C/A-code lines have varying amplitudes, some as high as 9 dB above the ideal value for a purely random digital waveform. Because of this, a conservative analysis of CW RFI includes a factor of 10 dB for the worst case scenario of a CW interferer falling directly on top of the worst case C/A-code spectral line. CW signals falling between spectral lines have minimal impact, which makes it difficult to bound the effect of CW RFI. Another harmful effect of CW interference occurs in the A/D converter. A/D converters in GPS receivers operate on the principle that the input signal is primarily AWGN, and the signal voltage samples will have a gaussian distribution. If a strong CW signal is present, it will "capture" the A/D converter, causing the samples to be dominated by the peaks of the sine wave. This will prevent any chance of de-correlating the weak GPS signals which are masked by the CW RFI [80].

2.2.3 Pulsed Interference

GPS receivers are quite immune to pulsed-type interference. The reason for this is that GPS receivers use fast AGC circuits which recover quickly from strong, short pulses of RF energy. Although the receiver is disabled while the pulse is on, it can track the C/A-code based on the off-period. Of course, very strong pulsed interference can completely disable a GPS receiver since the AGC recovery time is, after all, finite.

2.3 RFI Suppression Techniques

The weak satellite signal levels at the antenna make GPS receivers particularly vulnerable to jamming. Fortunately, the use of robust RF bandpass filtering and the correlation process itself provide substantial RFI resistance to signals outside the GPS L1 passband. However, in-band signals as low as -120 dBm can cause substantial interference to the point where accuracy is degraded or satellite tracking is altogether impossible. FCC regulations are the primary preventative measure for unintentional RFI sources. However, even if electronic devices meet FCC specifications, RFI can

still occur to GPS receiving equipment in special cases. Intentional jamming is a concern because it can happen anytime, anywhere, and there is no way to predict it in advance. Prudent manufacturers of GPS equipment for military applications need to plan for intentional jamming as part of their mission. As a result, robust anti-jam technologies have been developed by military GPS equipment designers. These techniques involve attenuating the interfering signal either at the antenna or in the receiver. This section will explore the various anti-jam technologies currently in use.

2.3.1 Receiver Techniques

Spectral Filtering

Aggressive RF filtering can significantly reduce RFI which is outside the GPS passband. Exceptionally sharp notch filters can even remove CW or CW-like RFI from within the GPS passband, e.g., the "in-band CW RFI" source in Fig. 2.2. Narrowband antenna designs can also help to reduce the sensitivity to out-of-band interference sources, such as those shown in Fig. 2.2. Tuned band-reject and adaptive digital signal processing (DSP) filtering techniques are sometimes embedded in modern GPS receivers. These filters adaptively attenuate in-band and out-of-band interference sources, and can provide up to 35 dB attenuation of narrowband interference. On the downside, spectral filtering techniques can slow GPS satellite signal acquisition time. Also, filters always have some loss, which attenuates the desired signal to some extent. Spectral filtering is not effective against wideband jammers [13]. Extremely strong out-of-band signals can overload the receiver RF amplifier stages in spite of the filter. Fortunately, PIN diode or ferrite limiters are effective in clipping high-power signals, and allow the weak GPS signals to pass through unaffected [80].

Temporal Filtering

Temporal or time filtering employs digital signal processing (DSP) at the digital IF stage. Temporal filters perform an FFT of the incoming signal and search for strong CW components. Any CW signals in the spectrum are removed by an adaptive FIR filter. An inverse FFT is performed, and the resulting digitized time waveform is

free of CW components. Temporal filters are extremely effective in removing CW interference, achieving attenuations up to 40 dB. However, temporal filters cannot detect and mitigate broadband RFI [80].

Inertial Aiding

Inertial navigation systems (INS) may be coupled with GPS in several ways to increase anti-jam performance. Narrowing the code and carrier tracking loop bandwidths reduces the noise power in these loops, increasing satellite C/N_0, thus increasing resistance to RFI. Since narrowing the tracking loop bandwidth reduces the line-of-sight dynamics each channel can tolerate, the tracking loops must be aided with velocity information from the INS. Increasing the loop filter order also serves to mitigate the loss of performance in the face of platform dynamics [80]. Tracking loop aiding provides up to 20 dB rejection of RFI. Coupling of the GPS and INS systems can also be accomplished by Kalman filtering techniques so that the navigation system can handle short GPS outages due to interference or jamming. The level of achievable performance in this case depends on the quality of the INS and the care taken in the design of the Kalman filter algorithm [13].

2.3.2 Antenna Techniques – Spatial Filtering

Spatial filtering is a means of distinguishing between signals arriving from different regions of space. Ideally, antennas should be designed to have high gain toward the desired signal(s), and low gain in the direction of undesired signal(s). This section discusses several antenna techniques used to spatially discriminate against RFI.

Spatial Null Steering

One popular anti-jam GPS antenna is the null-steering controlled radiation pattern antenna (CRPA). The null-steering CRPA is normally implemented as a phased array of printed microstrip patch antenna elements. The complex amplitudes of the array elements are weighted adaptively in real-time to minimize interference arriving from particular directions. If the CRPA has N patch elements, it can steer nulls

toward $N-1$ jammers. The depth of the null is a function of the number of nulls the antenna must steer simultaneously. Null-steering CRPAs are typically capable of steering a single 40 dB null, or multiple 15 – 25 dB nulls. The CRPA detects the presence of RFI by means of a jamming-to-noise power ratio (J/N) meter. The J/N meter monitors the AGC voltage at the IF stage of the receiver. If the AGC voltage is different from the value required to keep the IF signal set at the level of the thermal noise RMS level, then some other signal must be in the receiver passband controlling the AGC. This undesired signal is above the noise floor. The antenna works adaptively to minimize the J/N ratio. The adaptive weighting can occur directly at the RF frequency, or at a convenient IF frequency after down-conversion. Null-steering CRPAs are effective against all types of interference, including broadband noise sources. These antennas are complex and expensive (> $10,000), and are not popular with the civilian aviation community. Their use has been restricted to military applications.

Spatial Beam Forming

Beam steering or beam forming refers to a class of antennas which direct high gain pencil beams toward the GPS satellites. Naturally, the antenna gain is low in those directions other than toward the satellites. If interference sources are located in the directions of these minima, then the beam forming antenna serves to increase the C/N_0 of the satellite signals, while simultaneously reducing the received power from the interferers. The net gain can be quite large. Satellite ephemeral tracking is required in order to properly direct the beams. The three-dimensional attitude of the antenna is also required. In order to produce narrow beamwidths, the antenna effective aperture must be quite large. These antennas are best suited for land or marine use where antenna real estate is not a concern. Similar to null-steering CRPAs, beam-steering CRPAs are bulky, complex, expensive, and are rarely used by the civilian aviation community [13].

Amplitude and Phase Cancellation

This technique makes use of two GPS antennas mounted on a vehicle. One antenna receives the GPS satellite signals plus the interfering signals. The other antenna is located so as to receive only the interference source(s). Signals from the two antennas are then subtracted, yielding only the GPS signal. An example of this method would be to locate antennas on the top and bottom of an aircraft (assuming ground based RFI sources). This technique can produce 20 – 30 dB suppression of single or multiple CW or wideband sources. The method is sensitive to the attitude of the vehicle. Overlap between the two antenna patterns reduces the effectiveness of this technique [13].

Polarization Cancellation

Polarization cancellation relies on the assumption that the interfering signal will have a different polarization than the GPS satellite signals (RHCP). The receive antenna is designed to differentiate between the different polarizations of incoming signals. The polarization of the interfering signal is identified, and an adaptive algorithm works to cancel the undesired polarization. This technique works with both wideband and CW interference, and can attenuate multiple jammers if they are polarized identically. For wideband interferers, 25 dB of attenuation is possible, whereas CW interferers are attenuated by 40 dB. This technique is relatively low-cost, and can be integrated quite easily into either new or existing installations [13].

2.4 Effects of RFI on the GPS Receiver

2.4.1 Interference Free Case

Interference Free S/N_0

The GPS receiver is a direct sequence spread spectrum receiver. This makes the signal-to-noise analysis more complicated than that for receivers employing conventional analog or digital modulation. Consider a weak signal from a low elevation

GPS satellite. This signal would provide -130 dBm of C/A-code signal power to the receiver input, assuming a zero dBic gain receive antenna. Now consider a reasonable antenna such as a microstrip patch antenna, having a gain of +5 dBic. In this case, there would be -125 dBm of signal power at the receiver input terminals. Call this power S. We can compute the thermal noise power N_T with

$$N_T = k(T_A + T_{RX})B, \tag{2.1}$$

where T_A is the antenna noise temperature in Kelvin (K), T_{RX} is the receiver noise temperature in Kelvin (K), k is Boltzmann's constant (1.38 $\times 10^{-23}$ J/K), and B is the receiver RF bandwidth in Hz. If the noise figure of the receiver is 4 dB, and the antenna temperature is 100°K, then the thermal noise power N_T in a 2 MHz bandwidth would be -108 dBm. The resulting S/N_T ratio is -17 dB, meaning the GPS signal is beneath the noise floor! However, the correlation process provides 43 dB of processing gain, resulting in a positive post-correlation signal-to-noise ratio. In a spread spectrum system, the processing gain is the ratio of the RF bandwidth (2 MHz) to the data bandwidth (100 Hz). It is common practice to normalize the thermal noise power N_T to a 1 Hz bandwidth, and call this quantity N_{0T}. Then, the post-correlation signal-to-noise ratio (S/N_{0T}) for a GPS receiver is expressed as

$$\frac{S}{N_{0T}} = S - N_{0T} - L_{IF} - L_{A/D} - L_{SV} \text{ dB-Hz}, \tag{2.2}$$

where L_{IF} is the loss in the IF filter (0.4 dB for a 2 MHz bandwidth), $L_{A/D}$ is the loss in the A/D converter (1.2 dB for a 2-bit A/D with 2 MHz IF bandwidth), and L_{SV} is a loss due to modulation imperfections (typically 0.6 dB) [66]. S and N_{0T} are the received signal power (dBm) and the noise power in a 1 Hz bandwidth (dBm/Hz), respectively. The interference free signal-to-noise ratio S/N_{0T} is more commonly referred to as the *carrier-to-noise density ratio*, and denoted by C/N_0. In this section, we retain the more general notation of Eq. (2.2) for clarity. We can apply Eq. (2.2) to the previous example by computing the normalized thermal noise power in a 1 Hz bandwidth (N_{0T}) to be -171 dBm, resulting in an actual S/N_{0T} of

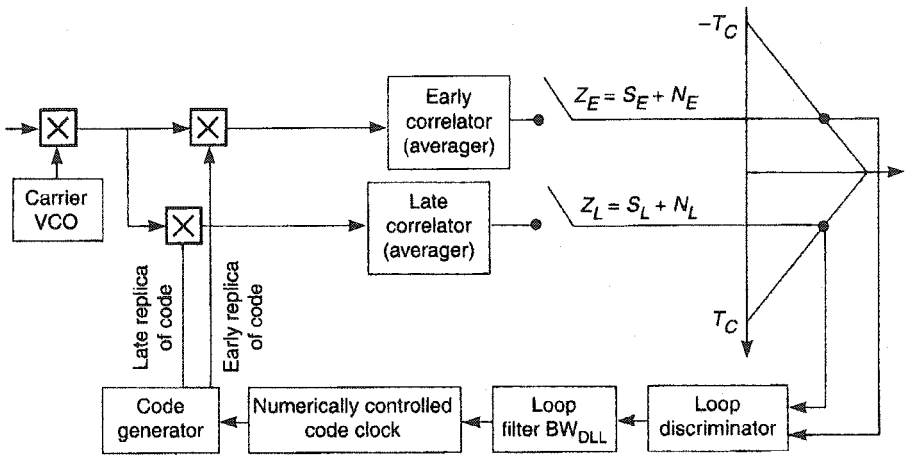

Figure 2.3: GPS Receiver DLL Block Diagram [25].

43.8 dB-Hz. The parameter S/N_{0T} is computed by nearly all modern GPS receivers, and is reported as C/N_0 to the user. C/N_0 is a very useful parameter, and may be used to properly locate and orient a GPS receive antenna. C/N_0 can also be used as an input to an RFI detector, along with the receiver automatic gain control (AGC) signal.

Delay Lock Loop

The GPS receiver employs a delay lock loop (DLL) which locks onto the PRN code of the satellite being tracked. In its simplest implementation, the DLL makes use of one early and one late correlator, each of which multiplies and integrates the incoming signal with a shifted replica of the C/A-code. The early-late code replicas are differentially offset by one chip spacing (1 μS, or 300 meters). The absolute phase of the incoming code (relative to the user's clock) is resolved when the difference between the early and late correlator outputs is zero. The DLL works to keep this difference zero in the face of noise and interference. Any deviation of the estimated early-late zero point from the true zero point shows up as a pseudorange error. This simple implementation is called an early-late correlator. A block diagram of the early-late correlator and DLL is shown in Fig. 2.3.

The dot-product correlator makes use of a third correlator called the prompt correlator. Here, the third C/A-code replica is spaced halfway between the early and late replicas, at the expected position of the incoming code. This action yields a prompt measurement, and should correspond to the correlation peak if the prompt replica and the incoming C/A-codes are lined up exactly. The pseudorange error is noisy in the short term, and has a standard deviation which is a mathematical function of the DLL loop bandwidth, early-late correlator spacing, strength of the satellite signal, and the thermal noise power [25]. By smoothing the noisy DLL code phase estimates with carrier phase measurements, an improvement in DLL performance is realized. Carrier smoothing is characterized by a time constant α, which is typically 1/100 Hz. With these considerations, and assuming AWGN, the 1-σ pseudorange jitter of the dot-product DLL is expressed as

$$\sigma_{\mathrm{DLL}} = cT_c\sqrt{\left(\frac{\alpha}{2}\right)\frac{B_{\mathrm{DLL}}d_c}{2\,S/N_0}\left[1+\frac{1}{S/N_0\,T}\right]}\ \text{meters}, \tag{2.3}$$

where B_{DLL} is the DLL loop bandwidth in Hz (typically 1 Hz), d_c is the early-late correlator chip spacing (1.0), T_c is the chip period (1 μS for the C/A-code), c is the speed of light, T is the pre-detection integration time (20 mS for GPS, 2 mS for WAAS), and S/N_0 is the signal-to-noise ratio in a 1 Hz bandwidth from Eq. (2.11), which includes RFI effects. As shown in Fig. 2.4, pseudorange error is rather insensitive to the S/N_0 of the GPS satellite signal being tracked [66]. Receiver parameters used to generate Fig. 2.4 are listed in Table 2.1. The DLL will not lose lock on the C/A-code until the tracking threshold is exceeded. A rule of thumb 1-σ tracking threshold is 1/6 chip, or 50 meters [80]. We will see shortly that in noisy conditions, the PLL loses lock long before the DLL.

Phase Lock Loop

In addition to tracking the phase of the C/A or P(Y)-code, GPS receivers also track the phase of the carrier. A phase lock loop (PLL) is used to perform this function. The PLL is required to keep the receiver locked on the center frequency

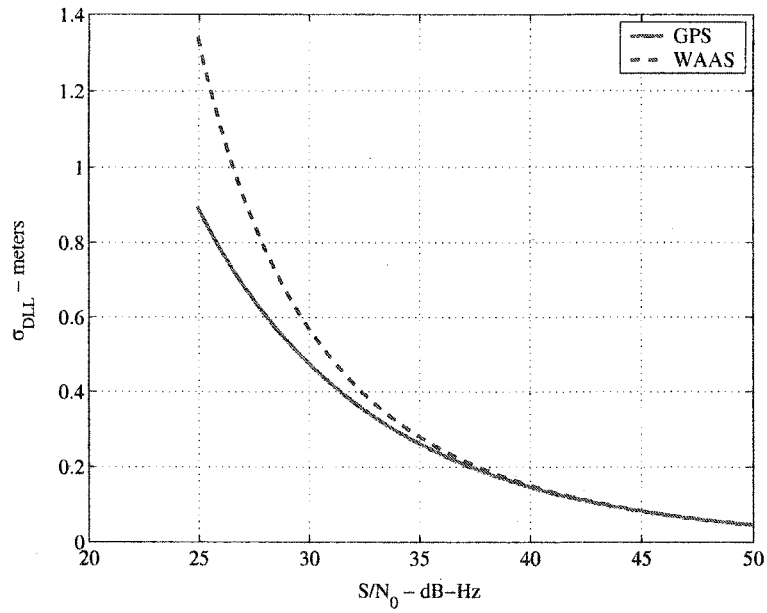

Figure 2.4: DLL 1-σ Pseudorange Error vs. S/N_0.

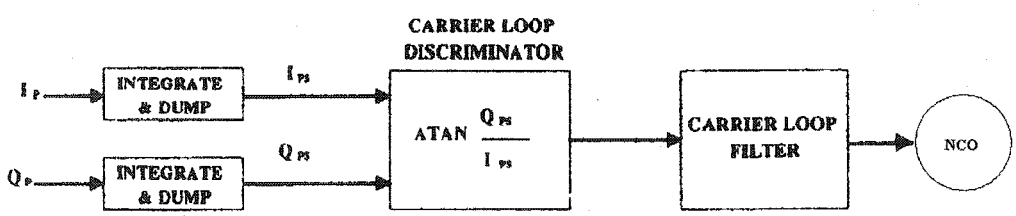

Figure 2.5: Costas Loop Discriminator Block Diagram [80].

of the received C/A-code. Apparent frequency offsets from the L1 center frequency of 1,575.42 MHz are always present and are caused mainly by Doppler shift of the satellite signals. Any residual frequency error will result in distorted correlator outputs, leading to excessive pseudorange error. The output of the PLL is the navigation data message, which provides the receiver with accurate, up-to-date satellite specific information. The PLL is implemented in a configuration known as a Costas loop, whose discriminator is shown in Fig. 2.5. Here, prompt correlator samples from the receiver tracking channel are used to estimate the phase tracking error. This error

signal is fed back into the receiver channel's numerically controlled oscillator (NCO). A third order loop is used to minimize errors due to user dynamics. The 1-σ phase error of the carrier tracking loop is expressed as

$$\sigma_{\phi,noise} = \sqrt{\frac{B_\phi d_c}{S/N_0}\left[1 + \frac{1}{2S/N_0 T}\right]} \text{ radians,} \tag{2.4}$$

where B_ϕ is the one-sided PLL loop bandwidth, typically 15 to 20 Hz for normal loop tracking. The oscillators in the GPS satellites and in the user's GPS receiver inherently posses phase noise which serves to increase the jitter in the output of the receiver carrier tracking loop. The jitter due to the GPS satellite $\sigma_{\phi,SV}$ is specified as 5.7°, while the jitter due to the receiver oscillator $\sigma_{\phi,RX}$ is taken to be 5°, assuming a high quality temperature compensated crystal oscillator (TCXO) [66]. The total PLL phase jitter is then given by

$$\sigma_\phi = \sqrt{\sigma^2_{\phi,noise} + \sigma^2_{\phi,osc}} \text{ radians,} \tag{2.5}$$

where

$$\sigma^2_{\phi,osc} = \sigma^2_{\phi,SV} + \sigma^2_{\phi,RX}. \tag{2.6}$$

In Fig. 2.6, we observe that the RMS carrier phase jitter increases rapidly at low values of S/N_0. The Costas loop loses lock on the carrier phase if the error σ_ϕ exceeds 15°. Comparing Fig. 2.4 and Fig. 2.6, we observe that the PLL is limiting in terms of maintaining lock on the GPS satellite signals, as the PLL tracking threshold will be exceeded long before the DLL threshold. For a C/A-code receiver having the parameters listed in Table 2.1, the tracking threshold is exceeded when S/N_0 falls below about 26 dB-Hz. For the WAAS ranging signals which have a wider pre-correlation bandwidth due to the increased data bit rate, the threshold S/N_0 is 28 dB-Hz [66].

Perhaps a more meaningful measure of carrier loop performance for aviation applications is the mean time between cycle slips. The mean time between cycle slips

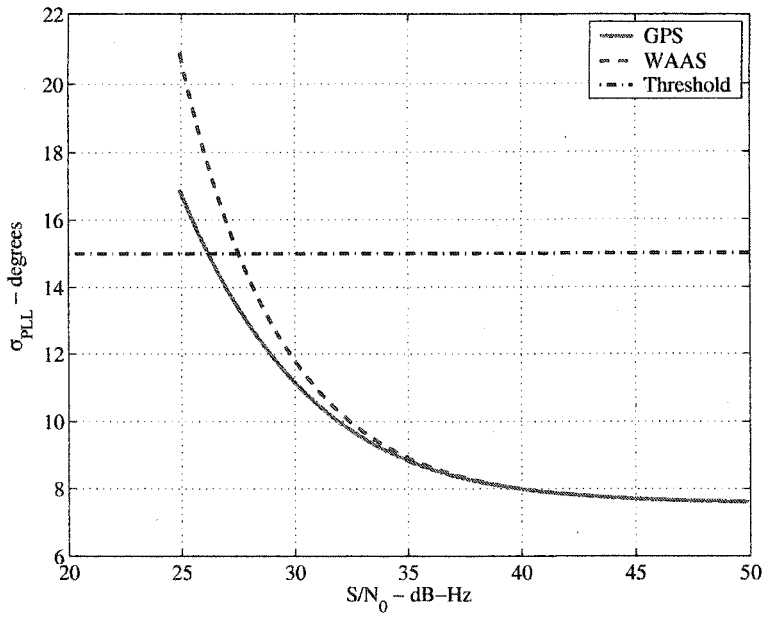

Figure 2.6: PLL 1-σ Phase Jitter vs. S/N_0.

for a first-order Costas loop is

$$\bar{T} = \frac{\pi}{2B_\phi \gamma} \tanh\left(\frac{\pi\gamma}{4\sigma_\phi^2}\right) \left[I_0^2\left(\frac{1}{4\sigma_\phi^2}\right) + 2\sum_{n=1}^{\infty}(-1)^n \frac{I_n^2\left(\frac{1}{4\sigma_\phi^2}\right)}{1+(4n\sigma_\phi^2/\gamma)^2} \right], \tag{2.7}$$

where I_n is the nth order modified Bessel function of the first kind, and γ is the phase tracking error due to dynamics, in Hz. The probability of a cycle slip over an exposure time of t seconds is

$$P_{cs}(t) = 1 - e^{-t/\bar{T}}. \tag{2.8}$$

No closed form slip rate expressions exist for second and third order Costas loops. However, simulations have revealed that slightly higher values of S/N_0 are required to achieve the same performance as first order loops. To simulate second or third order loops, one should subtract 1 dB or 2 dB, respectively, from the S/N_0 prior to using Eqs. (2.7) and (2.8). The maximum phase tracking error due to dynamics for

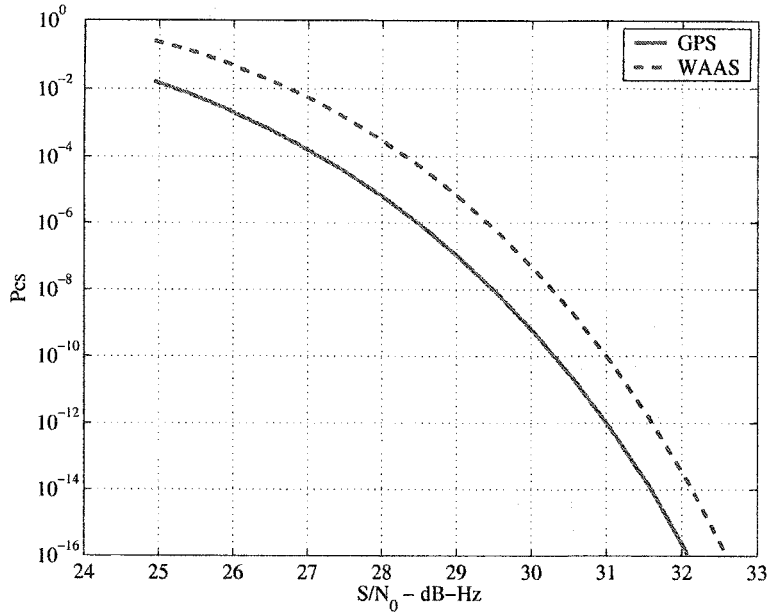

Figure 2.7: Cycle Slip Rates vs. S/N_0.

a second order Costas loop is

$$\gamma_{max} = \frac{\Delta f_{max}}{\omega_n^2} \approx \frac{2.76 a_{max}}{\lambda B_\phi^2}. \tag{2.9}$$

For a third-order loop, the maximum phase error is

$$\gamma_{max} = \frac{\Delta f_{max}}{\omega_n^3} \approx \frac{5.67 j_{max}}{\lambda B_\phi^3}. \tag{2.10}$$

For precision approaches, the maximum expected user acceleration and jerk are $a_{max} = 0.58$ g and $j_{max} = 0.25$ g/s, respectively. The probability of a cycle slip in a one second time interval with a 20 Hz third-order loop bandwidth is plotted in Fig. 2.7. Other receiver parameters used to generate Fig. 2.7 are listed in Table 2.1. A rule of thumb maximum allowable cycle slip rate for digital communication receivers is 10^{-5}. To meet this requirement, the S/N_0 must exceed 28 dB for GPS signals, and 29 dB for WAAS signals [66].

2.4.2 Interference Case

Now consider the case where interference is present at the GPS receiver antenna terminals. The post-correlation signal-to-noise ratio will be degraded by the interference, and is expressed mathematically by

$$\left(\frac{S}{N_0}\right)^{-1} = \left(\frac{S}{N_{0T}}\right)^{-1} + \left(\frac{S}{I_0}\right)^{-1} \text{ dB-Hz}, \tag{2.11}$$

where S/N_{0T} is from Eq. (2.2), and S/I_0 is from Eq. (2.12). Upon inspection of Eq. (2.11), we find that if the interferer power is zero, then S/N_0 becomes the interference free S/N_{0T} from Eq. (2.2), as expected. The expression for the post-correlation carrier-to-interference power density ratio S/I_0 is

$$\frac{S}{I_0} = S - I - 10\log T_c - L_{IF} - L_{A/D} - L_{SV} - L_{PG}, \text{ dB-Hz} \tag{2.12}$$

where I is the in-band interferer power (dBm), T_c is the chip period (1 μS for the GPS C/A-code), and L_{PG} is a processing gain error which accounts for the non-randomness of the repeating C/A-code. Use of the chip period T_c in this fashion assumes that the interference is uncorrelated with the signal. Thus, the full signal power will be recovered by the correlation process, while only a fraction (T_c/Hz) of the interference power will leak through the correlator. The factor L_{PG} accounts for interference sources which are partially correlated with the signal. L_{PG} is 0 dB for wideband RFI because the non-random variations in the C/A-code line spectrum average out over wide bandwidths. For narrowband RFI, L_{PG} can be negative if a CW signal falls between the C/A-code spectral lines. However, a conservative analysis would take L_{PG} to be 10 dB, which is worst case [66]. Here, a CW interferer falls directly on the strongest line of the C/A-code. L_{IF} accounts for signal loss through the IF bandpass filter, and is 0.4 dB for a 2 MHz wide IF filter, assuming wideband RFI. This parameter is doubled for the case of CW RFI since the interfering signal is not attenuated by the IF filter, as it is in the case of wideband interference. Thus, L_{IF} is 0.8 dB for narrowband RFI with a 2 MHz wide IF filter. Use of Eq. (2.11) yields an effective signal-to-noise ratio in the presence of thermal noise and interference. If

S/N_0 for a particular satellite is below the tracking threshold ($\approx$26 dB-Hz for the L1 C/A-code), the GPS receiver will lose lock on that satellite, and it will not be available for use in the position solution. If fewer than 4 satellites are available, a three-dimensional position fix cannot be obtained, and the receiver will be rendered useless for airborne navigation.

CW Interference

While wideband interference is accurately modelled with the equations in the previous sections, the effect of CW interference on S/N_0 is less predictable. The severity of this effect depends on the actual frequency of the offending CW signal within the GPS passband. Also, due to the varying Doppler frequencies of the GPS satellite signals, CW RFI affects each of the satellite channels to a different extent than the others. The time-varying nature of the effect of CW RFI makes the analysis more difficult. Fortunately, the degradation of S/N_0 due to CW interference can be conservatively bounded. Ignoring the navigation modulation for now, consider that the C/A-code is composed of a line spectrum having a $\text{sinc}^2(x)$ envelope. The lines are separated in frequency by the repetition rate of the C/A-code, which is 1 kHz. These C/A-code lines are vulnerable to continuous wave (CW) interference because partial correlation exists between the C/A-code lines and a CW signal falling on one of the lines. If strong enough, the offending CW RFI can "leak" through the correlator, having dire consequences for the GPS receiver. Especially sensitive are those lines of the C/A-code which are higher in amplitude than others. If the C/A-code were purely random, the lines close to the center frequency would be 30 dB down from the total signal power. However, since the Gold codes comprising the C/A-codes are not purely random, some lines are only 21 dB down from the signal power [80]. These lines are the most vulnerable to CW interference, and account for the use of a 10 dB processing gain in Eq. (2.12). If the receiver can still track the satellite, the CW RFI will likely distort the autocorrelation peak, causing pseudorange measurement errors. Another negative effect of CW RFI occurs in the PLL carrier tracking loop. Within the PLL, it is possible to falsely lock onto the CW signal instead of the C/A-code. These false locks are undesirable for obvious reasons. Detecting CW RFI is most

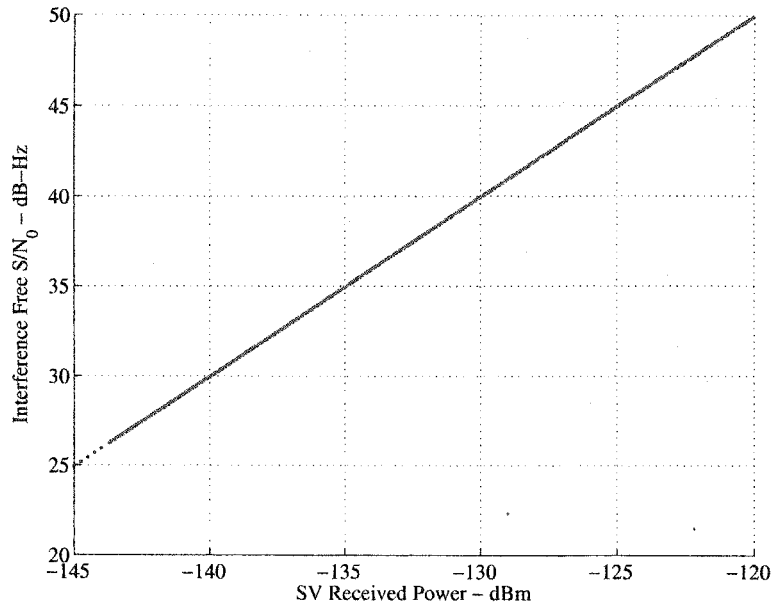

Figure 2.8: GPS Receiver S/N_0 for Various SV Received Power Levels.

effective within the PLL, as cycle-slips or navigation message bit errors can indicate the presence of CW RFI.

2.4.3 Typical Receiver Performance

It would be instructive to make use of the theory developed in the previous section to solve an example problem. Consider a GPS receiver having the parameters listed in Table 2.1, tracking a GPS satellite with no interference present. We can plot the S/N_0 vs. the satellite signal strength, shown in Fig. 2.8. This figure shows in red dots the satellite signal strengths for which the receiver has lost lock on the satellite. Now assume there is a 2 MHz wide broadband noise source present, and the satellite signal strength is fixed at -120 dBm, which represents a very strong signal. Fig. 2.9 shows the receiver S/N_0 for a range of interferer power levels. The receiver loses lock at a S/N_0 of 26 dB-Hz for the parameters listed in Table 2.1. This occurs when the RFI power level is at -88 dBm. Thus, the noise power can be 32 dB above the signal power, and the receiver can still track the satellite. This is obviously one of the

Parameter	Value
$\sigma_{\phi,\mathrm{RX}}$	5°
$\sigma_{\phi,\mathrm{SV}}$	5.7°
$\sigma_{\phi,\mathrm{thresh}}$	15°
$\sigma_{\mathrm{DLL,thresh}}$	50 m
$\mathrm{B_{IF}}$	2 MHz
$\mathrm{L_{A/D}}$	1.2 dB
$\mathrm{L_{PG}}$	0 dB (WB)
$\mathrm{L_{IF}}$	0.4 dB (WB)
$\mathrm{BW_{DLL}}$	1 Hz
$\mathrm{BW_{PLL}}$	20 Hz
$\mathrm{d_c}$	1.0 chips
τ_{smooth}	100 S
T	20 mS (GPS), 2 mS (WAAS)
NF	4.0 dB
RFI Type	WB Noise
$\mathrm{B_{RFI}}$	2 MHz

Table 2.1: GPS Receiver and RFI Parameters.

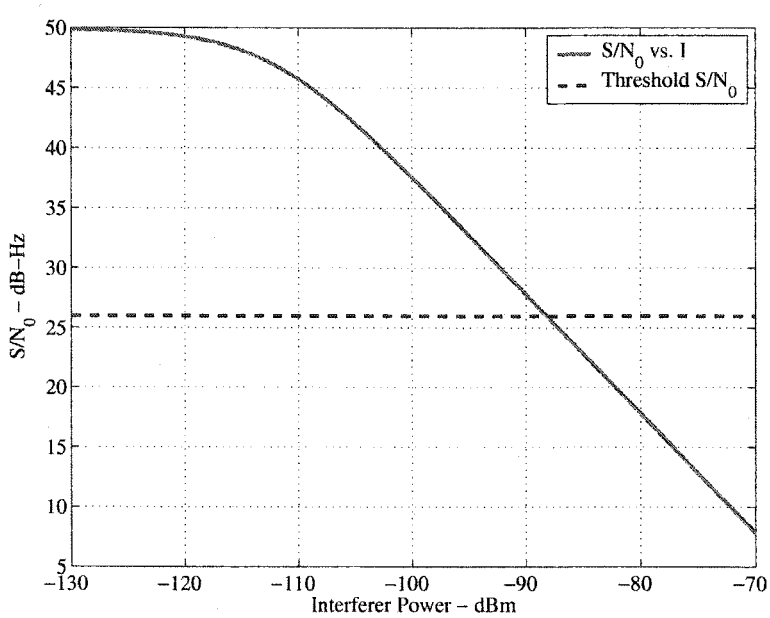

Figure 2.9: GPS Receiver S/N_0 for Various RFI Power Levels.

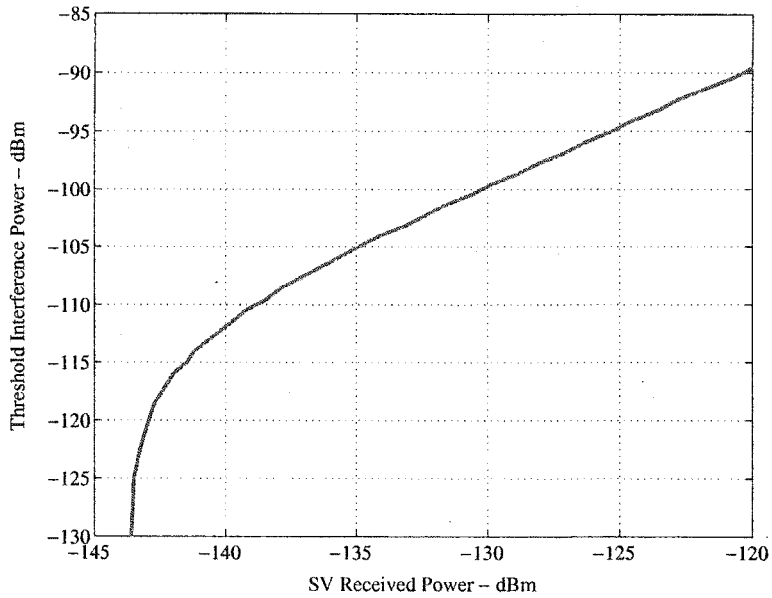

Figure 2.10: RFI Power Levels Causing Loss of Lock.

advantages of a CDMA system. From Fig. 2.9, we observe that the receiver begins experiencing difficulty when the interference level is at -120 dBm. If we consider the range of possible satellite signal strengths the receiver is likely to experience, we can plot the RFI power level at which the receiver will lose lock for each of these signal power levels. This is shown in Fig. 2.10. From Fig. 2.10, we observe that -90 dBm is required to prevent tracking the strongest satellite, and thus completely jam the GPS receiver. Lower interferer power levels will cause some satellites to be lost, while tracking will continue for others. Whether a position solution is available depends on the number of satellites which are still being tracked.

2.4.4 GPS WAAS Interference Mask

The Radio Technical Commission for Aeronautics (RTCA) has defined an RFI operating environment for airborne GPS WAAS receivers [66]. This "RFI mask" is intended to provide GPS receiver manufacturers with guidelines for designing receivers

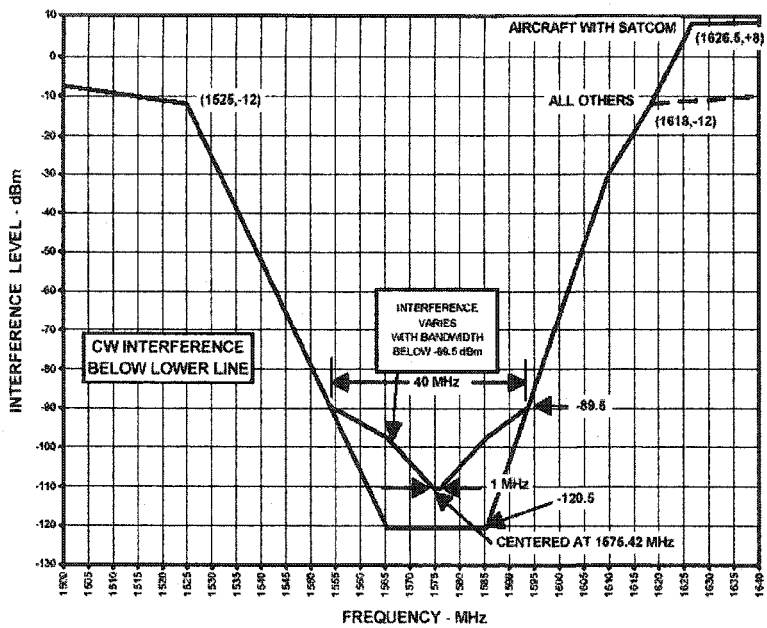

Figure 2.11: RTCA RFI Mask [66].

with acceptable RFI rejection performance. Specifically, WAAS receivers should continue to track satellites in the face of CW RFI having power levels at the input to the receiver below the lower line in Fig. 2.11. Allowable broadband interference levels depend on the bandwidth of the interference, and are shown with the funnel shaped trace in Fig. 2.11. For example, receivers must function in the presence of a 2 MHz wide noise source having at most -107.5 dBm total noise power. The receiver whose performance is plotted in Fig. 2.10 meets this requirement, as it loses lock on the weakest satellite (-134.5 dBm) with an interferer power greater than -104 dBm. There is only a 3.5 dB margin for this particular receiver though. For RFI sources having bandwidths less than 1 MHz, the requirements are not depicted in Fig. 2.11, but may be found in the literature [66].

2.4.5 MAAST

In order to determine the effect of RFI on GPS and WAAS availability, the Matlab Algorithm Availability Simulation Tool (MAAST) was used [43]. MAAST was developed by researchers in the Stanford GPS WAAS Laboratory as a tool for computing WAAS time availability and protection levels over wide geographical areas. MAAST uses either the WAAS MOPS or the current GPS satellite constellation, and time-steps through a 24 hour period to determine WAAS time availability for the entire United States. MAAST computes horizontal and vertical protection levels (H/VPL) as specified in the WAAS MOPS [65]. If either the HPL or VPL exceeds the HAL or VAL specified for a particular phase of flight, then WAAS is not available at that time. As an example, assume MAAST computes an HPL of 60 meters and a VPL of 30 meters at San Jose International Airport at a particular time. Considering that the HAL and VAL limits for an LPV precision approach with WAAS are 50 meters and 40 meters, respectively, WAAS would be unavailable for that approach because the HAL is exceeded. However, WAAS would meet the relaxed requirements for a non-precision approach (LNAV) or for terminal navigation. MAAST does not account for the receiver antenna radiation pattern, nor does it account for RFI effects. In order to use MAAST for WAAS availability calculations in the presence of RFI, several modifications to the code were required.

RFI Effects

Incorporating RFI effects into MAAST was relatively straightforward. As MAAST steps through time, it computes the azimuth and elevation angles of all GPS satellites for users located on a rectangular latitude/longitude grid. MAAST checks to see whether each of the satellites is above a user specified mask angle. The next step is to compute the (C/A-code) pseudorange error for each visible satellite. The pseudorange error for a given satellite is due to troposphere and ionosphere effects, satellite clock and ephemeris errors, WAAS message latency, and GPS receiver noise and multipath

considerations. The total pseudorange error for the ith satellite is computed from

$$\sigma_i^2 = \sigma_{i,flt}^2 + \sigma_{i,UIRE}^2 + \sigma_{i,air}^2 + \sigma_{i,tropo}^2, \tag{2.13}$$

where

$$\sigma_{i,air}^2 = \sigma_{i,mp}^2 + \sigma_{i,noise}^2. \tag{2.14}$$

The receiver noise ($\sigma_{i,noise}$) is the 1-σ jitter on the DLL output in meters for the ith satellite, as given by Eq. (2.3). The standard MAAST algorithm used to compute $\sigma_{i,noise}$ was modified to incorporate RFI effects. Namely, Eq. (2.11) was used in conjunction with Eq. (2.3) to compute the pseudorange error on a given satellite. However, it is not sufficient to only compute the DLL jitter and use it in Eq. (2.14). This does not account for the phase jitter on the PLL error signal, which is the limiting factor for maintaining lock on the satellites. Therefore, the MAAST code was modified again to compute the 1-σ PLL phase jitter for each satellite, and remove that satellite from the H/VPL calculation if it exceeds the 15° threshold. Only those satellites which are visible *and* are tracked by the PLL are used in MAAST from this point on. Next, the H/VPL is computed for each user location, at each specified time. Finally, MAAST compares the computed H/VPL to the user specified H/VAL to determine whether WAAS is available at each specified time. After performing these calculations at each user grid location over the entire specified time interval, MAAST can compute the WAAS time availability over the entire United States.

Antenna Radiation Pattern

The next step was to incorporate antenna effects into MAAST. Since MAAST already computes azimuth and elevation angles for all of the visible satellites at each time step, a large part of the work is completed already. It is reasonable to assume that the airborne receive antenna radiation pattern is symmetrical in azimuth for elevation angles greater than 0°. With this assumption, the GPS signal power at the receiver for each satellite (S_i) can be computed by adding the elevation gain of the receive antenna to the minimum specified signal power, -130 dBm [58]. Mathematically, this

is expressed as

$$S_i = -130 + 10 \log F(\theta_i) \text{ dBm}, \tag{2.15}$$

where $F(\theta_i)$ is the power pattern of the receive antenna, evaluated at the ith satellites's elevation angle. $F(\theta)$ was obtained from a computer code called NEWAIR3 [10]. NEWAIR3 is a FORTRAN code which makes use of the uniform theory of diffraction (UTD) [45] to simulate the radiation patterns of antennas mounted on aircraft and missiles. A microstrip patch antenna mounted on the top of a Cessna Caravan was simulated with NEWAIR3. Polynomial coefficients were then fit to the resulting radiation pattern, and this polynomial was evaluated repeatedly by MAAST at various elevation angles to compute the antenna gains for each satellite. Next, Eq. (2.15) is evaluated for each satellite to estimate the received signal power.

Eq. (2.12) requires the RFI power level at the input to the receiver. This power level depends on the range to the jammer, the jammer transmit power and antenna gain, and the angular location of the jammer relative to the aircraft. The airborne GPS antenna gain in the direction of the jammer is very important in this calculation. To compute the interferer power at the receiver input (I), the Friis transmission formula was used. This fundamental equation can yield RFI levels for various jammer transmit power levels and antenna gains at any distance from the aircraft. These calculations assume a bandlimited AWGN noise source with bandwidth equal to the GPS receiver IF filter, 2 MHz. The expression for the interference power level at the airborne GPS receiver input is

$$I = 10 \log \left(\frac{P_T G_T G_R \lambda^2}{(4\pi R)^2} \right) + 30 \text{ dBm}. \tag{2.16}$$

In Eq. (2.16), P_T is the jammer transmit power in watts, G_T and G_R are the gains of the transmit and receive antennas, respectively, and R is the distance between the aircraft and the jammer. I from Eq. (2.16) is used in conjunction with Eqs. (2.11) and (2.12) to determine the resulting S/N_0 for nearly any conceivable jammer capability and configuration. NEWAIR3 simulations and the flight test results from Chapter 6 suggest a gain of -7.6 dBic at -3° elevation for a standard patch antenna, or for the DPRA in wide-angle mode. This simulates a jammer located on the flight

path of an aircraft on final approach, and represents the actual conditions of the flight test discussed in Chapter 6. In anti-jam mode, the gain of the DPRA at -3° elevation is -23 dBic. These two assumptions were used in all MAAST simulations presented in Chapter 6.

Chapter 3

2.5-Dimensional FDTD Technique

This chapter deals with a computational electromagnetics method known as the finite difference time domain technique (FDTD). In solving electromagnetics problems, one is usually interested in the behavior of some structure in the presence of a source. For the purposes of this thesis, the interest is determining radiation patterns of GPS anti-jam antennas. This problem can be solved many different ways, in both the time and frequency domain. Some of the alternative techniques are briefly mentioned in this chapter, and reasoning is provided for choosing the FDTD method over the other methods. Although a three-dimensional solution is usually desired, it will be shown that for rotationally symmetric problems, a more efficient 2.5-dimensional formulation can be applied. The 2.5-dimensional FDTD formulation is rigorously derived in this chapter, and special consideration is given to modelling microstrip patch antennas. Finally, a canonical problem is solved with the 2.5-D FDTD code for validation purposes.

3.1 Computational Electromagnetics Basics

3.1.1 Antenna vs. Scattering Problems

Electromagnetics problems fall into two general categories – *antenna* problems and *scattering* problems. For an antenna problem, the sources are located close

to the structure, while for scattering problems, the source is located far from the structure. This thesis of course deals exclusively with antenna problems. However, it is interesting to note that methods for solving antenna problems are often directly applicable to scattering problems. By simply moving the source far from the structure being analyzed, the antenna problem becomes a scattering problem. A good example of this is the wire antenna modelling software known as the numerical electromagnetic code (NEC) [36]. This code very accurately predicts radiation patterns and input impedance for wire antennas. The source is usually a magnetic frill generator placed at the feedpoint of the antenna. However, if the source is taken to be a plane wave (a well-known, closed form function) arriving from incident angle θ_i, then the radar cross section (RCS) of the antenna at any scattering angle θ_s can be determined by computing the "radiation pattern" of the antenna due to the plane wave source.

In electromagnetics problems, the source is nearly always a well-known function, and may be represented by a closed form expression. Some popular source functions are the point source, line source, and plane wave. The source gives rise to an *incident field* which propagates in the medium of interest. If the medium is unbounded free space, which is isotropic and homogeneous, then the incident wave propagates forever without interruption or interaction with other objects. If the propagation medium is inhomogeneous, having some structure or discontinuity, then the incident field will interact with this discontinuity, resulting in a *scattered field.* The *total field* is equal to the sum of the incident and scattered fields. The scattered and total fields are unknown, and do not have closed form solutions. The job of the electromagnetics solver is to obtain approximate solutions for these unknown fields.

3.1.2 Time Domain vs. Frequency Domain

Electromagnetics solvers can be further categorized as employing *time domain* or *frequency domain* techniques. Both techniques have advantages and disadvantages, and one is usually preferred over the other for a certain class of problems. This chapter focuses exclusively on a time domain method, but traditionally, electromagnetic problems have been solved mainly in the frequency domain. In frequency domain

problems, one generally sets up and solves an integral equation relating the phasor electric and/or magnetic currents induced on the surface of and antenna or scatterer. These integral equations are usually solved as a matrix equation, which results from approximating the continuous integrals as finite summations. While the matrices can be quite large for problems exceeding several wavelengths in size, the method is quite efficient, especially for one-dimensional boundary integral problems. The method of moments (MoM) [36] is the most popular frequency domain technique for solving antenna and scatterer problems, and the most popular MoM software package for modelling wire antennas is NEC. One disadvantage of frequency domain techniques is that they require a sinusoidal source (at a single frequency), and do not allow for pulsed excitations or transient phenomena. Also, frequency domain techniques usually involve solving only for the current distribution on some metallic structure. While this current distribution is important for computing the input impedance of antennas and angular radiation and/or scattering patterns, it does not provide significant physical insight to the problem at hand. On the other hand, time domain techniques such as FDTD solve Maxwell's equations in real-time at any location in three-dimensional space. As suggested by its name, the FDTD method involves discretizing Maxwell's equations in space and time, so that the equations are solved in discrete time steps at discrete locations in space. The main strength of the FDTD technique is that any time varying source function can be modelled – it need not be sinusoidal. So time domain techniques can deal with pulsed sources, broadband sources having arbitrary spectral shape, step functions, or even approximations to the delta Dirac function. As a result, the frequency response of an antenna over a very wide bandwidth may be computed from a single run of an FDTD code, whereas a frequency domain code would need to be run at each frequency of interest. Another strength of the FDTD method is that any type of material can be handled rather easily. For instance, lossy dielectrics are easily modelled, as are semiconductors, or even exotic materials which have both electric and magnetic conductivity. Another plus is that the structure under evaluation can have any shape. Perhaps most importantly, time domain techniques provide a great deal of physical insight into the electromagnetic problem because the electromagnetic fields are solved directly at points on a

spatial grid. Capabilities of time domain techniques are summarized as follows [72]:

- Broadband response from a single excitation,
- Arbitrary three-dimensional (3-D) structure geometries,
- Conductivity, permittivity, and permeability variations handled easily,
- Lossy materials can be modelled,
- Various responses can be obtained,

  Scattered fields,

  Antenna patterns,

  Radar cross section (RCS),

  Surface fields,

  Current, power, and charge densities,

  Penetration,

  Mutual coupling.

3.2 FDTD History

The FDTD technique was first put forth by Yee in 1966 as a means of discretizing the differential form of Maxwell's equations [83]. Yee used an electric field (E) grid which was offset by one-half unit, spatially and temporally, from the magnetic field (H) grid. This fundamental grid unit is still known today as the *Yee cell.* He proposed the leapfrog scheme which is still in use today, whereby the electric and magnetic fields are updated incrementally with each time step. Unfortunately, Yee's work did not attract much attention at first. Although Yee's formulation of the problem is widely used today in its original form, it was only in the 1980's that researchers became interested in the FDTD technique [68], as computing power had begun to gain momentum. This is because one downside of the FDTD technique is the high computational power needed to solve problems in the time domain. In order to achieve good

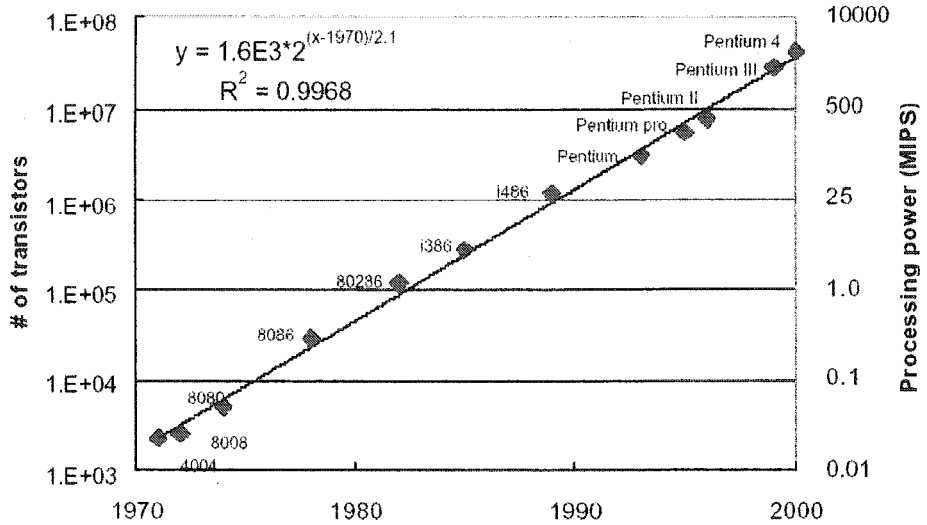

Figure 3.1: Maximum Desktop Computer Processor Speed and Number of Transistors per Processor [62].

frequency resolution, very small time steps are required, requiring a larger number of time steps until steady state conditions are reached, at which point the simulation is finished. To achieve high accuracy, a fine spatial resolution is required for modelling the structure. This means that a large computer memory is necessary to store the material properties (conductivity, permittivity, and permeability) of the structure. Fortunately, computational power and speed have increased exponentially over the years in accordance with Moore's Law, which states that the number of transistors per microprocessor (closely related to performance) will double every 18 months. Fig. 3.1 plots Moore's Law over a 30 year period [62]. Fig. 3.2 shows the number of FDTD publications in the IEEE journals in recent years [68]. The exponential increase in the publication rate after 1985 is evident, and compares with Moore's Law in Fig. 3.1. Of course, the debate continues as to whether Moore's Law will continue indefinitely. Regardless, the tremendous improvement in computer performance during recent years has led to more and more research into the FDTD technique, yielding more efficient codes which are applicable to a wider range of electromagnetics problems.

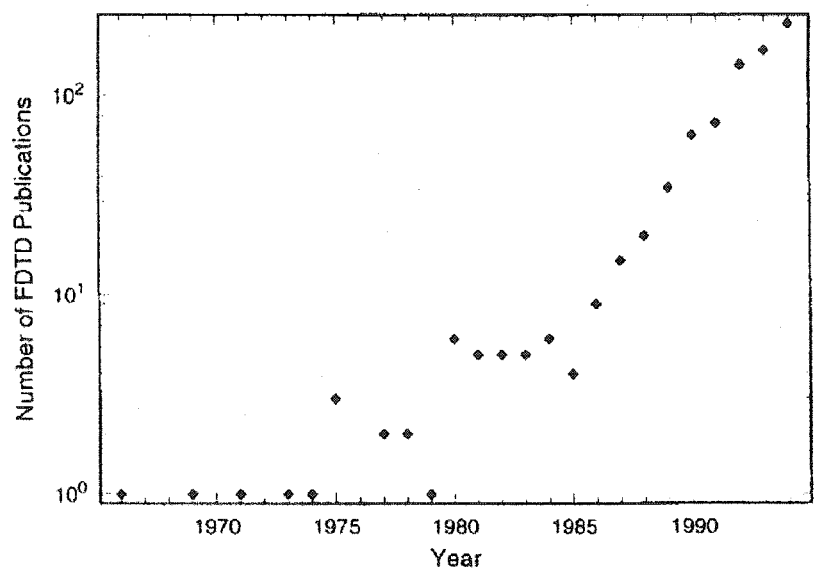

Figure 3.2: Number of FDTD Related Publications per Year [68].

3.3 Basic FDTD Derivation

3.3.1 Maxwell's Equations

As a starting point, we write Maxwell's curl equations in differential form as [2]

$$\nabla \times \vec{E} = -\mu \frac{\partial \vec{H}}{\partial t} - \vec{M}, \tag{3.1}$$

$$\nabla \times \vec{H} = \epsilon \frac{\partial \vec{E}}{\partial t} + \vec{J}. \tag{3.2}$$

Eqs. (3.1) and (3.2) apply in a homogeneous, isotropic unbounded medium having electric permittivity ϵ and magnetic permeability μ. In free space, we have $\epsilon = \epsilon_0$ and $\mu = \mu_0$. $\vec{E}$ and $\vec{H}$ are the field quantities at some observation point due to magnetic and electric current sources $\vec{M}$ and $\vec{J}$. We will be working exclusively in cylindrical coordinates throughout this chapter. In this case, there are three field components for both $\vec{E}$ and $\vec{H}$. Each field component is a three-dimensional function of ρ, z, and ϕ, in general. The cylindrical coordinate system is shown in Fig. 3.3 for reference.

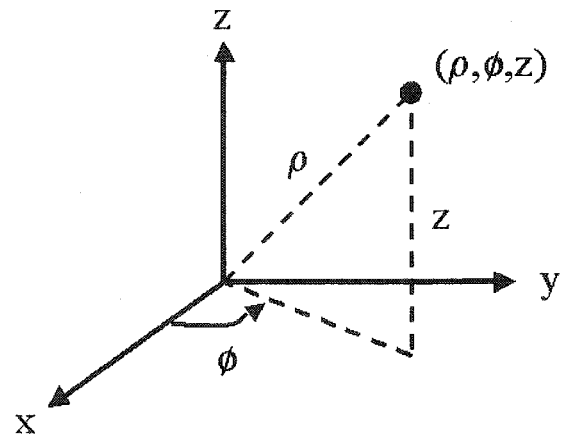

Figure 3.3: Cylindrical Coordinate System.

In cylindrical coordinates, the electric and magnetic current sources in Eqs. (3.1) and (3.2) are

$$\vec{M} = M_\rho \hat{\rho} + M_\phi \hat{\phi} + M_z \hat{z}, \tag{3.3}$$

$$\vec{J} = J_\rho \hat{\rho} + J_\phi \hat{\phi} + J_z \hat{z}. \tag{3.4}$$

In addition, we have in cylindrical coordinates that

$$\nabla \times \vec{A} = \hat{\rho}\left(\frac{1}{\rho}\frac{\partial A_z}{\partial \phi} - \frac{\partial A_\phi}{\partial z}\right) + \hat{\phi}\left(\frac{\partial A_\rho}{\partial z} - \frac{\partial A_\rho}{\partial \rho}\right) + \hat{z}\left(\frac{1}{\rho}\frac{\partial(\rho A_\phi)}{\partial \rho} - \frac{1}{\rho}\frac{\partial A_\rho}{\partial \phi}\right), \tag{3.5}$$

where $\vec{A}$ is an arbitrary vector field. Using Eq. (3.5) with Eqs. (3.4) and (3.3) to expand Eqs. (3.1) and (3.2), we obtain

$$\frac{1}{\rho}\frac{\partial E_z}{\partial \phi} - \frac{\partial E_\phi}{\partial z} = -\mu\frac{\partial H_\rho}{\partial t} - M_\rho, \tag{3.6}$$

$$\frac{\partial E_\rho}{\partial z} - \frac{\partial E_z}{\partial \rho} = -\mu\frac{\partial H_\phi}{\partial t} - M_\phi, \tag{3.7}$$

$$\frac{1}{\rho}\frac{\partial(\rho E_\phi)}{\partial \rho} - \frac{1}{\rho}\frac{\partial E_\rho}{\partial \phi} = -\mu\frac{\partial H_z}{\partial t} - M_z, \tag{3.8}$$

$$\frac{1}{\rho}\frac{\partial H_z}{\partial \phi} - \frac{\partial H_\phi}{\partial z} = \epsilon\frac{\partial E_\rho}{\partial t} + \sigma E_\rho + J_\rho, \tag{3.9}$$

$$\frac{\partial H_\rho}{\partial z} - \frac{\partial H_z}{\partial \rho} = \epsilon\frac{\partial E_\phi}{\partial t} + \sigma E_\phi + J_\phi, \tag{3.10}$$

$$\frac{1}{\rho}\frac{\partial(\rho H_\phi)}{\partial \rho} - \frac{1}{\rho}\frac{\partial H_\rho}{\partial \phi} = \epsilon\frac{\partial E_z}{\partial t} + \sigma E_z + J_z. \tag{3.11}$$

Eqs. (3.6) – (3.8) are due to Maxwell's E-field curl equation Eq. (3.1), while Eqs. (3.9) – (3.11) are due to the H-field curl equation Eq. (3.2). Now, consider that the materials comprising an inhomogeneous rotationally symmetric structure (which satisfies $\partial(\cdot)/\partial\phi = 0$) may be completely characterized in two dimensions by the parameters $\sigma(\rho, z)$, $\epsilon(\rho, z)$, and $\mu(\rho, z)$. In addition, let us propose that the electromagnetic fields $\vec{E}$ and $\vec{H}$ are composed of an infinite series of modes in $\cos m\phi$ and $\sin m\phi$, written succinctly as

$$\vec{E}_u = \hat{u}\, E_u(\rho, \phi, z) = \hat{u} \sum_{m=0}^{\infty} a_m^c E_u^c(\rho, z, m)\cos m\phi + a_m^s E_u^s(\rho, z, m)\sin m\phi, \tag{3.12}$$

$$\vec{H}_u = \hat{u}\, H_u(\rho, \phi, z) = \hat{u} \sum_{m=0}^{\infty} b_m^c H_u^c(\rho, z, m)\cos m\phi + b_m^s H_u^s(\rho, z, m)\sin m\phi, \tag{3.13}$$

where u can be ρ, ϕ, or z, as applicable, and a_m and b_m are complex modal coefficients. If we choose the source to have only sinusoidal variation in azimuth as in,

$$M_\phi(\rho, \phi, z) = M_\phi^c(\rho, z)\cos\phi, \tag{3.14}$$

then Eqs. (3.12) and (3.13) become

$$\vec{E}_\rho(\rho,\phi,z) = \hat{\rho}\, E^c_\rho(\rho,z)\cos\phi, \tag{3.15}$$

$$\vec{E}_\phi(\rho,\phi,z) = \hat{\phi}\, E^s_\phi(\rho,z)\sin\phi, \tag{3.16}$$

$$\vec{E}_z(\rho,\phi,z) = \hat{z}\, E^c_z(\rho,z)\cos\phi, \tag{3.17}$$

$$\vec{H}_\rho(\rho,\phi,z) = \hat{\rho}\, H^s_\rho(\rho,z)\sin\phi, \tag{3.18}$$

$$\vec{H}_\phi(\rho,\phi,z) = \hat{\phi}\, H^c_\phi(\rho,z)\cos\phi, \tag{3.19}$$

$$\vec{H}_z(\rho,\phi,z) = \hat{z}\, H^s_z(\rho,z)\sin\phi. \tag{3.20}$$

Note that the electric and magnetic fields in Eqs. (3.15) – (3.20) are functions of ρ and z only, with a known variation in azimuth. Substituting Eqs. (3.15) – (3.20) into Eqs. (3.6) – (3.11), we write the two-dimensional field equations as

$$\frac{1}{\rho}E^c_z + \frac{\partial E^s_\phi}{\partial z} = \mu\frac{\partial H^s_\rho}{\partial t} - M^s_\rho, \tag{3.21}$$

$$\frac{\partial E^c_\rho}{\partial z} - \frac{\partial E^c_z}{\partial \rho} = -\mu\frac{\partial H^c_\phi}{\partial t} - M^c_\phi, \tag{3.22}$$

$$\frac{1}{\rho}\frac{\partial(\rho E^s_\phi)}{\partial \rho} + \frac{1}{\rho}E^c_\rho = -\mu\frac{\partial H^s_z}{\partial t} - M^s_z, \tag{3.23}$$

$$\frac{1}{\rho}H^s_z - \frac{\partial H^c_\phi}{\partial z} = \epsilon\frac{\partial E^c_\rho}{\partial t} + \sigma E^c_\rho + J^c_\rho, \tag{3.24}$$

$$\frac{\partial H^s_\rho}{\partial z} - \frac{\partial H^s_z}{\partial \rho} = \epsilon\frac{\partial E^s_\phi}{\partial t} + \sigma E^s_\phi + J^s_\phi, \tag{3.25}$$

$$\frac{1}{\rho}\frac{\partial(\rho H^c_\phi)}{\partial \rho} - \frac{1}{\rho}H^s_\rho = \epsilon\frac{\partial E^c_z}{\partial t} + \sigma E^c_z + J^c_z. \tag{3.26}$$

Eqs. (3.21) – (3.26) are ready for discretization, which essentially replaces $\partial/\partial t$ with $1/\Delta t$, and $\partial/\partial(\rho,\phi,z)$ with $1/\Delta(\rho,\phi,z)$. The equations are then solved at successive steps until steady state conditions are reached, at which point the simulation is complete. Once the two-dimensional field quantities (e.g., $E^c_\rho(\rho,z)$) are determined in the steady state, the azimuthal variations in Eqs. (3.15) – (3.20) are applied to obtain the full three-dimensional field quantities (e.g., $E^c_\rho(\rho,z)\cos\phi$).

3.4 Absorbing Boundary Layer

If Eqs. (3.21) – (3.26) were discretized and solved in a two dimensional finite workspace, the resulting solution would be incorrect. This is because for a finite workspace, the computer code cannot solve for the fields beyond the edges of the grid. This means that the fields are assumed to be zero outside of the workspace, and one is effectively modelling the structure as if it were enclosed in a perfectly conducting box! In order to prevent this from happening, one must simulate a free space boundary condition at the edge of the grid. This is commonly done by placing an absorbing layer around the perimeter of the workspace, typically 10 cells thick. The purpose of this layer is to absorb all energy incident on the layer, and yield no reflections back into the workspace. Unfortunately, it is very difficult to obtain perfect absorption of the incident waves, especially for oblique reflections. The simplest way to approximate a perfectly matched layer (PML) is with the Mur absorbing boundary conditions (ABC) [52]. Here, reflections from the walls are cancelled numerically. The Mur ABC can be applied to multi-dimensional FDTD problems, but accuracy is degraded for three-dimensional problems in cylindrical coordinates where reflections are primarily oblique. Berenger devised a highly effective PML for use in three-dimensional problems in Cartesian coordinates [8] [9]. This layer consists of an exponentially decaying conductivity profile at the edge of the lattice. The layer has both electric and magnetic conductivity, σ and σ^*, respectively. The ratio of electric to magnetic conductivity can be optimized to minimize reflections from all incident angles. While very useful for three-dimensional Cartesian FDTD problems, the Berenger PML is not appropriate for use in cylindrical coordinates.

3.4.1 Split-Field PML

In cylindrical coordinates, we make use of a stretched coordinate perfectly matched layer (PML) [75] [76] [77]. This is a highly accurate technique for use in three-dimensional problems posed in cylindrical coordinates. The PML formulation in this section follows that of the literature very closely. The first step in deriving the PML

is to split each field component into two parts.

$$E_\rho^c = E_\rho^{c(\phi)} + E_\rho^{c(z)}, \tag{3.27}$$

$$E_\phi^s = E_\phi^{s(\rho)} + E_\phi^{s(z)}, \tag{3.28}$$

$$E_z^c = E_z^{c(\rho)} + E_z^{c(\phi)}, \tag{3.29}$$

$$H_\rho^s = H_\rho^{s(\phi)} + H_\rho^{s(z)}, \tag{3.30}$$

$$H_\phi^c = H_\phi^{c(\rho)} + H_\phi^{c(z)}, \tag{3.31}$$

$$H_z^s = H_z^{s(\rho)} + H_z^{s(\phi)}. \tag{3.32}$$

Following the previous works, the cylindrical spatial coordinates (ρ, ϕ, z) must be transformed to the new variables $(\tilde{\rho}, \tilde{\phi}, \tilde{z})$ in the complex variable domain according to

$$\tilde{\rho} = \int_0^\rho a_\rho + \frac{\omega_\rho}{j\omega}\, d\rho' \equiv A_\rho + \frac{\Omega_\rho}{j\omega}, \tag{3.33}$$

$$\tilde{z} = \int_0^z a_z + \frac{\omega_z}{j\omega}\, dz'. \tag{3.34}$$

The stretching variables obey

$$\frac{\partial(\cdot)}{\partial\tilde{\rho}} = \frac{1}{a_\rho + \frac{\omega_\rho}{j\omega}} \frac{\partial(\cdot)}{\partial\rho}, \tag{3.35}$$

$$\frac{\partial(\cdot)}{\partial\tilde{\phi}} = \frac{\rho}{\tilde{\rho}} \frac{\partial(\cdot)}{\partial\phi}, \tag{3.36}$$

$$\frac{\partial(\cdot)}{\partial\tilde{z}} = \frac{1}{a_z + \frac{\omega_z}{j\omega}} \frac{\partial(\cdot)}{\partial z}. \tag{3.37}$$

Applying the transformations in Eqs. (3.33) – (3.34) to Eqs. (3.21) – (3.26) using Eqs. (3.27) – (3.32), we obtain a set of twelve field equations which must be solved recursively in time. The full set of equations is not given here, but listed in Appendix A as Eqs. (A.1) – (A.12) for reference. For illustrative purposes, one of the equations is reproduced here in Eq. (3.38), and operations on it alone will continue throughout this section. It is assumed that similar operations are performed on the

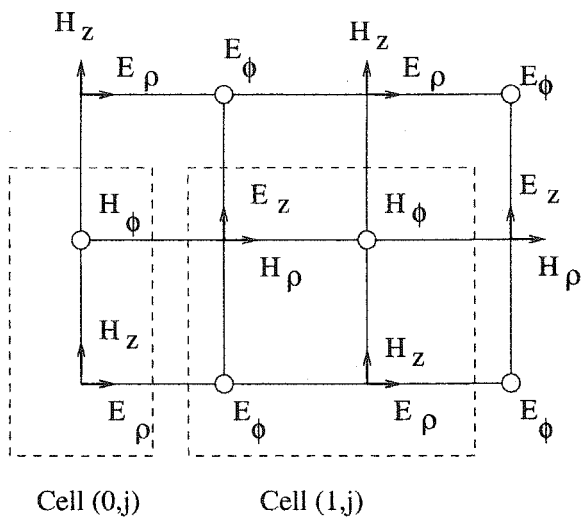

Figure 3.4: FDTD Lattice in Cylindrical Coordinates.

full set of Eqs. (A.1) – (A.12).

$$A_\rho \mu \frac{\partial H_\rho^{s(\phi)}}{\partial t} + \Omega_\rho \mu H_\rho^{s(\phi)} = E_z^c - \rho M_\rho^{s(\phi)} \tag{3.38}$$

3.5 Discretization

The next step is to discretize, in both space and time, the twelve Maxwell's equations as given in Eqs. (A.1) – (A.12). These equations are discretized in the normal fashion [83], with ϵ, μ, and σ defined for each two-dimensional cell of size $(\Delta\rho \times \Delta z)$, and with the electric and magnetic field components staggered in space by a half cell width, as shown in Fig. 3.4. This gridding scheme is identical to that in [16]. The quantities a_ρ, a_z, ω_ρ, ω_z, Ω_ρ, and A_ρ are also staggered, consistent with the electric and magnetic field definitions. Each cell is assigned coordinates (i, j) in the computer code where i corresponds to a ρ cell index, and j corresponds to a z cell index. The full set of twelve discretized equations is not reproduced here, but are listed in Appendix A as Eqs. (A.14) – (A.24). For illustration purposes, the discretized equation

corresponding to Eq. (3.38) is shown below, assuming $M_\rho = 0$.

$$H^{s(\phi)(n+1/2)}_{\rho(i+1/2,j+1/2)} = \frac{2A_\rho - \Omega_\rho \Delta t}{2A_\rho + \Omega_\rho \Delta t} H^{s(\phi)(n-1/2)}_{\rho(i+1/2,j+1/2)} + \frac{2\Delta t}{(2A_\rho + \Omega_\rho \Delta t)\mu} E^{c(n)}_{z(i,j)} \tag{3.39}$$

In Eq. (3.39), notice we solve for $H_\rho^{s(\phi)}$ at $t = (n + 1/2)\Delta t$. Also, prior to solving for $H_\rho^{s(\phi)(n+1/2)}$, we need to first solve for $H_\rho^{s(\phi)(n-1/2)}$ and $E_z^{c(n)}$. However, these field components are defined at times earlier than $(n + 1/2)\Delta t$. So both of these fields had already been calculated during previous updates. The process for recursively updating the field equations in Eqs. (A.13) – (A.24) is

1. Update the source excitation function at time $n + 1/2$,
2. Update the H-field components at time $n + 1/2$,
3. Update the E-field components at time $n + 1$,
4. Integrate the electric fields to time $n + 1$ and store,
5. Go to Step 1.

3.5.1 PML Practical Considerations

It was found by trial and error that a ten cell thick fourth order tapered profile for ω_ρ and ω_z yielded good solution accuracy. Throughout the working grid, a_ρ and a_z were set to 1.0. Since a_ρ, a_z and ω_ρ, ω_z in Eqs. (A.1) – (A.12) behave very much like ϵ_r and σ/ϵ, respectively, the maximum value for $\omega_{\rho,z}$ was chosen in accordance with

$$\omega_{\rho,z(\max)} = \frac{\sigma_{\rho,z(\max)}}{\epsilon} = \frac{n+1}{150\pi\Delta(\rho,z)a_{max}\epsilon_0} \cong \frac{1.2 \times 10^9}{\Delta(\rho,z)}, \tag{3.40}$$

which is based on the classic optimum choice for σ_{max} in Cartesian coordinates [32]. In Eq. (3.40), n is the polynomial order of the profile ($n = 4$) and $\Delta(\rho, z)$ is $\Delta\rho$ or Δz, as applicable. The resulting radial profile for ω_ρ is shown in Fig. 3.5.

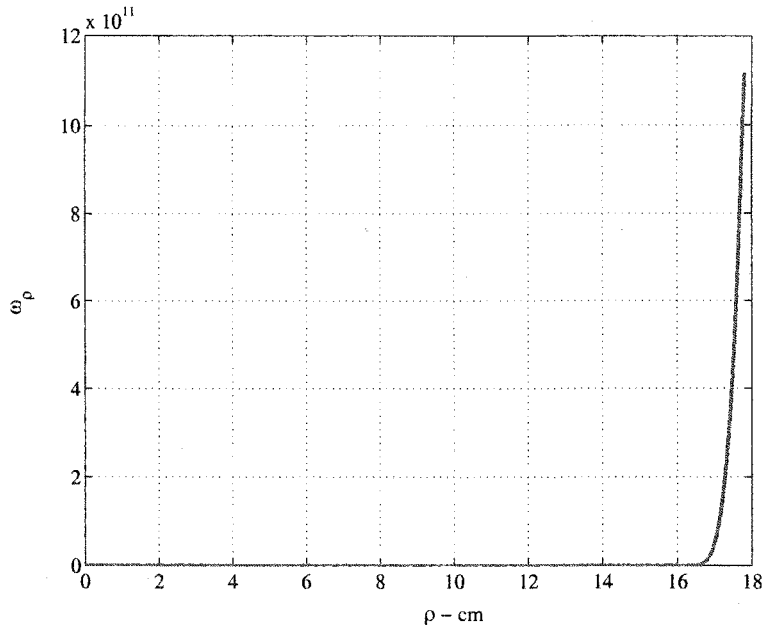

Figure 3.5: ω_ρ Radial Profile.

3.6 Source Considerations

3.6.1 Square Patch Approximation

It is well known that a rectangular microstrip patch antenna operating in the fundamental mode may be approximately modelled by two-dimensional linear magnetic current sources located at the effective radiating edges of the patch element (Chapter 5). In accordance with the cavity model ($\vec{M} = 2E_z\hat{z} \times \hat{n}$), the strength of the magnetic current is determined by E_z at the effective radiating edges of the patch element, shown in Fig. 3.6 [23]. This concept also applies to circular patch antennas. However, for the circular patch, the magnetic current would of course obey a $\cos\phi$ variation. A top view of the circular patch model is shown in Fig. 3.7. The source antenna used on the dielectric cavity antenna (Chapter 4) is a small rectangular patch approximately 2 cm square. In cylindrical coordinates, the linear magnetic currents associated with the rectangular patch, shown in Fig. 3.6 are difficult to model exactly. It would be possible to model the square patch by synthesizing a series of azimuthal

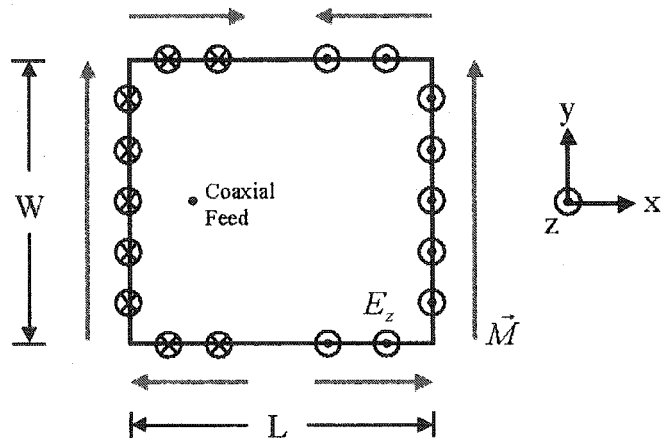

Figure 3.6: Rectangular Microstrip Patch Antenna Model.

modes, using multiple terms in Eqs. (3.12) and (3.13). However, the FDTD code would need to be executed many times, once for each required mode. For the purposes of this analysis, only the first azimuthal harmonic ($m = 1$) will be used to model the square patch antenna. This, means of course, that we are actually modelling a circular patch, as shown in Fig. 3.7. However, the fields radiated by a small square patch antenna are very nearly equal to those radiated by a small circular patch element. This can be shown by considering the closed form expressions for the far-fields radiated by the square and circular patches, given respectively as [3]

$$E_\theta^{\text{rect}} = \frac{jkWV_0}{\pi} \cos\left(\frac{kL}{2}\sin\theta\right)\frac{e^{-jkr}}{r}, \tag{3.41}$$

$$E_\theta^{\text{circ}} = \frac{jka_eV_0}{2} \cos\left[J_0(ka_e\sin\theta) - J_2(ka_e\sin\theta)\right]\frac{e^{-jkr}}{r}. \tag{3.42}$$

V_0 is the voltage at the radiating edges of the patch. We wish to determine the equivalent circular patch antenna diameter such that the far-fields radiated by the square and circular patches are equal. The use of this equivalent diameter circular patch in the FDTD code will accurately simulate the square patch antenna. To determine the equivalent circular patch diameter, we set the far-fields for the square and circular patches (Eqs. (3.41) and (3.42)) in the zenith direction ($\theta = 0$) equal, and

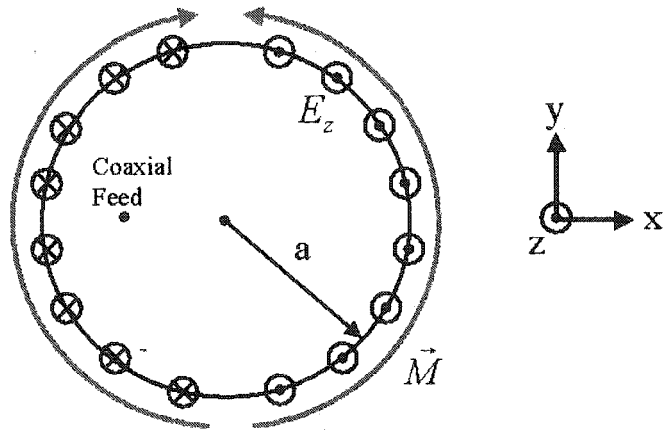

Figure 3.7: Circular Microstrip Patch Antenna Model.

solve for a_e, the equivalent radius of the circular patch. The result of this operation is

$$a_e = \frac{2}{\pi} W. \tag{3.43}$$

To confirm that a circular patch antenna having the radius given in Eq. (3.43) is equivalent to a square patch with side length W, we plot in Fig. 3.8 the far-field radiation pattern in the E-plane for both cases. In Fig. 3.8, we use a 4 cm square patch and a circular patch with equivalent radius 2.54 cm. These patterns are in close agreement, as the maximum error is only 0.24 dB, worst case.

3.6.2 Circular Polarization

To activate the source numerically, we employ a soft source at a single cell location (ρ_0, z_0), which is at the effective radiating wall of the circular patch ($\rho_0 = a_e$). To achieve right-hand circular polarization (RHCP), one would simply include an additional $\sin\phi$ source which is fed 90° out of phase with the $\cos\phi$ source. This compound source is expressed analytically as

$$\begin{aligned} M_\phi(\rho, \phi, z) &= a_1^c M_\phi^c(\rho, \phi, z) + a_1^s M_\phi^s(\rho, \phi, z) \\ &= \delta(\rho_0, z_0)\cos\phi - j\delta(\rho_0, z_0)\sin\phi. \end{aligned} \tag{3.44}$$

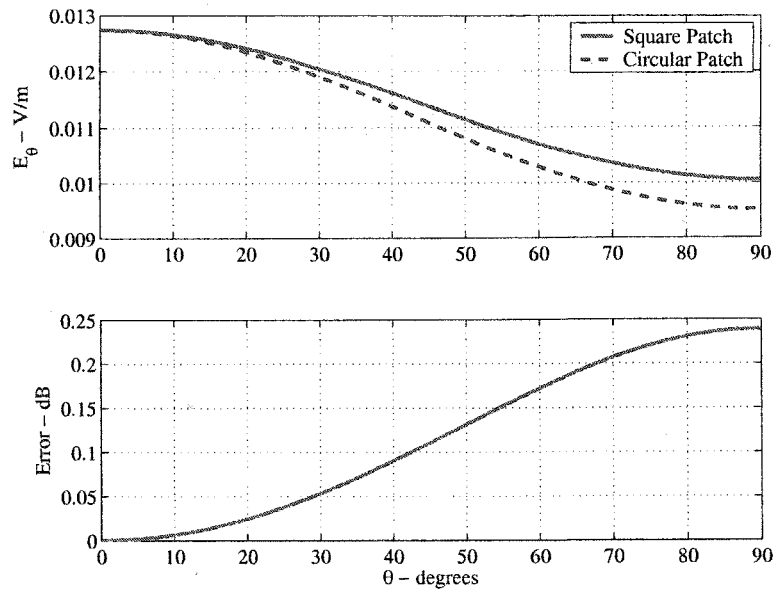

Figure 3.8: Circular vs. Square Patch Antenna Radiation Patterns.

To implement both M_ϕ^c and M_ϕ^s sources, one would need to, in theory, run the FDTD code twice. The first run would model radiation from the M_ϕ^c source, while the second run would model radiation from the M_ϕ^s source. However, a simple 90° rotation of the fields obtained from the M_ϕ^c source will yield (exactly) the fields due to the M_ϕ^s source. Mathematically,

$$\vec{A}_u^s(\rho, \phi, z) = \vec{A}_u^c(\rho, \phi - \pi/2, z), \tag{3.45}$$

where $\vec{A}^c$ is an arbitrary field vector due to a cosinusoidal magnetic current source. Therefore, one simply needs to run the code once with a $\cos\phi$ oriented source, then apply the transformation in Eq. (3.45) to all six field components to obtain the fields which would result from the source M_ϕ^s. The benefit of this operation is that an unnecessary execution of the FDTD code is avoided, halving the total time required for analysis of a circularly polarized patch antenna.

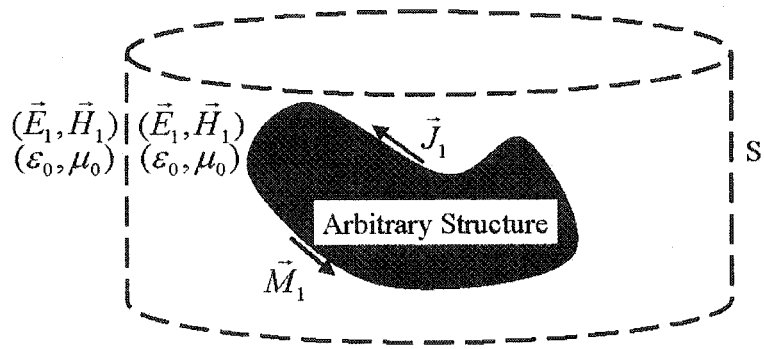

Figure 3.9: FDTD Electromagnetic Near-Field Structure.

3.7 Near-to-Far-Field Transformation

In order to obtain far-field radiation patterns from the FDTD technique, the near fields in the vicinity of the structure being simulated must be propagated out to the far-field region. This is made possible by the Equivalence Principle, which states that if one knows the tangential electric and magnetic fields on a closed surface enclosing the sources, the far-fields may be obtained by allowing those tangential fields to radiate in free space in absence of the original sources [2]. Since the FDTD method yields all six field components in the near field, we simply choose an arbitrary cylindrical surface enclosing the structure and the sources $\vec{M}_1$ and $\vec{J}_1$, as shown in Fig. 3.9. Inside and outside surface S, the fields are $\vec{E}_1$ and $\vec{H}_1$. However, the space inside S is inhomogeneous, and we cannot determine $\vec{E}_1$ and $\vec{H}_1$ easily. We rely on the FDTD code to solve for $\vec{E}_1$ and $\vec{H}_1$ due to $\vec{J}_1$ and $\vec{M}_1$. The equivalent electromagnetic problem is shown in Fig. 3.10, where the sources have been set to zero, the fields inside S are zero, and the fields outside S are due to electric and magnetic surface currents $\vec{J}_s$ and $\vec{M}_s$, respectively, flowing on surface S [2]. These surface currents radiate in free space, and therefore the far-field can be easily computed by standard vector potential integration techniques [2]. The details of this operation are omitted here, as the procedure is available in the literature [74] [72] [2]. However, the basic steps are

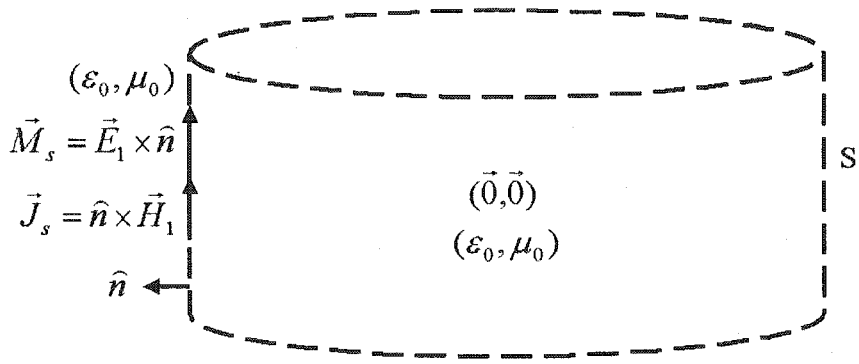

Figure 3.10: FDTD Equivalent Electromagnetic Problem.

to form the equivalent currents on the surface S, and carry out the surface integrals

$$\vec{E}_M(\rho, \phi, z) = -\frac{1}{4\pi}\nabla \times \iint_S \vec{M}_s \frac{e^{-jkR}}{R}\, dS', \tag{3.46}$$

$$\vec{E}_J(\rho, \phi, z) = -\frac{j\eta_0}{4\pi k_0}\nabla \times \nabla \times \iint_S \vec{J}_s \frac{e^{-jkR}}{R}\, dS', \tag{3.47}$$

where $\vec{E}_M$ is the field due to the magnetic current source, $\vec{E}_J$ is the field due to the electric current source, and R is the distance between the source point $\vec{r}'$ and the observation point $\vec{r}$ given as

$$R = |\vec{r} - \vec{r}'| = \sqrt{(x - x')^2 + (y - y')^2 + (z - z')^2}. \tag{3.48}$$

The magnetic field components in the far-field are

$$\vec{H} = \hat{\rho} \times \eta_0 \vec{E}, \tag{3.49}$$

where $\hat{\rho}$ points in the direction of propagation.

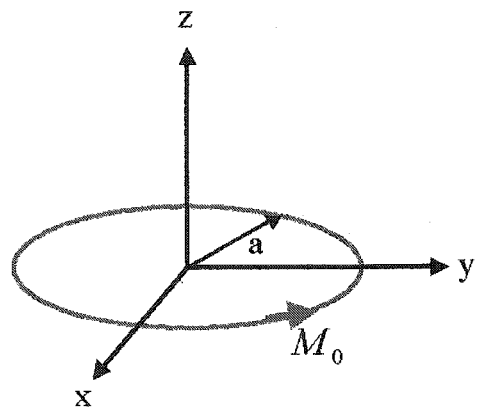

Figure 3.11: Magnetic Loop Antenna.

3.8 Canonical Problem – Small Magnetic Loop Radiator

In this section a simple problem is solved with a closed form expression and also with the 2.5-D FDTD code. Consider a small magnetic loop antenna in free space having radius a, as shown in Fig. 3.11. The loop has constant current M_0. The closed form far-field radiation pattern of this antenna is given in Eq. (3.50) [3].

$$E_\theta = -\frac{akM_0}{2\eta}\frac{e^{-jkr}}{r}J_1(ka\sin\theta) \tag{3.50}$$

This antenna was simulated with the 2.5-D FDTD code as well. The elevation radiation patterns (y-z plane) from the closed form and FDTD solutions are plotted in Fig. 3.12. These patterns agree closely enough that the code is considered to be working properly. If there were an error in the update equation code, the FDTD solution would diverge quickly, and the problem would be quite evident.

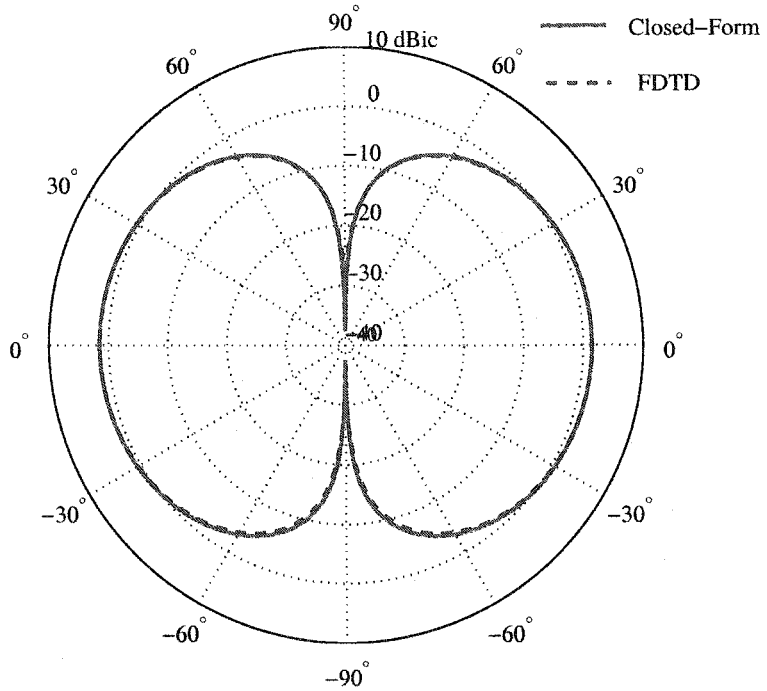

Figure 3.12: Radiation Pattern of Magnetic Loop Antenna.

Chapter 4

The Dielectric Cavity Antenna

This chapter deals with an interesting new antenna design known as the dielectric cavity antenna (DCA). The DCA is an antenna employing an artificially soft surface as a means to reduce the sensitivity to interfering signals arriving from below the horizon of the antenna. This arrangement results in an aviation antenna that is hardened against ground-based RFI. First, the concept of an artificially soft surface is introduced, and the theory behind these surfaces is explored. Next, it is shown how the theoretical two-dimensional surface can be used in a practical antenna design. A design procedure for the DCA is presented which optimizes the dimensions of the dielectric cavity for RFI rejection. Once a design is chosen, the DCA is simulated with the 2.5-D FDTD technique discussed in Chapter 3. Results from these simulations are presented in this chapter. Finally, a prototype DCA was constructed, and experimental results from roof-top testing are discussed. Some of the information in this chapter may found in the literature [4] as well, but a much more detailed discussion is presented here.

4.1 Hard and Soft Surfaces in Electromagnetics

This section introduces the concept of hard and soft surfaces in electromagnetics. In this section, we will consider the interaction between a propagating plane wave and a two dimensional surface. The applicable geometry is shown in Fig. 4.1. Here we have

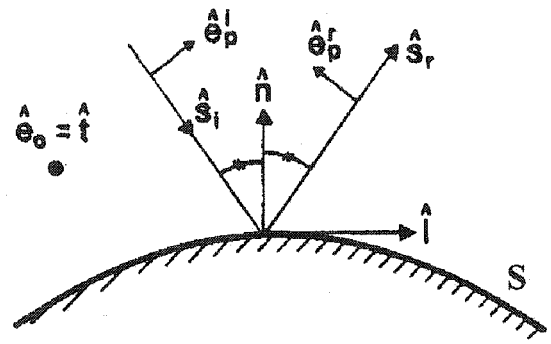

Figure 4.1: Geometry Relating to Hard and Soft Surfaces [44].

an incident plane wave propagating in the $\hat{s}_i$ direction, and a reflected wave travelling in the $\hat{s}_r$ direction. The surface S having arbitrary shape presents an electromagnetic boundary condition to the incident wave, which of course affects the properties of the reflected wave, and hence the total field. On the surface S, a longitudinal unit vector $\hat{l}$ points in the direction of power flow. The unit vector normal to the surface S is denoted by $\hat{n}$, while the unit vector tangential to the surface is $\hat{t}$. The incident and reflected fields have polarization $\hat{e}_p^i$ and $\hat{e}_p^r$, respectively. In the following discussion, we explore in detail the interaction between the surface and the incident electromagnetic field.

4.1.1 Electromagnetic Soft Surface

An electromagnetic soft surface is defined as any surface upon which the transverse (to the direction of propagation) electric and magnetic fields vanish. This condition results in both the normal and the tangential electric fields being zero on the surface. This structure will not support the propagation of TEM plane waves along its surface. If either of the above conditions is met separately, the surface can be referred to a soft surface for a single polarization. For example, a surface upon which the tangential electric field vanishes will not support horizontally polarized surface waves, and is said to be a soft surface for horizontal polarization. Conversely, a surface upon which the tangential magnetic field vanishes does not support vertically polarized surface waves,

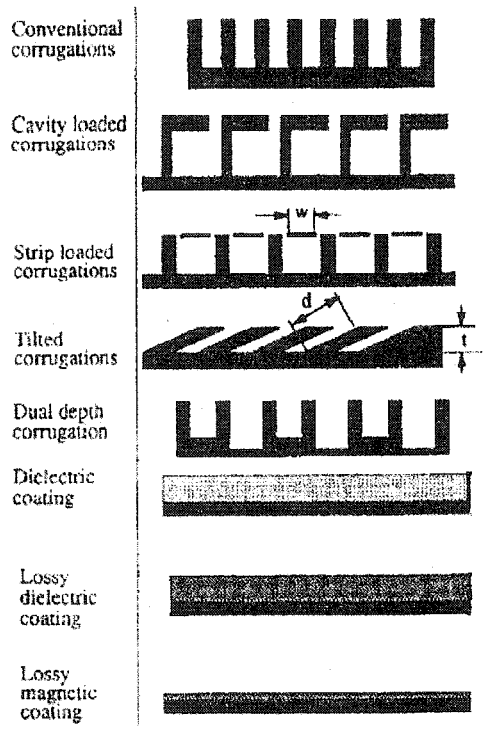

Figure 4.2: Various Implementations of Soft Surfaces [84].

and is called a soft surface for vertical polarization. Expressed another way, a surface is said to be soft for horizontal polarization if $Z_t = E_t/H_l = 0$, or soft for vertical polarization if $Z_l = -E_l/H_t \rightarrow \infty$. Z_t and Z_l are the transverse and longitudinal wave impedances of the surfaces, respectively [44]. As an example, consider a horizontally polarized plane wave travelling along an infinite planar surface. A perfectly electric conducting (PEC) surface will force the tangential electric field E_t to zero, and will prevent propagation of the plane wave along the surface. For a vertically polarized plane wave, the soft surface is achieved by instead making the surface a perfect magnetic conductor (PMC), which forces H_t to zero. The fictitious perfect magnetic conductor can be realized artificially by various structures. Several such structures are shown in Fig. 4.2 [84]. The most common is the corrugated surface, with the corrugations oriented transverse to the direction of propagation and made approximately $\lambda/4$ deep. This structure is very popular for a class of multipath rejecting GPS antennas known as choke ring antennas. Here, the corrugated ground plane is

Surface Type	Polarization	Boundary Condition	Surface Impedance	Reflection Coefficient	Example
Hard	Vertical	$\frac{\partial E_l}{\partial n} = 0$	$Z_l = -\frac{E_l}{H_t} = 0$	$\rho_n = 1$	PEC
Hard	Horizontal	$\frac{\partial E_t}{\partial n} = 0$	$Z_t = \frac{E_t}{H_l} = \infty$	$\rho_t = 1$	PMC
Soft	Vertical	$E_l = 0$	$Z_l = -\frac{E_l}{H_t} = \infty$	$\rho_n = -1$	PMC
Soft	Horizontal	$E_t = 0$	$Z_t = \frac{E_t}{H_l} = 0$	$\rho_t = -1$	PEC

Table 4.1: Properties of Hard and Soft Surfaces.

formed into a cylindrical shape surrounding a central driven element. The choke ring acts to "choke" off surface waves which try to attach to the ground plane surrounding the driven element. Thus, radiation arriving from below the antenna is extinguished before it can reach the central driven element, in receive mode. Corrugated surfaces are also used in feed horns which illuminate parabolic reflector antennas. By lining the interior of a conical horn antenna with transverse corrugations, one obtains symmetrical radiation patterns and low cross polarization. The reason for this is that the soft surface eliminates the electric field normal to the interior wall. The normal electric field appearing at the rim of a conical horn is the chief source of cross polarized fields and undesired side and back lobe radiation [44].

4.1.2 Electromagnetic Hard Surface

The analogue to the soft surface is the electromagnetic hard surface. An electromagnetic hard surface is defined as any surface upon which the longitudinal electric and magnetic fields vanish. This condition results in the tangential and normal electric field components being maximized on the hard surface. As such, a hard surface can support propagation of any polarization. This is opposite to the soft surface, where *no* propagation of *any* polarization is possible. If either of the above conditions is met separately, the surface can be referred to as a hard surface for a single polarization. For example, a surface upon which the longitudinal electric field vanishes is said to be a hard surface for vertical polarization only. Conversely, a surface upon which the longitudinal magnetic field vanishes is called a hard surface for horizontal polarization. In terms of the surface impedances, a surface is said to be hard

for vertical polarization if $Z_l = -E_l/H_t = 0$, or hard for horizontal polarization if $Z_t = E_t/H_l \rightarrow \infty$. An example of a hard surface for vertical polarization is a PEC ground plane. The PEC surface supports propagation of vertically polarized TEM waves. A PMC ground plane is a hard surface for horizontal polarization, as it supports the propagation of horizontally polarized surface waves. Common applications of the hard surface are hard cylindrical waveguides and hard feed horns. Unlike standard waveguides, the TEM mode can propagate in the hard waveguide. This is possible because the fields within the hard waveguide comprise a superposition of the TE_{11} and TM_{11} modes. This *hybrid mode* is commonly referred to as the HE_{11} mode. The significance of having the TEM mode propagate in a waveguide is that the field distribution within the guide can be made constant over the cross section of the guide. This means that hard feed horns, which are simply flared hard waveguides, can be designed with nearly uniform aperture field distributions, resulting in high directivity. Another advantage of the TEM mode is that the polarization is perfectly linear. Thus, hard horns will have very low cross polarization. In addition, the hard waveguide can have any cross sectional shape and still retain these properties. Another interesting application of hard surfaces is the transparent support strut. Normally, metallic struts oriented parallel to the radiated electric field of an antenna severely scatter the radiated field, reducing antenna efficiency. However, struts employing a hard surface will have minimal scattering cross section for any polarization, increasing antenna efficiency.

4.2 Grounded Dielectric Slab

While Fig. 4.2 shows several possible configurations for artificially soft surfaces, the grounded dielectric slab will be the primary focus of this chapter. It can be shown that an infinite grounded dielectric slab of critical thickness

$$d_c = \frac{\lambda_0}{4\sqrt{\epsilon_r - 1}} \tag{4.1}$$

functions as an electromagnetic soft surface [50].

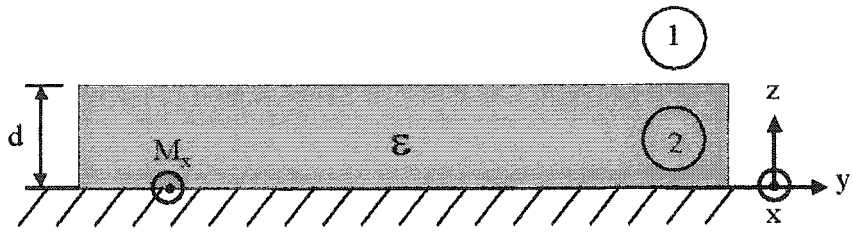

Figure 4.3: Geometry of the Grounded Dielectric Slab.

Consider the two-dimensional grounded dielectric slab shown in Fig. 4.3. The dielectric has permittivity ϵ, and the ground plane is a PEC. Imagine an infinitesimal magnetic current source is placed inside the dielectric, on the surface of the ground plane. Inside the dielectric (region 2), a surface wave is excited and travels outward from the source. Space waves are excited in region 1, which is taken to be unbounded free space. Also in regions 1 and 2, a surface wave propagates along the air-dielectric interface. Solving for the far-field radiation pattern of the magnetic current source embedded in a grounded dielectric slab is very complex procedure. Because of this, and since the procedure is documented in the literature [71], only an outline of the solution steps will be presented here. First, consider for thin dielectrics that only the fundamental mode surface wave will be excited along the air-dielectric interface. This lowest order propagating mode is the TM_0 mode. The first step in the procedure is to solve for the TM_0 propagation constant γ_p, which gives the phase velocity of surface waves bound to the air-dielectric interface. Obtaining γ_p is straightforward, and many electromagnetics texts [2] [60] will explain that γ_p is found by solving the transcendental equation

$$0 = \epsilon_r \gamma_z^{(1)} + \gamma_z^{(2)} \tanh \gamma_z^{(2)} d, \tag{4.2}$$

with

$$\gamma_z^{(1)} = j\sqrt{\gamma_x^2 + \gamma_y^2 + k_0^2}, \tag{4.3}$$

$$\gamma_z^{(2)} = j\sqrt{\gamma_x^2 + \gamma_y^2 + \epsilon_r k_0^2}, \tag{4.4}$$

and

$$\gamma_p^2 = \gamma_x^2 + \gamma_y^2. \tag{4.5}$$

Eq. (4.2) is the *characteristic equation* resulting from enforcing continuity of tangential electric and magnetic fields at the air-dielectric interface. In the next step, one must solve the Helmholtz equation in the spectral domain, and then obtain an asymptotic approximation to the resulting Sommerfeld integral. For a magnetic current element source on a PEC plane covered by a dielectric substrate of thickness d, the transverse magnetic field $H_\phi^{(2)}$ within the dielectric (region 2) in the far-field region of the source is [71]

$$\begin{aligned} H_{\phi,su}^{(2)} &= -j\omega\frac{\epsilon}{4}\sin\phi\frac{R_D}{\gamma_z^{(2)}\cosh(\gamma_z^{(2)}d)}\sqrt{\frac{2\gamma_p}{\pi}} \\ &\times\left[\gamma_z^{(2)}\cosh(\gamma_z^{(2)}(z-d)) - \epsilon_r\gamma_z^{(1)}\sinh(\gamma_z^{(2)}(z-d))\right]M_x\frac{e^{-\gamma_p\rho}}{\sqrt{\rho}}, \end{aligned} \tag{4.6}$$

with

$$R_D = \frac{1}{\gamma_p}\frac{[\gamma_z^{(2)}]^2\gamma_z^{(1)}\cosh^2(\gamma_z^{(2)}d)}{k_0^2\epsilon_r(\epsilon_r-1)\cosh^2(\gamma_z^{(2)}d) - d\,[\gamma_z^{(2)}]^2\gamma_z^{(1)}}. \tag{4.7}$$

In region 1, we have a propagating surface wave bound to the air-dielectric interface expressed as

$$H_{\phi,su}^{(1)} = -j\omega\frac{\epsilon}{4}\sin\phi\frac{R_D}{\cosh\gamma_{zp}^{(2)}d}\sqrt{\frac{j2\gamma_p}{\pi}}M_x e^{-\gamma_{zp}^{(1)}(z-d)}\frac{e^{-j\gamma_p\rho}}{\sqrt{\rho}}. \tag{4.8}$$

We also have a space wave in region 1, given as

$$H_{\phi,sp}^{(1)} = j\omega\frac{\epsilon}{4\pi}\sin\phi\frac{\cos\theta}{D_1\cosh jk_0Td}M_x e^{jk_0d\cos\theta}\frac{e^{-jk_0r}}{r}, \tag{4.9}$$

where

$$D_1 = \epsilon_r \cos\theta + T \tanh jk_0 Td, \tag{4.10}$$

$$T = \sqrt{\epsilon_r - \sin^2\theta}. \tag{4.11}$$

Consider an x directed magnetic current element and waves propagating in the y direction. We are interested in the space wave $H^{(1)}_{\phi,sp}$ in region 1 propagating along the surface of the slab. Considering Eq. (4.9), this field is proportional to

$$H^{(1)}_{\phi,sp} \propto \frac{\cos\theta}{D_1 \cosh jk_0 Td}. \tag{4.12}$$

In the denominator of Eq. (4.12),

$$D_1 = \epsilon_r \cos\theta + T \tanh jk_0 Td \approx T \tanh jk_0 Td\Big|_{\theta\to\frac{\pi}{2}}, \tag{4.13}$$

$$T = \sqrt{\epsilon_r - \sin^2\theta} = \sqrt{\epsilon_r - 1}\Big|_{\theta\to\frac{\pi}{2}}, \tag{4.14}$$

$$x \equiv jk_0 Td = jk_0\sqrt{\epsilon_r - 1}\frac{\lambda_0}{4\sqrt{\epsilon_r - 1}} = j\frac{\pi}{2}\Big|_{\substack{\theta\to\frac{\pi}{2}\\ d=d_c}}. \tag{4.15}$$

Using Eqs. (4.13) – (4.15) in Eq. (4.12), we have

$$H^{(1)}_{\phi,sp} \propto \frac{\cos\theta}{\tanh x \cosh x}\Big|_{\substack{\theta\to\frac{\pi}{2}\\ x\to j\frac{\pi}{2}}} \to 0\Big|_{\substack{\theta\to\frac{\pi}{2}\\ d=d_c}}. \tag{4.16}$$

Eq. (4.16) says that at the critical thickness d_c, a grounded dielectric slab will quench the vertically polarized space wave travelling along the surface of the air-dielectric interface. The surface wave still exists in both regions 1 and 2, but we will see in Section 4.3.1 that these waves do not lead to radiation below the antenna if the antenna is sized properly.

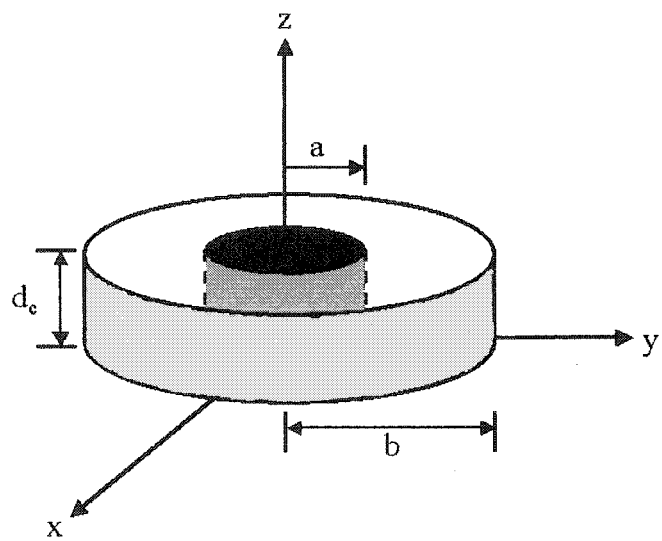

Figure 4.4: Geometry of Grounded Dielectric Disk.

4.3 Grounded Dielectric Disk

The first step toward creating a working antenna using the concepts derived in Section 4.2 is to truncate the grounded dielectric slab, forming the shape of a disk shown in Fig. 4.4. In this form, the dielectric slab takes the shape of an annulus, having critical thickness d_c, inner radius a, and outer radius b. The outer radius of the disk is terminated with a PEC ring. The centrally located symmetric PEC cylinder has radius a. To analyze this structure, we make use of the source free scalar Helmholtz wave equation for E_z, written as

$$(\nabla^2 + k^2)E_z = 0. \tag{4.17}$$

The general solution to Eq. (4.17) in cylindrical coordinates is [2]

$$E_z = [H_m^{(1)}(\gamma_p\rho) + AH_m^{(2)}(\gamma_p\rho)] \times [\cos m\phi + B\sin m\phi] \times [e^{-j\gamma_z^{(2)}z} + Ce^{+j\gamma_z^{(2)}z}]. \tag{4.18}$$

A, B, and C are complex constants which are obtained by enforcing the boundary conditions within the disk. As discussed in Chapter 3, we will be dealing with fields

having azimuthal variation in $\sin\phi$ and $\cos\phi$ only. Eq. (3.17) requires that E_z vary as $\cos\phi$. Thus, we take $m = 1$ in Eq. (4.18). Enforcing boundary conditions on the ground plane and the air-dielectric interface, we can simplify Eq. (4.18) to

$$E_z = [H_1^{(1)}(\gamma_p\rho) + AH_1^{(2)}(\gamma_p\rho)]\sinh(\gamma_z^{(2)}(z-d))\cos\phi, \tag{4.19}$$

where γ_p is the propagation constant for the fundamental TM_0 mode surface wave obtained from solving Eq. (4.2), and $\gamma_z^{(2)}$ is the wavenumber in the z direction within the dielectric, given by Eq. (4.4). The Hankel function of the second kind represents a cylindrical wave propagating outward from the origin, while the Hankel function of the first kind represents a cylindrical wave propagating inward toward the origin. Both of these cylindrical waves are required in our solution in order to satisfy the boundary conditions at the PEC surfaces located at radii a and b. The two cylindrical waves create a standing wave pattern within the dielectric, similar to that in a coaxial resonator. The total field in the grounded dielectric disk will comprise the sum of the incident and reflected radial waves. In the following discussion, we consider only the radial variation of this field structure. At the PEC boundaries located at radii of a and b, we have

$$E_z(\rho = a) \propto H_1^{(1)}(\gamma_p a) + AH_1^{(2)}(\gamma_p a), \tag{4.20}$$

$$E_z(\rho = b) \propto H_1^{(1)}(\gamma_p b) + AH_1^{(2)}(\gamma_p b). \tag{4.21}$$

Since the boundaries at a and b are assumed to be perfectly conducting, there are only two possibilities for A: $A = \pm 1$. Consider the case where $A = 1$. Then Eqs. (4.20) and (4.21) become

$$E_z(\rho = a) \propto 2J_1(\gamma_p a), \tag{4.22}$$

$$E_z(\rho = b) \propto 2J_1(\gamma_p b). \tag{4.23}$$

If $A = -1$,

$$E_z(\rho = a) \propto -j2Y_1(\gamma_p a), \tag{4.24}$$

$$E_z(\rho = b) \propto -j2Y_1(\gamma_p b). \tag{4.25}$$

In the first case, the field structure within the dielectric obeys the Bessel function of the first kind, while in the second case, the field obeys the Bessel function of the second kind. Recall that since $m = 1$, the order of the Bessel functions in both cases is 1. This arrangement is analogous to a coaxial cavity resonator having PEC radial walls which supports an infinite number of azimuthal modes that vary according to the sine or cosine function. The only difference is that the grounded dielectric disk is open to free space on the top surface. The fields expressed in Eqs. (4.22) – (4.25) "fit" within the cavity when a and b are chosen such that Eqs. (4.22) and (4.23) or Eqs. (4.24) and (4.25) are exactly zero, simultaneously. This means that in Eqs. (4.22) and (4.23), we require $\gamma_p a = x_n^J$ and $\gamma_p b = x_{n+1}^J$, where x_n^J is the nth zero of the Bessel function of the first kind $J_1(x)$. Similarly, we could require that $\gamma_p a = x_n^Y$ and $\gamma_p b = x_{n+1}^Y$, where x_n^Y is the nth zero of the Bessel function of the second kind $Y_1(x)$. In summary, the fields within the dielectric disk have two possible structures, expressed as

$$E_z(\rho, \phi, z) \propto J_1(\gamma_p \rho) \sinh(\gamma_z^{(2)}(z - d)) \cos\phi, \tag{4.26}$$

$$E_z(\rho, \phi, z) \propto Y_1(\gamma_p \rho) \sinh(\gamma_z^{(2)}(z - d)) \cos\phi. \tag{4.27}$$

It is interesting that two independent solutions are possible within the disk. In many problems, the $Y_m(\gamma_p \rho)$ solution is eliminated since it diverges at the origin. However, in this case the fields are forced to zero at the origin due to the presence of the PEC inner cylinder, and the solution obeying $Y_1(\gamma_p \rho)$ is permitted. As discussed in the next section, the radii a and b may be chosen by the designer to determine which of the two field structures exists within the cavity.

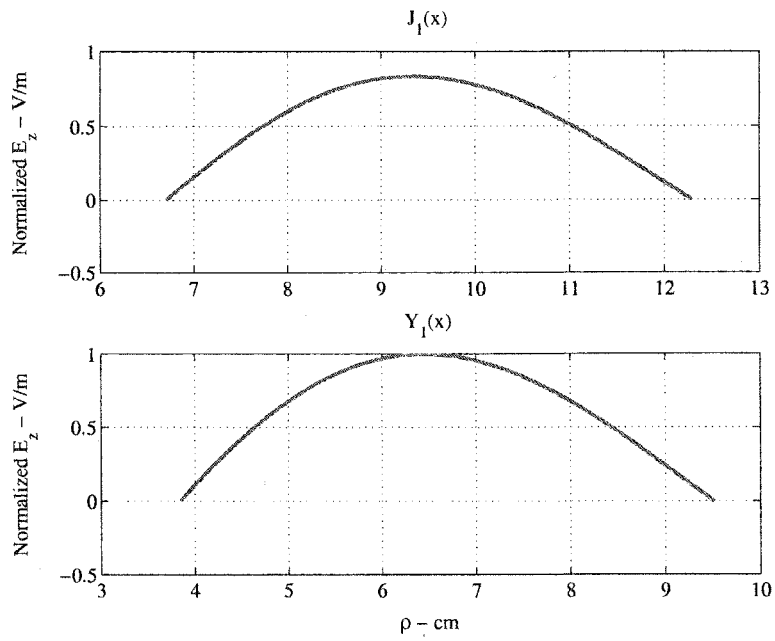

Figure 4.5: Grounded Dielectric Disk Radial Field Distribution.

4.3.1 Optimum Cavity Dimensions

The development in Section 4.3 assumes there is no interaction between the surface wave within the cavity and the structure of the disk outside the dielectric. This is untrue, as the disk is not infinite, and currents appearing on the bottom of the disk will alter the fields within the dielectric. Because of this, the actual field structure within the dielectric will be different from that derived in Section 4.3. Unfortunately, there is no closed form solution for the fields associated with the grounded dielectric disk. However, the simple development in Section 4.3 will be accurate to some degree, especially for high permittivity dielectrics. As such, the design guidelines developed in this section can be used as a starting point for the design of a dielectric cavity antenna, and the 2.5-D FDTD code may be used to further refine the design prior to building a prototype.

In this section, we discuss the optimum dimensions of the grounded dielectric disk introduced in Section 4.3. The mathematics have been developed to the point where we now have a means of estimating the optimum dimensions of the cavity, namely the

Field Structure	x_1	x_2	a (cm)	b (cm)
$J_1(\gamma_p\rho)$	3.83	7.02	6.71	12.29
$Y_1(\gamma_p\rho)$	2.20	5.43	3.85	9.51

$\epsilon_r = 10$, f = 1,575.42 MHz, $\gamma_p = 57.12$, $\gamma_z^{(2)} = 87.32$, $d_c = 1.583$ cm

Table 4.2: Example Grounded Dielectric Disk Properties.

inner and outer radii and the depth. We begin by considering the grounded dielectric disk shown in Fig. 4.4. A patch antenna placed on the central PEC cylinder will excite surface waves within the slab obeying Eqs. (4.26) or (4.27). The radial locations a and b of the PEC walls will determine which field distribution is excited. Consider the specific example of an alumina dielectric, having relative permittivity $\epsilon_r = 10$. Solving Eq. (4.2) we find that $\gamma_p = 57.12$ at the L1 GPS frequency of 1,575.42 MHz. The critical thickness d_c of the dielectric cavity is 1.583 cm. The two possible solutions for radii a and b are summarized in Table 4.2. Fig. 4.5 shows the normalized radial distribution of E_z within the cavity for the two possible cases. Notice that the field structure in Fig. 4.5 appear sinusoidal. Indeed, for large arguments, both $J_1(x)$ and $Y_1(x)$ may be approximated with the *cos* and *sin* functions, respectively [70]. More generally, Fig. 4.6 shows the optimum disk thickness d_c for a range of dielectrics, and Fig. 4.7 shows the optimum disk inner and outer radii. In Figs. 4.6 and 4.7, the operating frequency is the L1 GPS frequency of 1,575.42 MHz. The parameters plotted in Figs. 4.6 and 4.7 are idealized, and the actual optimum disk dimensions will differ because of the finite dimensions of the disk. For example, as discussed in Section 4.5, a prototype dielectric cavity antenna with $\epsilon_r = 2.37$ was constructed having an optimized cavity length of 9.3 cm, which is greater than the length of 7.5 cm suggested by Fig. 4.7. Since 2.37 is a rather low permittivity, the dielectric cavity was not well isolated from external effects, and the finite dimensions of the antenna significantly affected the field distribution within cavity. Fig. 4.7 should be used only as a starting point for the design of a DCA. Further iterations with the 2.5-D FDTD computer code are required before a working antenna can be constructed.

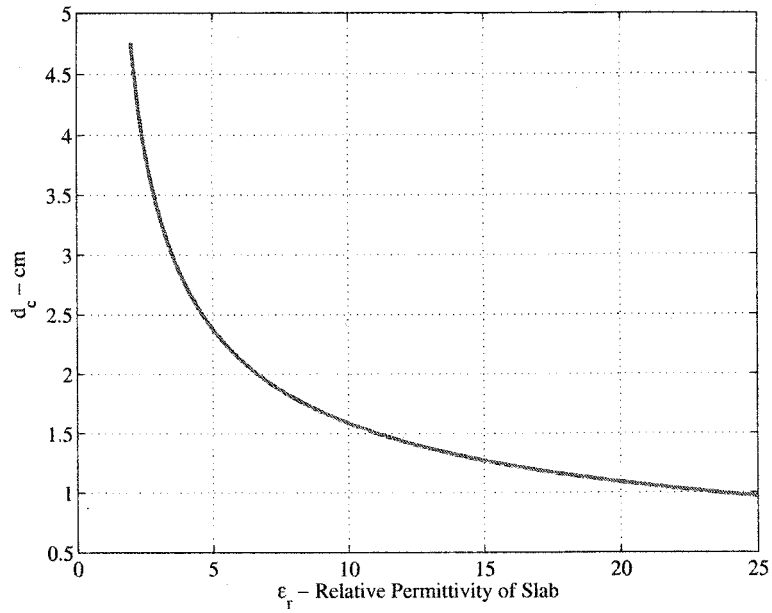

Figure 4.6: Disk Critical Thickness d_c.

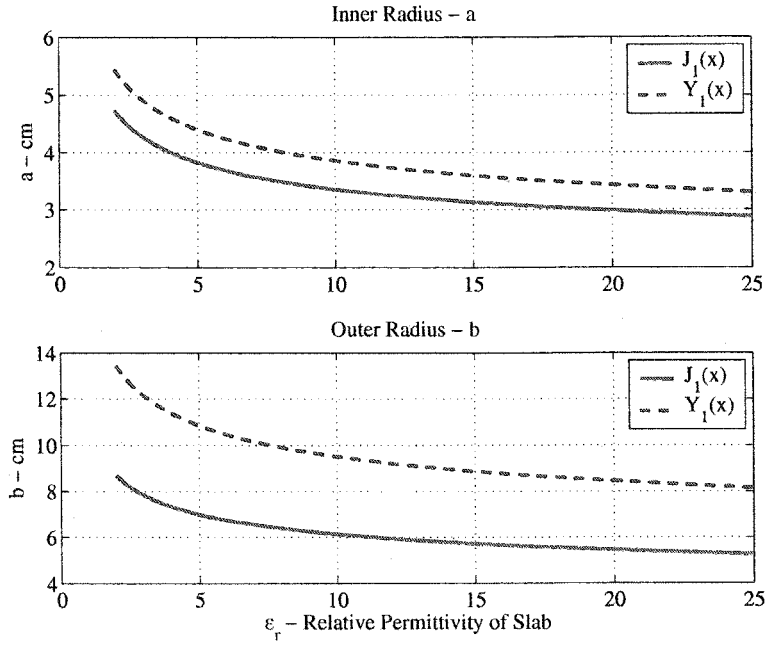

Figure 4.7: Disk Inner and Outer Radii, a and b.

4.4 2.5-D FDTD Simulations of the DCA

The 2.5-D FDTD code discussed in Chapter 3 has proven to be a useful tool for analyzing antennas having rotational symmetry and sources that have a sinusoidal azimuthal variation. To demonstrate the code's utility, simulations were run for three different types of antennas: a Trimble microstrip patch antenna mounted on a 30 cm diameter circular aluminum plate, a NovAtel 501 antenna mounted on a NovAtel 503 choke ring ground plane, and a dielectric cavity antenna. In all cases, the cell size $(\Delta\rho, \Delta z)$ was $\lambda/200$ square, and the time step Δt was set to 70% of the maximum Δt allowed for stability [29],

$$\Delta t = \frac{0.7}{c}\frac{\Delta}{\sqrt{2}}, \tag{4.28}$$

where $\Delta = \Delta\rho = \Delta z$. This is a conservative choice which guarantees stability. Steady state conditions were reached after 10,000 time steps. The dielectric material used in the DCA prototype is polyethylene, for which $\epsilon_r = 2.37$. Polyethylene is inexpensive, readily available, and has low loss ($\tan\delta = 0.00007$ at 1.575 GHz) [27]. The cavity depth d_c was chosen to be 4.08 cm, which is optimum for $\epsilon_r = 2.37$. The radial length of the cavity is 9.3 cm. This length was found by iteratively running the FDTD code until a minimum amount of radiation was observed in the backlobe region of the antenna. The starting point for these simulations was a 7.5 cm long cavity, as suggested by Fig. 4.7. Plots of the resulting radiation patterns for each case are shown in Figs. 4.8, 4.9, and 4.10. Comparing Figs. 4.9 and 4.10, we find that the DCA performs nearly as well as the choke ring with regard to cross polarization rejection, and sensitivity in the upper hemisphere. Both the choke ring and DCA are more resistant to interferers or multipath from below the horizon, compared to the simple circular ground plane antenna pattern in Fig. 4.8.

One advantage of running an FDTD analysis is that all six field components are known in the vicinity of the antenna structure. Figs. 4.11 and 4.12 show the magnitude of the transverse magnetic field (H_ϕ) in the near-field region of the NovAtel choke ring antenna and DCA, respectively. Notice that H_ϕ is minimized at the top surface of the corrugations in Fig. 4.11, and along the top surface of the cavity in Fig. 4.12. This confirms that the corrugations and the cavity are acting as artificially

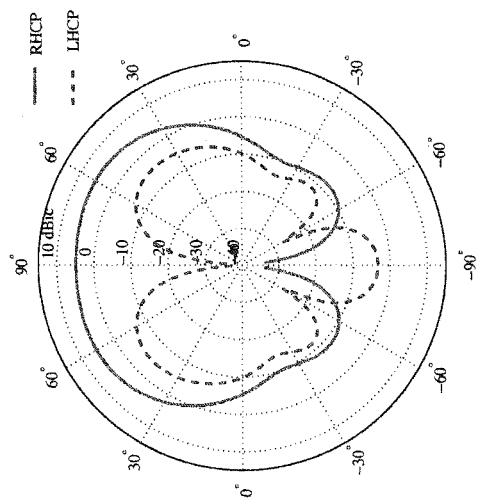

Figure 4.8: Theoretical Radiation Pattern of Trimble Patch Antenna Mounted on 30 cm Diameter Plate.

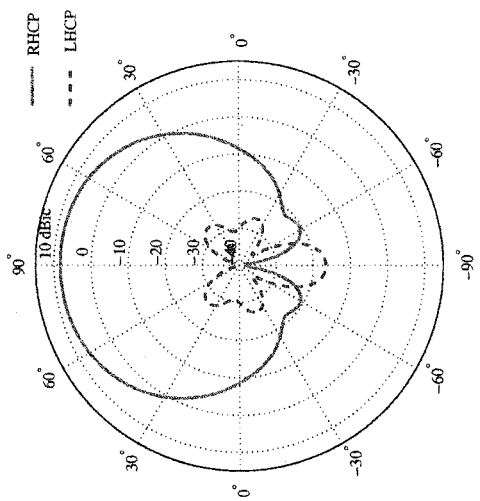

Figure 4.9: Theoretical Radiation Pattern of NovAtel Choke Ring Antenna.

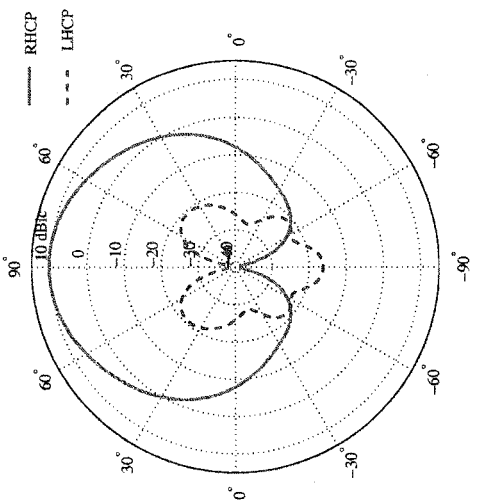

Figure 4.10: Theoretical Radiation Pattern of Prototype DCA.

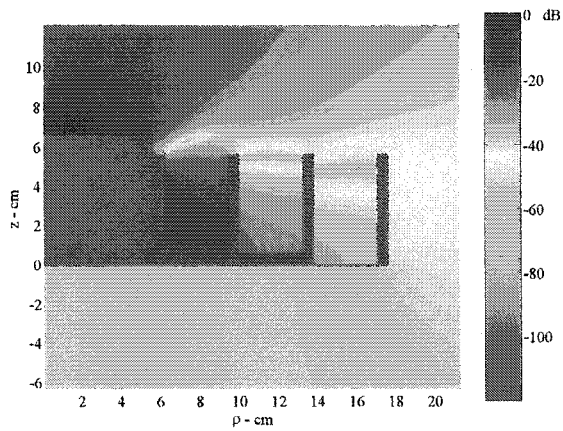

Figure 4.11: Near-Field H_ϕ Component of the NovAtel Choke Ring.

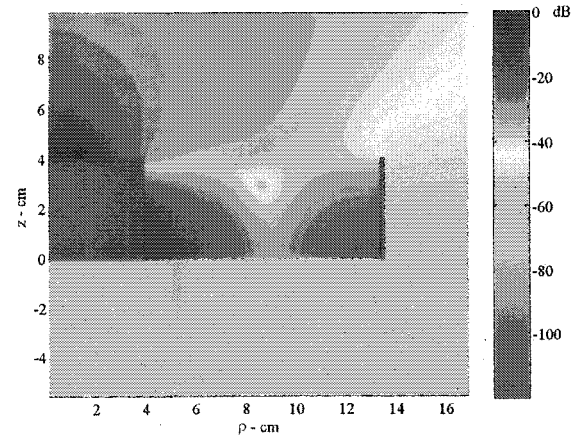

Figure 4.12: Near-Field H_ϕ Component of the Optimized DCA.

soft surfaces by creating a very high surface impedance. In addition, one observes that the field structure within the corrugations in Fig. 4.11 is primarily TEM, i.e., there is essentially no field variation in the ρ direction within the corrugations. Within the cavity of the DCA, all field components exhibit a standing wave pattern consistent with Eq. (4.26) or Eq. (4.27). The near fields of all three test antennas are shown for comparison purposes in Fig. 4.13. The figures highlight the usefulness of the FDTD method for providing valuable insight into the electromagnetic behavior of antenna systems. Solutions from moment methods and other boundary integral techniques do not provide as much information.

4.5 A Prototype DCA

A prototype DCA was built and tested to validate the concept of using a grounded dielectric slab as an artificially soft surface for RFI mitigation. Polyethylene was used as the cavity dielectric material, and aluminum was chosen as the structural metal. A photograph of the prototype DCA is shown in Fig. 4.14. The dimensions of the DCA were determined by first using Figs. 4.6 and 4.7, and then simulating the antenna numerous times to arrive at a final set of design parameters. These parameters are $a = 4$ cm, $b = 13.25$ cm, and $d_c = 4.08$ cm. The aluminum support structure was

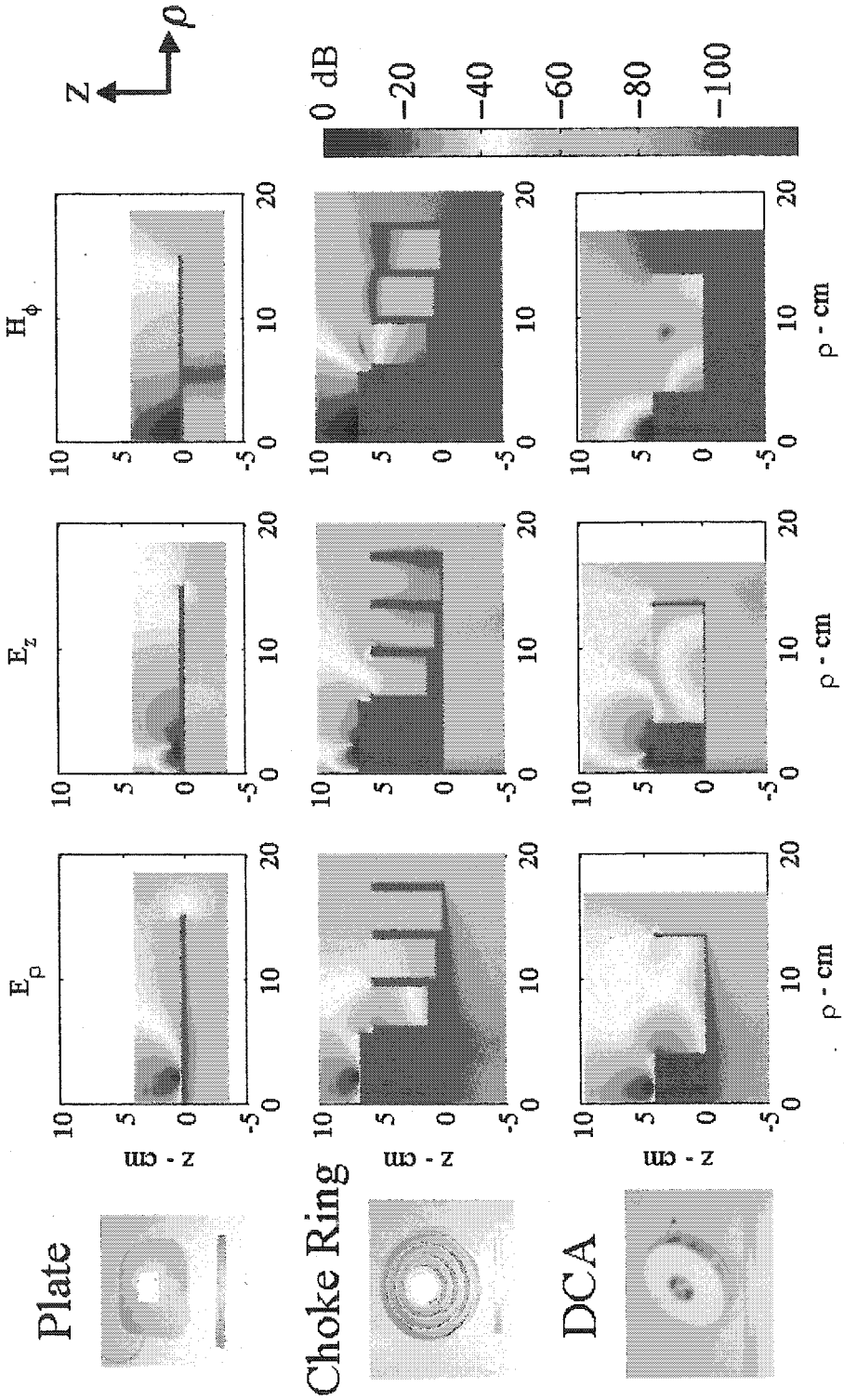

Figure 4.13: Near-Field Components of Three Antennas.

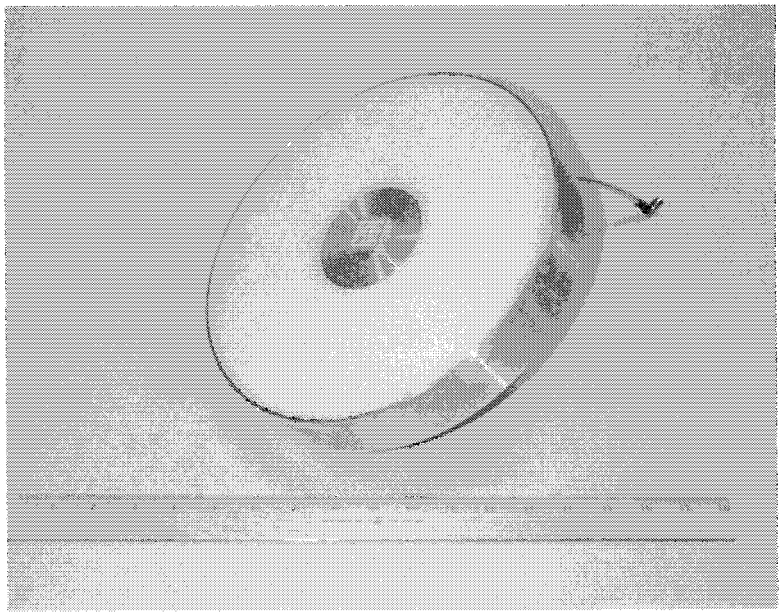

Figure 4.14: Prototype DCA.

machined from a cylindrical slab of metal. The polyethylene was provided by the manufacturer in the form of 3 mm diameter pellets. These pellets were melted into a cylindrically shaped slab, allowed to cool, and then machined to fit within the cavity of the aluminum structure. The dielectric was press fit into the aluminum housing. A 2 cm square microstrip patch antenna (Toko DAK1575MS50) was used as the radiating element. This element was placed at the center of the antenna, with a coaxial pig-tail extending from beneath the aluminum housing. The DCA was placed on the roof of the HEPL building on Stanford campus. A low noise pre-amplifier (LNA) was connected to the antenna feed point. Approximately 100 meters of coaxial cable ran from the roof to the lab below, where the coax was connected to a NovAtel OEM3 GPS receiver. A block diagram of the test setup is shown in Fig. 4.15. Three different antennas were tested: the DCA, a NovAtel choke ring antenna, and a Trimble patch antenna mounted on a 30 cm diameter circular ground plane. Each antenna was placed on the same tripod mount to ensure an identical multipath environment for the three cases. The receiver was set to track one satellite (PRN 29) over the course of three consecutive days. The satellite position (azimuth

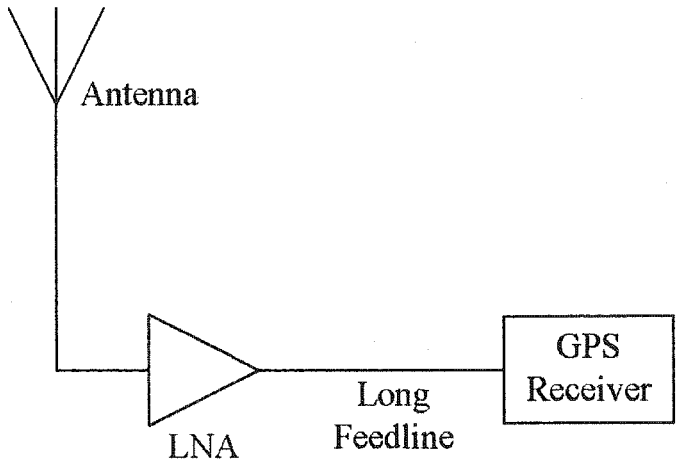

Figure 4.15: DCA Test Setup.

and elevation) and carrier-to-noise density ratio (C/N_0) were recorded for each of the three antennas on a different day. Consider that the raw C/N_0 data reported by the GPS receiver will not yield the actual radiation pattern of the antenna vs. elevation angle. Errors due to multipath, tropospheric loss, change in satellite range, and the GPS satellite transmit antenna pattern all contribute to the error in the received C/N_0. These effects become more pronounced for satellites near the horizon. To determine the actual radiation pattern, the known radiation pattern of the NovAtel 503 choke ring antenna [26] was used as a reference. The actual C/N_0 measured by the GPS receiver using the choke ring antenna was compared to the known radiation pattern, and the residual was removed. The residual, shown in Fig. 4.16, was used to correct the measured data from the other antennas being tested. The residual is simply subtracted from the raw C/N_0 values measured by the receiver, yielding a best estimate of the actual radiation pattern. The error function will vary for different antenna sites, for each particular satellite, and for different sky tracks. Since all measurements were taken at the same location from the same satellite on three consecutive days, it is assumed that the same error function is applicable to all three data sets.

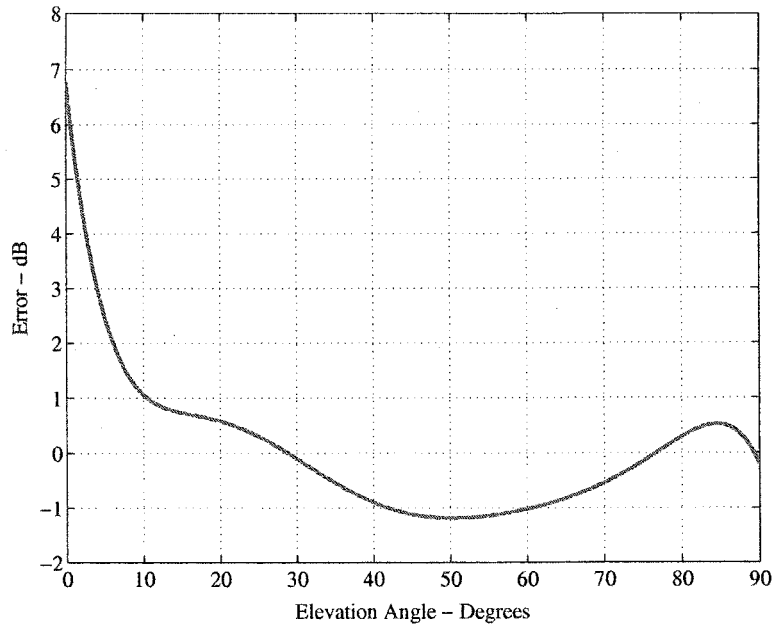

Figure 4.16: Residual Measurement Error.

4.5.1 Experimental Results

In Figs. 4.17, 4.18, and 4.19, the elevation radiation patterns measured on the roof are compared to the patterns obtained from the FDTD simulations. The measured choke ring and circular ground plane antenna patterns match the theoretical patterns well, to within 1.5 dB over the upper hemisphere. However, the theoretical DCA pattern using a dielectric having $\epsilon_r = 2.37$ does not match the experimental results. The likely reason for this is that during the dielectric melting and cooling process, pockets of air became trapped in the dielectric. Although many of these air pockets were plugged with dielectric slugs prior to assembling the prototype, it is evident that some air still remained trapped in the dielectric cavity. Shown also in Fig. 4.19 is a theoretical DCA radiation pattern using a dielectric having $\epsilon_r = 2.1$. This pattern matches the experimental pattern well, and we infer from this that the air pockets in the polyethylene have lowered the effective permittivity of the material from 2.37 to 2.1.

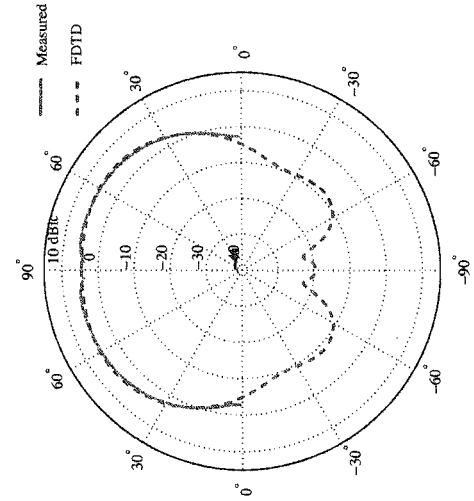

Figure 4.17: Radiation Pattern of Trimble Patch Antenna Mounted on 30 cm Diameter Plate.

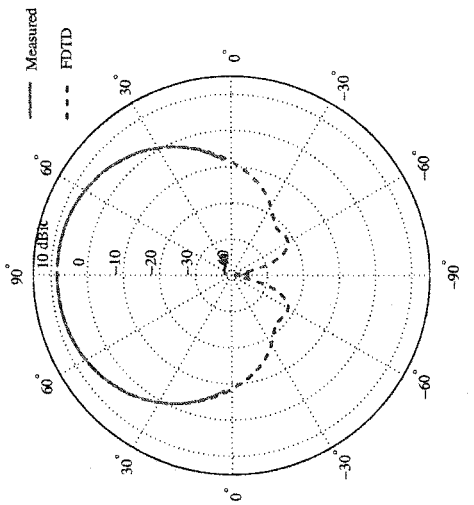

Figure 4.18: Radiation Pattern of NovAtel Choke Ring Antenna.

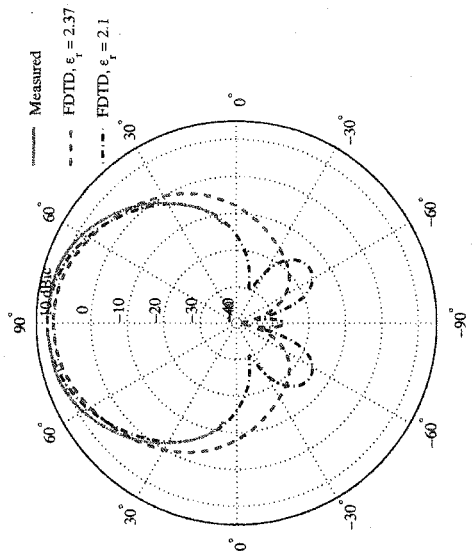

Figure 4.19: Radiation Pattern of Prototype DCA.

Although the prototype DCA is insensitive to interference and multipath originating from below the horizon, GPS satellite signals arriving from below 30° elevation are severely attenuated by the antenna, and the measured C/N_0 is consequently quite low at these elevation angles. In fact, the DCA lost PRN 29 at an elevation angle of 11°, while the choke ring tracked PRN 29 down to 4° elevation. The simple circular ground plane antenna permitted tracking down to the horizon. Of course, if the relative permittivity of the DCA cavity were actually 2.37, its performance would be more in line with the choke ring. This being true, the DCA would still provide poor reception of low elevation satellites, and is not an ideal stand alone anti-jam aircraft antenna. Such an antenna could, however, be useful in the event that interference is detected, and threatens or prevents airborne GPS navigation. The DCA could be used as a contingency antenna to provide minimal coverage of high elevation GPS satellites, while rejecting the ground based interference. This arrangement would require two separate antennas – a standard patch antenna for nominal conditions when no RFI is present, and the DCA for use in the event RFI jams the patch. This configuration is undesirable, as aircraft should have as few protrusions from the fuselage as possible. Combining the DCA and the nominal patch into a single package would be more practical.

4.6 Size Considerations

The prototype DCA discussed in Section 4.5 is large and heavy, and thus ill-suited for airborne applications. However, when high-permittivity dielectrics are used in the cavity, the height of the antenna is reduced in accordance with Fig. 4.6. A DCA with a ceramic cavity having $\epsilon_r = 20$ is only 1 cm tall and 18 cm in diameter. By comparison, the Trimble airborne patch antenna is 2 cm tall and 13 cm wide along its diagonal. So the idea of building a DCA small enough for airborne applications is reasonable. However, as mentioned in the previous section, an additional antenna would be required to obtain good position accuracy when no RFI is present. In addition, the high permittivity substrate would have a rather narrow bandwidth. Because of this, the antenna would be sensitive to manufacturing errors and random

variability in the permittivity of the ceramic substrate. For these reasons, fabricating the DCA in high volumes would be more difficult than for other types of antennas such as crossed dipoles and microstrip patches.

Chapter 5

Modelling Microstrip Patch Antennas

This chapter describes an efficient technique for modelling microstrip patch antennas. Namely, the multiport network method (MNM) is derived in detail for single and multiple patches. This model allows one to compute radiation patterns and input impedance for single or multiple rectangular patches. Mutual coupling is computed for multiple patches as well. In contrast to the time domain technique described in Chapter 3, the MNM method is a frequency domain analysis technique. MNM is chosen for this particular problem since a full field solution in the time and spatial domain is not required. Knowledge of the electromagnetic fields at the perimeter of the patch antenna only is sufficient for the purposes of this work. In addition, only square patches will be modelled with MNM. The 2.5-D FDTD technique developed in Chapter 3 is applicable only to circular patches. MNM is first derived for standard rectangular patch antennas with homogeneous substrates. Later, the model is extended to handle patches having lumped loads embedded within their dielectric substrates. The purpose of this modification is to model the effect of PIN diodes within the substrate. The model is not limited to PIN diodes though, as it can handle any number of loads having arbitrary impedances. Two canonical problems are solved to validate the MNM computer code. First, the input impedance and radiation pattern of a single patch antenna are computed. Next, and array of four patch

antennas is simulated, and the corresponding radiation pattern is shown.

5.1 The Microstrip Patch Antenna

Microstrip patch antennas make excellent antennas for GPS aviation applications. They are small, lightweight, inexpensive, easy to manufacture, and best of all, have a very low vertical profile ($0.01\lambda - 0.05\lambda$). Coincidentally, they naturally possess the radiation pattern most desired for satellite communication – a hemispherical pattern. Because of this broad radiation pattern, patch antennas are low gain antennas, typically with +5 dBic gain toward the zenith. They can be designed to have either linear or circular polarization. Although patch antennas are inherently narrowband, techniques exist for widening the response of these antennas. Patch antennas can have nearly any shape, though common shapes are rectangular, circular, triangular, and pentagonal. The most popular fabrication technique is to etch the metallic patch element on a printed circuit board. This method yields accurate patch dimensions, which are important for achieving the correct resonant frequency and polarization purity. Etched printed antennas also facilitate the design of arrays, which often include a corporate feed network directly on the circuit board containing the array. This section explores the history and basic operation of patch antennas, and provides sufficient detail for those wishing to build patch antennas for applications other than GPS.

5.1.1 History

The microstrip antenna concept originally dates back to the 1950's. However, the patch antenna did not attract much attention until the 1970's when Byron described an antenna consisting of a conducting strip radiator separated from the ground plane by a dielectric substrate [11]. This antenna was a half-wavelength wide, several wavelength long microstrip element fed periodically along the radiating edges by coaxial connections. R. Munson received a patent for a different microstrip element in 1973 [51]. Other important developments around that time include the design

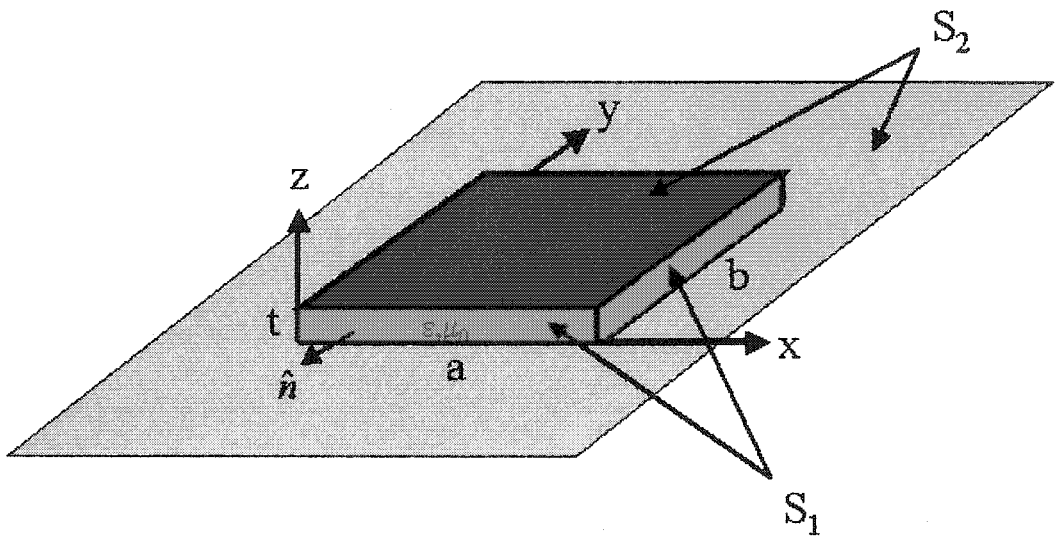

Figure 5.1: Rectangular Patch Antenna Geometry.

of rectangular and circular elements [40], cylindrical patches for use on rockets and missiles [81], and conformal arrays [63]. The early work by Munson on developing microstrip antennas for use on rockets and missiles validated the microstrip patch antenna concept, demonstrating that it performed well in practical applications. This research paved the way for a new antenna industry which is still growing today [12]. Patch antennas are heavily used for GPS aviation, marine, and automotive applications. Even handheld GPS receivers make use of a compact microstrip patch element. Patches are also found in military and space applications such as military aircraft, missiles, rockets, and satellites.

5.1.2 The Rectangular Patch Antenna

The basic geometry of the rectangular patch antenna is shown in Fig. 5.1. Here, we show a thin rectangular metal element supported by a dielectric substrate having permittivity ϵ and free space permeability μ_0. The microstrip patch element has dimensions a and b in the x and y directions, respectively. The antenna extends vertically in the z direction, having substrate thickness t. The thickness is usually

very small with respect to the wavelength ($0.01\lambda_0 - 0.05\lambda_0$) while a and b range from $0.05\lambda_0 - 0.5\lambda_0$. The substrate is bonded to a metallic ground plane, which acts both as a support for the antenna and as the electromagnetic complement to the patch element upon which the electric field lines terminate. The ground plane is shown as being finite in Fig. 5.1. However, the MNM technique developed in this chapter will assume an infinite ground plane. As such, radiation characteristics beneath a finite sized ground plane will not be available from the MNM technique. This limitation is overcome by using the results from the MNM model as input to a diffraction code which accounts for the finite sized ground plane.

Basic Operation

To first order, the patch antenna can be thought of as a cavity resonator with perfect magnetic conducting (PMC) perimeter walls S_1 and perfect electric conducting (PEC) top and bottom S_2, as shown in Fig. 5.2. Since an infinite ground plane is assumed, image theory [2] is used to remove the ground plane to create the equivalent electromagnetics problem shown in Fig. 5.2. Here, the cavity exists in free space, without the ground plane, and the electric field is doubled on the radiating walls of the patch (surface S_1) to account for the image. The accuracy of the resonator approximation increases as the substrate permittivity and conductivity of the patch and ground plane approach infinity. For practical dielectrics and metals, the antenna can be thought of as a resonator with some loss. For well designed patches, this loss is due mainly to radiation from the walls of the patch, S_1. Losses in the dielectric and conducting surfaces can also be accounted for. The electromagnetic boundary conditions for the resonator are as follows,

1. The tangential magnetic fields are zero on the PMC wall surface S_1
2. The tangential electric fields are zero on the PEC surface S_2.

Solving the homogeneous wave equation subject to these boundary conditions yields the Green's function for this electromagnetic structure [2]. This procedure will be discussed in more detail in Section 5.2, but we note here that an infinite number of

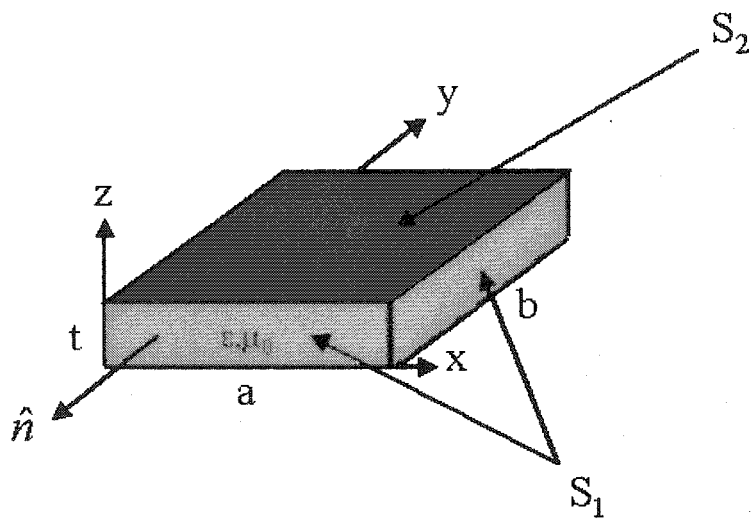

Figure 5.2: Rectangular Patch Antenna Equivalent Problem.

modes can exist within this structure. The two lowest order modes are of primary importance for satellite antenna applications. Far-field radiation patterns due to the higher order modes have a null directed toward the zenith, resulting in an antenna which is unusable for satellite communication. The TM_{100} and TM_{010} modes are the lowest order modes for the rectangular patch, and yield the desirable hemispherical radiation pattern we seek. Note that since $t << \lambda_0$, there can be no field variation in the z direction. Thus, the field distribution within the resonator will only have structure in the x and y directions. Let us consider the TM_{100} mode only, since the TM_{010} mode has the same electromagnetic characteristics, except for a coordinate change. Ignoring the excitation for now, and skipping all of the details involved with solving the wave equation, the fields under the patch for the TM_{100} mode are expressed as

$$E_z = E_0 \cos \frac{\pi x}{a}, \tag{5.1}$$

$$H_y = \frac{\pi}{j\omega\mu_0 a} E_0 \sin \frac{\pi x}{a}. \tag{5.2}$$

Observe that these field distributions satisfy the boundary conditions listed earlier. There is no tangential magnetic field present at the PMC dielectric-air interface S_1, and there is no tangential electric field component on the top or bottom PEC patch and ground plane surfaces S_2. The electric field is constant along the $x = 0$ and $x = a$ walls. These walls are referred to as the *radiating edges* of the patch because radiation from these two walls adds in phase in the far-field, in the zenith direction. The electric field distribution along the $y = 0$ and $y = b$ walls is sinusoidal, and radiation from these walls cancels in the far-field. These walls are referred to as the *non-radiating edges* of the patch. As the fields are not entirely contained within the resonator, radiation occurs due to the fringing fields extending outward from the radiating edges. While the effective radiating area (effective aperture) of these walls is small compared to other types of aperture antennas, the microstrip patch antenna can still be a very efficient antenna for both receive and transmit applications.

5.2 Basic Cavity Model

The cavity model is a well known method for predicting the performance of microstrip patch antennas [12]. It is very simple and fast, and can provide results which are accurate to about 2.0%. The geometry in Fig 5.2 will be used to derive the cavity model. The cavity model provides the electric field distribution at any location (x, y) underneath the patch. Only the z directed electric field exists within the patch, as the thickness t is too small to support the modes required to sustain the x and y directed electric field components. Consider that the electric field within the patch substrate satisfies the inhomogeneous scalar Helmholtz wave equation

$$(\nabla_t^2 + k^2)E_z = -j\omega\mu_0 J_z(x_0, y_0), \tag{5.3}$$

where

$$\nabla_t^2 = \frac{\partial^2}{\partial x^2} + \frac{\partial^2}{\partial y^2}. \tag{5.4}$$

In Eq. (5.3), $k^2 \equiv k_0^2\epsilon_{r,eff}$ where k_0 is the free space wavenumber and $\epsilon_{e,eff}$ the effective permittivity of the substrate. This effective permittivity is reduced from the

actual bulk permittivity of the substrate because of the fringing fields extending into free space. $J_z(x_0, y_0)$ is a z-directed current source located at (x_0, y_0). Time harmonic fields will be assumed throughout this chapter, and the $e^{j\omega t}$ time dependence factor will be suppressed. The boundary condition satisfied by E_z on S_1 is

$$\frac{\partial E_z}{\partial n} = 0, \tag{5.5}$$

where $\hat{n}$ is the outward looking normal. The consequence of Eq. (5.5) is that $\hat{n} \times \vec{H} = 0$ on S_1. In addition, since $E_x = E_y = 0$, $\hat{n} \times \vec{E} = 0$ on S_2. Using the Green's function for the rectangular patch, the solution for E_z with a z directed current source at (x_0, y_0) can be obtained by solving

$$E_z(x, y) = \iint_{S'} G(x, y|x_0, y_0) J_z(x_0, y_0)\, dS. \tag{5.6}$$

The Green's function for the two-dimensional patch antenna is

$$G(x, y|x_0, y_0) = jk_0 \sum_{m=0}^{\infty} \sum_{n=0}^{\infty} \frac{\Psi_{mn}(x, y)\Psi_{mn}(x_0, y_0)}{k^2 - k_{mn}^2}. \tag{5.7}$$

The eigenfunctions Ψ_{mn} and eigenvalues k_{mn} must satisfy the homogeneous wave equation

$$(\nabla_t^2 + k_{mn}^2)\Psi_{mn} = 0, \tag{5.8}$$

subject to the boundary condition

$$\frac{\partial \Psi_{mn}}{\partial n} = 0 \quad \text{on } S_1. \tag{5.9}$$

For a rectangular patch of width a and length b, the sinusoidal and co-sinusoidal functions expressed in Eq. (5.10) satisfy Eqs. (5.8) and (5.9).

$$\Psi_{mn}(x, y) = \frac{\chi_{mn}}{\sqrt{ab}} \cos k_n x \cos k_m y \tag{5.10}$$

In Eq. (5.10), χ_{mn} is a normalizing constant given in Eq. (5.11) [12], while $k_0 = \omega\sqrt{\mu_0\epsilon_0}$ and $Z_0 = \sqrt{\mu_0/\epsilon_0}$.

$$\chi_{mn} = \begin{cases} 1 & m = 0 \text{ and } n = 0 \\ \sqrt{2} & m = 0 \text{ or } n = 0 \\ 2 & m \neq 0 \text{ and } n \neq 0 \end{cases} \tag{5.11}$$

The modal eigenvalues (wavenumbers) are functions of the dimensions of the patch, a and b, and are expressed as

$$k_n = \frac{n\pi}{a}, \tag{5.12}$$

$$k_m = \frac{m\pi}{b}, \tag{5.13}$$

with

$$k_{mn}^2 = k_m^2 + k_n^2. \tag{5.14}$$

Eq. (5.15) is the solution to Eq. (5.6) using the basis functions from Eq. (5.10). I_0 is the complex amplitude of the driving current source filament, which is located at (x_0, y_0) and has dimensions (d_x, d_y, t). Eq. (5.15) is referred to as the *basic cavity model.*

$$E_z(x,y) = I_0(x_0,y_0) \cdot \left[jk_0 \sum_{m=0}^{\infty}\sum_{n=0}^{\infty} \frac{\Psi_{mn}(x,y)\Psi_{mn}(x_0,y_0)}{k^2 - k_{mn}^2} G_{mn}(d_x,d_y) \right], \tag{5.15}$$

where

$$G_{mn}(d_x,d_y) = \frac{\sin\left(\frac{n\pi d_x}{2a}\right)}{\left(\frac{n\pi d_x}{2a}\right)} \frac{\sin\left(\frac{m\pi d_y}{2b}\right)}{\left(\frac{m\pi d_y}{2b}\right)}. \tag{5.16}$$

This model assumes a lossless cavity resonator filled with substrate having permittivity ϵ and permeability μ_0. However, practical patch antennas have lossy dielectrics and metal surfaces. To model these losses, we lump all losses into a complex wavenumber

k_{eff}, given by

$$k_{eff} = \sqrt{\epsilon_r(1 - j\delta_{eff})}\, k_0, \tag{5.17}$$

where $\delta_{eff} = 1/Q$, and the Q of the cavity resonator is due to losses in the dielectric and conducting walls, expressed as

$$Q = \frac{\omega W}{P_{in}} = \frac{Q_{di}Q_{cu}}{Q_{di} + Q_{cu}}. \tag{5.18}$$

W is the average energy stored in the resonator. Q_{di} is due to dielectric losses, and Q_{cu} is due to conductor losses [61]. These quantities are obtained from

$$Q_{di} = \frac{1}{\tan\delta}, \tag{5.19}$$

$$Q_{cu} = \frac{t}{\delta_s}, \tag{5.20}$$

where δ_s is the skin depth of the conductor given by

$$\delta_s = \sqrt{\frac{2}{\omega\mu\sigma}}. \tag{5.21}$$

In Eq. (5.21), σ is the conductivity of the metal patch and ground plane.

5.2.1 Radiation Effects

The model derived in the previous section assumes that the patch antenna is a lossy cavity resonator, with losses arising in the dielectric substrate and metal walls only. However, properly designed patches are expected to radiate, and this radiation is another source of "loss" which is manifested in the *radiation resistance* of the antenna. A substantial radiation resistance reduces the effective Q of the antenna, and indicates an efficient antenna. One way to account for the radiation resistance is to compute the quality factor due to the radiation resistance (Q_r) and incorporate this into Eq. (5.18). Eq. (5.17) would then be used in Eq. (5.15), yielding the electric field distribution within the patch substrate with all losses and radiation accounted for [12]. This very common approach yields accurate field distributions, input impedance, and

radiation patterns for a single patch antenna. However, by keeping the radiation effects separate from the internal losses, one can develop a more general modelling technique which is applicable to multiple patches operating in close proximity to each other. This integrated solution technique is called the multiport network method, and is the subject of the following section.

5.3 Multiport Network Method (MNM)

The multiport network method takes the cavity model two steps further by incorporating effects of free space radiation and mutual effects from other nearby antennas [59] [7] [67]. To start, consider the basic cavity model result from Eq. (5.15). The factor in brackets is mathematically similar to a *transimpedance* between the current source at location (x_0, y_0) and the voltage at observation location (x, y). In this and following sections, the transimpedance will be used quite frequently to describe the interaction between source and observation points. To make this development more tractable, the transimpedance factor from Eq. (5.15) will be referred to as Z_{ij}, where j indicates a source point and i indicates an observation point. In addition, the transimpedance Z_{ij} will be used to map current to voltage, rather than current to electric field, as in Eq. (5.15). With these considerations, the transimpedance Z_{ij} is expressed as

$$Z_{ij} = -jtk_0 \sum_{m=0}^{\infty} \sum_{n=0}^{\infty} \frac{\Psi_{mn}(x_i, y_i)\Psi_{mn}(x_j, y_j)}{k_{eff}^2 - k_{mn}^2} G_{mn}(d_{x_j}, d_{y_j}). \tag{5.22}$$

In Eq. (5.22), Z_{ij} is the transimpedance between source point j and observation point i. $G_{mn}(d_{x_j}, d_{y_j})$ is obtained from Eq. (5.16). Dielectric and conductor losses are absorbed in k_{eff}. Consider a patch antenna having P current sources located at (x_p, y_p) with complex amplitudes specified in the vector $[I_p]$, which is of size $(P \times 1)$. Now divide the perimeter of the patch S_1 into Q segments at locations (x_q, y_q). This process is called segmentation [59]. The complex voltage across each segment and the current flowing into each segment are denoted by $[V_q]$ and $[I_q]$, respectively. These vectors are of size $(Q \times 1)$. Fig. 5.3 shows a patch with a single feed at (x_p, y_p), and a single segment at (x_q, y_q). Voltages present at all of the segments p and q can be

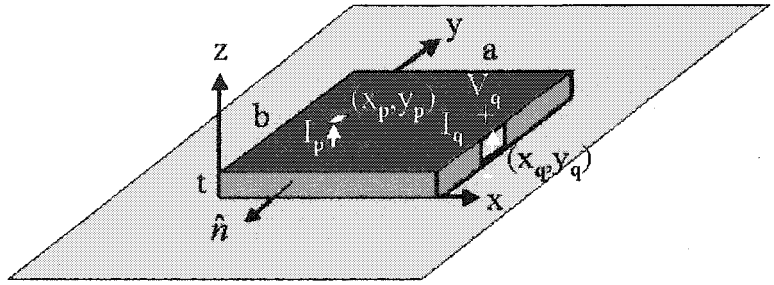

Figure 5.3: Segment Geometry.

expressed as a function of the source currents I_p and the segment currents I_q using the basic cavity model transimpedance kernel from Eq. (5.22).

$$\begin{bmatrix} V_p \\ V_q \end{bmatrix} = \begin{bmatrix} Z_{pp} & Z_{pq} \\ Z_{qp} & Z_{qq} \end{bmatrix} \begin{bmatrix} I_p \\ I_q \end{bmatrix} \tag{5.23}$$

In Eq. (5.23), all of the factors in the Z-matrix are computed using the cavity model kernel in Eq. (5.22), replacing i and j with p or q, as necessary. If we take I_q to be zero, then Eq. (5.23) reduces to the basic cavity model in Eq. (5.15). In this degenerate case, the cavity walls are assumed to be PMC, and there is no radiation from the patch. Fortunately, real patch antennas do not have PMC walls, and energy can pass through these walls. This requires I_q to be non-zero. In Section 5.3.1, we present a procedure for obtaining the ratio of the wall current to the wall voltage, which is appropriately called the wall admittance. It is important to properly model the wall admittance, so that the radiation characteristics of the patch can be computed accurately.

5.3.1 Wall Admittance

This section introduces the concept of microstrip patch antenna wall admittance. The wall admittance is the ratio of current to voltage present at the perimeter of the patch. Simply put, the real part of the wall admittance represents the loss due to radiation, and the imaginary part accounts for energy storage in the fringing fields.

Accurate modelling of the wall admittance is important for computing the input impedance of the antenna. Also, the wall admittance impacts the field distribution at the walls, directly affecting the far-field radiation pattern of the antenna. The patch wall admittance is due to external loading from

- Free space,
- The radiation from other segments on the same patch,
- The radiation from segments of other nearby patch antennas.

A non-zero wall admittance supports a tangential magnetic field at the perimeter of the patch, allowing current (I_q) to flow into or out of the walls. This contradicts the assumption in Section 5.2 that the walls are perfect magnetic conductors (PMC), whereby the wall admittance would be zero. As mentioned earlier, one can modify the basic cavity model of Section 5.2 to account for both radiation losses (non-PMC walls) and dielectric/conductor losses by absorbing them into δ_{eff} in Eq. (5.17). This adaptation of the cavity model is quite popular, as it gives accurate results, and is adequate for the initial design stages of patch antennas [12]. However, mutual coupling between nearby patch antennas can drastically affect the wall admittance, and is not accounted for in the basic cavity model. This section describes a technique which accounts for all three effects simultaneously.

Consider a single rectangular patch antenna divided into Q segments. The external wall admittance for a single segment q on the patch antenna perimeter is

$$Y_q^{ext} = -\frac{I_q}{V_q}\bigg|_{q=1\ldots Q,} \tag{5.24}$$

where V_q is the voltage across segment q, and I_q is the current into segment q. The current into segment q is due to the external tangential magnetic field presented to the segment. This magnetic field is caused by radiation from all Q segments on the patch wall. For a single segment q, the total current into the segment is expressed as

$$I_q = \sum_{r=1}^{Q} I_{qr}\bigg|_{q=1\ldots Q,} \tag{5.25}$$

where I_{qr} is the current into segment q due to radiation from segment r. One can combine Eqs. (5.24) and (5.25) to obtain the following compact expression for Y_q^{ext}

$$Y_q^{ext} = -\frac{1}{V_q}\sum_{r=1}^{Q} I_{qr}\Big|_{q=1\ldots Q.} \tag{5.26}$$

Y_q^{ext} can be written in column vector form, having size $(Q \times 1)$. However, Eq. (5.26) may be written in matrix form as well, which facilitates analysis of patch antennas using matrix equations. The entries in this *external admittance matrix* are the mutual admittances between all of the individual Q segments on the wall. The matrix is constructed using

$$Y_{qr}^{ext} = -\frac{I_{qr}}{V_q}\Big|_{\substack{q=1\ldots Q\\ r=1\ldots Q.}} \tag{5.27}$$

Eq. (5.27) sets up the matrix whose entries are the mutual admittances between the qth and r^{th} segments of the patch. Y_{qr}^{ext} is a $(Q \times Q)$ matrix. The self-admittances of the segments are contained in the diagonal (i.e., Y_{qr}^{ext} with $r = q$) while the mutual admittances between different segments are contained in the non-diagonal entries (i.e., Y_{qr}^{ext} with $r \neq q$). For example, $Y_{12,32}^{ext}$ is the mutual admittance between the 12th and 32nd segments. Solving for the individual entries of the admittance matrix Y_{qr}^{ext} is a rather involved affair. The procedure will be discussed in detail in the following sections.

5.3.2 Segment Self-Admittance

This section deals with computing the self-admittance of a single segment, Y_{qq}^{ext}. The self-admittance consists of a real self-conductance and imaginary self-susceptance, as in

$$Y_{qq}^{ext} = G_{qq} + jB_{qq}. \tag{5.28}$$

The self-conductance of a segment G_{qq} is a measure of the power flow through the segment, while the self-susceptance of the segment B_{qq} accounts for reactive energy stored in the fringing fields. In the following sections, the segment will be treated as a slot embedded in an infinite ground plane, and the *edge* or *wall* conductance

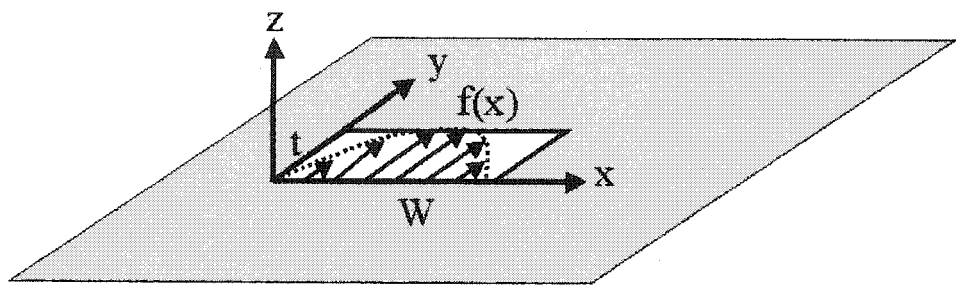

Figure 5.4: Slot Embedded in an Infinite Ground Plane.

and susceptance of such a slot will be computed. While the slot approximation is a seemingly crude model of the actual physical configuration of the patch antenna, it yields surprisingly accurate results.

Slot Conductance

A simple method for obtaining the conductance G_r of a slot embedded in an infinite ground plane is presented in this section. The geometry of the slot is shown in Fig. 5.4. By computing the power flow (P_r) through such a slot, the effective conductance of the slot can be obtained. This idea is expressed mathematically by

$$G_r = \frac{2WP_r}{\int_0^W f^2(x)dx}, \tag{5.29}$$

where W is the width of the slot and $f(x)$ is the normalized electric field distribution along the length of the slot. Assuming a uniform field distribution for $f(x)$, Eq. (5.29) may be simplified to [42]

$$G_r = \begin{cases} \frac{W^2}{90\lambda_0^2} & W < 0.35\,\lambda_0 \\ \frac{W}{120\lambda_0} - \frac{1}{60\pi^2} & 0.35\lambda_0 < W < 2\lambda_0 \\ \frac{W}{120\lambda_0} & W > 2\lambda_0. \end{cases} \tag{5.30}$$

This is the most widely used formula for computing slot conductance. Eq. (5.30) may be used directly in the MNM model if the segments on the patch wall are small,

say 0.1λ. If the segment width is denoted by Δ_q, then the segment would have a self-conductance of

$$G_{qq} = \frac{\Delta_q^2}{90\lambda_0^2}. \tag{5.31}$$

This simple expression for G_{qq} yields very good results. A more accurate expression may be obtained by considering the height of the slot [79]. For a slot of width W and height t, the slot conductance is

$$\begin{aligned} G_r = \frac{1}{\pi\eta_0}\Bigg\{ & \left[k_0 W\,\mathrm{si}(k_0 W) + \cos k_0 W + \frac{\sin k_0 W}{k_0 W} - 2\right] \\ & \times \left[1 - \frac{(k_0 t)^2}{24}\right] + \frac{(k_0 t)^2}{12} \cdot \left[\frac{1}{3} + \frac{\cos k_0 W}{(k_0 W)^2} - \frac{\sin k_0 W}{(k_0 W)^3}\right]\Bigg\}, \end{aligned} \tag{5.32}$$

where

$$\mathrm{si}(x) = \int_0^x \frac{\sin u}{u} du. \tag{5.33}$$

To use Eq. (5.32) in the MNM, one would simply replace W with the segment width, Δ_q. Since this second expression is simple, accurate, and fast, it was used for the bulk of the MNM simulations described in this thesis. Even so, a more rigorous formulation of the wall self-conductance is available for increased accuracy. In this case, the field distribution within the slot need not be assumed *a priori*. This solution procedure requires that the slot be divided into N infinitesimal segments which are allowed to radiate in the presence of each other. The mutual coupling between the infinitesimal segments is computed, and an accurate field distribution is obtained for the slot by means of a moment method formulation.

$$G_{qq} = Re\left\{\frac{j\Delta}{2\pi k_0 Z_0}\sum_{m=1}^{N}\left[G_{mm} + \sum_{\substack{n=1\\ n\neq m}}^{N}\int_{\Delta}\left(\frac{2}{R^3} + \frac{j2k_0}{R^2}\right)e^{-jk_0R}dx_m\right]\right\}, \tag{5.34}$$

where

$$R = \mid x_m - x_n \mid, \tag{5.35}$$

and G_{mm} is the conductance of the infinitesimal slot of width Δ, obtained from Eq. (5.30) or (5.32). A plot of the slot conductance using these three techniques for a

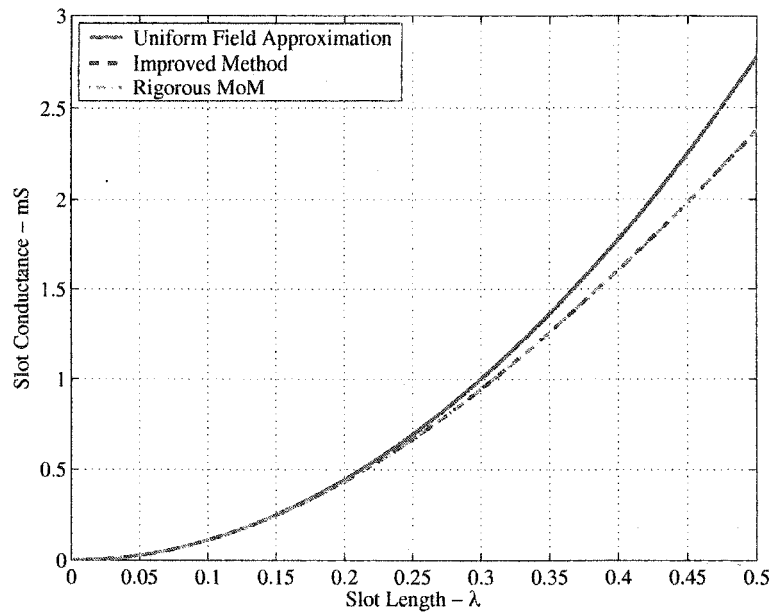

Figure 5.5: Comparison of Slot Conductance Formulations.

range of slot lengths is shown in Fig. 5.5. All three methods agree very well for slots shorter than $\lambda/4$. For longer slots, the simple uniform field approximation formula in Eq. (5.30) diverges, as one would expect, as the field distribution is sinusoidal for long slots. For modelling patch antenna walls with fairly well-known field distributions, there is no advantage to using the MoM technique, especially since it is very time consuming compared to the other two methods discussed. However, the MoM technique would be useful for modelling slots having a very complex field distribution which is not known *a priori*. Based on Fig. 5.5, one could argue that the simple uniform field approximation of Eq. (5.30) would be sufficient for patch wall segments shorter than 0.1λ.

Slot Susceptance

The susceptance of a slot is more difficult to compute than the conductance. This is because the *relative* amplitude and phase of the electric field distribution along the slot is very important in this calculation. In other words, the *shape* and relative

polarity of the field distribution along a patch wall affect the amount of reactive energy stored in the fringing fields, which determines the slot susceptance. Unfortunately, the amplitude and phase of the field distribution are not generally known *a priori*. In fact, our goal is to determine these unknown quantities! However, for simple patch geometries (e.g., rectangular and circular), the relative amplitude and phase of the fields along the walls can be assumed with fair accuracy – good enough to provide an estimate of the wall susceptance. Any error in the wall susceptance estimate will be observed as a frequency error in the solution. It should be noted that once the initial field solution is obtained with MNM using an estimate of the wall susceptance, it is possible to use the results of that simulation as an input to a second MNM computation. This process can continue until the solution converges.

Another error source associated with the slot susceptance calculation has to do with the nature of the dielectric substrate outside the rectangular cavity. This affects the edge susceptance considerably. Up to this point, it was assumed that the dielectric is physically truncated at the patch walls. However, this is rarely the case for printed microstrip antennas, and significant reactive energy is stored in the fringing fields extending away from the edge into the dielectric. Fortunately, this effect is accounted for in the susceptance models discussed in this section for simple patch geometries. A simple edge susceptance model which is based on the open-end capacitance of a microstrip line is

$$B_{qq} = 0.01668 \cdot \Delta L \frac{W}{\lambda_0} \epsilon_{r,eff}, \tag{5.36}$$

where ΔL is the extension of the fringing fields into the substrate given by the standard Hammerstad expression in Appendix B [35]. Improved expressions exist for the effective dielectric constant of the slot. One such equation is also presented in Appendix B. This improved model was used for all MNM simulations described in this thesis. Another means to approximate the edge susceptance is to model the edge as a parallel plate waveguide. This model yields an edge susceptance of

$$B_{qq} = \frac{W\omega}{2} \left\{ \epsilon_0 \sqrt{\epsilon_{r,eff}} - \frac{\epsilon W}{t} \right\}, \tag{5.37}$$

where W is the width of the slot. Fig. 5.6 compares Eqs. (5.36) and (5.37) for a range

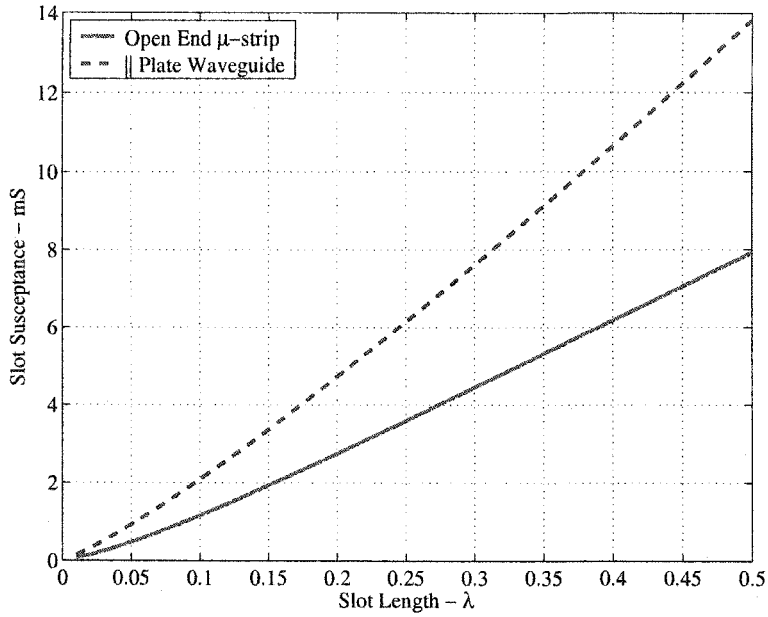

Figure 5.6: Comparison of Slot Susceptance Formulations.

of slot lengths. The two models diverge quickly. It was found in the literature [30] and experimentally that Eq. (5.36) gave the best results for the edge susceptance, so it was used for the MNM simulations described in this thesis.

5.3.3 Patch Wall Field Distributions

Linearly Polarized Patches

For patch antennas operating in the fundamental TM_{100} or TM_{010} modes, the electric field distribution is uniform along the radiating edges. Therefore, those equations presented in Section 5.3.1 which assume a uniform field distribution work well for computing the admittance of the radiating walls. However, the non-radiating walls have sinusoidally varying field distributions. For these walls, the conductance is handled by the mutual coupling network, discussed later in Section 5.3.4. Fortunately, the edge susceptance of the non-radiating walls is zero, as there are equal inductive and capacitive components of susceptance, which cancel.

Circularly Polarized Patches

Now consider the circularly polarized patch antenna which operates in both the TM_{100} and TM_{010} modes. In this case, the field distributions around the patch perimeter are known exactly, and are given by [12]

$$E_{z,(y=0,b)} = \pm\frac{Q}{2ab\epsilon f_0}\left[-(1+j)+(j-1)\cos\frac{\pi x}{a}\right], \tag{5.38}$$

$$E_{z,(x=0,a)} = \pm\frac{Q}{2ab\epsilon f_0}\left[-(1+j)+(j-1)\cos\frac{\pi y}{b}\right], \tag{5.39}$$

where Q is the quality factor of either the TM_{100} or the TM_{010} mode, as both are very nearly equal. $E_{z,(x=0,a)}$ is the field distribution along the walls parallel to the y-axis, while $E_{z,(y=0,b)}$ is the distribution along the walls parallel to the x-axis. Consider Eq. (5.29), which gives the conductance of a slot having an arbitrary field distribution $f(x)$. If we adapt this equation to slot susceptance, we may write

$$B = \frac{B_0 W}{\int_0^W f^2(x)dx}, \tag{5.40}$$

where B_0 is the susceptance of a slot having a uniform field distribution, and the slot has width W. Inspection of Eqs. (5.38) and (5.39) reveals that

$$f(x) = \frac{1}{\sqrt{2}}\sqrt{3+\cos\frac{2\pi x}{W}}. \tag{5.41}$$

Using Eq. (5.41) in Eq. (5.40), one finds that $B = \frac{2}{3}B_0$. So the edge susceptance of a circularly polarized patch wall is 2/3 that of a linearly polarized patch antenna. If this effect is not accounted for, the resonant frequency of the circularly polarized patch antenna will be overestimated.

5.3.4 Segment Mutual Admittance

Now that the self-admittance of a segment has been computed, it is time to address the mutual admittance between segments. Again, consider a single segment q on the

wall of a rectangular patch antenna. The admittance presented to this segment by free space is the self-admittance of the segment Y_{qq}. The self-admittances of each of the Q segments fill the diagonal of the impedance matrix Y_{qr}^{ext} in Eq. (5.27). We now focus on filling in the other entries of the matrix. To determine the external impedance at segment q due to all the adjacent segments on the patch wall, one makes use of the reaction integral between the source and observation segments [2]. If q is the observation segment, and r is the source segment, then the mutual admittance between the segments q and r is

$$Y_{qr}^{ext} = -\frac{1}{V_q V_r} \iint_{S_q'} \vec{M}_q \cdot \vec{H}_{qr}\, dS, \tag{5.42}$$

where S_q' is the surface area of the observation segment q, and V_q and V_r are the voltages appearing across segments q and r, respectively. $\vec{H}_{qr}$ is the magnetic field present at segment q due to radiation from segment r. Appendix C contains a detailed derivation of Y_{qr}^{ext}, but only the result is reproduced here.

$$Y_{qr}^{ext} = \frac{\Delta_q \Delta_r e^{-jk_0 R}}{j2\pi k_0 Z_0} (\hat{n}_q \times \hat{z}) \cdot \vec{G}_{qr} \Big|_{\substack{q=1\ldots Q \\ r=1\ldots Q,}} \tag{5.43}$$

with

$$G_{x,qr} = (\hat{z} \times \hat{n}_r) \cdot \left\{ \hat{x} \left[G_1 + (x_q - x_r)^2 G_2 \right] + \hat{y}\, G_2 (x_q - x_r)(y_q - y_r) \right\}, \tag{5.44}$$

$$G_{y,qr} = (\hat{z} \times \hat{n}_r) \cdot \left\{ \hat{x}\, G_2 (x_q - x_r)(y_q - y_r) + \hat{y} \left[G_1 + (y_q - y_r)^2 G_2 \right] \right\}, \tag{5.45}$$

and

$$G_1 = \frac{-1 - jk_0 R + k_0^2 R^2}{R^3}, \tag{5.46}$$

$$G_2 = \frac{3 + j2k_0 R - k_0^2 R^2}{R^5}, \tag{5.47}$$

$$R = \sqrt{(x_q - x_r)^2 + (y_q - y_r)^2}. \tag{5.48}$$

The total admittance presented to segment q is

$$Y_q^{ext} = Y_{qq}^{ext} + \sum_{\substack{r=1 \\ r \neq q}}^{Q} Y_{qr}^{ext} \Big|_{q=1...Q,} \tag{5.49}$$

where Y_{qq}^{ext} is the segment self-admittance obtained from Eq. (5.28).

5.3.5 Computing Relevant Antenna Parameters

Now that the internal and external factors affecting a patch antenna have been derived, a compact expression for the fields within the patch may be formulated. Consider Eq. (5.23). This equation sets up the basic cavity model for the patch antenna. It was assumed that the current into the patch wall segments q was zero, implying PMC cavity walls. However, in Section 5.3.1, expressions for the edge admittance of an actual radiating patch antenna were derived, and now these results can be incorporated into a more general model. Consider Eq. (5.23), where V_p and I_p are $(P \times 1)$ vectors representing the source voltage and current, respectively, and V_q and I_q are $(Q \times 1)$ vectors representing the observation point voltage and current, respectively. It is assumed that the segments q are located on the perimeter of the patch antenna wall. Expanding the matrix in Eq. (5.23), one obtains

$$V_p = Z_{pp} I_p + Z_{pq} I_q, \tag{5.50}$$

$$V_q = Z_{qp} I_p + Z_{qq} I_q. \tag{5.51}$$

Substituting Eq. (5.27) into Eqs. (5.50) and (5.51), one can derive compact expressions for various important patch antenna parameters.

Electric Field

Using Eq. (5.27) in Eqs. (5.50) and (5.51), one finds that the voltage across any segment on the perimeter of the patch wall is

$$V_q = Z_{qp}\, I_p [\overline{\overline{I}} + Z_{qq}\, Y_{qr}^{ext}]^{-1}. \tag{5.52}$$

The z directed electric field is obtained from

$$E_z = E_q = -V_q/t. \tag{5.53}$$

Input Impedance

The input impedance of the patch antenna is the ratio of the complex voltage developed at the feed (V_p) to the complex amplitude of the driving current source (I_p). Again, Eqs. (5.50) and (5.51) can be manipulated with the help of Eq. (5.27) to obtain

$$Z_p = Z_{pp} - Z_{pq}\left[Z_{qq} + \left[Y_{qr}^{ext}\right]^{-1}\right]^{-1} Z_{qp}. \tag{5.54}$$

Z_p is a $(P \times 1)$ impedance matrix for the patch antenna having multiple feeds. For a single feed, $Z_p = Z_{\text{in}}$, and the scattering parameter s_{11} is defined as

$$s_{11} = \frac{Z_p - Z_0}{Z_p + Z_0}, \tag{5.55}$$

where $Z_0 = 50\Omega$.

5.4 MNM – Multiple Patch Antennas

The theory developed in Section 5.3 applies to a single patch antenna mounted on an infinite ground plane. The only external influence affecting this antenna is the interaction between segments located on the radiating walls of the same patch. However, consider the more general case where N patch antennas are mounted on the same ground plane, operating simultaneously. Of course, the overall radiation pattern, input impedance, and other radiation characteristics will be dependent on the geometry of the patches, and their locations relative to one another. Mutual coupling between the antennas affects the overall radiation characteristics as well as the input impedance of each antenna. In this section, the MNM technique is generalized so that N patches may be simulated. It is assumed for simplicity in this section that the patches are identical, but this need not be the case.

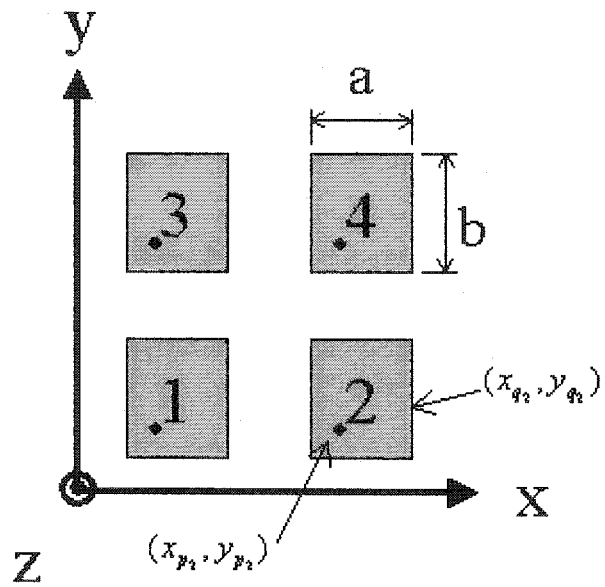

Figure 5.7: An Array of Four Patch Antennas.

5.4.1 Basic Model

Consider the geometry in Fig. 5.7. N patch antennas have radiating walls located at (x_{q_n}, y_{q_n}), and feeds located at (x_{p_n}, y_{p_n}), with $n = 1 \ldots N$. The basic NMN equation in Eq. (5.23) applies to a single patch only. However, it may be rewritten as follows

$$\left[\frac{V_P}{V_Q}\right] = \left[\begin{array}{c|c} Z_{PP} & Z_{PQ} \\ \hline Z_{QP} & Z_{QQ} \end{array}\right] \left[\frac{I_P}{I_Q}\right], \tag{5.56}$$

where V_P is a column vector containing the unknown voltages at all feeds located at (x_{p_n}, y_{p_n}), V_Q and I_Q are column vectors containing the NQ unknown wall perimeter voltages and currents at (x_{q_n}, y_{q_n}). I_P is the column vector of NP current source complex amplitudes, located at (x_{p_n}, y_{p_n}). V_P has size $(NP \times 1)$, while V_Q and I_Q have size $(NQ \times 1)$. Z_{PP} is an $(NP \times NP)$ matrix whose entries are the transimpedances between all of the current source locations. Z_{PQ} and Z_{QP} are matrices (of size $(NP \times NQ)$ and $(NQ \times NP)$, respectively) comprising the transimpedances between the

source points P and the wall segments Q. Z_{QQ} is an $(NQ \times NQ)$ matrix which contains the transimpedances between all the segments on the walls of the patches. The overall Z matrix is symmetric, so only the upper triangular entries need be computed. To account for mutual coupling between the wall segments of the patches, one needs to compute the external admittance matrix as in Eq. (5.27). For the case of multiple patches, the admittance matrix becomes

$$Y_{q_n r_m}^{EXT} = -\frac{I_{q_n r_m}}{V_{q_n}}\bigg|_{\substack{q=1\ldots Q\\ r=1\ldots Q\\ m=1\ldots N\\ n=1\ldots N}}, \tag{5.57}$$

where $I_{q_n r_m}$ is the current into segment q of patch n due to radiation from segment r of patch m, and V_{q_n} is the voltage across segment q of patch n. At this point, a shorthand notation will be adopted,

$$Y_{QR}^{EXT} \equiv Y_{q_n r_m}^{EXT}. \tag{5.58}$$

Y_{QR}^{EXT} is an $(NQ \times NQ)$ matrix.

As an illustrative example, consider two patches ($N = 2$). In this case, Eq. (5.56) is written as

$$\left[\begin{array}{c} V_{p_1} \\ V_{p_2} \\ \hline V_{q_1} \\ V_{q_2} \end{array}\right] = \left[\begin{array}{cc|cc} Z_{p_1p_1} & [0] & Z_{p_1q_1} & [0] \\ [0] & Z_{p_2p_2} & [0] & Z_{p_2q_2} \\ \hline Z_{q_1p_1} & [0] & Z_{q_1q_1} & [0] \\ [0] & Z_{q_2p_2} & [0] & Z_{q_2q_2} \end{array}\right] \left[\begin{array}{c} I_{p_1} \\ I_{p_2} \\ \hline I_{q_1} \\ I_{q_2} \end{array}\right]. \tag{5.59}$$

Zero entries correspond to segments which do not interact. For example, current sources at the feeds p_1 do not directly generate voltages at the feeds p_2 because these sources are associated with two separate patch elements. Therefore, $Z_{p_2p_1} = [0]$. The external admittance matrix for the $N = 2$ case is given as

$$Y_{QR}^{EXT} = \left[\begin{array}{c|c} Y_{q_1q_1}^{ext} & Y_{q_1q_2}^{ext} \\ \hline Y_{q_2q_1}^{ext} & Y_{q_2q_2}^{ext} \end{array}\right], \tag{5.60}$$

where the entries are obtained from

$$Y^{EXT}_{q_n r_m} = -\frac{I_{q_n r_m}}{V_{q_n}}\Bigg|_{\substack{q=1\ldots Q\\ r=1\ldots Q\\ m=1,2\\ n=1,2.}} \tag{5.61}$$

5.4.2 Electric Field

Similar to the case of a single patch, the electric field on the multiple patch walls is denoted as $E_Q = -V_Q/t$ where

$$V_Q = Z_{QP} I_P \left[\overline{\overline{I}} + Z_{QQ} Y^{EXT}_{QQ}\right]^{-1}. \tag{5.62}$$

In solving Eq. (5.62), the resulting field is due to to all patches operating in the presence of each other.

5.4.3 Input Impedance

The impedance matrix for the system of patch antennas is

$$Z_P = Z_{PP} - Z_{PQ}\left[Z_{QQ} + \left[Y^{EXT}_{QQ}\right]^{-1}\right]^{-1} Z_{QP}. \tag{5.63}$$

Z_P in Eq. (5.63) is a $(NP \times NP)$ matrix comprising the self and mutual impedances of the N patch antennas. For a system of two patch antennas, each having a single feed, Z_P has the following form

$$Z_P = \left[\begin{array}{c|c} Z_{11} & Z_{12} \\ \hline Z_{21} & Z_{22} \end{array}\right], \tag{5.64}$$

where Z_{11} and Z_{22} are the *self-impedances* of patches 1 and 2, respectively. Z_{21} and Z_{12} are the *mutual impedance* between patches 1 and 2, and are equal due to reciprocity. Consider that

$$\begin{bmatrix} V_1 \\ V_2 \end{bmatrix} = \begin{bmatrix} Z_{11} & Z_{12} \\ Z_{21} & Z_{22} \end{bmatrix} \begin{bmatrix} I_1 \\ I_2 \end{bmatrix}, \tag{5.65}$$

where V_n and I_n are the voltages and currents appearing at the patch feeds. From Eq. (5.65), one finds that the input impedances of the antennas are

$$Z_{\text{in},1} = Z_{11} + Z_{12}\frac{I_2}{I_1} \tag{5.66}$$

$$Z_{\text{in},2} = Z_{22} + Z_{21}\frac{I_1}{I_2}. \tag{5.67}$$

If the patches are located very far from each other, mutual coupling effects would be minimal ($Z_{21} = Z_{12} \approx 0$), and the input impedances of the patches would be equal to the self-impedances Z_{11} and Z_{22}. One can also form a scattering matrix S_P for the system of N antennas, given as

$$S_P = [Z_P + \overline{\overline{I}}Z_0]^{-1}[Z_P - \overline{\overline{I}}Z_0], \tag{5.68}$$

where $Z_0 = 50\Omega$. For a two element array,

$$S_P = \left[\begin{array}{c|c} s_{11} & s_{12} \\ \hline s_{21} & s_{22} \end{array}\right]. \tag{5.69}$$

The scattering parameters are often expressed in dB, where s_{mn} (dB) $= 20\log|s_{mn}|$. In dB form, one refers to s_{11} and s_{22} as the *return loss* of the antennas. The return loss characterizes the impedance match to 50Ω. In dB form, s_{21} and s_{12} are measures of the *mutual coupling* between the patches. For patches separated by a large distance, s_{12} and s_{21} approach $-\infty$ dB, while for very closely spaced patches, the mutual coupling may be as high as -3 dB.

Probe Impedance

All microstrip patch antennas described in this thesis utilize a coaxial probe feed. This is a simple feed arrangement whereby a metallic probe extends through the ground plane to the patch element. The probe feed can be thought of as an electric current filament. The probe is inherently inductive, and also adds a few ohms of resistance to the input impedance of patch antennas. To model this effect, we draw

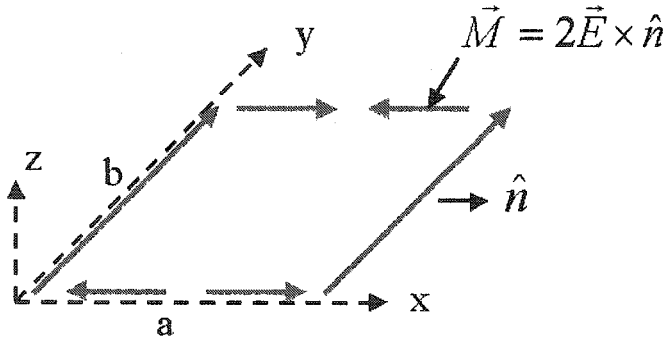

Figure 5.8: Equivalent Problem for Rectangular Patch Antenna.

upon previous work in this area [1]

$$Z_p^{\text{probe}} = \frac{60\pi}{\sqrt{\epsilon_r}} \frac{\tan^2(k_0 t/2)}{k_0 t/2} + j\frac{120}{\sqrt{\epsilon_r}} \tan\frac{k_0 t}{2} \ln\left(\frac{1.125}{2k_0 d_p}\right), \tag{5.70}$$

where d_p is the diameter of the probe. To include this effect in the input impedance calculation, we simply modify Z_P as follows

$$\breve{Z}_P = Z_P + \text{Diag}[Z_p^{\text{probe}}], \tag{5.71}$$

where Z_p^{probe} is a column vector of probe impedances for each patch in the array, and $\text{Diag}[Z_p^{\text{probe}}]$ is a diagonal matrix having the vector Z_p^{probe} as its diagonal.

5.5 Far-Field Radiation Patterns

Antennas act as transducers between guided wave transmission systems and unbounded free space. The antenna converts the guided electromagnetic fields to a field configuration which can launch efficiently into free space. Efficient antennas enable this transition with minimal loss to due reflections from the interface between the transmission line and free space. The field configuration at the antenna aperture determines how the energy will be spatially distributed as it radiates. This spatial distribution of energy is called the radiation pattern of the antenna, and is of great

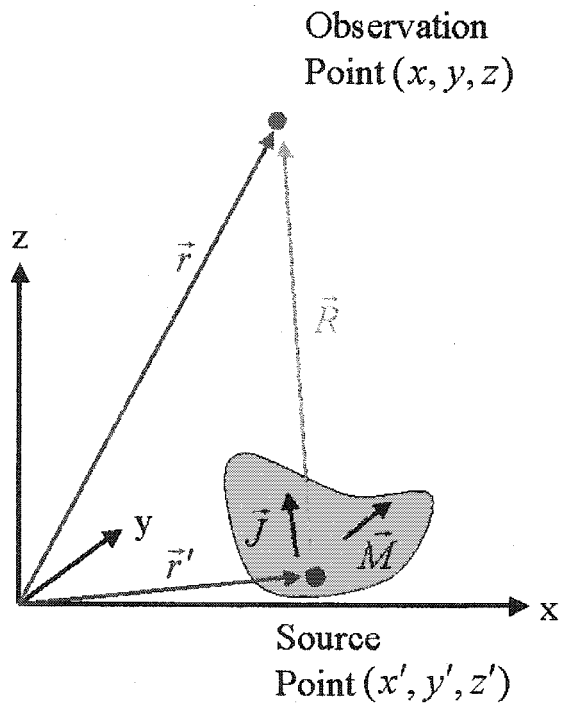

Figure 5.9: Coordinate System for Near-Field Calculations.

importance to antenna designers. This section describes how to compute a far-field radiation pattern, given the geometrical configuration of electric or magnetic currents at the aperture of an antenna. In this section, the antenna will be treated as a transmitting antenna. Due to reciprocity, the receive radiation pattern of an antenna is identical to the transmit radiation pattern [2]. Earlier, image theory was used to transform the inhomogeneous problem in Fig. 5.1 to an equivalent problem in free space (Fig. 5.2). Next, it will be shown that the Equivalence Principle allows one to replace the problem shown in Fig. 5.2 with the equivalent problem shown in Fig. 5.8.

The tangential electric and magnetic fields are completely specified on the closed surface S_1 and S_2 in Fig. 5.2. Therefore, the Equivalence Principle allows the sources to be set to zero, and the tangential electric and magnetic fields are permitted to radiate in free space. The electric field is replaced by an equivalent magnetic current

source $\vec{M}$. This magnetic current source is given by

$$\vec{M} = 2\,\vec{E} \times \hat{n}, \tag{5.72}$$

where $\hat{n}$ is an outward looking unit vector normal to the patch wall. This results in a magnetic current sheet $\vec{M}$ radiating into free space, giving rise to a radiation pattern which is a function of the amplitude and phase distribution of $\vec{M}$. Using this equivalent model for the patch antenna, the radiation pattern is computed from well documented techniques [2]. In the most general case, consider an arbitrary free space distribution of electric current $\vec{J}$ and magnetic current $\vec{M}$ sources, located at $\vec{r}'$. In the Cartesian coordinate system shown in Fig. 5.9, these sources are expressed as

$$\vec{J}(x', y', z') = J_x\hat{x} + J_y\hat{y} + J_z\hat{z}, \tag{5.73}$$

$$\vec{M}(x', y', z') = M_x\hat{x} + M_y\hat{y} + M_z\hat{z}. \tag{5.74}$$

Assume that there is no electric current on the antenna aperture ($\vec{J} = 0$). This is approximately true on the radiating walls of a microstrip patch antenna. We seek the electric field at any observation point in space ($\vec{r}$) due to the magnetic current $\vec{M}$. This field is expressed as

$$\vec{E}(x, y, z) = -\frac{1}{4\pi}\nabla \times \iiint_{V'} \vec{M}\frac{e^{-jkR}}{R}\,dV, \tag{5.75}$$

where R is the distance from the source point (x', y', z') to the observation point (x, y, z), given by

$$R = |\vec{r} - \vec{r}'| = \sqrt{(x - x')^2 + (y - y')^2 + (z - z')^2}, \tag{5.76}$$

and the integral in Eq. (5.75) is taken over the volume of the source, V'. This general formulation is exact, and will yield accurate field solutions in the near and far-field regions of an antenna. However, if the observation point happens to be far from the source, a simplifying assumption can be made which makes the integration in

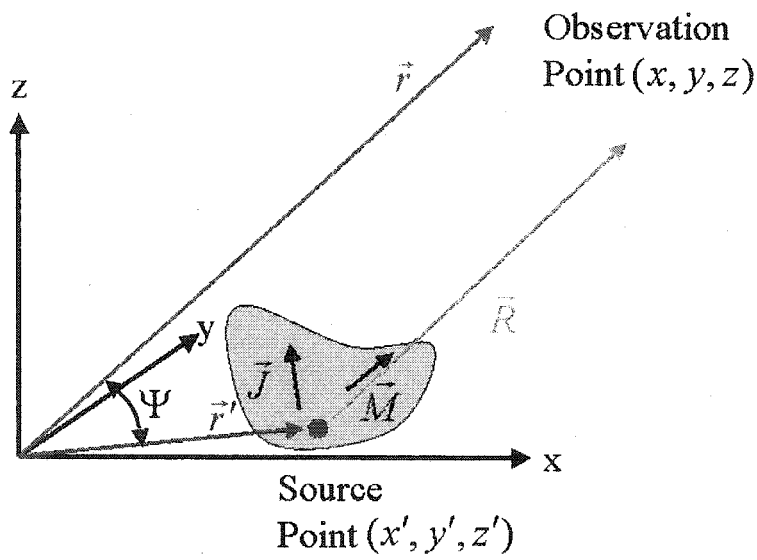

Figure 5.10: Coordinate System for Far-Field Calculations.

Eq. (5.75) much more tractable. Consider the geometry in Fig. 5.10. Here, $\vec{R}$ and $\vec{r}'$ are nearly parallel, so that $R \approx r - r' \cos\psi$. This approximate expression is used in place of Eq. (5.76) for phase variations, such as in the exponent of Eq. (5.75). For amplitude variations, we can use $R \approx r$. This approximation for R holds if the observation point is at least $2D^2/\lambda_0$ meters from the source, where D is the largest linear dimension of the source. For patch antennas, we will further assume that the magnetic current source is limited to a current sheet around the perimeter of the patch element. The current sheet has no variation in the z direction. Also, since $t << \lambda_0$, the current sheet can be collapsed to a line current around the perimeter of the patch, and placed at $z' = 0$. This concept is illustrated in Fig. 5.8. With these approximations in effect, the electric field radiated by the patch antenna $\vec{E} = E_\theta\hat{\theta} + E_\phi\hat{\phi}$ becomes

$$E_\theta = -\frac{jkte^{-jkr}}{4\pi r} \oint_C \left[-M_x \sin\phi + M_y \cos\phi\right] e^{jkr'\cos\psi} dl', \tag{5.77}$$

$$E_\phi = \frac{jkte^{-jkr}}{4\pi r} \oint_C \left[M_x \cos\theta\cos\phi + M_y \cos\theta\sin\phi\right] e^{jkr'\cos\psi} dl', \tag{5.78}$$

where

$$r' \cos\psi = x' \sin\theta \cos\phi + y' \sin\theta \sin\phi. \tag{5.79}$$

These integrals are readily evaluated by Simpson's Rule or other suitable methods. M_x and M_y are obtained from the MNM as

$$M_x = 2\,\frac{V_Q}{t}\,\hat{x}\cdot(\hat{n}\times\hat{z})\,, \tag{5.80}$$

$$M_y = 2\,\frac{V_Q}{t}\,\hat{y}\cdot(\hat{n}\times\hat{z})\,. \tag{5.81}$$

In the far-field, the magnetic field may be obtained from

$$\vec{H} = \hat{r}\times\eta_0\vec{E}. \tag{5.82}$$

5.5.1 Axial Ratio

Once the far-field electric and magnetic fields are computed with Eqs. (5.77), (5.78), and (5.82), then other important parameters can be determined. For example, the axial ratio in dB is defined as

$$\mathrm{AR}(\phi,\theta) = \left|20\log\frac{|E_\phi(\phi,\theta)|}{|E_\theta(\phi,\theta)|}\right|. \tag{5.83}$$

Low axial ratios indicate that the orthogonally polarized field components are nearly equal in magnitude. However, the axial ratio gives no information about the phase of these vectors, which must be offset by 90° to achieve circular polarization. Nonetheless, the axial ratio is a popular metric for judging the purity of circularly polarized signals.

5.5.2 Gain

Consider a transmitting antenna giving rise to $\vec{E} = E_\theta\hat{\theta} + E_\phi\hat{\phi}$ in the far-field region of the antenna. A test antenna located in the far-field region is used to sample $\vec{E}$ in order to determine the angular radiation pattern of the transmit antenna. The

normalized field response of a RHCP test antenna is

$$F(\theta,\phi) = \left[\frac{E_\theta\hat{\theta} + E_\phi\hat{\phi}}{\max\{E\}}\right] \cdot \left[\hat{\theta} + j\hat{\phi}\right]. \tag{5.84}$$

The gain of the transmitting antenna is obtained directly from

$$G(\theta,\phi) = \eta\,\frac{4\pi|F(\theta,\phi)|^2}{\int_0^{2\pi}\int_0^{\pi}|F(\theta,\phi)|^2\sin\theta d\theta d\phi}, \tag{5.85}$$

where η is the efficiency of the antenna. The gain of the antenna is often expressed in dB as 10 log $G(\theta,\phi)$.

5.5.3 Efficiency

The efficiency of an antenna η is the ratio of the power radiated by the antenna to the power input to the antenna,

$$\eta = \frac{P_{rad}}{P_{in}}. \tag{5.86}$$

The radiated power is found from

$$\frac{1}{2}\sum_{q=1}^{Q}\mathrm{Re}\{V_q I_q^*\}, \tag{5.87}$$

while the input power is

$$\frac{1}{2}\mathrm{Re}\{V_p I_p^*\}, \tag{5.88}$$

leading to an efficiency of

$$\eta = \frac{\sum_{q=1}^{Q}\mathrm{Re}\{V_q I_q^*\}}{\mathrm{Re}\{V_p I_p^*\}}. \tag{5.89}$$

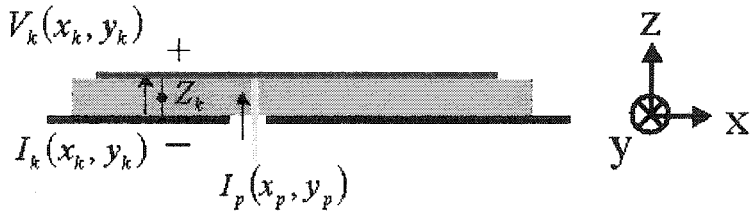

Figure 5.11: Patch Antenna with Lumped Loads Embedded in Substrate.

5.6 Inhomogeneous Substrates

The MNM technique derived in Sections 5.3 and 5.4 is a compact, efficient means of computing input impedance and radiation patterns of patch antennas. This formulation made use of the Green's function in Eq. (5.7), which applicable to rectangular patches on a homogeneous substrate. However, in Chapter 6, we introduce a new type of patch antenna having lumped loads (PIN diodes) embedded within the substrate. It is very important to accurately model this modified antenna, especially the mutual coupling between multiple patches. In order to model a patch antenna with an inhomogeneous substrate, we need to modify the MNM technique to account for the presence of these lumped loads. Consider a single patch antenna shown in Fig. 5.11 having K lumped loads located at (x_k, y_k). The loads have arbitrary complex impedances of Z_k. Each load will draw current $-I_k$ and have a voltage drop V_k. The minus sign on I_k accounts for the fact that the current flowing into the load is opposite to the definition used in Eq. (5.15). The patch in Fig. 5.11 has P current sources located at (x_p, y_p). Now suppose we replace each lumped impedance with an ideal current source having complex amplitude I_k [53]. It is possible to compute the complex amplitudes of these current sources I_k required to establish the same field distribution under the patch as that existing with only the lumped loads present. The complex amplitudes of the current sources are determined by enforcing the boundary conditions at the locations of the lumped loads, namely

1. The voltage to current ratio at the locations of the current sources must be equal to Z_k, and

2. The voltage present at the locations of the current sources is due to the superposition of *all* current sources under the patch.

Mathematically, these conditions are expressed as

$$1. \quad V_k = -I_k \, Z_k \big|_{k=1\ldots K,} \tag{5.90}$$

$$2. \quad V_k = \sum_{m=1}^{K} I_m \, Z_{km} + \sum_{p=1}^{P} I_p \, Z_{kp}. \tag{5.91}$$

Z_{ij} in Eqs. (5.90) and (5.91) is the standard cavity model transimpedance from Eq. (5.22), reproduced here for completeness.

$$Z_{ij} = -jtk_0 \sum_{m=0}^{\infty} \sum_{n=0}^{\infty} \frac{\Psi_{mn}(x_i, y_i)\Psi_{mn}(x_j, y_j)}{k_{eff}^2 - k_{mn}^2} G_{mn}(d_{x_j}, d_{y_j}). \tag{5.92}$$

Eqs. (5.90) and (5.91) may be solved simultaneously to obtain an expression for the required source currents

$$I_k = -\left[[Z_{kk} + \mathrm{Diag}[Z_k]]^{-1} \, Z_{kp} \right] I_p, \tag{5.93}$$

where the operation Diag $[A]$ creates a diagonal matrix with the column vector A along its diagonal. Alternately, Eq. (5.93) may be used in conjunction with Eq. (5.23) to obtain a compact expression for the voltage at any location under the patch due to source currents I_p.

$$V_q = \left[Z_{qp} - Z_{qk} \, [Z_{kk} + \mathrm{Diag}[Z_k]]^{-1} \, Z_{kp} \right] I_p \tag{5.94}$$

Using a change in notation consistent with Eq. (5.92), Eq. (5.94) may be written simply as

$$V_i = \tilde{Z}_{ij} I_j, \tag{5.95}$$

with

$$\tilde{Z}_{ij} = Z_{ij} - Z_{jk}\left[Z_{kk} + \mathrm{Diag}[Z_k]\right]^{-1} Z_{ki}, \tag{5.96}$$

where Z_{ij} is again obtained from Eq. (5.92). The general MNM formulation may now be modified to account for the presence of lumped loads by substituting the new kernel $\tilde{Z}_{ij}$ in place of Z_{ij}. Note that if $Z_k \to \infty$, then $\tilde{Z}_{ij} \to Z_{ij}$, as expected. For a single patch Eq. (5.23) becomes

$$\begin{bmatrix} V_p \\ V_q \end{bmatrix} = \begin{bmatrix} \tilde{Z}_{pp} & \tilde{Z}_{pq} \\ \tilde{Z}_{qp} & \tilde{Z}_{qq} \end{bmatrix} \begin{bmatrix} I_p \\ I_q \end{bmatrix}, \tag{5.97}$$

while for multiple patch antennas Eq. (5.56) becomes

$$\left[\begin{array}{c} V_P \\ \hline V_Q \end{array}\right] = \left[\begin{array}{c|c} \tilde{Z}_{PP} & \tilde{Z}_{PQ} \\ \hline \tilde{Z}_{QP} & \tilde{Z}_{QQ} \end{array}\right] \left[\begin{array}{c} I_P \\ \hline I_Q \end{array}\right]. \tag{5.98}$$

To account for external effects, Y_{qr}^{ext} and Y_{QR}^{EXT} are computed as usual from Eqs. (5.27) and (5.61), respectively. For multiple patches, the electric fields and input impedance follow from Eqs. (5.62) and (5.63) as

$$V_Q = \tilde{Z}_{QP} I_P \left[\overline{\overline{I}} + \tilde{Z}_{QQ} Y_{QR}^{EXT}\right]^{-1} \tag{5.99}$$

$$Z_P = \tilde{Z}_{PP} - \tilde{Z}_{PQ}\left[\tilde{Z}_{QQ} + \left[Y_{QR}^{EXT}\right]^{-1}\right]^{-1} \tilde{Z}_{QP}. \tag{5.100}$$

5.7 Canonical Problems

This section presents simulation results intended to validate the MNM computer code. Two rectangular patch antenna problems are solved. The first problem is an analysis of a simple rectangular patch antenna, designed for the L1 GPS frequency of 1,575.42 MHz. The second problem extends the first by arranging four of the single patches in a 2 × 2 square array. The input impedance and radiation pattern are computed for both cases. In the case of the single rectangular patch, the simulated

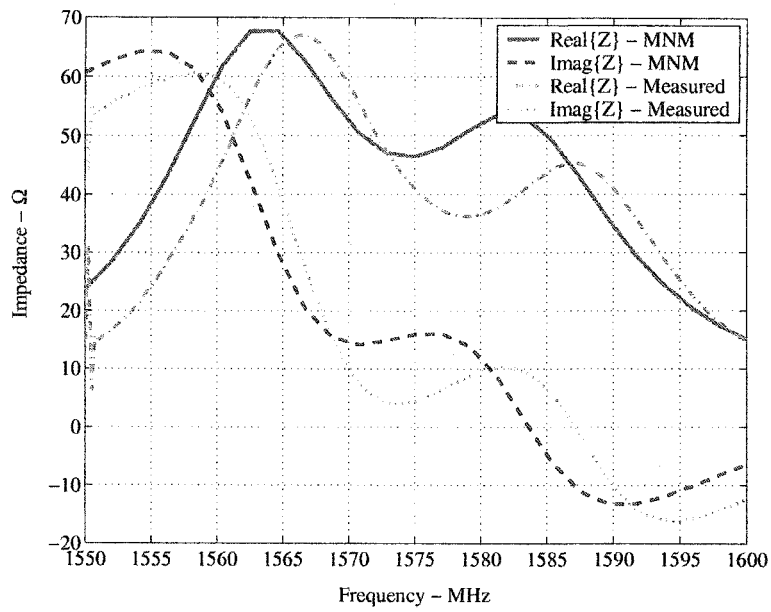

Figure 5.12: Input Impedance of Rectangular Patch Antenna.

results are compared to measurements taken from an actual prototype patch antenna.

5.7.1 Rectangular Patch Antenna

A rectangular patch antenna was simulated with a computer code employing the MNM technique outlined in this chapter. The physical characteristics of this antenna are listed in Table 5.1, and the applicable geometry is shown in Fig. 5.1. The feed is a coaxial probe, and the antenna is assumed to be mounted on an infinite ground plane. The input impedance of this patch antenna obtained with the MNM code is plotted in Fig. 5.12 over a 50 MHz bandwidth. A near 50Ω match was achieved at the GPS L1 design frequency of 1,575.42 MHz. The input return loss is -15.5 dB at a phase angle of 92.7°. This represents a good match to 50Ω, having a VSWR of only 1.4:1. Furthermore, the slightly inductive reactance at L1 can be tuned out with a series capacitor. The measured input impedance of a prototype patch antenna is also plotted in Fig. 5.12. This antenna was built to the specifications listed in

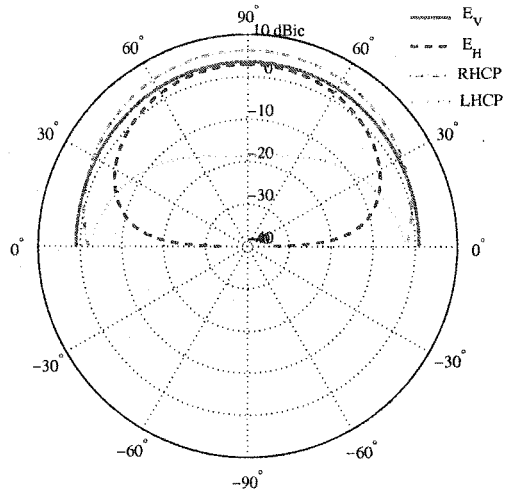

Figure 5.13: Radiation Pattern of Rectangular Patch Antenna.

ϵ_r	tan δ	t (mm)	a (cm)	b (cm)	feed (x_p, y_p) (cm)
4.50	0.002	1.52	4.39	4.45	(1.67,1.69)

Table 5.1: Rectangular Patch Antenna Physical Characteristics.

Table 5.1. The agreement is very good, as the frequency error is on the order of only 0.3%. In Fig. 5.13, the simulated elevation radiation pattern of the patch is plotted at the design frequency. The gain of the antenna is +6 dBic, and the axial ratio is 0.58 dB. As expected, the response of the antenna is down 3 dB at the zenith for the two linearly polarized components. The LHCP polarization component is down 24 dB from the RHCP component at the zenith, indicating good polarization purity. As with all antennas mounted on metallic ground planes, the axial ratio suffers near 0° elevation angle.

5.7.2 Patch Antenna Array

Four patch antennas, each having the characteristics listed in Table 5.1, were placed in a 2 × 2 rectangular array and spaced $\lambda_0/2$ apart, as suggested by the geometry in Fig. 5.7. The antennas were excited with equal currents, so as to achieve

a high gain antenna system having a pencil beam directed toward the zenith. The scattering matrix for the antenna system reported by the MNM code is

$$S = \begin{bmatrix} -15.3\angle 89.6^\circ & -25.6\angle 83.9^\circ & -24.0\angle -97.3^\circ & -29.6\angle -46.1^\circ \\ -25.6\angle 83.9^\circ & -15.3\angle 89.4^\circ & -29.7\angle -46.2^\circ & -24.0\angle -97.3^\circ \\ -24.0\angle -97.3^\circ & -29.7\angle -46.2^\circ & -15.4\angle 89.9^\circ & -25.5\angle 84.7^\circ \\ -29.6\angle -46.1^\circ & -24.0\angle -97.3^\circ & -25.5\angle 84.7^\circ & -15.3\angle 89.7^\circ \end{bmatrix} (\text{dB}, \angle^\circ). \tag{5.101}$$

The input return loss to each antenna is roughly -15.4 dB, similar to the case of the single patch. The mutual coupling between each of the patches is only -24.0 dB, maximum. This low mutual coupling leaves the input impedance of each element undisturbed. The elevation radiation pattern of this array is shown in Fig. 5.14. The gain of the antenna system is found to be 12 dB, and the axial ratio is 1.8 dB. Since the mutual coupling is so low between the patch elements, the radiation pattern is very clean with no perturbations. In reality, the pattern will not be quite so clean. Edge diffraction from a finite ground plane will cause ripple in the main beam. In addition, some energy will be diffracted below the ground plane, reducing the gain and producing side and back lobes. Finally, the MNM technique described in this chapter does not account for surface waves in the substrate. Surface waves will increase the mutual coupling between the patches and also diffract around the edges of a finite ground plane, causing ripple in the radiation pattern and adversely affecting the input impedance of the patches. The main effect of the finite ground plane and surface wave diffraction would be observed in the lower hemisphere, which is not modelled by MNM. Fortunately, the effects are second-order in the upper hemisphere. For an actual array, the main beam will retain the shape shown in Fig. 5.14, except that some ripple and increased radiation near 0° elevation will appear. The gain will also drop slightly, due to the diffraction of power to the lower hemisphere. Input impedance and axial ratio will degrade, primarily due to surface waves.

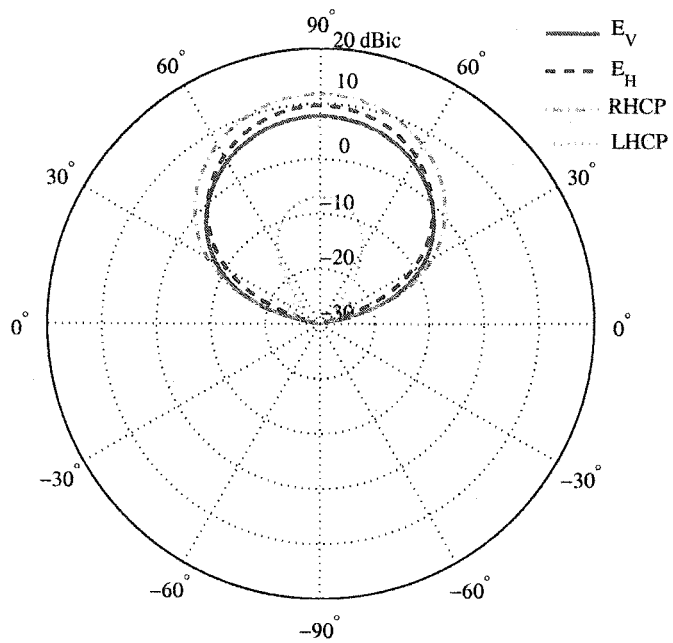

Figure 5.14: Radiation Pattern of 2 × 2 Array of Rectangular Patch Antennas.

5.8 Summary

This chapter described an efficient means for modelling rectangular microstrip patch antennas having inhomogeneous substrates. The multiport network method (MNM) allows one to compute radiation patterns and input impedance for single or multiple rectangular patches, including mutual coupling effects. An accurate model for closely spaced patch antennas is required for modelling the dual-patch reconfigurable antenna (DPRA), to be introduced in the next chapter. Since the DPRA requires that two patch antennas be stacked on top of each other, the mutual coupling is naturally very high for this case. In order to defeat this strong interaction, PIN diodes are used to inactivate one of the patches, allowing the other to operate normally, as if the undesired patch were not present. The use of PIN diodes within the substrate in this manner required an improved MNM model, designed to handle these lumped loads. The MNM technique will be used in Chapter 6 to optimize the DPRA for rejecting interference sources located at negative elevation angles.

Chapter 6

The Dual-Patch Reconfigurable Anti-Jam Antenna

This chapter introduces a novel GPS anti-jam antenna known as the dual-patch reconfigurable antenna (DPRA). The chapter opens by presenting the concept of using a half-wavelength square patch antenna as an anti-jam GPS antenna. The need for a dual-patch antenna is explained, and the interaction between closely spaced patch elements is discussed. A technique for isolating the closely spaced elements from one another is suggested. Namely, PIN diodes embedded within the dielectric substrate can be used to selectively disable a patch element, while enabling the other element. Simulations of a dual-patch antenna are performed with the improved MNM technique developed in Chapter 5. Specifically, a modified kernel is used in place of the standard cavity model kernel to account for the presence of lumped loads within the dielectric substrate. A prototype DPRA was constructed and tested in flight. A description of the flight test, along with selected results are presented. Finally, benefits of the DPRA to airborne users of WAAS are quantified with an analysis tool known as MAAST.

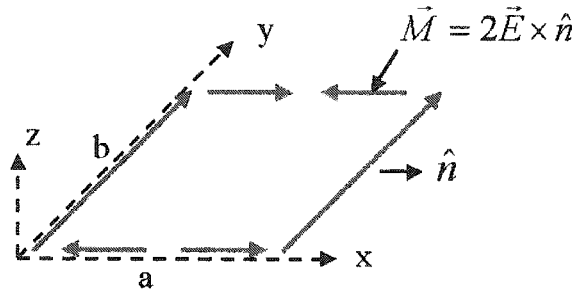

Figure 6.1: Simplified Model of a Patch Antenna.

6.1 Single-Element Anti-Jam Antenna

One way to reject ground-based interference from an aircraft is to focus more of the antenna's sensitivity toward the upper hemisphere where the GPS satellites are, and less sensitivity toward the ground, where the interference is likely to be. By definition this involves an increase in antenna directivity. One can design a single element patch antenna to have high gain in the upper hemisphere, and significantly reduced sensitivity in the lower hemisphere below the aircraft. To see how this works, consider the simple model of a patch antenna shown in Fig. 6.1. This model was put forth in Section 5.2. The antenna is operating in the TM_{100} mode, with the radiating edges parallel to the y axis. The antenna is linearly polarized. Consider what happens when the length of the patch a is made very small. This is accomplished by using a high permittivity dielectric for the patch substrate. In this case, the radiating edges will be located very close to one another, and will radiate in phase. Contributions from the non-radiating edges will be very small. In the limit as $a \rightarrow 0$, the patch antenna can be approximated by a single slot in an infinite ground plane. The elevation radiation pattern of a small patch antenna on an infinite ground plane is shown in Fig. 6.2. In the E-plane ($x - z$ plane), the pattern is nearly uniform, while in the H-plane ($y - z$ plane), there is a null at the horizon. This null arises because at the horizon in the H-plane, we are seeing the radiating magnetic current edge on. Neither electric nor magnetic currents radiate along their axes in the far-field. The strong radiation along the horizon in the E-plane gives rise to significant radiation below

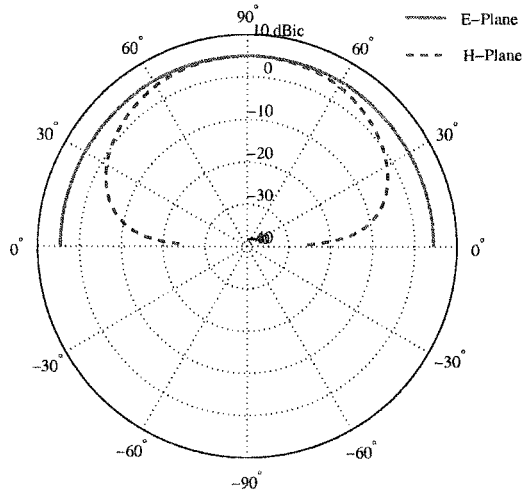

Figure 6.2: Radiation Pattern of a Small Patch Antenna on an Infinite Ground Plane.

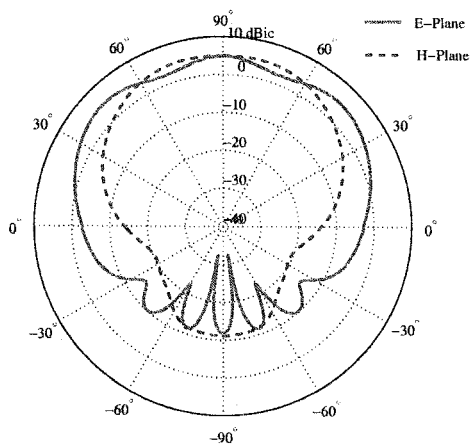

Figure 6.3: Radiation Pattern of a Small Patch Antenna on a 3λ Ground Plane.

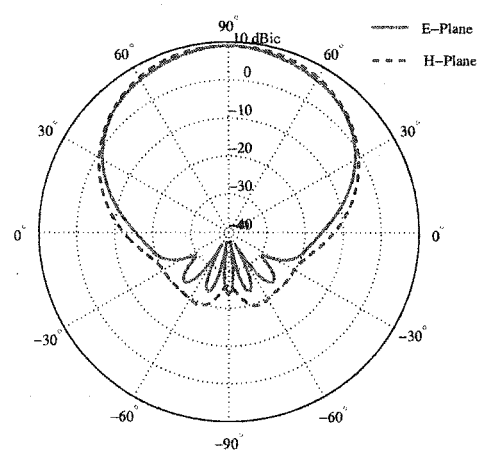

Figure 6.4: Radiation Pattern of a $\lambda/2$ Square Patch Antenna on a 3λ Ground Plane.

the antenna if mounted on a finite-sized ground plane. Fig. 6.3 shows the radiation pattern of a small patch antenna mounted on a 3λ square ground plane. Notice the significant backlobe radiation. This condition translates directly to ground-based RFI susceptibility for airborne GPS antennas. Now consider the effect of increasing the size of the patch antenna. This is accomplished of course be decreasing the permittivity

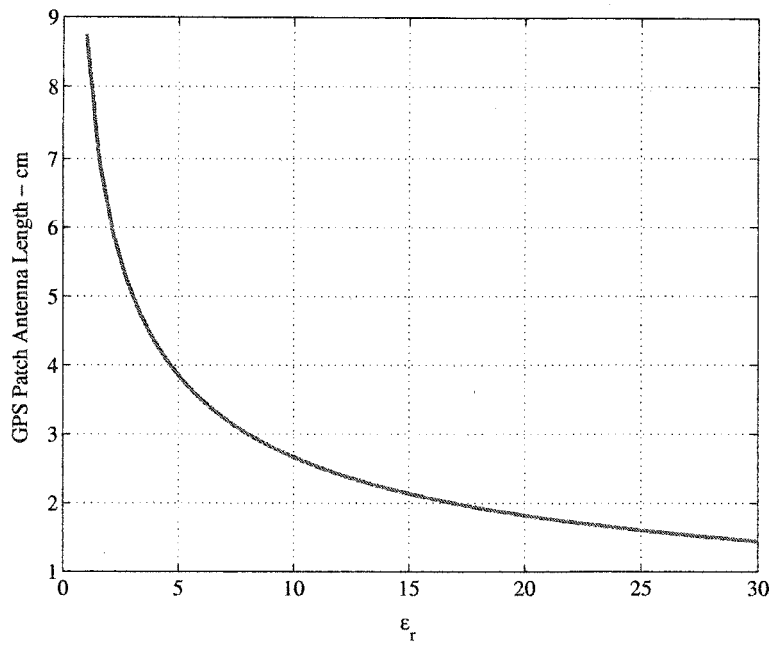

Figure 6.5: Patch Antenna Substrate Permittivity vs. Length.

of the substrate. Fig. 6.5 shows the tradeoff between substrate permittivity and antenna size. If air is used as a dielectric, the antenna is slightly less than $\lambda/2$ long. The radiating edges in this case are effectively located approximately $\lambda/2$ apart. This has an interesting effect. Signals arriving from near the horizon in the E-plane will arrive at the radiating edges 180° out of phase. Fortunately, this is exactly the effect we wish to achieve. Signals from the upper hemisphere still add in phase at the radiating edges, but signals at or below the horizon will be severely attenuated by the antenna. Shown in Fig. 6.4 is the elevation radiation pattern of a patch antenna using an air substrate mounted on a 3λ square ground plane. Backlobe radiation is almost non-existent, and the antenna has a high gain toward the zenith. One problem with this design is that low elevation satellites will also be attenuated by the antenna.

6.2 The Need for a Dual-Element Antenna

Both the small and $\lambda/2$ patch antennas discussed in Section 6.1 have advantages and disadvantages. The small, high permittivity substrate patch antenna has excellent GPS satellite coverage, but is susceptible to interference which may be present at negative elevation angles. The $\lambda/2$ air dielectric patch rejects interference from negative elevation angles, but does not track low elevation satellites. Recall that our goal is to develop a specialized interference resistant antenna which ideally has a uniform radiation pattern for elevation angles greater than 5°, and no response below. Both the small and $\lambda/2$ patches individually possess these characteristics in part. As a compromise, the two antennas could be combined into a single package and steps taken so that they operate independently from each other.

6.3 Concept of the DPRA

As suggested in the previous section, the DPRA concept involves using stacked patch antennas employing a wide-angle microstrip patch element for use when no interference is present, and an anti-jam patch element for attenuating ground-based interference. The antenna concept, shown in Fig. 6.14, uses a single coaxial probe feed. PIN diodes are embedded in the substrates of both patch elements. Since the upper patch element has low zenith gain (+5 dBic) and a broad radiation pattern, it is able to acquire and track GPS satellites down to the horizon. However, this patch is susceptible to RFI arriving from negative elevation angles. If GPS navigation is threatened by a jammer, the user may switch to the RFI resistant patch antenna which is located beneath the upper patch. This is a half-wavelength nearly-square patch element which has high gain (+9 dBic) toward the zenith and low gain (-20 dBic) toward the horizon. The anti-jam mode enhances signals from satellites at high elevation angles, while rejecting interference from negative elevation angles. Since the anti-jam patch cannot acquire and track satellites below 5° elevation, it should not generally be used when no RFI is present, especially for high-precision applications. The wide-angle mode should be used in this case.

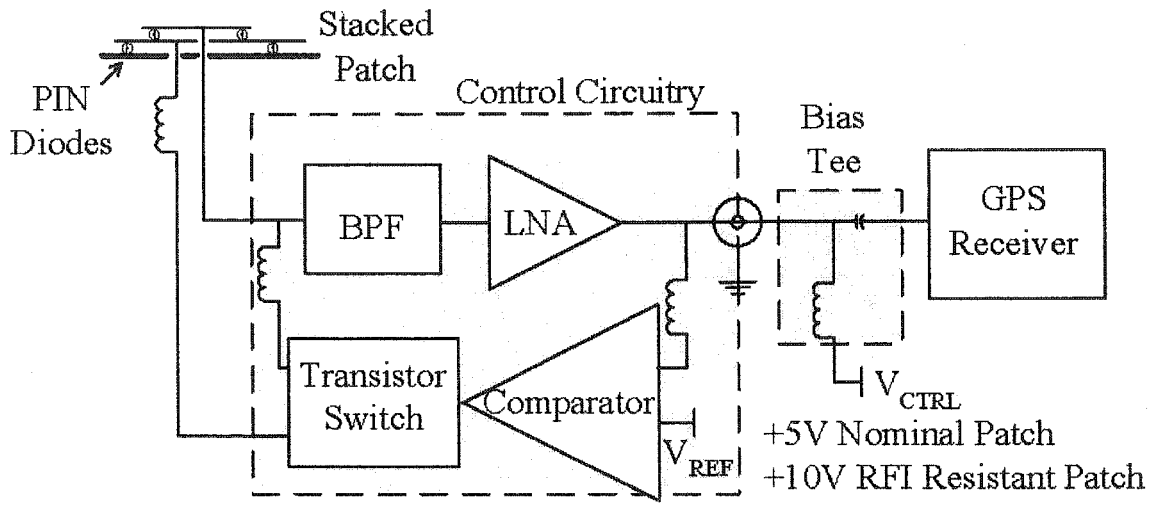

Figure 6.6: Block Diagram of the DPRA.

Switching between the two antenna elements is accomplished by varying the DC voltage on the center conductor of the coaxial cable feedline connecting the antenna to the GPS receiver. PIN diodes embedded in the patch elements are used to select the desired patch, while disabling the undesired patch. The PIN diodes effectively isolate the two patches from each other, so that their radiation patterns are independent. Switching may be performed manually, or automatically by a smart GPS receiver that can detect the presence of RFI and respond accordingly. The only external connection to the antenna is the coaxial RF feedline, which carries the received GPS RF signals, as well as a DC voltage that serves to power the LNA and to switch between the two patch antennas. A system level block diagram of the antenna is shown in Fig. 6.6. A nominal control voltage of +5 volts DC (+3 volts minimum) powers the LNA and selects the wide-angle mode. In this case, the PIN diodes within the upper patch substrate are reverse biased so that they appear as open circuits, while the PIN diodes in the lower patch substrate are forward biased, appearing as very low-valued resistors. This operation has the effect of shorting the lower patch to

ground, while allowing the upper patch to function normally. The wide-angle mode radiation pattern is identical to that of a standard aviation microstrip patch antenna. This means that the dual-patch antenna can replace an aviation patch antenna and remain transparent to the user. If the control voltage is raised to +10 volts DC (+7.5 volts minimum), the anti-jam mode is activated. Here, the PIN diode bias voltages are reversed with respect to the wide-angle mode, and only the lower patch is allowed to operate. The LNA is active in both modes, of course. The bias tee shown in Fig. 6.6 provides for manual control of the antenna. In the simplest case, a variable power supply can be used to provide the desired voltage to the antenna. However, a pilot would likely desire a fully automated system whereby a smart GPS receiver decides that RFI is present, and switches to the anti-jam mode automatically. This level of sophistication may be achieved fairly easily by making a simple firmware change in the GPS receiver, and performing a minor power supply modification. For example, the receiver could provide +5 volts DC to the antenna if the receiver's AGC voltage were normal. If CW or broadband interference alters the AGC voltage, the receiver could provide the required +10 volt DC signal to the antenna to select the anti-jam mode.

6.4 PIN Diodes

In Section 6.3, the need for a technique to electrically isolate stacked patch antennas was emphasized. PIN diodes embedded within the patch antenna substrate were proposed as RF switching devices. Before discussing the detailed design and analysis procedure for the DPRA, a short background on PIN diodes is necessary. A PIN diode is very similar to a garden variety PN junction diode, except that between the highly doped semiconductor junction materials is a layer of intrinsic silicon material which is highly resistive. PIN diode applications include RF switches, attenuators, modulators, and phase shifters. The PIN diode is a very useful RF component because it behaves like a current controlled impedance. In the forward biased condition, charge is injected into the I-region, effectively reducing the RF resistance of the I-region to a value denoted as R_s. In the reverse bias state, there is no charge in the

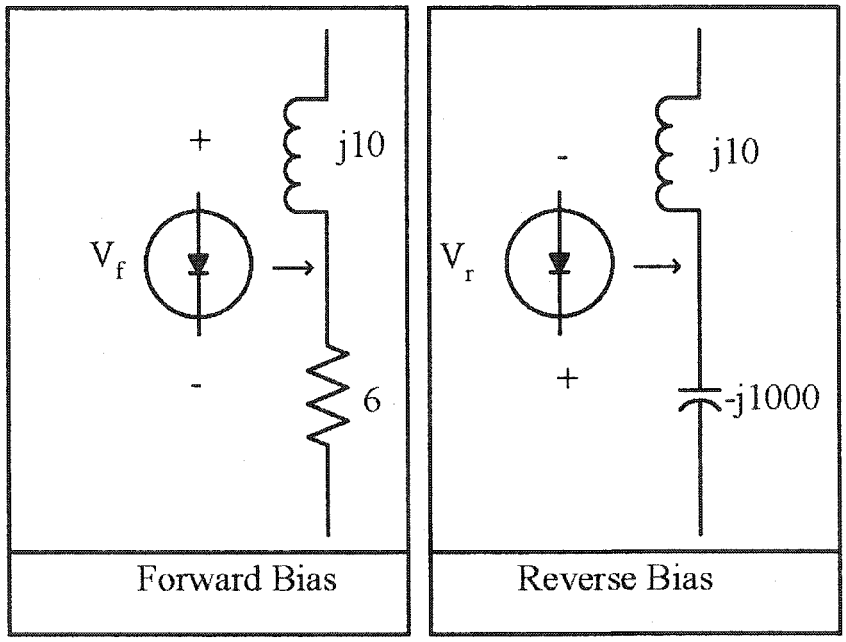

Figure 6.7: Circuit Model for the PIN Diode.

Part Number	V_R (VDC)	Typical $R_s(\Omega)$ (I_f = 10 mA)	Max. $R_s(\Omega)$ (I_f = 10 mA)	Max. C (pF) (V_r = 10 VDC)
MBP-1030-B11	100	5.7	6.5	0.095

Table 6.1: PIN Diode Specifications.

I-region, and the diode appears as a capacitor C_T in parallel with a resistor R_p. An equivalent circuit model for the PIN diode in the forward and reverse bias states is shown in Fig. 6.7. The parallel resistor R_p is not included in this model, as it has a very high resistance, and is essentially an open circuit. From the figure, we model the reverse biased PIN diode as a low-valued capacitor, with a small amount of series lead inductance. The Metellics MBP-1030-B11 PIN diode in an epoxy bead package was used in the DPRA. The specifications for this diode are listed in Table 6.1. When forward biased, the PIN diode turns on and becomes resistive, with a small amount of series lead inductance. The equivalent impedance is approximately $Z_f = 6 + j10\ \Omega$ for the MBP-1030-B11 at the L1 frequency of 1,575.42 MHz. This is a low impedance

relative to a 50 Ω characteristic impedance, and will present a near short circuit condition to the circuit. Placing a forward biased PIN diode in a microwave device at a location of electric field maximum will severely disrupt operation of that device. For example, a microstrip patch antenna can be disabled by placing forward biased PIN diodes on the radiating edges of the patch. At the L1 frequency of 1,575.42 MHz, the equivalent impedance across the reverse biased diode is on the order of $Z_f = -j1000\ \Omega$. In a 50 Ω circuit, this capacitive reactance presents a nearly open circuit condition, and will have very little loading effect on the circuit. If the application happens to be a patch antenna, the only impact would be to shift the resonant frequency of the antenna downward slightly (several MHz, maximum). This effect can be countermanded by simply designing the patch for a higher frequency than the desired operating frequency [38].

6.5 Analyzing the DPRA

Analysis of the dual-patch antenna is performed by means of the improved MNM technique presented in Chapter 5. The conventional MNM model cannot handle lumped loads embedded within the patch antenna substrate, and was modified to account for lumped loads as discussed in Section 5.6. This is necessary to accurately model the effect of the PIN diodes which are located under both of the stacked antenna elements. As with the traditional cavity model or MNM modelling technique, input impedance and far-field radiation patterns are available from the improved model. Evaluating the radiation pattern requires knowledge of the field distribution around the perimeter of the patch element, which is easily obtained from MNM. Mutual coupling is also computed with the improved MNM model. This allows one to evaluate the degree to which the antenna elements may be operated independently from each other. For example, it has been shown that the mutual coupling between two stacked patches is negligible (-25 dB) if one of the antennas is deactivated with forward biased PIN diodes. Finally, the improved MNM model is used to determine the optimum locations of the PIN diodes within the substrate to achieve this effect.

Patch Element	ϵ_r	tan δ	t (mm)	a (cm)	b (cm)	feed (x_p, y_p) (cm)
Upper (WA)	4.50	0.002	1.52	4.39	4.45	(1.67,1.69)
Lower (AJ)	1.07	0.0002	2.00	8.95	9.06	(3.04,3.08)

Table 6.2: Prototype DPRA Dimensional and Material Data.

6.5.1 Substrate Materials

As discussed in Section 6.1, the permittivity of the dielectric used as the patch substrate determines the size of the patch antenna and the shape of its radiation pattern. In this section, we make design choices for the DPRA substrate dielectrics. First, consider the upper patch antenna. We desire a high permittivity material for the substrate to reduce the size of the antenna, yielding the broad radiation pattern shown in Fig. 6.3. The dielectric used for the upper patch is a 0.060 inch Rogers TMM 4 ceramic substrate. This product is inexpensive and suitable for patch antennas because of its low loss and stable thermal expansion coefficient, which is matched to that of copper. The ϵ_r is 4.50 and the loss tangent is 0.002 for this material [22]. A thickness of 0.125 – 0.25 inches would have been a better choice for the upper patch, as the bandwidth would be wider, and the patch would be less susceptible to machining errors during fabrication. However, only samples of the 0.060 inch material were available from the manufacturer. The dielectric chosen for the lower patch is Rohacell 51, which has a relative permittivity (ϵ_r) of 1.07 and a loss tangent of 0.0002 [21]. The material is made in 1 mm thick sheets. The low ϵ_r allows the dimensions of the lower patch to extend to nearly $\lambda/2$. The Rohacell dielectric thickness was chosen to be 2 mm. Thinner substrates push the linear dimensions of the patch closer to the desired $\lambda/2$, but thicker substrates yield greater bandwidth, easier tuning, and less susceptibility to fabrication errors. Also, the PIN diode package needs to fit within the dielectric. These epoxy diode packages were slightly larger than 1 mm in diameter, so a 1 mm thick substrate would not have been suitable. Theory predicts that a 1 mm substrate would be a better choice than 2 mm, as the bandwidth of the low-permittivity patch is wide anyway, so tuning would probably not be a concern. The main advantage of going to a thinner substrate is that the dimensions of the

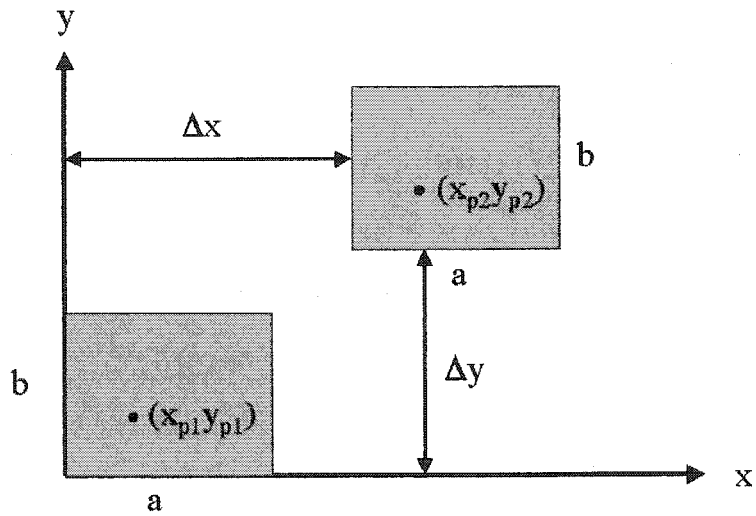

Figure 6.8: Geometry for Mutual Impedance Study.

patch would approach $\lambda/2$, and several more dB of ground-based RFI rejection would be obtained.

6.5.2 Closely Spaced Patch Antennas

In Chapter 5, an improved MNM modelling technique was derived which handles multiple patch antennas with multiple feeds having any number of lumped loads of arbitrary impedance embedded within the patch substrates. This versatile tool will be used to evaluate the specific case of two patch antennas operating in close proximity to each other. Consider two identical patch antennas shown in Fig. 6.8. One patch is located at the origin, and is referred to as the *fixed antenna.* The other patch antenna is offset by $(\Delta x, \Delta y)$ from the origin, and is referred to as the *movable patch antenna.* Both patches have dimensions and material properties identical to the DPRA upper patch, listed in Table 6.2. In this section, the mutual coupling between the fixed and movable patches will be computed. Also, changes in radiation pattern and input impedance due to mutual coupling will be investigated.

Mutual Coupling

The first question we wish to address is the amount of mutual coupling which occurs between closely spaced patch antennas. In Fig. 6.8, we show two closely spaced patch antennas with separate feeds located at (x_{p1}, y_{p1}) and (x_{p2}, y_{p2}). Consider a specific case where the movable patch is offset along the x axis such that the vertical edges of the patches are 1 cm apart. The patches are not offset along the y axis. This requires that $\Delta x = 5.39$ cm, and $\Delta y = 0$. After running the MNM code for this case, we find that the impedance matrix is

$$Z = \begin{bmatrix} 57.5 + j7.3 & -20.1 + j13.6 \\ -20.1 + j13.6 & 57.6 + j6.7 \end{bmatrix} \Omega, \tag{6.1}$$

and the scattering matrix is

$$S = \begin{bmatrix} -17.7\angle 57.8^\circ & -13.5\angle 135.3^\circ \\ -13.5\angle 135.3^\circ & -18.1\angle 57.0^\circ \end{bmatrix} (\text{dB}, \angle^\circ). \tag{6.2}$$

Note that the mutual impedance and mutual coupling matrices are symmetrical due to reciprocity, but the self-impedance of each patch (in the presence of the other) is not equal, owing to the asymmetry of the feeds. The mutual coupling between the patches is quite high, at -13.5 dB. Fig. 6.9 plots the more general mutual impedance between the fixed and movable patch antennas, with the separation between the vertical edges of the patches varying from 1 cm to 40 cm. The mutual coupling increases very rapidly when the edges of the patches are within a centimeter of each other. For large separations, the mutual coupling falls 20 dB per decade, as expected for antennas in free space. Also, the phase of the mutual coupling is linear for large separations. For very closely spaced patches, the mutual coupling is strong enough to disturb the field distribution underneath the patches, perturbing the linear phase behavior. This effect is clearly visible in the close-in phase of s_{21} in Fig. 6.9.

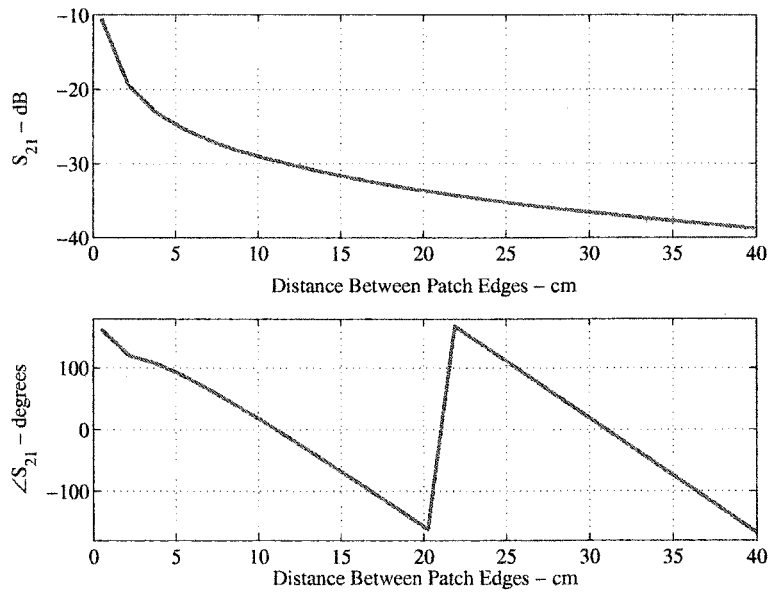

Figure 6.9: Mutual Coupling vs. Edge Separation.

Input Impedance

The input impedance of the single fixed patch antenna is $46.5 + j16.1\ \Omega$. However, if two patches are separated by 1 cm, the input impedance of the fixed patch becomes $37.4 + j20.9\ \Omega$, while that of the movable patch becomes $37.5 + j20.3\ \Omega$. Obviously, the presence of the movable patch has a significant effect on the input impedance of both patches. This de-tuning effect will adversely affect the antenna performance by reducing received satellite signal strengths. Fig. 6.10 plots the input impedance of the fixed patch as the separation between the fixed and movable patches varies. Of course, as the separation approaches infinity, the input impedance of each patch will approach the "single-patch" value.

Radiation Pattern

Fig. 6.11 shows the elevation radiation pattern of the single isolated patch antenna on an infinite ground plane. In Fig. 6.12, the radiation pattern of the fixed antenna is again plotted, except that the movable patch antenna is present, and its edge is only

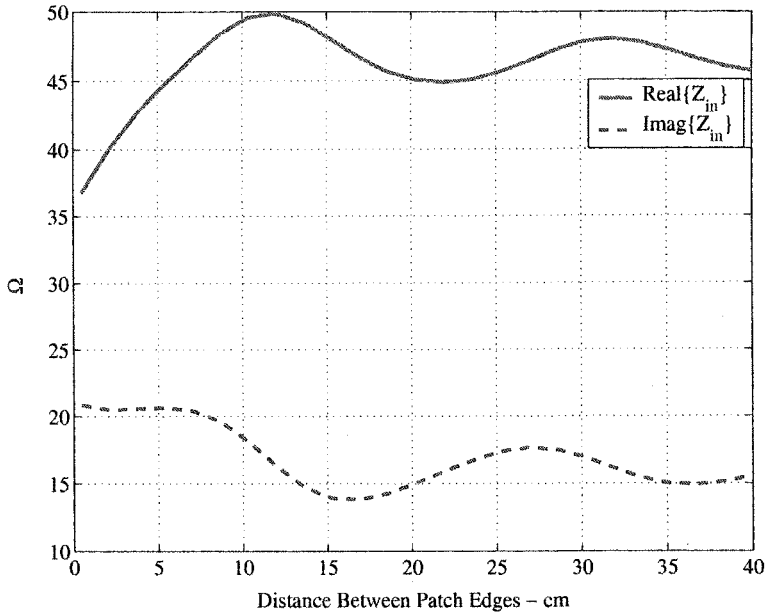

Figure 6.10: Input Impedance vs. Edge Separation.

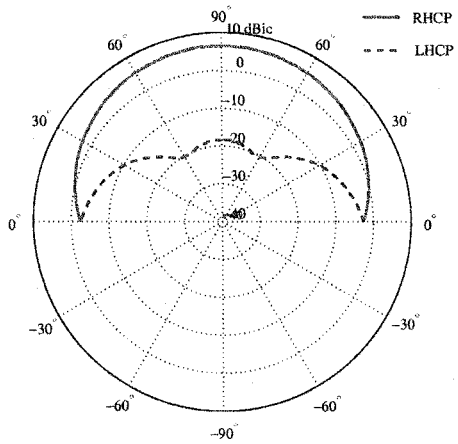

Figure 6.11: Radiation Pattern of Isolated Patch Antenna.

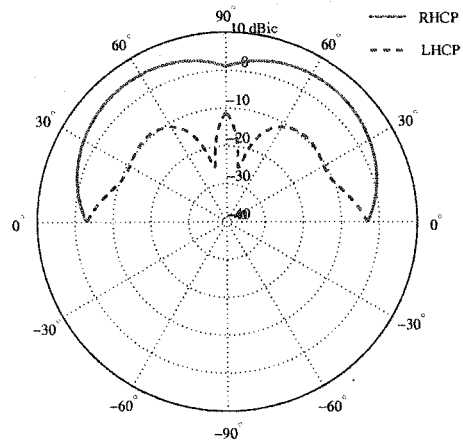

Figure 6.12: Radiation Pattern of Closely-Spaced Patch Antennas.

5 mm away from the edge of the fixed patch. The radiation pattern of the fixed patch is adversely affected by the presence of the adjacent movable patch. The shape of the pattern has been altered, and the axial ratio has increased, reducing the polarization purity.

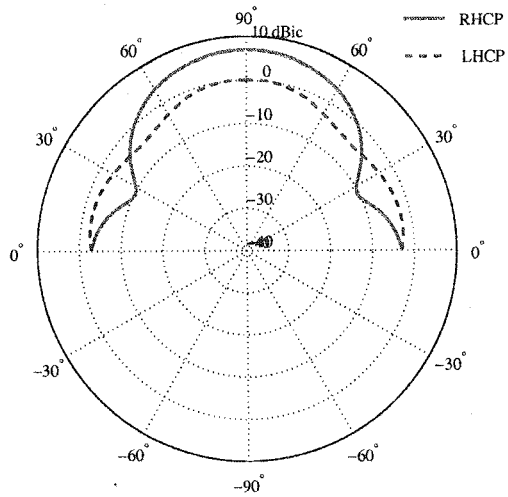

Figure 6.13: Radiation Pattern of Lower Patch Antenna – no PIN Diode Isolation.

6.5.3 Stacked Patches

Stacking patches on top of each other will only make matters worse with respect to mutual coupling, input impedance, and radiation pattern. If we stack the upper wide-angle patch on the lower anti-jam patch, the mutual coupling rises to -3.3 dB. Also, the input impedance of the lower patch becomes $37.8 + j17.0\ \Omega$, which will present a significant impedance mismatch in a 50 Ω system. Fig. 6.13 shows the radiation pattern of the lower patch antenna with the upper patch stacked on top. The simulation is performed such that only the lower patch is being excited by a current source. The upper patch is not being driven with a source. Still, the upper patch antenna is excited by radiation from the lower patch, and ends up radiating to the extent that the lower patch radiation pattern is highly distorted. Compare Fig. 6.13 to the desired pattern shown in Fig. 6.4. We observe in Fig. 6.13 that the lower patch antenna will no longer serve as an anti-jam antenna if the upper patch is present. Some means of isolating the upper and lower patches is required if the antennas are to operate independently of each other.

6.5.4 Stacked Patches with PIN Diodes – The DPRA

The need for some sort of isolation between the upper and lower stacked patch elements is evident. PIN diodes are proposed because of their desirable RF switching properties discussed in Section 6.4. This section first discusses the dielectric choices for the dual-patch reconfigurable anti-jam antenna. Next, optimum placement of the PIN diodes is investigated. From these results, a design choice is made regarding diode placement. The DPRA is formally introduced in this section as a viable solution to the airborne GPS jamming problem. Mutual coupling, input impedance, and radiation patterns are given for the DPRA. The theory derived in this section is summarized in the literature [5], but the details are more thoroughly discussed here.

DPRA – Basic Concept

The fundamental ideas behind the DPRA were developed in the previous sections, and the culmination of these ideas results in the antenna concept shown in Fig. 6.14. A five layered structure is visible, with three metal and two dielectric layers. Two stacked patches with a common feed are shown. Four PIN diodes per patch are embedded in the substrates. Since a single feed drives both patches in series, it is very important to achieve a high degree of isolation between the patches.

Placement of the PIN Diodes

In this section, the effect of PIN diode placement within the substrate is investigated. The goal is to use the fewest diodes possible in the physical locations that yield maximum isolation between the two patches. This analysis was performed numerically with the MNM code. First, consider a single patch antenna. Circularly polarized patch antennas have two active orthogonal modes TM_{100} and TM_{010}. In order to inactivate the patch antenna, both modes must be disabled. A mode is effectively disabled by placing a short circuit at or near points where the electric field is maximum. Since the z directed electric field is cosinusoidal for these two modes, and is maximum along the radiating edges, we would ideally want a short circuit at the radiating edges of the patch. This condition can be approximated by placing a

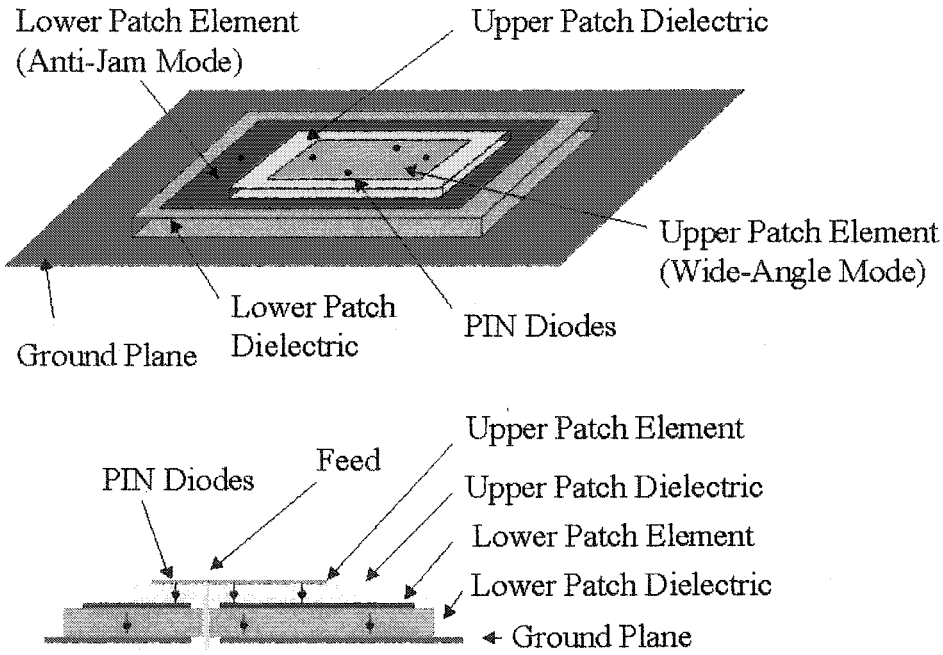

Figure 6.14: The DPRA Concept.

forward biased PIN diode on each of the two edges of the patch. Intuitively, using multiple diodes would be more effective than using a single diode. Placing several diodes in a line along the radiating edge more closely approximates the short circuit condition than using a single diode. However, using more diodes would cause an undesirable shift in resonant frequency when the diodes are reverse biased. In order to explore this tradeoff, the MNM code was used to perform numerous simulations of the patch antenna with PIN diodes in various locations under the patch. For each case, four PIN diodes were placed in the locations listed in Table 6.3. The geometry of the patch and the PIN diode locations are shown in Fig. 6.15. In Fig. 6.15, the feed is placed along a diagonal, to achieve circular polarization. PIN diodes are shown along the principal axes (dashed lines) and along the diagonals (dotted lines). The MNM code was used to compute input impedance and maximum field strength at the edge of the patch for forward biased diodes, and shift in resonant frequency for reverse biased diodes in these locations. The input impedance and field strength are

Case Number	$(\Delta x_1, \Delta y_1)^\dagger$	$(\Delta x_2, \Delta y_2)$	$(\Delta x_3, \Delta y_3)$	$(\Delta x_4, \Delta y_4)$
1	$(a/10, 0)$	$(0, b/10)$	$(-a/10, 0)$	$(0, -b/10)$
2	$(a/5, 0)$	$(0, b/5)$	$(-a/5, 0)$	$(0, -b/5)$
3	$(3a/10, 0)$	$(0, 3b/10)$	$(-3a/10, 0)$	$(0, -3b/10)$
4	$(7a/20, 0)$	$(0, 7b/20)$	$(-7a/20, 0)$	$(0, -7b/20)$
5	$(2a/5, 0)$	$(0, 2b/5)$	$(-2a/5, 0)$	$(0, -2b/5)$
6	$(9a/20, 0)$	$(0, 9b/20)$	$(-9a/20, 0)$	$(0, -9b/20)$
7	$(a/2, 0)$	$(0, b/2)$	$(-a/2, 0)$	$(0, -b/2)$
8	$r/5(\cos\phi, \sin\phi)^{\ddagger *}$	$r/5(-\cos\phi, \sin\phi)$	$r/5(-\cos\phi, -\sin\phi)$	$r/5(\cos\phi, -\sin\phi)$
9	$2r/5(\cos\phi, \sin\phi)$	$2r/5(-\cos\phi, \sin\phi)$	$2r/5(-\cos\phi, -\sin\phi)$	$2r/5(\cos\phi, -\sin\phi)$
10	$3r/5(\cos\phi, \sin\phi)$	$3r/5(-\cos\phi, \sin\phi)$	$3r/5(-\cos\phi, -\sin\phi)$	$3r/5(\cos\phi, -\sin\phi)$
11	$4r/5(\cos\phi, \sin\phi)$	$4r/5(-\cos\phi, \sin\phi)$	$4r/5(-\cos\phi, -\sin\phi)$	$4r/5(\cos\phi, -\sin\phi)$
12	$r(\cos\phi, \sin\phi)$	$r(-\cos\phi, \sin\phi)$	$r(-\cos\phi, -\sin\phi)$	$r(\cos\phi, -\sin\phi)$

† $(\Delta x, \Delta y)$ are the offsets from $(a/2, b/2)$, respectively.
‡ $\phi = \tan^{-1}(b/a)$.
$*$ $r = \frac{1}{2}\sqrt{a^2 + b^2}$.

Table 6.3: PIN Diode Locations.

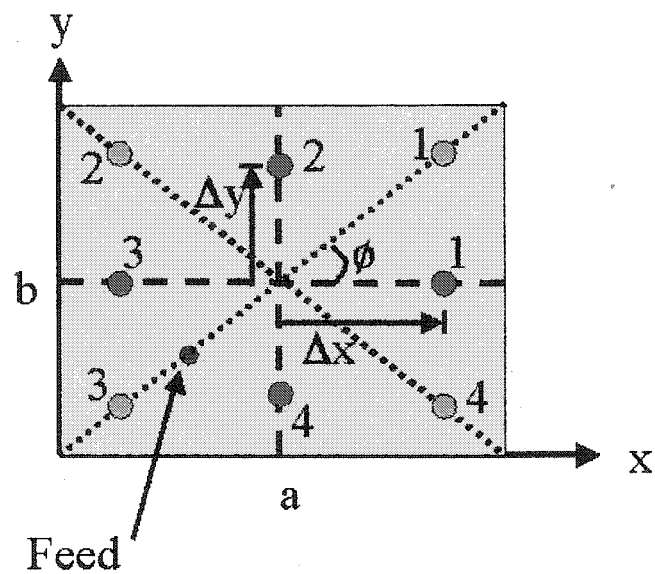

Figure 6.15: PIN Diode Placement Geometry.

computed with the diodes forward biased. If the PIN diodes are truly deactivating the patch, then the input impedance will be mainly reactive, as there will be no radiation resistance. The real part of the input impedance should be small, and would arise only from conductor and dielectric losses. Also, the field strength should be zero at the edges of a deactivated patch. This would indicate that there is no radiation from these edges. When reverse biased, the capacitive PIN diodes will cause a slight shift in the resonant frequency of the antenna. This frequency shift is undesirable, and should be minimized. Fig. 6.16 shows the real part of the input impedance, the patch wall field strength, and the change in resonant frequency for Cases 1 – 7 in Table 6.3. In these cases, the PIN diodes are placed along the principal axes of the patch antenna. The real part of the input impedance and the edge field strength decrease as the diodes are displaced outward from the center. The resonant frequency also decreases as the reverse biased PIN diodes are moved outward toward the edge of the patch. Fig. 6.17 shows the effect of placing PIN diodes along the diagonals of the patch antenna. Locations of the PIN diodes for these cases are listed in cases 8 – 12 of Table 6.3. In Fig. 6.17, we find that the patch is maximally disabled when the

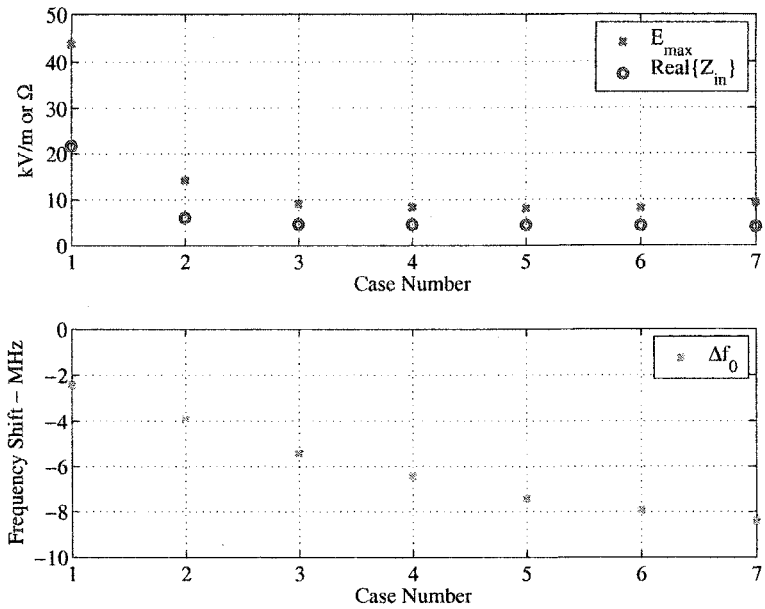

Figure 6.16: Effect of PIN Diodes Along Principal Axes.

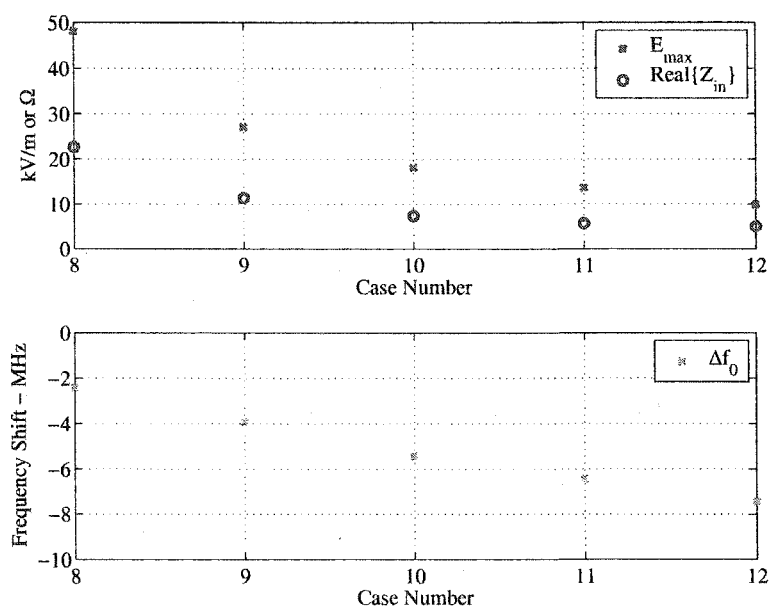

Figure 6.17: Effect of PIN Diodes Along Diagonals.

diodes are located at the corners of the patch. Comparing Figs. 6.16 and 6.17, we find that PIN diodes along the principal axes deactivate the antenna more effectively than diodes along the diagonals. This conclusion is based on the fact that the real part of the input impedance and the field strength at the radiating edges are lower for PIN diodes along the principal axes than for diodes along the diagonals. For the prototype antenna, the diodes were placed at the 50% point, or $\Delta x = a/4$ and $\Delta y = b/4$. This corresponds to diode locations between cases 2 and 3 of Table 6.3. This choice was made since there is not a significant decrease in the real input impedance and wall field strength for diodes located closer to the wall. It is beneficial to have the diodes closer to the center of the patch, as there is less change in resonant frequency when the diodes are reverse biased, simplifying the design.

Input Impedance

Now consider the DPRA, having stacked patches, and with the PIN diodes in place. We now compute the input impedance of the the patch antenna when either the wide-angle or anti-jam mode is selected. Using the MNM code, the input impedance in wide-angle mode was computed as $44 + j42\ \Omega$, while in anti-jam mode the input impedance is $53 + j37\ \Omega$. There is a fairly high inductive reactance associated with both modes. This is a result of the long coaxial probe feeding both antennas. In addition, higher order modes, which are present in both patches, generate an inductive reactance. These inductive reactance components all add in series. This effect can be mitigated simply with a 2.2 pF chip capacitor in series with the feed.

Mutual Coupling

The scattering matrix obtained from the MNM code yields the mutual coupling between the stacked patch antennas. It is most important that the mutual coupling be low in anti-jam mode, since any coupling between the patches will add undesired radiation toward the horizon. The scattering matrix in anti-jam mode is

$$S = \begin{bmatrix} -17.7\angle 46.9^\circ & -21.3\angle 145.9^\circ \\ -21.3\angle 145.9^\circ & -1.5\angle 125.2^\circ \end{bmatrix} (\text{dB}, \angle^\circ). \tag{6.3}$$

Antenna 1 is the lower patch, while antenna 2 is the upper patch. The mutual coupling between the patches is only -21.3 dB. Therefore, the inactive upper patch will have essentially no effect on the radiation pattern of the active lower patch. Notice that s_{11} is -17.7 dB, indicating a good impedance match for the active lower patch antenna, while s_{22} is -1.5 dB, indicating a poor impedance match for the inactivated upper patch.

Radiation Patterns

The MNM technique derived in Chapter 5 assumes an infinite ground plane. While this assumption is sufficient for computing input impedance and mutual coupling, it provides no information about the field strength beneath a patch antenna having a finite sized ground plane. In order to obtain this information, the radiation patterns of the DPRA are computed with a commercial diffraction code called NEWAIR3 [10] which accounts for a finite sized mounting structure. In fact NEWAIR3 can model antennas mounted on aircraft and missiles. NEWAIR3 works by modelling slots in the aircraft fuselage. As discussed in Chapter 5, microstrip patch antennas can be effectively modelled by slots in a ground plane, located at the radiating walls of the patch. Four slots can be used to approximate a RHCP patch antenna. In this case, each slot has a uniform electric field distribution with a 90° sequential phase shift. The aircraft used in this simulation was a Cessna Caravan – the same aircraft used to test the prototype antenna. In Fig. 6.18, we show the pitch plane radiation pattern of the DPRA mounted on the Cessna Caravan. Notice that ground based interferers located at shallow negative elevation angles are attenuated by 15 dB in anti-jam mode, relative to wide-angle mode. In addition, the anti-jam mode has approximately 4 dB more gain toward the zenith than the wide-angle mode. These characteristics will serve to reduce the sensitivity to ground based jammers, while enhancing reception of high-elevation GPS satellites. These desirable properties of the anti-jam mode suggest other possible applications for the DPRA. For example, the higher gain afforded by the anti-jam mode may be used to combat amplitude scintillations caused by ionospheric disturbances. The increased zenith gain will also help mobile GPS users located in an urban canyon, forest, or high multipath environment. In Fig. 6.19 we show the

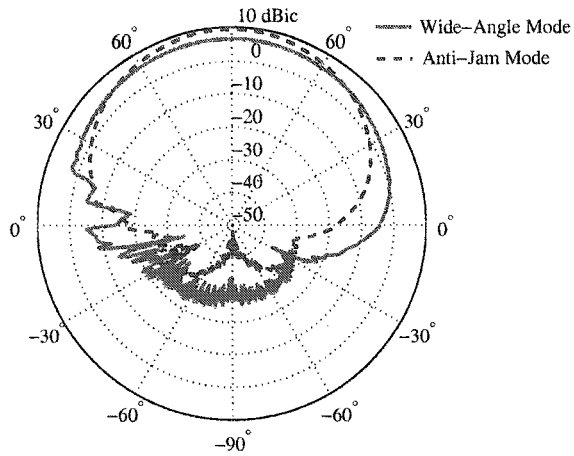

Figure 6.18: Pitch Plane Radiation Pattern of the DPRA.

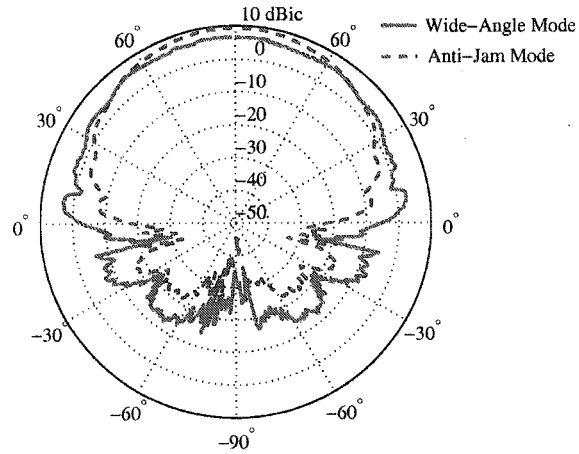

Figure 6.19: Roll Plane Radiation Pattern of the DPRA.

roll plane radiation pattern of the DPRA. The same ground based RFI rejection performance is anticipated in the roll plane as that observed in the pitch plane. One striking feature in Fig. 6.19 is the effect of edge diffraction by the wings. The edge diffraction results in significant side lobe radiation below the aircraft in the roll plane.

6.6 A Prototype DPRA

In order to validate the concept of the DPRA, it was essential to construct and test a prototype antenna. If the prototype performs as expected on the bench, then a flight model should be constructed and flown on a test aircraft.

6.6.1 Design Procedure

In this section, some important design considerations are presented relating to the DPRA. The end goal is to construct a prototype antenna and test it in flight. As a start, consider the RF signal path in Fig. 6.6, which is very simple. High quality GPS antennas have a built-in low noise amplifier (LNA) and band-pass filter (BPF) to improve system noise figure and to reject out-of-band interference, respectively. Accordingly, the RF circuitry within the DPRA should contain these components.

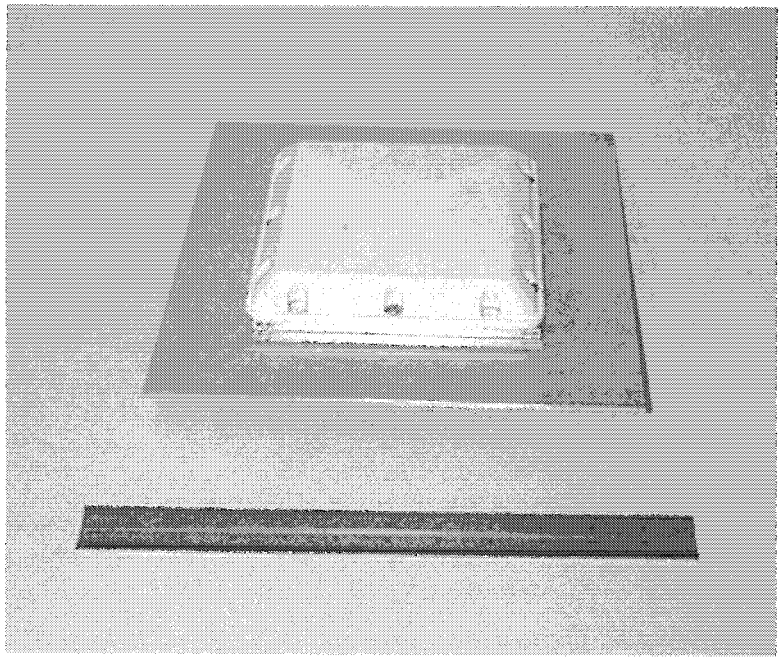

Figure 6.20: Perspective View of the Prototype DPRA.

The LNA is an Agilent MGA-86576 MMIC, which is a general purpose GaAs low-noise gain block usable to 10 GHz. This MMIC has 50Ω input and output impedance over much of its bandwidth, simplifying the RF design. The broadband MMIC allows for a smaller PCB, as the impedance matching circuitry may be omitted. The MMIC provides 22 dB gain at the L1 frequency of 1,575.42 MHz, and 12 dB gain at 10 GHz. Due to the broadband response of the amplifier, filtering is absolutely essential to reject out-of-band signals appearing at the antenna. The BPF is a TOKO part 4DFA-1575B-10 which has a 3 dB bandwidth of 10 MHz and an insertion loss of 1.4 dB. The attenuation rises to 7 dB 35 MHz from the center frequency, and reaches 30 dB at 140 MHz from center. This is a surface mount part, with a relatively low profile of 5 mm. Smaller parts are available at increased cost. The measured response of the LNA/BPF combination is shown in Fig. 6.21. The response of the LNA/BPF combination is flat in the GPS passband, providing 22 dB net gain. In Fig. 6.21, we observe that the out-of-band interference is significantly attenuated by the BPF.

A schematic of the overall RF and DC circuitry is shown in Fig. 6.22. We now

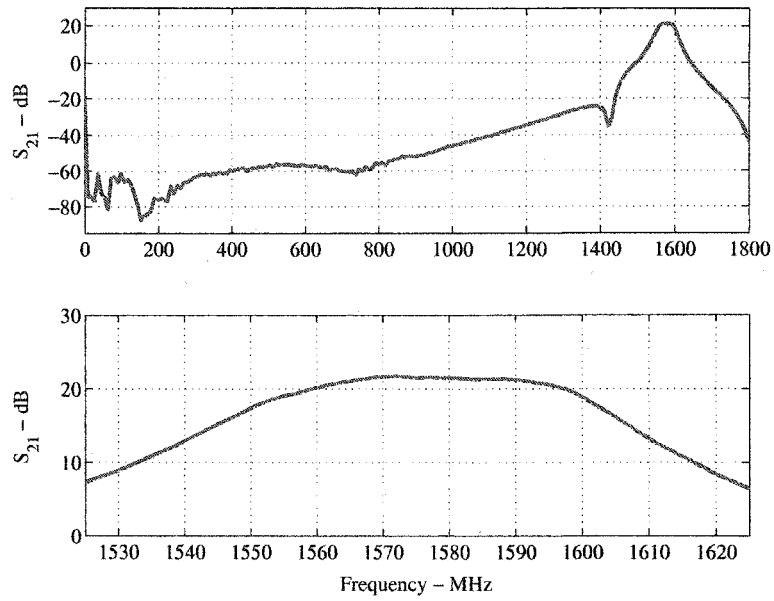

Figure 6.21: BPF/LNA Response.

discuss operation of the DC switching circuitry used to drive the PIN diodes embedded in the patch antennas. The RF path is simple as described above, with the BPF ahead of the LNA to prevent strong interference from overloading the MMIC amplifier. The DC circuitry operates independently from the RF path. Inductor L1 samples the DC voltage on the coaxial feedline and sends it to a comparator U16. The comparator checks the input DC voltage against a reference. If the input voltage is +7.5 volts or less, the output of the comparator goes high, and the transistor switch comprising Q7, Q9, Q10, and Q11 responds by providing +5 volts DC to the lower patch element, and -5 volts DC to the upper patch element. The four PIN diodes in the lower patch are forward biased, and conduct about 15 mA DC each through Q10. The four PIN diodes in the upper patch are reverse biased so that they draw no current, and appear as $-j990\ \Omega$ lumped reactive loads. The antenna is said to be in wide-angle (WA) mode for this case. If the DC voltage on the coax exceeds +7.5 volts DC, the comparator goes low, and the transistor switch provides +5 volts to the upper patch, and -5 volts to the lower patch. This allows 60 mA DC (15 mA per diode) to flow through Q9 to the four upper patch PIN diodes. The PIN diodes in the lower patch

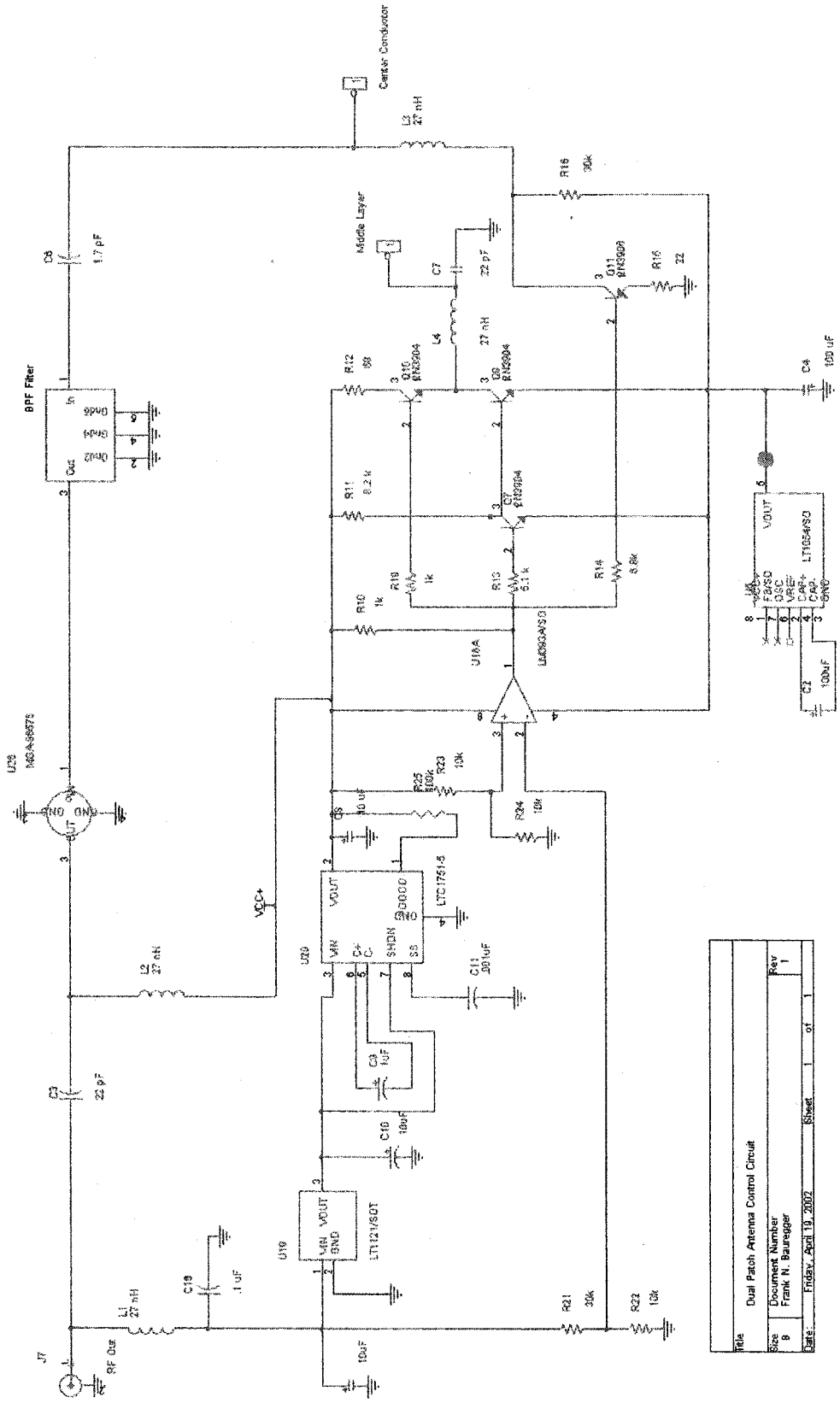

Figure 6.22: Schematic of the DPRA Circuitry.

are reverse biased in this case, appearing as near-open circuits. The antenna is thus placed in anti-jam (AJ) mode. Notice that the DC voltage on the feedline also powers voltage regulators U19 and U20. U19 is a switching regulator which can provide +5 volts DC output even at input voltages as low as 3 volts. Because of this, the DPRA is able to function with very long cable runs that drop up to 2 volts DC. The +5 volt DC output at U20 powers the LNA U26 in both WA and AJ modes. U5 is a voltage converter which converts +5 volts DC to -5 volts DC. The negative voltage is required to properly bias the PIN diodes, as discussed above.

6.6.2 Structural Considerations

Since the prototype antenna is intended to fly on a test aircraft, it must be able to withstand the shock, vibration, and bending forces which occur when mounted on such a platform. This was the foremost consideration while designing the prototype DPRA. Aluminum is used as the structural support material. Because of its high electrical conductivity ($\sigma = 5.6 \times 10^8 S$), copper was used wherever significant RF currents would be flowing. As such, the lower patch element was machined from a sheet of 0.025 inch copper, while the ground plane was machined from a sheet of 1/16 inch copper. Oxygen free copper makes a great structural material because of its high yield strength (as high as 50,000 psi). Thus, the ground plane is very strong and also has very low loss at microwave frequencies. The PIN diodes in the upper patch element are soldered to the copper plating which is bonded to the top and bottom of the ceramic substrate. This ceramic material is very rigid, and as a result, the PIN diodes in the upper element do not experience significant bending forces, and are not limiting with respect to structural integrity. On the other hand, the PIN diodes embedded in the lower patch substrate are the limiting parts of the antenna with respect to vibration or bending forces. The Rohacell substrate in the lower patch element is similar in composition and strength to styrofoam. In addition, the lower patch element is not bonded to this material. Instead, five nylon threaded fasteners clamp the copper patch and Rohacell to the 1/16 inch thick copper ground plane. The four PIN diodes are bonded with conducting silver epoxy and extend from the

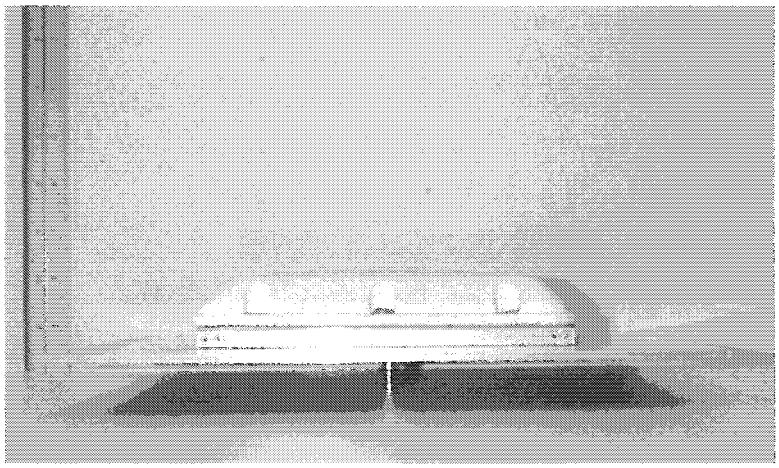

Figure 6.23: Side View of the DPRA.

lower patch element to the ground plane through the Rohacell. These PIN diodes are somewhat fragile, and their 0.003 inch diameter leads will shear off if they are over-stressed. If the lower patch element moves or distorts with respect to the ground plane due to vibration or bending forces, the result could be a change in resonant frequency and axial ratio, or shearing of the PIN diodes in extreme cases. Because of these concerns, the prototype antenna was over designed for strength. As a result, the antenna is probably larger and heavier than it needs to be. The prototype has over 50 threaded fasteners and several metal layers, each intended to add to the rigidity of the structure. A perspective view of the assembled prototype DPRA is shown in Fig. 6.20, and a side view of the antenna is shown in Fig. 6.23. The bottom 3/16 inch aluminum support plate acts as a platform for mounting to the aircraft fuselage. Threaded holes are drilled into the support plate in a pattern which is common for aviation patch antennas. It is intended that this antenna directly replace common aviation patch antennas with no modification to the aircraft fuselage. Photographs of the prototype DPRA internals are shown in Figs. 6.24 and 6.25. As mentioned above, the 1/16 inch thick copper ground plane provides rigid support for the Rohacell 51 substrate and lower anti-jam patch element. The upper patch with its white TMM 4 substrate is visible on top of the lower patch in Fig. 6.24. The feed can be seen along the patch diagonal, while the solder joints for the four PIN diodes in the upper patch

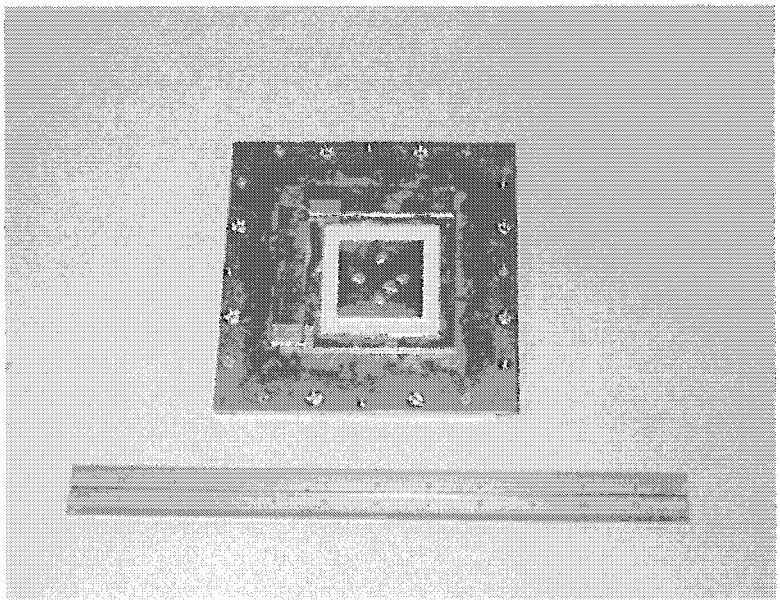

Figure 6.24: Top View of the DPRA.

are visible in a diamond pattern. In Fig. 6.25, a custom printed circuit board that contains the LNA, BPF, and the circuitry required to switch between the wide-angle and anti-jam modes is visible. A thin plastic radome was attached to the top of the antenna during flight to protect the internals. This radome was obtained from a surplus GPS survey grade antenna, and had no adverse effect on the performance of the antenna.

6.7 Flight Test Experiment

The prototype DPRA described in Section 6.6 performed according to expectations in the lab, but the true test of the antenna's performance would be its ability to attenuate ground based interference from an aircraft. Accordingly, a flight test experiment was designed to validate the prototype DPRA. This section describes the flight test procedure and equipment, and provides results from the flight testing. These raw results are then used to further quantify the benefits of the DPRA for airborne users of WAAS who may experience RFI in flight. The flight test experiment and its

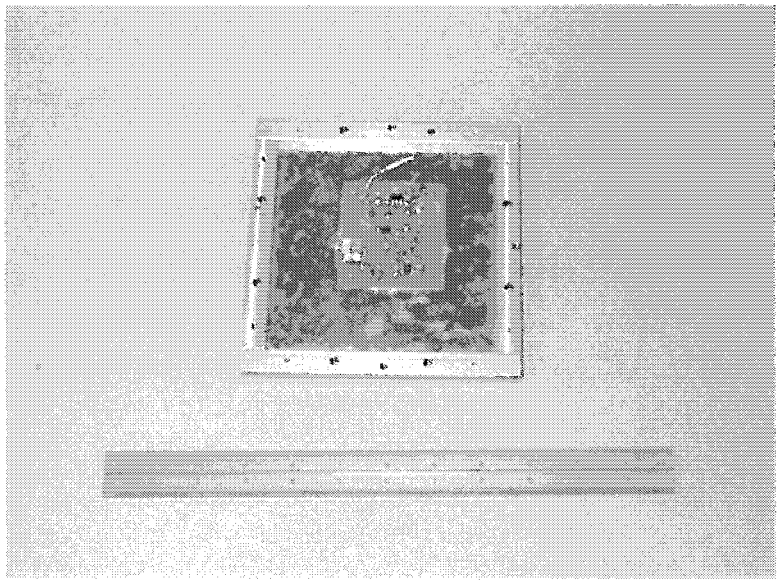

Figure 6.25: Bottom View of the DPRA.

Figure 6.26: Moffett Federal Air Field, Mountain View, CA, 16 September 2002.

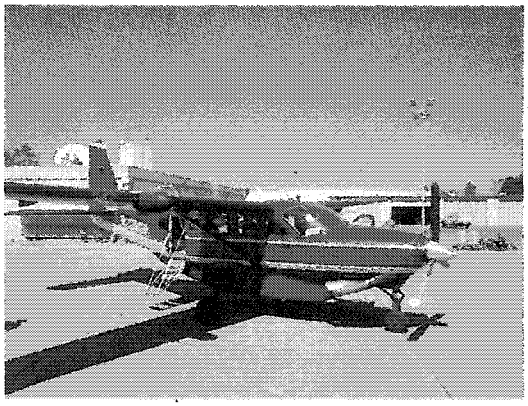

Figure 6.27: Flight Test Aircraft – Cessna Caravan.

Figure 6.28: DPRA Mounted on the Caravan.

results are summarized in the literature [6], but this section provides a more thorough discussion.

6.7.1 Procedure and Equipment

Flight trials of the DPRA were performed on 16 and 18 September 2002 at Moffett Federal Air Field in Mountain View, CA. This air field has two parallel runways oriented at 320°/140°. Because of the prevailing winds, approaches are usually made from the southeast on a bearing of 320° with a 3° glide slope. An aerial view of Moffett Field is shown in Fig. 6.26. This photograph was taken on Monday, 16 September 2002 during one of the approaches. The test aircraft depicted in Fig. 6.27 was a Cessna Caravan, owned and operated by Sky Research Inc. The DPRA was mounted on top of the fuselage, as shown in Fig. 6.28. The aluminum mounting plate of the DPRA was designed to mate with the four pre-existing 10-24 mounting screw holes in the Caravan, allowing seamless replacement of the previously installed GPS antenna. The flight test procedure was fairly straightforward. A simulated GPS jammer was placed at the approach end of the runway. The Caravan flew numerous low approaches over the jammer at a minimum altitude of 75 feet. The final approaches began at approximately 3 – 5 km out. A pseudolite transmitter was used to simulate an actual ground-based GPS jammer. The pseudolite transmits a C/A-code on 1,575.42 MHz and can be tracked by a GPS receiver on board the aircraft. This equipment is

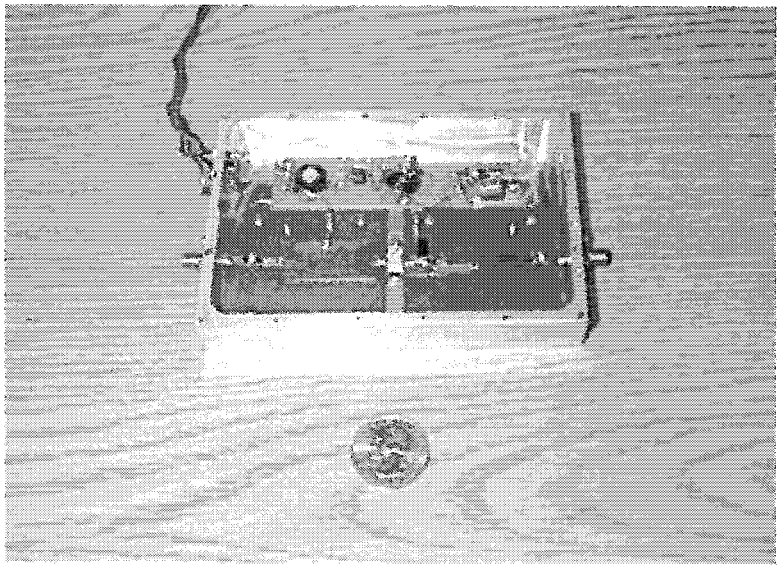

Figure 6.29: 2-Watt Power Amplifier.

licensed to the Integrinautics Corporation by the FCC to operate up to 2 watts ERP from Moffett Field. The Stanford GPS Laboratory maintains a close relationship with Integrinautics, so their FCC license was shared for the purpose of this flight test. Integrinautics personnel were on-site to ensure compliance with the conditions of the license. A 2-watt power amplifier (PA) was built to take advantage of the maximum allowable output power. A variable attenuator (adjustable in 1 dB steps) was placed in line with the PA to control the power level. The aircraft was in contact with the ground crew via VHF radio during the approaches, and the output power was adjusted iteratively until a reasonable signal was received on board the aircraft. A transmit power of only 1 milliwatt was required to track the pseudolite out to ranges greater than 5 km. A 12 dBic gain helix antenna was employed to direct the pseudolite C/A-code toward the aircraft. This antenna served to focus power toward the aircraft and away from other GPS users in the vicinity of the air field. The main beam of the helix was held fixed along the Caravan's approach path. As the aircraft flew directly over the helix, it passed through the side/back-lobe region of the antenna. This configuration was intended to reduce the signal power present at the aircraft antenna when the aircraft was at the point of closest approach. This helps to

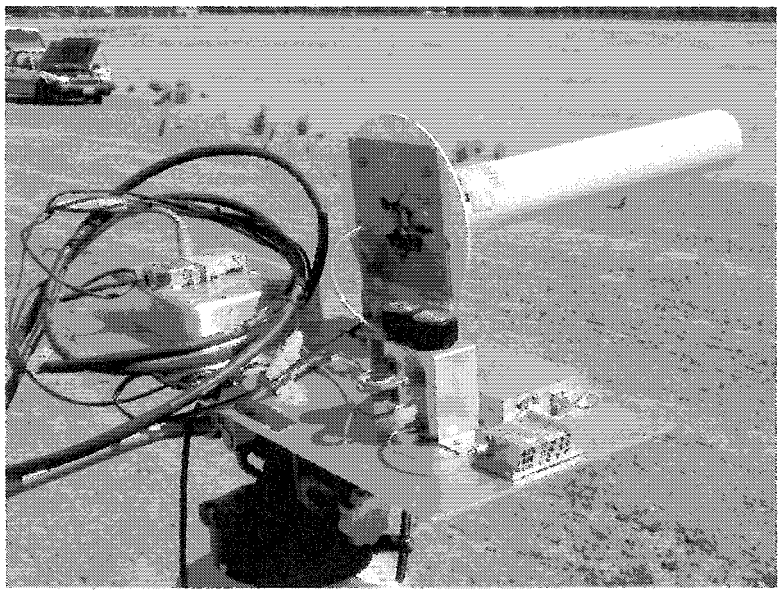

Figure 6.30: Pseudolite Transmitter Setup.

reduce signal "peaking" that occurs due to the $1/r^2$ effect, and prevents jamming the airborne receiver. The C/A-code was pulsed at a 12.5% duty cycle to further reduce the chance of causing RFI to GPS users in the area. The pulsed C/A-code also increases the effective dynamic range of the GPS receiver on board the aircraft [19]. The pseudolite transmissions were monitored at the transmitting antenna to ensure that nearby GPS receivers would be unaffected by the pseudolite. A photograph of the pseudolite setup is shown in Fig. 6.30. On board the aircraft, the DPRA and a standard Micropulse aviation GPS patch antenna were connected to separate NovAtel OEM4 GPS receivers. Two separate computers recorded the GPS satellite signal strengths and the pseudolite signal strength. Of course, aircraft position, velocity, and accurate time information were available from the GPS receivers, and were recorded as well. A high quality INS provided aircraft attitude information which was also recorded in flight on a third computer. A photograph of the airborne data recording equipment rack is shown in Fig. 6.31. Inside the Caravan, the feedline from the DPRA was connected to a bias Tee as shown in Fig. 6.6. A simple voltage regulator was built which provided outputs of +5 volts or +10 volts DC in response to a hand

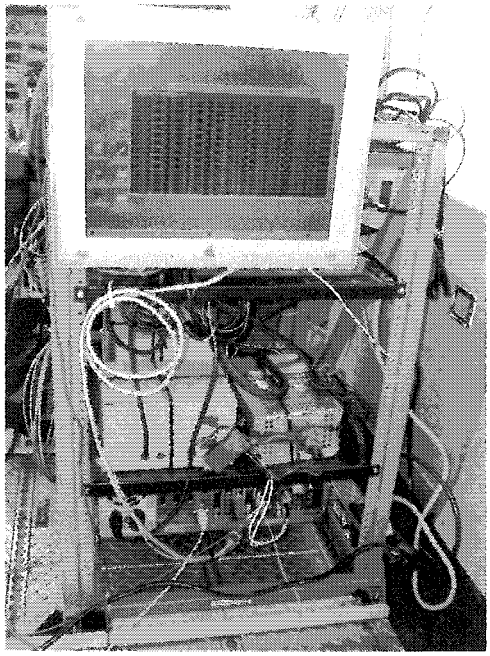

Figure 6.31: Airborne Data Recording Equipment Rack.

held toggle switch. This voltage was fed to the bias Tee and appeared on the coaxial feedline to the DPRA. This arrangement made it easy to switch between wide-angle and anti-jam modes in-flight with the toggle switch.

6.8 Flight Test Results

The aircraft made a total of 20 approaches during the two days of flight testing. The flight test yielded a significant amount of data which were stored in MATLAB binary format after parsing. The main data product from the experiment was the received power from the pseudolite. Since the received powers from the visible GPS satellites were also recorded, these two data sets could be compared directly. In order to determine the absolute power in dBm present at the antenna terminals during the flight test, the GPS receiver was calibrated in the laboratory prior to flight. Fig. 6.32 shows a plot of the C/N_0 reported by the GPS receiver vs. the signal power at the receiver antenna terminals. This measurement was made with a

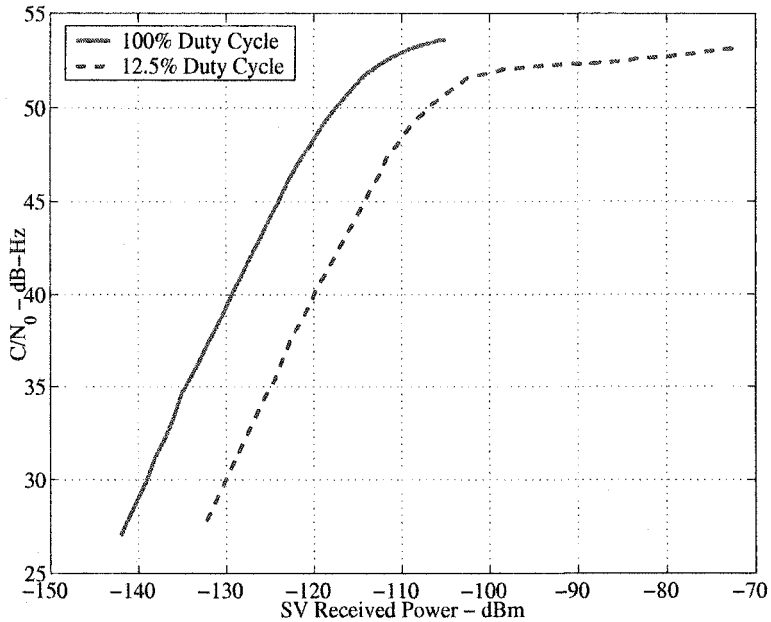

Figure 6.32: Receiver C/N_0 vs. Received Power.

very accurate power meter and calibrated step attenuators. The reported C/N_0 is linear with received signal power until a C/N_0 of 51 dB is reached, which is the 1 dB compression point for this measurement. Notice that the pulsed C/A-code produces meaningful C/N_0 measurements well beyond the range of the full duty cycle C/A-code. Absolute accuracy degrades at these high signal levels however, due to the severe compression of the reported C/N_0 values. During the flight test, received C/N_0 values were kept below 50 dB during critical phases of the experiment, such as a switch between antenna modes or during direct comparisons between pseudolite and GPS satellite signal powers. The results from Fig. 6.32 were used to generate all figures in this section which report signal powers in dBm.

In Fig. 6.33 we show data from two separate approaches. In the first approach indicated by the solid blue line, the antenna is in wide-angle mode. In the second approach indicated by the dashed red line, the antenna is in anti-jam mode. Notice that these traces have very similar large-scale features, indicating that the pilot was able to repeat the approaches very accurately. The pilot was flying VFR approaches

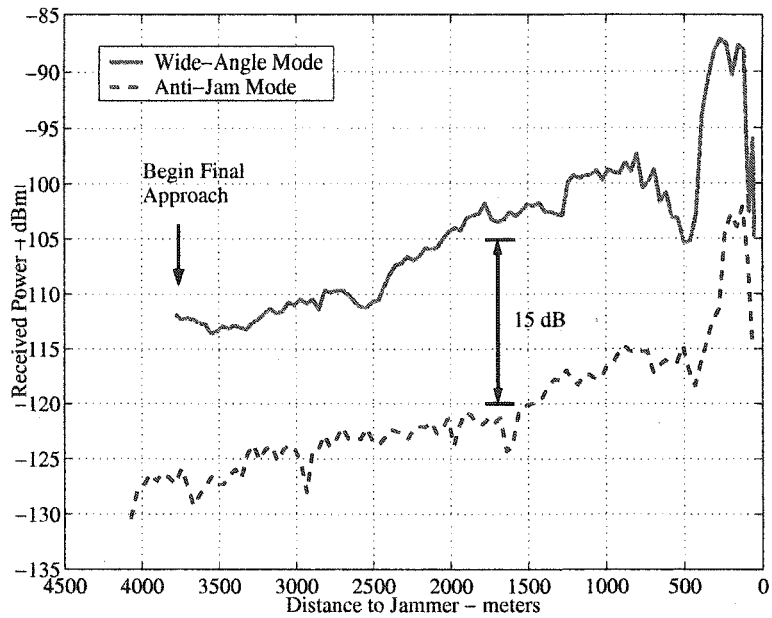

Figure 6.33: Received Jammer Power in Wide-Angle and Anti-Jam Modes.

with no additional aiding from a flight display or other guidance system. The weather was sunny and warm on this day with <5 knot head winds, so the pilot had excellent control of the aircraft. The figure shows the received jammer (pseudolite) power in dBm vs. the distance between the aircraft and the jammer. Final approach begins at 4 km out, and the received power increases at roughly 20 dB per decade as expected for free space propagation. The most striking feature of this plot is the fact that the anti-jam mode attenuates the ground-based jammer by 15 dB compared to the wide-angle mode. Since the wide-angle mode radiation pattern is identical to the pattern of commonly available aviation patches, this improvement in RFI rejection is applicable to these patches as well. The null at 500 meters distance is likely due to a null in the helix radiation pattern, or perhaps a strong ground reflection adding out of phase with the direct signal. Fig. 6.34 is the same type of plot as Fig. 6.33, except that the antenna is switched from wide-angle mode to anti-jam mode in real-time. Data from two separate approaches are plotted. Again, we observe a 15 dB drop in the received jammer power when switching to the anti-jam mode.

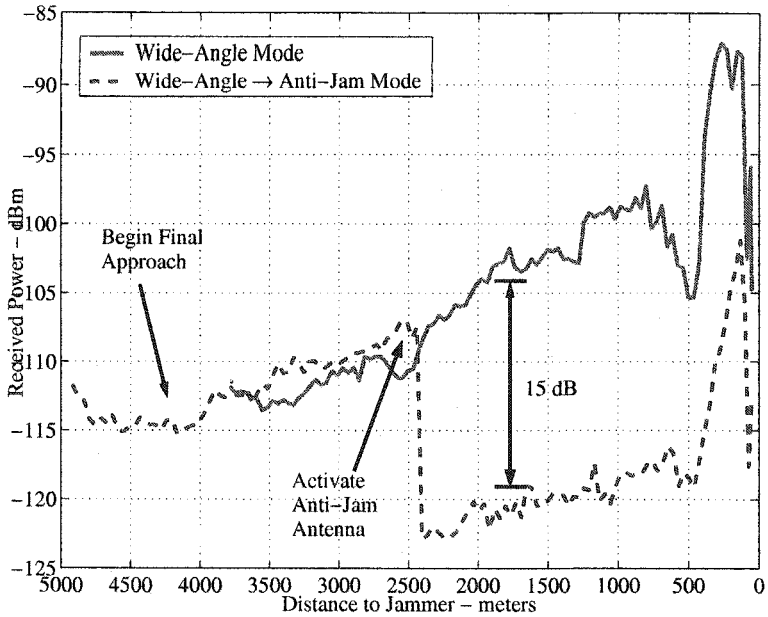

Figure 6.34: Real-Time Switching from Wide-Angle to Anti-Jam Mode.

It was stated previously that the anti-jam mode has several dB more gain toward high elevation GPS satellites than the wide-angle mode. To observe how this effect helps to mitigate RFI, consider the ratio of the received jammer signal power to that of the GPS satellite, commonly referred to as the J/S ratio. This metric accounts for the strength of the desired signal as well as the interfering signal, and provides more information about the performance of an anti-jam antenna in the face of RFI. In Fig. 6.35 we plot the J/S ratio for both DPRA antenna modes as a function of distance to the jammer. Here, the desired signal is PRN 1, which is at an elevation angle of 65°. As expected, the J/S ratio steadily worsens (increases) as the aircraft approaches the jammer. However, at a distance of 2,500 meters, the anti-jam mode is activated, and the J/S ratio drops by 20 dB. This significant improvement is due to the combination of low gain at negative elevation angles and high zenith gain of the anti-jam mode. This flight test was considered a successful demonstration of the dual-patch reconfigurable antenna. A simulated ground-based jammer was significantly attenuated (15 dB) by this antenna relative to a conventional patch

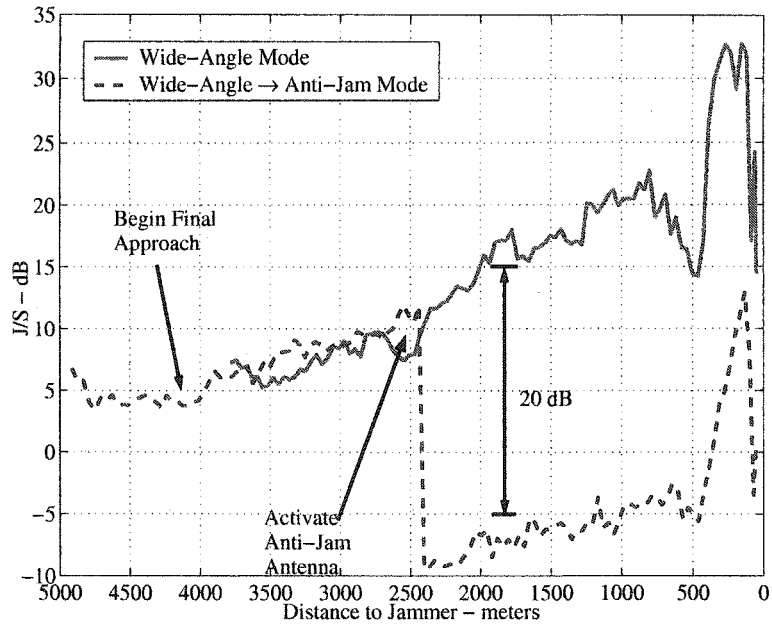

Figure 6.35: J/S Ratio in the Wide-Angle and Anti-Jam Modes.

antenna. In addition, the antenna decreases the J/S ratio by 20 dB for ground based RFI sources. It is desirable to mount the DPRA away from other metallic structures which could diffract ground-based signals into the antenna main beam. However, the DPRA did perform well on the Caravan even though it was mounted near two large vertical blade antennas visible in Fig. 6.28.

The NEWAIR3 diffraction code can predict radiation patterns at negative elevation angles for antennas mounted on aircraft. It is interesting to plot the expected received power from the pseudolite transmitter on board the Caravan using this code. In Fig. 6.36, we find that the measured signal levels at the airborne receiver match the values predicted by the diffraction code fairly well. Hence, the diffraction code can be used as a tool for computing WAAS availability for airborne users, as described in Section 6.9.

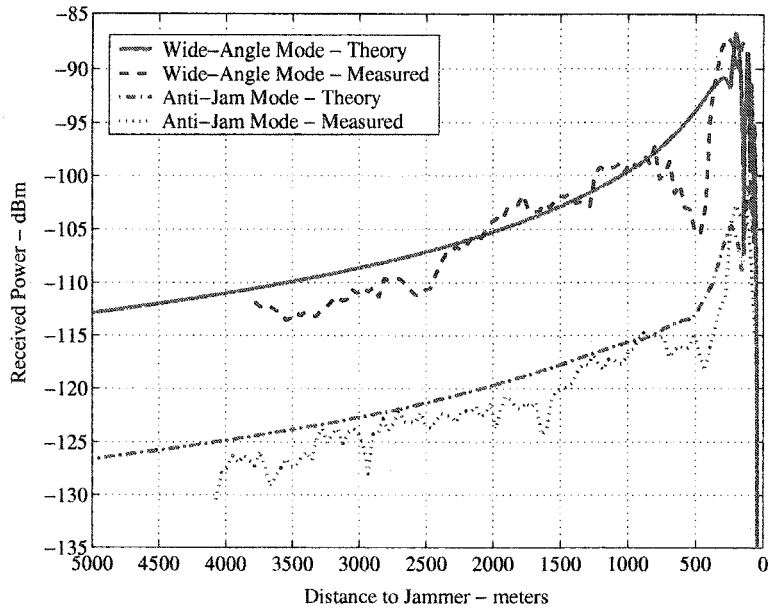

Figure 6.36: Theoretical vs. Measured Received Pseudolite Power.

6.8.1 Differential Phase Response

The two DPRA patches each have a different phase response as a function of satellite azimuth and elevation angle. Thus, in switching between wide-angle and anti-jam modes, the GPS receiver will measure a different carrier phase in each mode. If the phase shift between modes is too great for a particular satellite, the receiver could lose lock on that satellite. In order to quantify this effect, the DPRA was placed on the roof of a tall building, and connected to a GPS receiver. The antenna was switched between wide-angle and anti-jam modes, and the lock time for each satellite was measured and recorded. Fig. 6.37 shows the percentage of time the receiver stayed locked on a particular satellite as the DPRA was switched between wide-angle and anti-jam mode eight times. For satellites above 25° elevation (except for one case), the receiver was able to track the satellites through all eight switching events. However, the receiver frequently lost phase lock on the lower elevation satellites. If we assume that the PLL loses lock with a 15° minimum instantaneous phase shift, then we can infer that the differential phase response of the DPRA is less than 8 mm

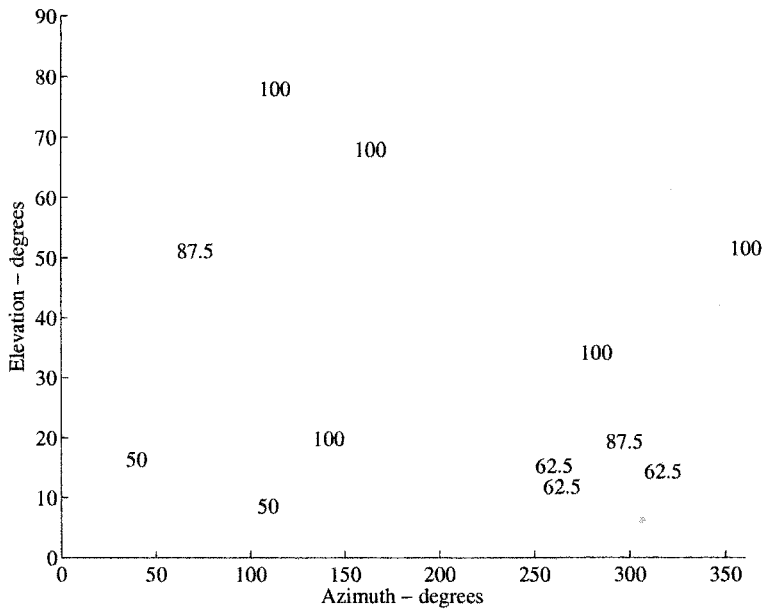

Figure 6.37: Percentage of Time the Receiver Remains Locked.

for satellites above 25°. The differential phase variation is greater at low elevation angles, and likely increases rapidly near the horizon. It should be noted that both the MNM simulations and lab measurements indicate that the differential phase shift between the wide-angle and anti-jam modes is 35° at zenith. This result would seem to contradict the observations in Fig. 6.37. The most likely explanation is that the GPS receiver was indeed able to track the satellites through the large (35° or more) phase excursions. This would indicate that the carrier tracking loop within the receiver is much better than the standard Costas loop, for which we assume a 15° threshold for loss of lock.

The differential group delay between the wide-angle and anti-jam modes was measured in the lab to be 3 nS at zenith. This amounts to 0.9 meters in code phase differential group delay between the two modes. This code phase bias would show up as a pseudorange error for the particular satellite being tracked. However, such a small error will not cause the DLL to lose lock. In fact, this pseudorange error due to switching between the wide-angle and anti-jam modes could not be observed in the data taken from the GPS receiver, as it was obscured by the much larger short term

errors due to multipath.

6.9 Benefits to Airborne WAAS Users

The raw flight test data presented in Section 6.8 demonstrated that the DPRA provides increased protection against ground based jammers for airborne users. This section takes the analysis a step further and describes how the DPRA will benefit aviators using WAAS during a precision approach. Theory from Section 2.4.5 of Chapter 2 is used to obtain the results discussed in this section. Users in CONUS currently receive WAAS messages from two geosynchronous satellites, which also provide GPS-like ranging signals. WAAS availability is targeted at 99.9% for users in CONUS, assuming no RFI. However, a strong local interference source can reduce availability to 0% in the vicinity of an airport, disrupting flight operations or worse. MAAST is a valuable tool for computing the time availability of WAAS for users in CONUS. As a starting point, consider the WAAS time availability plot in Fig. 6.38. Here, we are using the DPRA in wide-angle mode, which is identical in performance to any conventional aviation grade patch antenna. There is no RFI present. WAAS is available 95% of the time over 99.2% of CONUS assuming LPV navigation performance (Table 1.2). The current 2003 GPS constellation was used for all simulations in this section. If we switch to the anti-jam mode, we achieve the WAAS time availability shown in Fig. 6.39. WAAS availability has been reduced to 98.8% because fewer satellites are tracked in anti-jam mode. Those satellites near the horizon which are tracked have increased pseudorange error due to the higher attenuation of the anti-jam mode for low elevation satellites. Because of the reduced WAAS availability in anti-jam mode, it would be wise to keep the DPRA in wide-angle mode unless RFI were present. Now consider a 500 mW wideband jammer on the ground located 10 km from the runway touchdown point. In Fig. 6.40 we show the WAAS time availability for users in CONUS using the DPRA in wide-angle mode. Again, this is equivalent to using a conventional aviation patch antenna. This jammer is strong enough to render WAAS completely unavailable to users in CONUS. If the DPRA

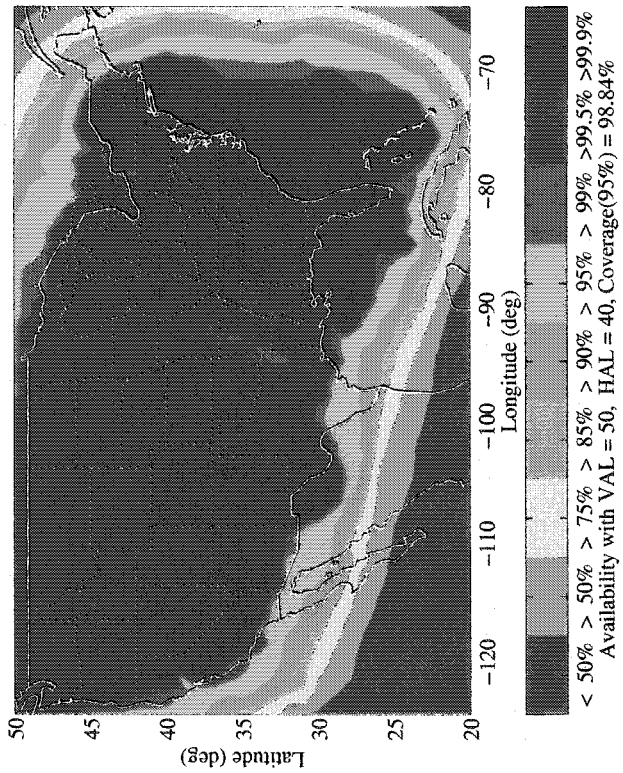

Figure 6.39: LPV WAAS availability with no RFI in Anti-Jam Mode.

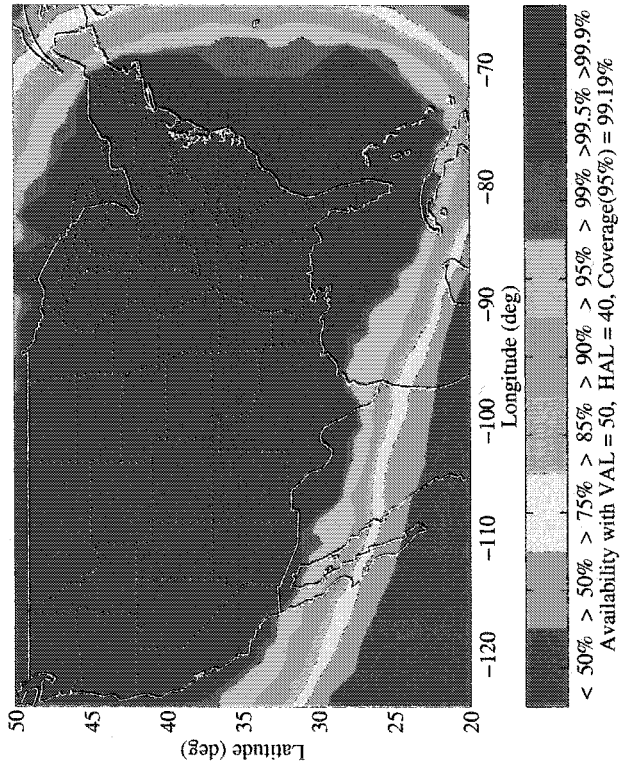

Figure 6.38: LPV WAAS Availability with no RFI in Wide-Angle Mode.

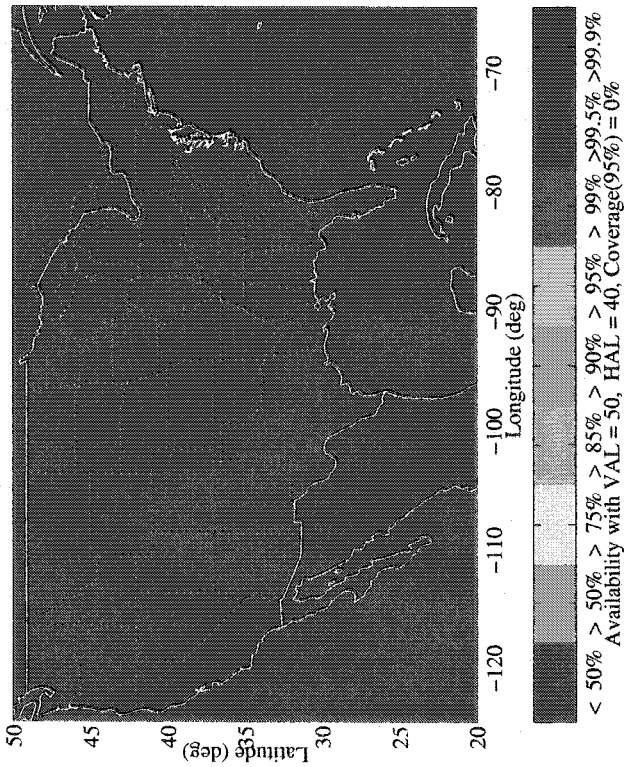

Figure 6.40: LPV WAAS Availability with 500 mW Jammer at 10 km in Wide-Angle Mode.

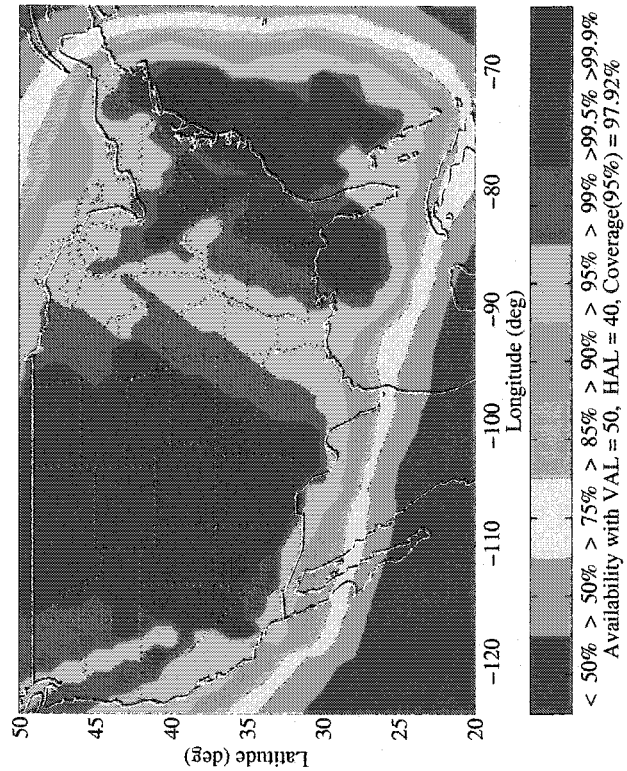

Figure 6.41: LPV WAAS Availability with 500 mW Jammer at 10 km in Anti-Jam Mode.

is placed in anti-jam mode with the same 500 mW jammer present, WAAS availability is increased to 97.9%, as shown in Fig. 6.41. While this does not meet the FAA requirement for availability, the DPRA anti-jam mode will provide LPV navigation capability much of the time for airborne users experiencing RFI. In fact, the DPRA can protect against higher powered jammers as well. Fig. 6.42 shows WAAS availability for a 1 watt jammer located 10 km from the runway.

So far, we have required LPV navigation performance requirements, which apply during a precision approach. If the jamming is so severe that even the anti-jam mode cannot protect the aircraft, a missed approach procedure must be performed. The required navigation performance requirements are less stringent during a missed approach, as a 0.3 NM horizontal alert limit is applicable (Table 1.2). As shown in Fig. 6.43, the DPRA will be able to provide GPS navigation during this procedure over 99.8% of CONUS assuming a 4 watt jammer. The results from these MAAST simulations indicate that the DPRA has the potential to bring an aircraft down to the LPV minimum decision height, even in the face of moderate ground based interference. In the event that a missed approach procedure is required, the DPRA can still provide GPS guidance to the pilot. Conventional patch antennas cannot provide this level of performance. It should be noted that throughout the analysis, we have assumed that WAAS messages will be available from the geosynchronous satellites. This may not be true at some locations in the presence of severe RFI, where only the high elevation satellites are available. For this reason, the DPRA may be better suited for LAAS applications, where the differential corrections are broadcast to the user in a different frequency band, and will likely be available.

6.10 Antenna Performance Summary

This section summarizes the performance specifications of the DPRA. The specifications were derived both theoretically and empirically from the flight test results.

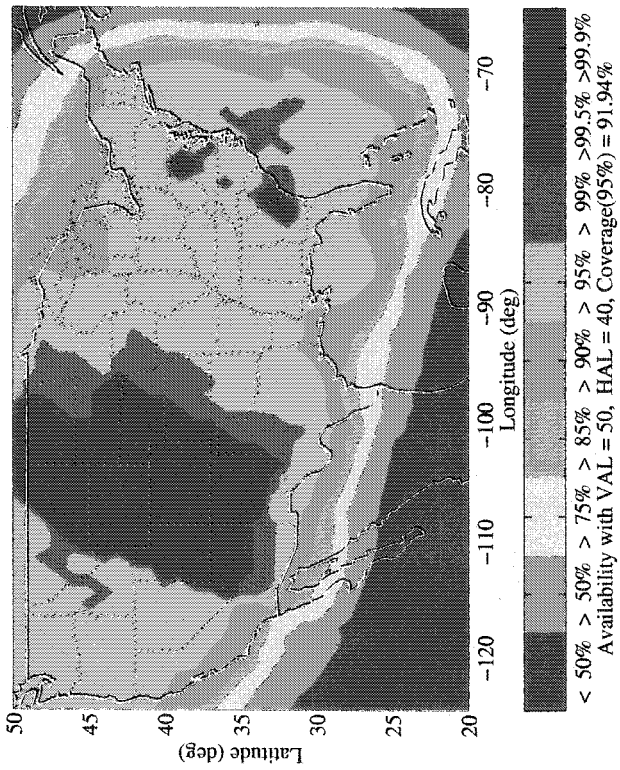

Figure 6.42: LPV WAAS Availability with 1 Watt Jammer at 10 km in Anti-Jam Mode.

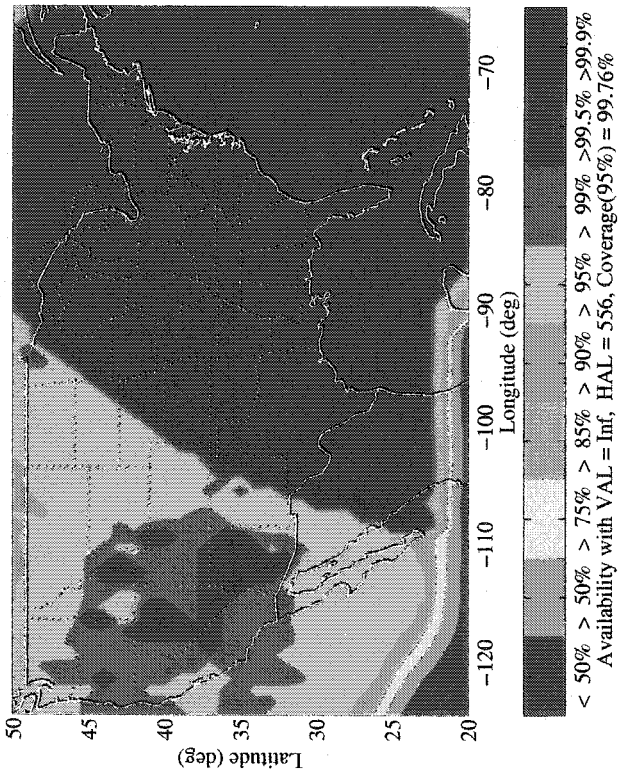

Figure 6.43: Missed Approach WAAS Availability with 4 Watt Jammer at 10 km in Anti-Jam Mode.

GENERAL SPECIFICATIONS		
Center Frequency	1,575.42 MHz	
Nominal Impedance	50 Ω	
Polarization	RHCP	
SWR	< 1.8	
LNA Gain	22 dB	
Noise Figure	3.3 dB†	
Connector	TNC	
Power Requirements	190 mA @ 3 – 15 VDC	
Mounting	NovAtel 512 Footprint, 4 10-24 screws	
RADIATION PATTERN	**Wide-Angle Mode**	**Anti-Jam Mode**
Gain @ 90° Elevation	6.7 dBic	9.6 dBic
Gain @ −3° Elevation	-7.6 dBic	-23 dBic
3 dB Beamwidth	108°	68°
3 dB Axial Ratio Bandwidth	7 MHz	12 MHz
SELECTIVITY	**Wide-Angle Mode**	**Anti-Jam Mode**
3 dB Passband	31 MHz	40 MHz
Out-of-Band Rejection @ 50 MHz‡	24 dB	20 dB
Out-of-Band Rejection @ 100 MHz‡	43 dB	38 dB
Element Efficiency	82%	97%

† $T_{sky} = 100°$K
‡ With 4DFA-1575B-10 BPF installed

Table 6.4: DPRA Specifications.

Chapter 7

Conclusions

7.1 Summary of Research

The purpose of the research reported in this thesis was to develop novel GPS anti-jam antennas which are simple, small, lightweight, inexpensive, and suitable for aircraft. This goal has been met, as two novel antenna designs have been analyzed, constructed and successfully tested.

7.1.1 DCA

The dielectric cavity antenna (DCA) uses an artificially soft surface to reduce sensitivity to RFI arriving from below the antenna. This antenna is similar to a choke ring antenna in both appearance and function, except that the soft surface is realized with a grounded dielectric slab rather than a corrugated ground plane. It is possible to use a high permittivity dielectric to shrink the antenna so that it is suitable for use on aircraft. For example, using a dielectric having a relative permittivity of 20, the DCA would have a vertical dimension of just over 1 cm. A 2.5-dimensional FDTD computer code was written to simulate this antenna, and the code was tested on a canonical problem. A method was presented for determining the proper dimensions of the antenna, namely the height of the cavity, and the inner and outer radii of the cavity. Since the sizing equations are not exact, the FDTD

code is required to ensure that the actual constructed antenna performs as expected, reducing the possibility of rework. A prototype DCA was designed and constructed using the techniques outlines in this thesis. This antenna used polyethylene as the dielectric material within the cavity, which has a relative permittivity of 2.37, and low loss at the GPS L1 frequency of 1,575.42 MHz. The prototype DCA described in this thesis did not perform according to theory and the simulations. The suspected reason for this is that the dielectric used in the cavity contained air pockets which reduced the effective permittivity of the material. Further FDTD simulations seemed to justify this hypothesis. Improved material processing techniques are required to maintain purity of the dielectric during construction. While the design concept of the DCA was validated in theory and in practice, the DCA is not the best stand-alone choice for aviation applications because of its size, and the fact that low elevation satellite signals are strongly attenuated by the antenna. In order to use the DCA for airborne applications, an additional antenna is required for use when no RFI is present. This second antenna ensures a maximum number of satellites are visible to the GPS receiver during RFI free conditions. This undesirable requirement for two antennas led to the development of the dual-patch reconfigurable antenna (DPRA), which comprises a dual-state reconfigurable antenna in a single package.

7.1.2 DPRA

The dual-patch reconfigurable anti-jam antenna (DPRA) has proven to be a worthy antenna design. This is a new concept in GPS antenna design, whereby two independent antennas are packaged into a single unit. Either of the two antennas may be selected remotely by means of a DC voltage floating on the antenna's coaxial feedline. One of the antennas has a broad, wide-angle radiation pattern that can acquire and track all visible GPS satellites down to the horizon, including the two low elevation WAAS geosynchronous satellites. The second antenna has high zenith gain, and reduced sensitivity toward negative elevation angles. The aim of using this second mode is to attenuate ground based jammers appearing at negative elevation angles, and to enhance the signals from high elevation GPS satellites. Normally, such

closely spaced (stacked) antennas would interact strongly with one another, and the desired radiation pattern characteristics would not be achieved. However, PIN diodes embedded within the substrates of the patch antenna elements allow one antenna to be transparent, while the other antenna remains active. The DPRA met all of the goals of this research. In fact, the DPRA has been proven in flight to significantly reduce RFI from below a Cessna Caravan test aircraft. The RFI was attenuated by 15 dB when switching from the wide-angle to anti-jam mode. The RFI rejection performance of the wide-angle mode happens to be identical to that of a conventional aviation grade patch antenna. Thus the 15 dB improvement is directly applicable to traditional aviation patch antennas as well. The DPRA was able to improve the J/S ratio by 20 dB, for a high elevation satellite and a ground based jammer. This is a significant accomplishment for an antenna which is only slightly larger than a conventional aviation patch antenna. This antenna is well suited for civilian aviation applications. It is small, lightweight, and inexpensive to manufacture. The DPRA functions by a relatively simple principle which does not necessitate additional external hardware or a microprocessor. While the DPRA does not provide the anti-jam performance available from null-steering CRPAs, it may serve as an alternative to military anti-jam antennas when used in conjunction with another RFI mitigation technique, such as temporal filtering or IMU aiding. If so, the DPRA could replace the bulky, expensive null-steering CRPAs for military fighter/attack aircraft or uninhabited aerial vehicles (UAV). The DPRA would not be effective on missiles or precision munitions because the attitude of these platforms changes rapidly in time.

7.2 Future Research

7.2.1 DCA

The main drawback of the DCA is the fact that it attenuates signals from low elevation satellites, and a separate GPS antenna is required to track these satellites during RFI free conditions. It would be desirable to "turn off" the artificially soft surface surrounding the patch antenna at these times to take advantage of the full

GPS constellation. One technology which might enable this need is the photonic band gap (PBG) surface [69]. A PBG surface embedded with PIN diodes could act as a dual-state ground plane. Forward biasing the PIN diodes would short the elements in the PBG lattice, creating a nearly-PEC surface. The antenna would then have a wide-angle radiation pattern. Reverse biasing the PIN diodes would cause the lattice elements to be resonant at the design frequency, effectively creating a high impedance surface (i.e., an artificially soft surface v. Chapter 4). If varactor diodes were used instead, one could control the resonant frequency of the PBG surface electronically. This would allow one to change the shape of the radiation pattern electronically, in a continuous fashion if desired. Once the high impedance surface is established, surface waves would be extinguished on that surface, and the antenna would possess a radiation pattern similar to that of the DCA, or the DPRA in anti-jam mode. The use of the tunable PBG concept would result in a very flexible antenna design. If the continuously variable pattern option were implemented, then real-time pattern shaping would be possible.

7.2.2 DPRA

PIN Diode Placement

The PIN diodes were initially placed within the dielectric of the DPRA patch elements using good engineering judgement. The locations of the diodes were chosen to be near the high electric field regions of the antenna for each of the orthogonal modes (four diodes total). However, they were not placed directly at the electric field peaks, so as not to shift the resonant frequency of the antenna significantly. It may be possible to employ a genetic algorithm, or other convergence technique, to determine the minimum number of diodes required, and the optimal locations for those diodes within the substrate. The problem would be constrained by a specified maximum level of allowable mutual coupling between the upper and lower patches, and also by a maximum allowable frequency shift when the diodes are reverse biased. It is unlikely that fewer than three diodes would yield an effective antenna. However, removing one of the diodes would decrease the power consumption.

Air Substrate

The first improvement to the DPRA would be to use an air dielectric for the lower anti-jam element substrate. This would cause the dimensions of the lower patch to approach $\lambda_0/2$. The result would be a more highly focussed radiation pattern, with higher zenith gain and reduced gain at negative elevation angles. This improvement could result in 20 dB attenuation of ground based interference, with respect to a standard aviation patch antenna. The prototype DPRA described in this thesis achieved 15 dB of raw RFI suppression. The reason Rohacell was chosen as the substrate for the prototype DPRA was that some degree of structural support was desired for the PIN diodes embedded within the lower patch. With an air dielectric, the lower patch would be free to flex in response to bending forces or vibration. This could damage the delicate PIN diodes after prolonged exposure to these forces. However, with access to better manufacturing techniques, it is conceivable that an arrangement could be found which provides structural support for the PIN diodes, yet allows the use of an air dielectric.

Dual-Frequency Antenna

An important extension of the DPRA described in this thesis is a dual-frequency version of the antenna. The upper patch would operate at the L1 frequency of 1,575.42 MHz, while the lower patch would operate at either the L5 or L2 frequencies of 1,176.45 MHz or 1,227.6 MHz, respectively. Civilian GPS signals may begin appearing on these frequencies as early as 2004. If there is no interference present, the antenna will function as dual frequency antenna, providing the capability to remove position errors associated with ionospheric delay. If strong RFI appears on one of the two frequencies, that particular patch antenna would be deactivated with the PIN diodes, leaving the other patch active, and the antenna will function as a standard single frequency antenna. This type of RFI mitigation can be classified as frequency diversity, as opposed to spatial diversity, which is the concept behind the DPRA.

Of course, this idea could be taken one step further, by envisioning a quad-patch

dual-frequency antenna. This antenna would be similar to the dual-frequency antenna just described, except that two additional $\lambda_0/2$ nearly-square patches would be available as well. If interference is detected on one frequency, say L1, the GPS receiver would switch to anti-jam mode on that frequency. If RFI on L1 were still jamming the receiver, both L1 patches would be deactivated, leaving the antenna to function as a single frequency antenna, on L5. If RFI is detected on L5 as well, the GPS receiver may switch to anti-jam mode on L5. At this point, the options for RFI mitigation are exhausted. But consider that this antenna concept provides three layers of protection against RFI, whereas the DPRA and dual-frequency DPRA provide only one, and a standard aviation patch provides none. This advanced antenna concept can be considered a dual spatial-frequency diversity antenna, and thus provides the most robust solution to GPS RFI considered in this thesis. Perhaps one day if the need arises for a simple yet effective GPS anti-jam antenna for the civil aviation community, these additional antenna concepts can be explored and put into practice.

Operation in a High Intensity RF Environment

The DPRA was flight tested in an RF friendly environment with a very small chance of damage due to electrostatic discharge, high-power transmitters, or lightning. The question arises as to how the antenna will perform in a high intensity RF environment, especially with respect to the delicate PIN diodes located at the antenna which would potentially be exposed to a variety of electromagnetic sources. High power RF transmissions from antennas located on the fuselage are likely to couple energy into the DPRA. Transmissions near multiples of 1,575.42 MHz are most likely to cause damage to the antenna, as high electric fields can be generated within the patch at these frequencies. If significant electric fields were generated across the diodes, they would generate and radiate harmonics as well. Very strong fields (at a level of 250 mW power dissipation per diode) would destroy the diodes. In addition, a single lightning strike would destroy the diodes, and a static discharge through the diodes would likely destroy them as well. The static discharge concern may be alleviated by simply placing high valued resistors in parallel with the diodes, so as to bleed

off any static charge which may build up on the patch elements. Some consideration of proper antenna placement would be necessary if the aircraft made use of high power RF sources (e.g., C-band radar). There is no protection available for lightning strikes. However, the DC current to the antenna may be monitored to determine whether damage had occurred due to lightning. The antenna would be replaced if it were determined that the PIN diodes had either been shorted or opened as a result of a lightning strike.

Appendix A

Relevant 2.5-D FDTD Equations

A.1 Split-Field PML Field Equations

The full set of split-field PML equations are given below for reference. Eqs.(A.1) – (A.12) are derived in Section 3.4.1 of Chapter 3.

$$A_\rho \mu \frac{\partial H_\rho^{s(\phi)}}{\partial t} + \Omega_\rho \mu H_\rho^{s(\phi)} = E_z^c - \rho M_\rho^{s(\phi)} \tag{A.1}$$

$$a_z \mu \frac{\partial H_\rho^{s(z)}}{\partial t} + \omega_z \mu H_\rho^{s(z)} = \frac{\partial E_\phi^s}{\partial z} - M_\rho^{s(z)} \tag{A.2}$$

$$a_\rho \mu \frac{\partial H_\phi^{c(\rho)}}{\partial t} + \omega_\rho \mu H_\phi^{c(\rho)} = \frac{\partial E_z^c}{\partial \rho} - M_\phi^{c(\rho)} \tag{A.3}$$

$$a_z \mu \frac{\partial H_\phi^{c(z)}}{\partial t} + \omega_z \mu H_\phi^{c(z)} = -\frac{\partial E_\rho^c}{\partial z} - M_\phi^{c(z)} \tag{A.4}$$

$$a_\rho \mu \frac{\partial H_z^{c(\rho)}}{\partial t} + \omega_\rho \mu H_z^{c(\rho)} = -\frac{\partial E_\phi^s}{\partial \rho} - M_z^{c(\rho)} \tag{A.5}$$

$$A_\rho \mu \frac{\partial H_z^{s(\phi)}}{\partial t} + \Omega_\rho \mu H_z^{s(\phi)} = -E_\phi^s - E_\rho^c - \rho M_z^{s(\phi)} \tag{A.6}$$

$$A_\rho \epsilon \frac{\partial E_\rho^{c(\phi)}}{\partial t} + (\Omega_\rho \epsilon + A_\rho \sigma) E_\rho^{c(\phi)} + \Omega_\rho \sigma \int_{-\infty}^{t} E_\rho^{c(\phi)}(\tau) d\tau = H_z^s - \rho J_\rho^{c(\phi)} \tag{A.7}$$

$$a_z \epsilon \frac{\partial E_\rho^{c(z)}}{\partial t} + (\omega_z \epsilon + a_z \sigma) E_\rho^{c(z)} + \omega_z \sigma \int_{-\infty}^{t} E_\rho^{c(z)}(\tau) d\tau = -\frac{\partial H_\phi^c}{\partial z} - J_\rho^{c(z)} \tag{A.8}$$

$$a_\rho \epsilon \frac{\partial E_\phi^{s(\rho)}}{\partial t} + (\omega_\rho \epsilon + a_\rho \sigma) E_\phi^{s(\rho)} + \omega_\rho \sigma \int_{-\infty}^{t} E_\phi^{s(\rho)}(\tau) d\tau = -\frac{\partial H_z^c}{\partial \rho} - J_\phi^{s(\rho)} \tag{A.9}$$

$$a_z \epsilon \frac{\partial E_\phi^{s(z)}}{\partial t} + (\omega_z \epsilon + a_z \sigma) E_\phi^{s(z)} + \omega_z \sigma \int_{-\infty}^{t} E_\phi^{s(z)}(\tau) d\tau = \frac{\partial H_\rho^s}{\partial z} - J_\phi^{s(z)} \tag{A.10}$$

$$a_\rho \epsilon \frac{\partial E_z^{c(\rho)}}{\partial t} + (\omega_\rho \epsilon + a_\rho \sigma) E_z^{c(\rho)} + \omega_\rho \sigma \int_{-\infty}^{t} E_z^{c(\rho)}(\tau) d\tau = \frac{\partial H_\phi^c}{\partial \rho} - J_z^{c(\rho)} \tag{A.11}$$

$$A_\rho \epsilon \frac{\partial E_z^{c(\phi)}}{\partial t} + (\Omega_\rho \epsilon + A_\rho \sigma) E_z^{c(\phi)} + \Omega_\rho \sigma \int_{-\infty}^{t} E_z^{c(\phi)}(\tau) d\tau = H_\phi^c - H_\rho^s - \rho J_z^{c(\phi)} \tag{A.12}$$

A.2 Discretized 2.5-D FDTD Equations with Split-Field PML

Maxwell's equations, as given by Eqs. (A.1) – (A.12), may be discretized by approximating $\partial f(x_n)/\partial x \approx (f(x_{n+1}) - f(x_{n-1}))/2\Delta x$, where x is a spatial variable (ρ, ϕ, z) or time (t), as applicable. The extensive algebraic manipulations required to carry out these operations are not presented here. However, the results are presented for completeness, and so that one can make use of them in another application, if

desired. The six magnetic field update equations are

$$H^{s(\phi)(n+1/2)}_{\rho(i+1/2,j+1/2)} = \frac{2A_\rho - \Omega_\rho \Delta t \mu_r}{2A_\rho + \Omega_\rho \Delta t \mu_r} H^{s(\phi)(n-1/2)}_{\rho(i+1/2,j+1/2)} + \frac{2\Delta t}{(2A_\rho + \Omega_\rho \Delta t \mu_r)\mu} E^{c(n)}_{z(i,j)}, \tag{A.13}$$

$$H^{s(z)(n+1/2)}_{\rho(i+1/2,j+1/2)} = \frac{2a_z - \omega_z \Delta t \mu_r}{2a_z + \omega_z \Delta t \mu_r} H^{s(z)(n-1/2)}_{\rho(i+1/2,j+1/2)} + \frac{2\Delta t}{(2a_z + \omega_z \Delta t \mu_r)\mu \Delta z} \left(E^{s(n)}_{\phi(i,j+1)} - E^{s(n)}_{\phi(i,j)} \right), \tag{A.14}$$

$$H^{c(\rho)(n+1/2)}_{\phi(i+1/2,j+1/2)} = \frac{2a_\rho - \omega_\rho \Delta t \mu_r}{2a_\rho + \omega_\rho \Delta t \mu_r} H^{c(\rho)(n-1/2)}_{\phi(i+1/2,j+1/2)} + \frac{2\Delta t}{(2a_\rho + \omega_\rho \Delta t \mu_r)\mu \Delta \rho} \left(E^{c(n)}_{z(i+1,j)} - E^{c(n)}_{z(i,j)} \right) - M^{c(\rho)(n+1/2)}_{\phi(i+1/2,j+1/2)}, \tag{A.15}$$

$$H^{c(z)(n+1/2)}_{\phi(i+1/2,j+1/2)} = \frac{2a_z - \omega_z \Delta t \mu_r}{2a_z + \omega_z \Delta t \mu_r} H^{c(z)(n-1/2)}_{\phi(i+1/2,j+1/2)} - \frac{2\Delta t}{(2a_z + \omega_z \Delta t \mu_r)\mu \Delta z} \left(E^{c(n)}_{\rho(i,j+1)} - E^{c(n)}_{\rho(i,j)} \right) - M^{c(z)(n+1/2)}_{\phi(i+1/2,j+1/2)}, \tag{A.16}$$

$$H^{s(\rho)(n+1/2)}_{z(i+1/2,j+1/2)} = \frac{2a_\rho - \omega_\rho \Delta t \mu_r}{2a_\rho + \omega_\rho \Delta t \mu_r} H^{s(\rho)(n-1/2)}_{z(i+1/2,j+1/2)} - \frac{2\Delta t}{(2a_\rho + \omega_\rho \Delta t \mu_r)\mu \Delta \rho} \left(E^{s(n)}_{\phi(i+1,j)} - E^{s(n)}_{\phi(i,j)} \right), \tag{A.17}$$

$$H^{s(\phi)(n+1/2)}_{z(i+1/2,j+1/2)} = \frac{2A_\rho - \Omega_\rho \Delta t \mu_r}{2A_\rho + \Omega_\rho \Delta t \mu_r} H^{s(\phi)(n-1/2)}_{z(i+1/2,j+1/2)} - \frac{2\Delta t}{(2A_\rho + \Omega_\rho \Delta t \mu_r)\mu} E^{c(n)}_{\rho(i,j)} - \frac{\Delta t}{(2A_\rho + \Omega_\rho \Delta t \mu_r)\mu} \left(E^{s(n)}_{\phi(i+1,j)} + E^{s(n)}_{\phi(i,j)} \right), \tag{A.18}$$

while the electric field update equations are

$$
\begin{aligned}
E^{c(\phi)(n+1)}_{\rho(i,j)} &= \frac{2A_\rho\epsilon - \Delta t(\Omega_\rho\epsilon + A_\rho\sigma)}{2A_\rho\epsilon + \Delta t(\Omega_\rho\epsilon + A_\rho\sigma)} E^{c(\phi)(n)}_{\rho(i,j)} + \frac{2\Delta t}{2A_\rho\epsilon + \Delta t(\Omega_\rho\epsilon + A_\rho\sigma)} H^{s(n+1/2)}_{z(i+1/2,j+1/2)} \\
&\quad - \frac{2\Omega_\rho\sigma\Delta t}{2A_\rho\epsilon + \Delta t(\Omega_\rho\epsilon + A_\rho\sigma)} \sum_{n'=-\infty}^{n} E^{c(\phi)(n')}_{\rho(i,j)}, \qquad \text{(A.19)}
\end{aligned}
$$

$$
\begin{aligned}
E^{c(z)(n+1)}_{\rho(i,j)} &= \frac{2a_z\epsilon - \Delta t(\omega_z\epsilon + a_z\sigma)}{2a_z\epsilon + \Delta t(\omega_z\epsilon + a_z\sigma)} E^{c(z)(n)}_{\rho(i,j)} \\
&\quad - \frac{2\Delta t}{(2a_z\epsilon + \Delta t(\omega_z\epsilon + a_z\sigma))\Delta z} \left(H^{c(n+1/2)}_{\phi(i+1/2,j+1/2)} - H^{c(n+1/2)}_{\phi(i+1/2,j-1/2)} \right) \\
&\quad - \frac{2\omega_z\sigma\Delta t}{2a_z\epsilon + \Delta t(\omega_z\epsilon + a_z\sigma)} \sum_{n'=-\infty}^{n} E^{c(z)(n')}_{\rho(i,j)}, \qquad \text{(A.20)}
\end{aligned}
$$

$$
\begin{aligned}
E^{s(\rho)(n+1)}_{\phi(i,j)} &= \frac{2a_\rho\epsilon - \Delta t(\omega_\rho\epsilon + a_\rho\sigma)}{2a_\rho\epsilon + \Delta t(\omega_\rho\epsilon + a_\rho\sigma)} E^{s(\rho)(n)}_{\phi(i,j)} \\
&\quad - \frac{2\Delta t}{(2a_\rho\epsilon + \Delta t(\omega_\rho\epsilon + a_\rho\sigma))\Delta\rho} \left(H^{s(n+1/2)}_{z(i+1/2,j+1/2)} - H^{s(n+1/2)}_{z(i-1/2,j+1/2)} \right) \\
&\quad - \frac{2\omega_\rho\sigma\Delta t}{2a_\rho\epsilon + \Delta t(\omega_\rho\epsilon + a_\rho\sigma)} \sum_{n'=-\infty}^{n} E^{s(\rho)(n')}_{\phi(i,j)}, \qquad \text{(A.21)}
\end{aligned}
$$

$$
\begin{aligned}
E^{s(z)(n+1)}_{\phi(i,j)} &= \frac{2a_z\epsilon - \Delta t(\omega_z\epsilon + a_z\sigma)}{2a_z\epsilon + \Delta t(\omega_z\epsilon + a_z\sigma)} E^{s(z)(n)}_{\phi(i,j)} \\
&+ \frac{2\Delta t}{(2a_z\epsilon + \Delta t(\omega_z\epsilon + a_z\sigma))\Delta z}\left(H^{s(n+1/2)}_{\rho(i+1/2,j+1/2)} - H^{s(n+1/2)}_{\rho(i+1/2,j-1/2)}\right) \\
&- \frac{2\omega_z\sigma\Delta t}{2a_z\epsilon + \Delta t(\omega_z\epsilon + a_z\sigma)} \sum_{n'=-\infty}^{n} E^{s(z)(n')}_{\phi(i,j)}, \qquad \text{(A.22)}
\end{aligned}
$$

$$
\begin{aligned}
E^{c(\rho)(n+1)}_{z(i,j)} &= \frac{2a_\rho\epsilon - \Delta t(\omega_\rho\epsilon + a_\rho\sigma)}{2a_\rho\epsilon + \Delta t(\omega_\rho\epsilon + a_\rho\sigma)} E^{c(\rho)(n)}_{z(i,j)} \\
&+ \frac{2\Delta t}{(2a_\rho\epsilon + \Delta t(\omega_\rho\epsilon + a_\rho\sigma))\Delta \rho}\left(H^{c(n+1/2)}_{\phi(i+1/2,j+1/2)} - H^{c(n+1/2)}_{\phi(i-1/2,j+1/2)}\right) \\
&- \frac{2\omega_\rho\sigma\Delta t}{2a_\rho\epsilon + \Delta t(\omega_\rho\epsilon + a_\rho\sigma)} \sum_{n'=-\infty}^{n} E^{c(\rho)(n')}_{z(i,j)}, \qquad \text{(A.23)}
\end{aligned}
$$

$$
\begin{aligned}
E^{c(\phi)(n+1)}_{z(i,j)} &= \frac{2A_\rho\epsilon - \Delta t(\Omega_\rho\epsilon + A_\rho\sigma)}{2A_\rho\epsilon + \Delta t(\Omega_\rho\epsilon + A_\rho\sigma)} E^{c(\phi)(n)}_{z(i,j)} \\
&+ \frac{\Delta t}{2A_\rho\epsilon + \Delta t(\Omega_\rho\epsilon + A_\rho\sigma)}\left(H^{c(n+1/2)}_{\phi(i+1/2,j+1/2)} + H^{c(n+1/2)}_{\phi(i-1/2,j+1/2)}\right) \\
&- \frac{2\Delta t}{2A_\rho\epsilon + \Delta t(\Omega_\rho\epsilon + A_\rho\sigma)} H^{s(n+1/2)}_{\rho(i+1/2,j+1/2)} \\
&+ \frac{2\Omega_\rho\sigma\Delta t}{2A_\rho\epsilon + \Delta t(\Omega_\rho\epsilon + A_\rho\sigma)} \sum_{n'=-\infty}^{n} E^{c(\phi)(n')}_{z(i,j)}. \qquad \text{(A.24)}
\end{aligned}
$$

Appendix B

Microstrip Design Formulas

B.1 Effective Permittivity

The effective relative permittivity ($\epsilon_{r,eff}$) of a microstrip patch antenna is a very important parameter. Any error in $\epsilon_{r,eff}$ will result in an error in the estimated resonant frequency of the patch. One formula for ($\epsilon_{r,eff}$) obtained by curve fitting empirical data is described in the literature [30] and reproduced in Eq. (B.6). The first step is to compute the relative permittivity at DC. This is given by

$$\epsilon_{r,0} = \frac{\epsilon_r + 1}{2} + \frac{\epsilon_r - 1}{2}\left(1 + \frac{10}{u}\right)^{-ab}, \tag{B.1}$$

where

$$a = 1 + \frac{1}{49}\ln\left[\frac{u^4 + (u/52)^2}{u^4 + 0.432}\right] + \frac{1}{18.7}\ln\left[1 + \left(\frac{u}{18.1}\right)^3\right], \tag{B.2}$$

$$b = 0.564\left(\frac{\epsilon_r - 0.9}{\epsilon_r + 0.3}\right)^{0.053}, \tag{B.3}$$

$$u = \frac{W}{t}. \tag{B.4}$$

Referring to Fig. B.1, W is the width of the radiating wall, and t is the thickness of the dielectric substrate. Next, dynamic effects are taken into account by computing

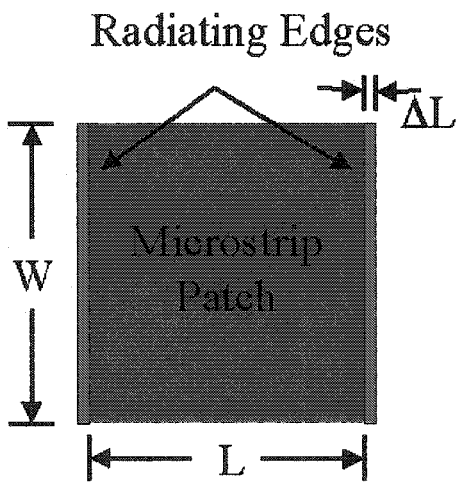

Figure B.1: Microstrip Patch Dimensions.

ξ_f using

$$
\begin{aligned}
f_n &= f_{\mathrm{GHz}} t_{\mathrm{mm}}, \\
\xi_1 &= 0.27488 + u\left(0.6315 + \frac{0.525}{(1+0.0157 f_n)^{20}}\right) - 0.065683 e^{-8.7513u}, \\
\xi_2 &= 0.33622\left(1 - e^{-0.03442\epsilon_r}\right), \\
\xi_3 &= 0.0363 e^{-4.6u}\left(1 - e^{-(f_n/38.7)^{4.97}}\right), \\
\xi_4 &= 1 + 2.751\left(1 - e^{-(\epsilon_r/15.916)^8}\right), \\
\xi_f &= \xi_1 \xi_2 [(0.1844 + \xi_3 \xi_4) f_n]^{1.5763}.
\end{aligned} \tag{B.5}
$$

Finally, the effective permittivity at the design frequency is computed using Eqs. (B.1) and (B.5), and is expressed as

$$
\epsilon_{r,eff} = \epsilon_r - \frac{\epsilon_r - \epsilon_{r,0}}{1 + \xi_f}. \tag{B.6}
$$

The accuracy of Eq. (B.6) is better than 0.2% for $\epsilon_{r,eff} \leq 128$ and $0.01 \leq u \leq 100$.

B.2 Microstrip Patch Wall Extension

In addition to estimating the effective permittivity of the patch, it is also important to determine the effective increase in the length of the patch, due to fringing fields. Referring again to Fig. B.1, the effective extension of the patch beyond the physical edge of the patch wall is defined as ΔL. The most popular and nearly universal expression for the extension of the microstrip patch antenna wall is given by the Hammerstad equation [3]

$$\frac{\Delta L}{t} = 0.412\frac{(\epsilon_{r,eff} + 0.3)(W/t + 0.264)}{(\epsilon_{r,eff} - 0.258)(W/t + 0.8)}. \tag{B.7}$$

Although Eq. (B.7) yields excellent results, improved expressions exist for the effective length extension. One such formulation is given in Eq. (B.8) [30]. It was obtained by fitting functions to empirical data. Accuracy of Eq. (B.8) is better than 2.5% for $\epsilon_r < 50$ and $0.01 < W/t < 100$.

$$\frac{\Delta L}{t} = \frac{\xi_1\xi_3\xi_5}{\xi_4}, \tag{B.8}$$

with

$$\begin{aligned}
\xi_1 &= 0.434907\frac{\epsilon_{r,eff}^{0.81} + 0.26}{\epsilon_{r,eff}^{0.81} - 0.189}\frac{(W/t)^{0.8544} + 0.236}{(W/t)^{0.8544} + 0.87},\\
\xi_2 &= 1 + \frac{(W/t)^{0.371}}{2.358\epsilon_r + 1},\\
\xi_3 &= 1 + \frac{0.5274\arctan[0.084(W/t)^{1.9413/\xi_2}]}{\epsilon_{r,eff}^{0.9236}},\\
\xi_4 &= 1 + 0.0377\arctan[0.067(W/t)^{1.456}]\{6 - 5e^{0.036(1-\epsilon_r)}\},\\
\xi_5 &= 1 - 0.218e^{-7.5W/t}.
\end{aligned}$$

These expressions are rather cumbersome, and difficult to program, but they yield excellent results.

Appendix C

MNM Segment Mutual Admittance

The purpose of this appendix is to derive the mutual impedance between the source and observation segments on the wall of a rectangular patch antenna. The geometry of the patch is shown in Fig. C.1. The source segment is denoted by r, is centered at (x_r, y_r), and has width Δ_r. The observation segment q is centered at (x_q, y_q) and has width Δ_q. The mutual admittance between segments q and r is determined by evaluating the reaction integral

$$Y_{qr}^{ext} = -\frac{1}{V_q V_r} \iint_{S'_q} \vec{M}_q \cdot \vec{H}_{qr} \, dS, \tag{C.1}$$

where S'_q is the surface of the observation segment q. Because the segment widths are very small (typically 0.05 λ_0), and since there is no field variation in the z direction, the double integral in Eq. (C.1) need not be rigorously evaluated, but may be approximated by assuming the kernel to be constant over the width of each segment.

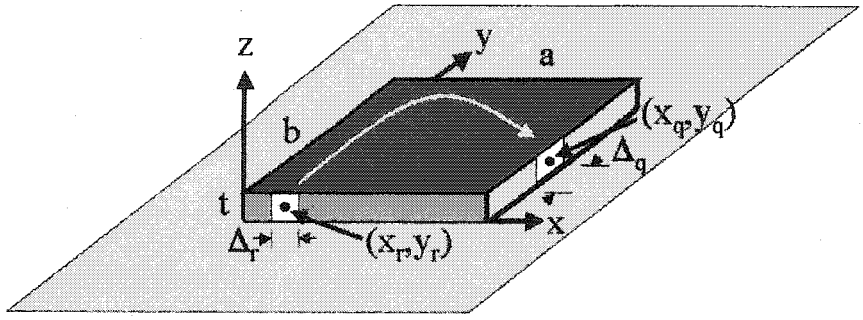

Figure C.1: Segment Geometry.

With this assumption, Eq. (C.1) simplifies as follows

$$Y_{qr}^{ext} = -\frac{1}{V_q V_r} \int_0^t \int_{x_q-\Delta_q/2}^{x_q+\Delta_q/2} (\vec{E}_q \times \hat{n}_q) \cdot \vec{H}_{qr} \, dx'_q \, dz', \tag{C.2}$$

$$= -\frac{t}{V_q V_r} \int_{x_q-\Delta_q/2}^{x_q+\Delta_q/2} (\vec{E}_q \times \hat{n}_q) \cdot \vec{H}_{qr} \, dx'_q, \tag{C.3}$$

$$\approx -\frac{\Delta_q t(-\frac{V_q}{t}\hat{z} \times \hat{n}_q) \cdot \vec{H}_{qr}}{V_q V_r}, \tag{C.4}$$

and finally,

$$Y_{qr}^{ext} \approx \left. \frac{\Delta_q(\hat{z} \times \hat{n}_q) \cdot \vec{H}_{qr}}{V_r} \right|_{q=1\ldots Q,\, r=1\ldots Q.} \tag{C.5}$$

Note that the magnetic current $\vec{M}_q$ at the wall perimeter is not doubled, as is customary when evaluating radiation from patch antennas mounted on an infinite ground plane. The reason for this is that in evaluating Eq. (C.1), $\vec{M}_q$ is the physical magnetic current at the aperture, not the equivalent current. In other words, segment q is not considered to be radiating, so $\vec{M}_q = \vec{E}_q \times \hat{n}_q$. On the other hand, segment r is the radiating segment, and while computing $\vec{H}_{qr}$, one needs to consider the image current as well. In this case, $\vec{M}_r = 2\vec{E}_r \times \hat{n}_r$. The magnetic field present at segment q due to radiation from segment r is denoted by $\vec{H}_{qr} = H_{x,qr}\hat{x} + H_{y,qr}\hat{y}$, and is found by

solving [2]

$$H_{x,qr} = \frac{t}{j4\pi k_0 Z_0} \iint_{C'} G_1 M_{x,r} + (x_q - x_r')G_2$$
$$\times \left[(x_q - x_r')M_{x,r} + (y_q - y_r')M_{y,r}\right] e^{-jk_0 R} dx_r' dy_r', \tag{C.6}$$
$$H_{y,qr} = \frac{t}{j4\pi k_0 Z_0} \iint_{C'} G_1 M_{y,r} + (y_q - y_r')G_2$$
$$\times \left[(x_q - x_r')M_{x,r} + (y_q - y_r')M_{y,r}\right] e^{-jk_0 R} dx_r' dy_r', \tag{C.7}$$

with

$$G_1 = \frac{-1 - jk_0 R + k_0^2 R^2}{R^3}, \tag{C.8}$$
$$G_2 = \frac{3 + j2k_0 R - k_0^2 R^2}{R^5}, \tag{C.9}$$

and

$$R = \sqrt{(x_q - x_r)^2 + (y_q - y_r)^2}. \tag{C.10}$$

Eqs. (C.6) and (C.7) are evaluated as follows,

$$H_{x,qr} = \frac{t}{j4\pi k_0 Z_0} M_{x,r} \int_{x_r - \Delta_r/2}^{x_r + \Delta_r/2} \left[G_1 + (x_q - x_r')^2 G_2\right] e^{-jk_0 R}\, dx_r'$$
$$+ \frac{t}{j4\pi k_0 Z_0} M_{y,r} \int_{y_r - \Delta_r/2}^{y_r + \Delta_r/2} G_2 (x_q - x_r)(y_q - y_r') e^{-jk_0 R} dy_r', \tag{C.11}$$
$$H_{y,qr} = \frac{t}{j4\pi k_0 Z_0} M_{x,r} \int_{x_r - \Delta_r/2}^{x_r + \Delta_r/2} G_2 (x_q - x_r')(y_q - y_r) e^{-jk_0 R} dx_r'$$
$$+ \frac{t}{j4\pi k_0 Z_0} M_{y,r} \int_{y_r - \Delta_r/2}^{y_r + \Delta_r/2} \left[G_1 + (y_q - y_r')^2 G_2\right] e^{-jk_0 R}\, dy_r'. \tag{C.12}$$

Since the magnetic current at the source segment is a known function of the z directed electric field present at the segment ($\vec{M}_r = 2\vec{E}_r \times \hat{n}_r$), Eqs. (C.11) and (C.12) can be

further simplified to

$$H_{x,qr} = \frac{E_z t}{j2\pi k_0 Z_0}[(\hat{z}\times\hat{n}_r)\cdot\hat{x}]\int_{x_r-\Delta_r/2}^{x_r+\Delta_r/2}\left[G_1+(x_q-x_r')^2G_2\right]e^{-jk_0R}\,dx_r'$$
$$+\frac{E_z t}{j2\pi k_0 Z_0}[(\hat{z}\times\hat{n}_r)\cdot\hat{y}]\int_{y_r-\Delta_r/2}^{y_r+\Delta_r/2}G_2(x_q-x_r)(y_q-y_r')e^{-jk_0R}dy_r', \tag{C.13}$$
$$H_{y,qr} = \frac{E_z t}{j2\pi k_0 Z_0}[(\hat{z}\times\hat{n}_r)\cdot\hat{x}]\int_{x_r-\Delta_r/2}^{x_r+\Delta_r/2}G_2(x_q-x_r')(y_q-y_r)e^{-jk_0R}dx_r'$$
$$+\frac{E_z t}{j2\pi k_0 Z_0}[(\hat{z}\times\hat{n}_r)\cdot\hat{y}]\int_{y_r-\Delta_r/2}^{y_r+\Delta_r/2}\left[G_1+(y_q-y_r')^2G_2\right]e^{-jk_0R}\,dy_r'. \tag{C.14}$$

Although Eqs. (C.13) and (C.14) can be evaluated numerically, this procedure is slow. Instead, it was assumed that the source segment width Δ_r is small, so that the kernel of the integrals is approximately constant in the interval Δ_r. This same assumption was made in Eq. (C.4), for the observation segment q. With this assumption, Eqs. (C.13) and (C.14) simplify to

$$H_{x,qr} \approx \frac{\Delta_r V_r}{j2\pi k_0 Z_0}\,e^{-jk_0R}\,(\hat{n}_r\times\hat{z})$$
$$\cdot\left\{\hat{x}\left[G_1+(x_q-x_r)^2G_2\right]+\hat{y}\,G_2(x_q-x_r)(y_q-y_r)\right\}, \tag{C.15}$$
$$H_{y,qr} \approx \frac{\Delta_r V_r}{j2\pi k_0 Z_0}\,e^{-jk_0R}\,(\hat{n}_r\times\hat{z})$$
$$\cdot\left\{\hat{x}\,G_2(x_q-x_r)(y_q-y_r)+\hat{y}\left[G_1+(y_q-y_r)^2G_2\right]\right\}. \tag{C.16}$$

Eqs. (C.15) and (C.16) may be substituted into Eq. (C.5) to obtain a final expression for the mutual admittance between segments q and r,

$$Y_{qr}^{ext} = \frac{\Delta_q\Delta_r e^{-jk_0R}}{j2\pi k_0 Z_0}(\hat{n}_q\times\hat{z})\cdot\vec{G}_{qr}\Big|_{\substack{q=1\ldots Q\\ r=1\ldots Q,}} \tag{C.17}$$

where $\vec{G}_{qr} = G_{x,qr}\hat{x} + G_{y,qr}\hat{y}$, and is given by

$$G_{x,qr} = (\hat{z} \times \hat{n}_r) \cdot \left\{\hat{x}\left[G_1 + (x_q - x_r)^2 G_2\right] + \hat{y}\, G_2(x_q - x_r)(y_q - y_r)\right\}, \tag{C.18}$$

$$G_{y,qr} = (\hat{z} \times \hat{n}_r) \cdot \left\{\hat{x}\, G_2(x_q - x_r)(y_q - y_r) + \hat{y}\left[G_1 + (y_q - y_r)^2 G_2\right]\right\}. \tag{C.19}$$

Note that Y_{qr}^{ext} is strictly a function of geometry, as all reference to the sources $\vec{M}_q$ and $\vec{M}_r$ has cancelled. This makes sense, since the mutual admittance between two apertures should not be a function of the strength of the sources at those apertures. Eq. (C.17) is compact and can be evaluated quickly.

Bibliography

[1] I. J. Bahl and P. Bhartia. *Microstrip Antennas.* Artech House, Boston, MA, 1980.

[2] C. A. Balanis. *Advanced Engineering Electromagnetics.* John Wiley and Sons, Inc., New York, New York, 1989.

[3] C. A. Balanis. *Antenna Theory: Analysis and Design.* John Wiley and Sons, Inc., New York, New York, 1997.

[4] F. N. Bauregger. The Dielectric Cavity Antenna - an Alternative to the Choke Ring Antenna. *Proceedings of the Institute of Navigation National Technical Meeting ION-NTM*, January 2001.

[5] F. N. Bauregger. A Novel Dual-Patch Anti-Jam GPS Antenna. *Proceedings of the 58th Institute of Navigation Annual Meeting*, June 2002.

[6] F. N. Bauregger. Flight Trials of a Novel Dual-Patch Anti-Jam GPS Antenna. *Proceedings of the Institute of Navigation National Technical Meeting ION-NTM*, January 2002.

[7] A. Benalla and K. C. Gupta. Multiport Network Model and Transmission Characteristics of Two-Port Rectangular Microstrip Patch Antennas. *IEEE Transactions on Antennas and Propagation*, AP-38(10):1337 – 1342, October 1988.

[8] J. Berenger. A Perfectly Matched Layer for the Absorption of Electromagnetic Waves. *Journal of Computational Physics*, 114:185 – 200, October 1994.

[9] J. Berenger. Three-Dimensional Perfectly Matched Layer for the Absorption of Electromagnetic Waves. *Journal of Computational Physics*, 127:363 – 379, 1996.

[10] W. D. Burnside et al. *NEWAIR3 Airborne Antenna Radiation Pattern Code.* Ohio State University Electroscience Laboratory, September 1985.

[11] E. V. Byron. A New Flush-Mounted Antenna Element for Phased Array Application. *Proceedings of the Phased-Array Antenna Symposium*, pages 187 – 192, 1970.

[12] K. R. Carver and J. W. Mink. Microstrip Antenna Technology. *IEEE Transactions on Antennas and Propagation*, AP-29(1):2 – 24, January 1981.

[13] M. M. Casabona and M. W. Rosen. Discussion of GPS Anti-Jam Technology. November 1999.

[14] National Geophysical Data Center. *International Geomagnetic Reference Field 4.0.* National Oceanic and Atmospheric Administration, 1999.

[15] NOAA Aviation Weather Center. *Aviation Flight Conditions.* http://aviationweather.noaa.gov/awc/afc.html.

[16] Y. Chen, R. Mittra, and P. Harms. Finite-Difference Time-Domain Algorithm for Solving Maxwell's Equations in Rotationally Symmetric Geometries. *IEEE Transactions on Microwave Theory and Techniques*, MTT-44(6):832 – 839, June 1996.

[17] P. J. B. Clarricoats and A. D. Oliver. *Corrugated Horns for Microwave Antennas.* Peter Peregrinus, London, 1984.

[18] J. R. Clynch et al. Multiple GPS RFI Sources in a Small California Harbor. *Proceedings of the Institute of Navigation ION-GPS Conference*, September 2002.

[19] H. Stewart Cobb. *GPS Pseudolites: Theory, Design, and Applications.* Ph.D. Thesis, Stanford University, Stanford, CA 94305, September 1997.

[20] Federal Communications Commission. *Code of Federal Regulations, Part 15 – Radio Frequency Devices.* Washington D.C., October 2000.

[21] Composite Structures Technology. *http://www.cstsales.com.* Material Data.

[22] Rogers Corporation. TMM Temperature Stable Microwave Laminate. *Data Sheet*, TM1.1000.

[23] A. G. Derneryd. Linearly Polarized Microstrip Antennas. *IEEE Transactions on Antennas and Propagation*, AP-24(6):846 – 851, November 1976.

[24] P. Enge. Local Area Augmentation of GPS for the Precision Approach of Aircraft. *Proceedings of the IEEE*, 87(1):111 – 132, January 1999.

[25] P. Enge and P. Misra. *Global Positioning System – Signals, Measurements, and Performance.* Ganga-Jamuna Press, Lincoln, MA, 2001.

[26] R. Faulkner. *Personal Communication.* NovAtel Corporation, 31 August 2000.

[27] D. J. Frankowski. *Personal Communication.* Union Carbide Corporation, 30 August 2000.

[28] R. A. Fuller. *Aviation Utilization of Geostationary Satellites for the Augmentation to GPS: Ranging and Data Link.* Ph.D. Thesis, Stanford University, Stanford, CA 94305, May 2000.

[29] M. Fusco. FDTD Algorithm in Curvilinear Coordinates. *IEEE Transactions on Antennas and Propagation*, AP-38(1):76 – 89, January 1990.

[30] R. Garg et al. *Microstrip Antenna Design Handbook.* Artech House, Boston, MA, 2001.

[31] D. Gebre-Egziabher. *Design and Performance Analysis of a Low-Cost Aided Dead Reckoning Navigator.* Ph.D. Thesis, Stanford University, Stanford, CA 94305, December 2001.

[32] S. D. Gedney. An Anisotropic Perfectly Matched Layer-Absorbing Medium for the Truncation of FDTD Lattices. *IEEE Transactions on Antennas and Propagation*, AP-44(12):1630 – 1639, December 1996.

[33] H. Gershanoff. Russian GPS Jammer Introduced. *Journal of Electronic Defense*, August 1999.

[34] M. Geyer and R. Frazier. FAA GPS RFI Mitigation Program. *Proceedings of the Institute of Navigation ION-GPS Conference*, September 1999.

[35] E. O. Hammerstad. Equations for Microstrip Circuit Design. *Proceedings of the Fifth European Microwave Conference*, pages 268 – 272, September 1975.

[36] R. F. Harrington. *Field Computation by Moment Methods.* IEEE Press, Piscataway, New Jersey, 1993.

[37] G. Hein et al. Status of Galileo Frequency and Signal Design. *Proceedings of the Institute of Navigation ION-GPS Conference*, September 2002.

[38] G. Hiller. Design with PIN Diodes. *MA-COM Application Note*, AG312.

[39] S. Houck. *Multi Aircraft Dynamics, Navigation and Operation.* Ph.D. Thesis, Stanford University, Stanford, CA 94305, April 2001.

[40] J. Q. Howell. Microstrip Antennas. *Antenna and Propagation Society International Symposium Digest*, pages 177 – 180, December 1972.

[41] A. D. Hutchinson and J. Weitzen. Television Interference to GPS. *Presentation to the ION GPS Test Standards Working Group*, June 1994.

[42] J. R. James et al. *Microstrip Antenna Theory and Design.* Peter Peregrinus, London, 1981.

[43] S. S. Jan et al. Matlab Simulation Toolset for SBAS Availability Analysis. *Proceedings of the Institute of Navigation ION-GPS Conference*, September 2001.

[44] P.-S. Kildal. Artificially Soft and Hard Surfaces in Electromagnetics. *IEEE Transactions on Antennas and Propagation*, AP-38(10):1537 – 1544, October 1990.

[45] R. G. Kouyoumjian and P. H. Pathak. A Uniform Geometrical Theory of Diffraction for an Edge in a Perfectly Conducting Surface. *Proceedings of the IEEE*, 62(11):1448 –1461, November 1974.

[46] L. Kovarcik, CFI. *Personal Communication.* February 2003.

[47] Y. T. Lo, C. E. Skupien, and S. S. Zhong. A Study of Microstrip Antennas for Multiple Band Operation. *Report RADC-TR-82-236*, September 1982.

[48] M. Luo et al. Potential Interference to GPS from UWB Transmitters: Test Plan Version 4.5. May 2000.

[49] M. Luo et al. Potential Interference to GPS from UWB Transmitters, Phase II Test Results. March 2001.

[50] S. Maci, S. Raffaelli, M. Leoncini, L. Borselli, and P.-S. Kildal. Analysis of Surface-Wave Excitation and Radiation Mechanisms of a Monopole on a Circular Grounded Dielectric Slab with Critical Thickness. *IEE Proceedings on Microwaves, Antennas and Propagation*, 143(4):335 – 340, August 1996.

[51] R. E. Munson. Single Slot Cavity Antennas Assembly. *U. S. Patent No. 3 713 162*, January 1973.

[52] G. Mur. Absorbing Boundary Conditions for the Finite-Difference Approximation of the Time Domain Electromagnetic Field Equations. *IEEE Transactions on Electromagnetic Compatibility*, EMC-23:377 – 382, November 1981.

[53] S. Mutlu and M. I. Aksun. Hybrid Model for Probe-Fed Rectangular Microstrip Antennas with Shorting Pins. *IEEE Antennas and Propagation Society International Symposium*, 3:1448 – 1451, 2000.

[54] P. Ngamjanyaporn and M. Krairiksh. Switched-Beam Single Patch Antenna. *Electronics Letters*, 38(1):7 – 8, January 2002.

[55] Office of Architecture and Investment Analysis (ASD-1). *Navigation and Landing Transition Strategy.* FAA, Washington D.C., August 1995.

[56] Office of Architecture and Investment Analysis (ASD-1). *Navigation and Landing Transition Strategy.* FAA, Washington D.C., August 2002.

[57] Department of Defense and Department of Transportation. *1994 Federal Radionavigation Plan.* Washington D.C., May 1995.

[58] U.S. Department of Defense. *GPS Standard Positioning Service Performance Standard.* Washington D.C., October 2001.

[59] V. Palanisamy and R. Garg. Analysis of Arbitrarily Shaped Microstrip Patch Antennas Using Segmentation Technique and Cavity Model. *IEEE Transactions on Antennas and Propagation*, AP-34(10):1028 – 1213, October 1986.

[60] D. M. Pozar. *Microwave Engineering.* John Wiley and Sons, Inc., New York, New York, 1998.

[61] W. F. Richards, Y. T. Lo, and D. D. Harrison. An Improved Theory for Microstrip Antennas and Applications. *IEEE Transactions on Antennas and Propagation*, AP-29(1):38 – 46, January 1981.

[62] P. Rutten et al. *Is Moore's Law Infinite? The Economics of Moore's Law.* Kellogg School of Management, Northwestern University, 2001.

[63] G. G. Sanford. Conformal Microstrip Phased Array for Aircraft Tests with ATS-6. *Proceedings of the National Electronics Conference*, 29:252 – 257, October 1974.

[64] RTCA SC-159. Minimum Operational Performance Standards for GNSS Airborne Antenna Equipment. *RTCA/DO-228*, October 1995.

[65] RTCA SC-159. Minimum Operational Performance Standards for Global Positioning System/Wide Area Augmentation System Airborne Equipment. *RTCA/DO-229C*, November 2001.

[66] RTCA SC-159. Assessment of Radio Frequency Interference Relevant to the GNSS. *RTCA/DO-235A*, December 2002.

[67] P. C. Sharma and K. C. Gupta. Analysis and Optimized Design of Single Feed Circularly Polarized Microstrip Antennas. *IEEE Transactions on Antennas and Propagation*, AP-31(6):949 – 955, November 1983.

[68] K. L. Shlager and J. B. Schneider. A Selective Survey of the Finite-Difference Time-Domain Literature. *IEEE Antennas and Propagation Magazine*, 37(4):39 – 56, August 1995.

[69] D. Sievenpiper et al. High-Impedance Electromagnetic Surfaces with a Forbidden Frequency Band. *IEEE Transactions on Microwave Theory and Techniques*, 47:2059 – 2074, November 1999.

[70] M. R. Spiegel and J. Liu. *Mathematical Handbook of Formulas and Tables, Second Edition.* McGraw-Hill, New York, New York, 1999.

[71] B. Stockbroeckx and A. Vander Vorst. Asymptotic Green's Function of a Surface Magnetic Current Element on a Perfect Electric Conductor Plane Covered by a Lossy Dielectric Substrate. *IEEE Transactions on Antennas and Propagation*, AP-47(2):309 – 316, February 1999.

[72] W. L. Stutzman and G. A. Thiele. *Antenna Theory and Design.* John Wiley and Sons, Inc., New York, New York, 1998.

[73] T. Walter. *Personal Communication.* Stanford GPS WAAS Laboratory, February 2002.

[74] A. Taflove. *Computational Electrodynamics: The Finite Difference Time Domain Method.* Artech House, Boston, MA, 1995.

[75] F. L. Teixeira and W. C. Chew. PML-FDTD in Cylindrical and Spherical Grids. *IEEE Microwave and Guided Wave Letters*, 7(9):285 – 287, September 1997.

[76] F. L. Teixeira and W. C. Chew. A Nonuniform Cylindrical FDTD Algorithm with Improved PML and Quasi-PML Absorbing Boundary Conditions. *IEEE Transactions on Geoscience and Remote Sensing*, 37(2):1066 – 1072, March 1999.

[77] F. L. Teixeira and W. C. Chew. Finite-Difference Computation of Transient Electromagnetic Waves for Cylindrical Geometries in Complex Media. *IEEE Transactions on Geoscience and Remote Sensing*, 38(4):1530 – 1543, July 2000.

[78] Florida International University. *Aeronautic Learning Laboratory for Science, Technology, and Research.* http://www.allstar.fiu.edu/aerojava/.

[79] A. van de Capelle. A Simple Accurate Formula for the Radiation Conductance of a Microstrip Patch Antenna. *IEEE Antennas and Propagation Symposium Digest*, pages 23 – 26, 1981.

[80] P. W. Ward. GPS Receiver RF Interference Monitoring, Mitigation, and Analysis Techniques. *Journal of Navigation*, 41(4):367 – 391, Winter 1994.

[81] H. D. Weinschel. Progress Report on Development of Microstrip Cylindrical Arrays for Sounding Rockets. *Physics and Science Lab, New Mexico State University*, 1973.

[82] F. Yang and Y. Rahmat-Samii. A Reconfigurable Patch Antenna Using Switchable Slots for Polarization Diversity. *IEEE Microwave and Wireless Components Letters*, 12(3):96 – 98, March 2002.

[83] K. S. Yee. Numerical Solution of Initial Boundary Value Problems Involving Maxwell's Equations in Isotropic Media. *IEEE Transactions on Antennas and Propagation*, AP-14(3):302 – 307, May 1966.

[84] Z. Ying, P.-S. Kildal, and A. A. Kishk. Study of Different Realizations and Calculation Models for Soft Surfaces by Using a Vertical Monopole on a Soft

Disk as a Test Bed. *IEEE Transactions on Antennas and Propagation*, AP-44(11):1474 – 1481, November 1996.